Arterial-Spin-Labeling-Sequenzentwicklung zur Optimierung der 3 T- & 7 T-Perfusionsbildgebung und zur Permeabilitätsmodellierung

DISSERTATION

zur

Erlangung des Doktorgrades (Dr. rer. nat.)

der

Mathematisch-Naturwissenschaftlichen Fakultät

der

Rheinischen Friedrich-Wilhelms-Universität Bonn

vorgelegt von

Martin Schidlowski

aus Detmold

Bonn, November 2021

Angefertigt mit Genehmigung der Mathematisch-Naturwissenschaftlichen Fakultät der
Rheinischen Friedrich-Wilhelms-Universität Bonn

1. Gutachter: Prof. Dr. Tony Stöcker
2. Gutachter: Prof. Dr. Frank Bertoldi

Tag der Promotion: 31. März 2022
Erscheinungsjahr: 2022

Abstract

Pseudo-continuous arterial spin labeling (pCASL) is a magnetic resonance technique for imaging and quantifying cerebral blood flow. Magnetically labeled arterial blood serves as an endogenous tracer. Special extensions of the fundamental method fascilitate a modeling of additional physiological parameters besides cerebral perfusion. Good quantifiability and non-invasiveness make pCASL of interest for clinical use and for scientific research, which is enhanced by a wide availability and technical development of magnetic resonance scanners. The first 7 Tesla ultra-high field scanner has been approved for clinical use in 2017. Stronger magnetic fields provide the advantages of a higher signal-to-noise ratio (SNR) and a longer persisting pCASL signal. However, magnetic field inhomogeneities and energy limitations make an application more difficult.

This thesis contributes to pCASL-based perfusion measurements and a modeling of blood-brain barrier permeabilities at 3 Tesla and it addresses the challenges to further develop pCASL imaging at 7 Tesla.

The first part focuses on the development and application of pCASL for the quantitative measurement of cerebral blood flow at 3 Tesla. An efficient pCASL encoding method using Hadamard matrices is implemented and its theoretical advantages are experimentally demonstrated. Application-optimized protocols and a data processing pipeline are obtained. In vivo measurements confirm a solid data quality. The applicability for clinical measurements is demonstrated in a single case. A test-retest measurement series reveals the suitability for longitudinal and multicenter studies.

The second part considers the T_2 relaxation of the pCASL signal at 3 Tesla. It focuses on a T_2-based investigation of the tracer transition from the intravascular to the extravascular compartment and a potential inference on the blood-brain barrier integrity. Therefore, a sequence module is implemented for the acquisition of T_2-weighted data and a study protocol implemented. Additionally, the reliability of quantitative T_2 times is validated within a test-retest study. Then, a modeling approach is developed to compartmentalize the pCASL tracer into intra- and extravascularly localized fractions based on the T_2 times. Additional supplementing measurements and highly simplified model assumptions stabilize the compartmentalization

model, as demonstrated in vivo. As a result, pCASL-T_2 times may be a relevant parameter for the investigation of physiological processes.

The third part addresses the implementation of pCASL measurements at 7 Tesla. Parallel pulse transmission techniques adapt the magnetic labeling pulses to compensate for non-ideal magnetic field distributions. Multiple adjustment concepts are implemented in a 7 Tesla pCASL sequence. Simulations and first in vivo investigations, using some of these methods, demonstrate a feasibility also at ultra-high field and an improvement of the pCASL signal compared to non-adjusting approaches.

Zusammenfassung

Die pseudo-kontinuierliche arterielle Spinmarkierung (pCASL) ist ein Verfahren der Magnetresonanzperfusionsbildgebung zur Darstellung und Quantifizierung des zerebralen Blutflusses. Bei dieser Technik wird einströmendes, arterielles Blut magnetisch markiert und so als körpereigener Tracer verwendet. Durch spezielle Erweiterungen eröffnen sich Ansätze, neben der zerebralen Perfusion, zusätzliche physiologische Parameter zu modellieren. Die einfache Quantifizierbarkeit und die Nicht-Invasivität, sowie die Verfügbarkeit und technische Entwicklung von Magnetresonanztomographen machen dieses Verfahren interessant für klinische und für wissenschaftliche Anwendungen. Im Jahr 2017 wurde der erste 7 Tesla Ultrahochfeld-Scanner für die klinische Anwendung zugelassen. Stärkere Magnetfelder bieten die Vorteile eines höheren Signal-zu-Rausch-Verhältnisses und eines länger bestehenden pCASL-Signals. Gleichzeitig führen Magnetfeldinhomogenitäten und Energieeinschränkungen zu einer erschwerten Anwendbarkeit.

Die vorliegende Arbeit befasst sich mit der pCASL-basierten Perfusionsmessung und einer Modellierung von Blut-Hirn-Schranken-Durchlässigkeiten bei 3 Tesla, sowie der Sequenzweiterentwicklung zur Messung perfusionsgewichteter Daten bei 7 Tesla.

Der erste Teil konzentriert sich auf die Entwicklung und Anwendung von pCASL zur quantitativen Messung des zerebralen Blutflusses bei 3 Tesla. In diesem Rahmen wird ein effizientes pCASL-Kodierungsverfahren mittels Hadamard-Matrizen implementiert. Dessen theoretischen Vorteile werden experimentell gezeigt. Es resultieren anwendungsoptimierte Protokolle und eine Auswertungspipeline. In vivo Messungen bestätigen eine solide Datenqualität. Die Eignung für klinische Messungen wird an einem Einzelfall demonstriert. Die Ergebnisse einer Test-Retest-Messreihe lassen auf die Eignung für longitudinale und multizentrische Studien schließen.

Der zweite Teil beschäftigt sich mit der T_2-Relaxation des pCASL-Signals bei 3 Tesla. Dabei stehen die T_2-basierte Untersuchung des Tracerübergangs aus dem intravaskulären in das extravaskuläre System und ein möglicher Schluss auf die Integrität der Blut-Hirn-Schranke im Fokus. Für die Aufnahme T_2-gewichteter

Daten wird ein geeigetes Sequenzmodul implementiert und ein Studienprotokoll entworfen. Innerhalb einer Test-Retest-Studie wird die Zuverlässigkeit quantitativer T_2-Zeiten validiert. In einem zweiten Schritt wird ein Modellierungsverfahren erarbeitet, um den pCASL-Tracer, basierend auf den gemessenen T_2-Zeiten, in intra- und extravaskuläre Anteile zu kompartmentalisieren. In vivo Messungen demonstrieren eine Stabilisierung des Kompartmentalisierungsmodells durch das Hinzuziehen von Hilfsmessungen und die Anwendung stark vereinfachter Modellannahmen. Es resultiert eine potenzielle Relevanz von pCASL-T_2-Zeiten als Parameter für die Untersuchung physiologischer Prozesse.

Der dritte Teil befasst sich mit der Realisierung von pCASL-Messungen bei 7 Tesla. Spezielle Techniken der parallelen Pulstransmission passen die Pulse, welche die magnetischen Markierung vornehmen, an nicht-idealen Magnetfeldverteilungen an. Es werden verschiedene Anpassungskonzepte in einer 7 Tesla pCASL-Sequenz implementiert. Simulationen und erste in vivo Messungen mit einem Teil dieser Verfahren zeigen neben der Realisierbarkeit im Ultrahochfeld eine Verbesserung des pCASL-Signals gegenüber bisherigen, nicht-anpassenden Ansätzen.

Contents

1

Introduction

1.1 Motivation & thesis outline

Today, magnetic resonance imaging (MRI) is a routine imaging technique for a non-invasive clinical and scientific investigation of the human brain. Besides a purely anatomical structural imaging, this technique also allows the analysis of brain function and physiology. (Detre 2006; Symms et al. 2004)

The cerebral blood flow is such a physiological parameter of interest. It is used for the investigation of numerous diseases as stroke, cancer and epilepsy, but also for the study of neurodegenerative processes (Alsop et al. 2014). There already exist clinically established conventional imaging techniques for this purpose, including positron emission tomography (PET), single photon emission computed tomography (SPECT), computed tomography (CT), and contrast agent-based dynamic susceptibility contrast (DSC) MRI. However, these methods have not only the disadvantage of radiation or contrast agent exposure but also the difficulty of quantifying physiological values. Pseudo-continuous arterial spin labeling is a completely non-invasive MRI perfusion imaging technique, which can be performed on conventional MRI scanners and fascilitates a simple quantification, but is clinically not yet established. (Borogovac & Asllani 2012; Grade et al. 2015)

The blood-brain barrier permeability is another physiological parameter which is difficult to access with established methods. Previous studies have shown matched pCASL sequences and modeling approaches for investigating this parameter. However, these methods showed disadvantages in terms of spatial resolution, scan duration, or modeling robustness. (Gregori et al. 2012; Heye et al. 2014; Lawrence et al. 2011; Lin et al. 2018; Liu et al. 2010; Ohene et al. 2019; Veiseh et al. 2009; Wells et al. 2009; Wells et al. 2012)

An essential prerequisite for the clinical and (neuro)scientific relevance of pCASL perfusion imaging is the availability of suitable sequences and measurement protocols that provide solid data quality within a reasonable scan time. It involves adequate robustness, reliability, accuracy, and reproducibility. In 2015, a consensus proposal was made by the ISMRM Perfusion Study Group as an attempt to provide a sequence and protocol direction (Alsop et al. 2014).

A further, to-date not fully used potential of pCASL imaging arises from the development of new ultra-high field MRI scanners. Higher magnetic fields provide the advantages of an improved signal-to-noise ratio and a longer pCASL tracer lifetime. At present, however, technical challenges limit the applicability, in particular due to SAR limitations and magnetic field inhomogeneities, causing an inefficient labeling. (Meixner et al. 2021; Teeuwisse et al. 2010; Tong et al. 2020; Wang et al. 2021)

This work addresses the abovementioned potentials and challenges. It aims to make pCASL accessible by a translation between MRI physical development and clinical-scientific application. After an introduction to the fundamentals of magnetic resonance and pCASL perfusion imaging, and an overview of human brain anatomy and perfusion physiology, this thesis is divided into three main parts:

The first part, Chapter [4], presents the practical in vivo application of pCASL perfusion measurements at 3 Tesla. For clinical and scientific use, the sequence is extended by the efficient Hadamard encoding method. Protocols and a suitable data processing routine are developed. Measurements with elderly subjects are performed to investigate the suitability for the use in multicenter, longitudinal population studies. Additionally, the clinical feasibility is demonstrated in a single epilepsy patient.

The second part, Chapter [5], focuses on the T_2 relaxation of the pCASL signal at 3 Tesla. A T_2 preparation module is implemented to introduce a T_2 weighting. The reliability of obtained pCASL signal T_2 times is investigated within a test-retest measurement series. In order to compartmentalize the pCASL tracer into intravascularly and extravascularly localized fractions based on T_2 times, study protocols and a data modeling procedure are developed.

The third part, Chapter [6], covers the implementation of pCASL measurements at 7 Tesla on a parallel pulse transmission (pTx)-based system. The background suppression is optimized to the higher field. pTx-based B_1 adjustment techniques are implemented, from which full pTx spoke pulses are simulated. Further static pTx shimming approaches and setups are analyzed by B_1 mapping. Finally, these are also applied in vivo and compared with CP mode measurements.

1.2 Academic output & scientific contributions

Journal publications

Schidlowski M, Boland M, Rüber T and Stöcker T (2020). Blood-brain barrier permeability measurement by biexponentially modeling whole-brain arterial spin labeling data with multiple T2-weightings. NMR Biomed 33:e4374, doi:10.1002/nbm.4374.

Schidlowski M, Stirnberg R, Stöcker T and Rüber T (2020). Reliability of quantitative transverse relaxation time mapping with T2-prepared whole brain pCASL. SciRep 10:18299, doi: 10.1038/s41598-020-74680-y.

Schidlowski M, Bauer T, David B, Bitzer F, Ostermann L, Racz A, von Wrede R, Radbruch A, Stöcker T, Surges R and Rüber T (2021). Ictal hypoperfusion and iron deposition in symptomatogenic zone of epilepsia partialis continua - A case report. Seizure 89:56-58, doi:10.1016/j.seizure.2021.04.019.

Zimmer T S, David B, Broekaart D W M, **Schidlowski M**, Ruffolo G, Korotkov A, van der Wel N N, van Rijen P C, Mühlebner A, van Hecke W, Baayen J C, Idema S, François L, van Eyll J, Dedeurwaerdere S, Kessels H W, Surges R, Rüber T, Gorter J A, Mills J D, van Vliet E A and Aronica E (2021). Seizure-mediated iron accumulation and dysregulated iron metabolism after status epilepticus and in temporal lobe epilepsy. Acta Neuropathol, doi:10.1007/s00401-021-02348-6.

Neumann K, **Schidlowski M**, Günther M, Stöcker T and Düzel E (2021). Reliability and reproducibility of Hadamard encoded pseudo-continuous arterial spin labeling in healthy elderly. Front Neurosci, doi:10.3389/fnins.2021.711898.

Conference proceedings

Schidlowski M, Boland M, Rüber T and Stöcker T (2019). Cerebral spin compartmentalization based on biexponential modeling of T2-prepared pseudo-continuous arterial spin labeling 3D GRASE MRI data. In proceedings of the 5th Scientific Meeting of the International Society for Magnetic Resonance in Medicine.

Schidlowski M, Boland M, Rüber T and Stöcker T (2020). Cerebral spin compartmentalization based on biexponential modeling of T2-prepared pCASL 3D GRASE data. In proceedings of the 27th Scientific Meeting of the International Society for Magnetic Resonance in Medicine.

Schidlowski M, Boland M, Rüber T and Stöcker T (2020). Zerebrale Spin-Kompartimentalisierung durch biexponentielle Modellierung T2-gewichteter ASL-MRT-Daten. In proceedings of the 93th Congress of the German Society for Neurology (DGN). (Best Poster Award: Interdisciplinary Research)

Conference contributions

Annual Meeting on Imaging and Electrophysiology (AMIE, 2019). Scientific Symposium: MR Physics - Advanced Neuroimaging Methods. Contribution: MRI of Brain Perfusion (**Schidlowski M**).

Annual Meeting on Imaging and Electrophysiology (AMIE, 2020). Scientific Symposium: MR-Physics - Finding your focus on MRI today and tomorrow. Workshop Co-Organizers and Chairs: **Schidlowski M** and Carmichael D.

1.3 Abbreviations

ACQ, Acquistion
AFI, Actual Flip Angle Imaging
AFP, Adiabatic Full-Passage
AHP Adiabatic Half-Passage
ANOVA, Analysis Of Variance
AP, Anterior-Posterior
ASL, Arterial Spin Labeling
ATT, Arterial Transit Time
BA, Basilar Artery
BBB, Blood-Brain Barrier
BS, Background Suppression
BW, Bandwidth
CAIPIRINHA, Controlled Aliasing In Parallel Imaging Results In Higher Acceleration
CBF, Cerebral Blood Flow
CP, Circular Polarized
CSF, Cerebrospinal Fluid
CT pair, Control-Tag Pair
DIM, Dimension
DSC, Dynamic Susceptibility Contrast
DUR, Duration
EPC, Epilepsia Partialis Continua
EPI, Echo-Planar Imaging
ETL, Echo Train Length
EV, Extravascular
FA, Flip Angle
FFT, Fast Fourier Transform
FH, Foot-Head
FID, Free Induction Decay
FLAIR, Fluid-Attenuated Inversion Recovery
FLASH, Fast Low Angle Shot
FOV, Field Of View
FSL, FMRIB's Software Library
FWHM, Full Width At Half Maximum
G, Gradient
Gd, Gadolinium
GKM, General Kinetic Model
GM, Gray Matter
GOIA, Gradient-Modulated Offset-Independent Adiabaticity
GRAPPA, Generalized Autocalibrating Partial Parallel Acquisition
GRASE, Gradient And Spin Echo
GRE, Gradient Echo
HAD, Hadamard
HS, Hyperbolic Secant
ICC, Intraclass Correlation Coefficient
ICE, Image Reconstruction Environment
IV, Intravascular
LD, Labeling Duration
LICA, Left Internal Carotid Arteries
LV, Left Vertebral Arteries
MEAS, Measurement(s)
MIP, Maximum Intensity Projection
MLEV, Malcom Levitt
MNI, Montreal Neurological Institute
MPRAGE, Magnetization Prepared Rapid Gradient Echo
MRI, Magnetic Resonance Imaging
MT, Magnetization Transfer
NLLS, Non-Linear Least Squares
NMR, Nuclear Magnetic Resonance
PA, Posterior-Anterior
PAT, Parallel Acquisition Techniques
pCASL, Pseudocontinuous Arterial Spin Labeling
PF, Partial Fourier
PFF, Partial Fourier Factor
pTx, Parallel Transmission
PC, Phase Correction
PE, Phase Encoding
PI, Parallel Imaging
PLD, Post Labeling Delay
PPD, pTx Pulse Design
PROT, Protocol
QSM, Quantitative Susceptibility Mapping
RF, Radio Frequency
RICA, Right Internal Carotid Arteries
RL, Right-Left
ROI, Region Of Interest
RV, Right Vertebral Arteries

SAR, Specific Absorption Rate
SDD, Smallest Detectable Difference
SE, Spin Echo
SEG, Segment
SLSQP, Sequential Least Squares Programming
SNR, Signal-To-Noise Ratio
STA, Small-Tip-Angle Approximation
sTx, Single Transmission
TA, Acquisition Time
TBW, Time-Bandwidth Product
TE, Echo Time
TI, Inversion Time
TMS, Transcranial Magnetic Stimulation
TR, Repetition Time
tSNR, Temporal SNR
T2Prep, T_2 Preparation
UI, User Interface
VERSE, Variable-Rate Selective Excitation
VOI, Voxel Of Interest
VOP, Virtual Observation Point
WET, Water Suppression Enhanced Through T_1 Effects
WM, White Matter
WSCV, Within-Subject Coefficient Of Variation
WURST, Wideband Uniform Rate Smooth Truncation

2

Fundamentals of MRI

Nuclear magnetic resonance (NMR) was discovered independently by two research groups from Harvard and Stanford University in 1946. Edward Purcell (Harvard) and Felix Bloch (Stanford) were part of these groups (Hecht 1967; Slichter 1963). The research of nuclear magnetic resonance imaging started in the 1970s, and the first MR image was published by Paul Lauterbur in 1973 (Bernstein et al. 2004; Davidovits 2008). Today, MRI has become an important investigational technique in medicine and science (Jancke 1998; Meyerand et al. 1999). The subsequent presentation of the NMR and MRI principles is based on the work of (Abragam 1961; Callaghan 1993) and additional references are given in the respective sections. It also includes contents of the author's Bachelor thesis *Concentration analysis and structure elucidation of emulsions and microcapsules by single and multivoxel spectroscopy* submitted to the Faculty of Physics at TU Dortmund University in 2015.

2.1 Physical principles of NMR

The total angular momentum of an atomic nucleus is termed nuclear spin. In the following, hydrogen protons, or H-nuclei, will be considered as they are commonly used for NMR imaging. Hydrogen protons have the nuclear spin $\vec{I} = \frac{1}{2}$, which causes a magnetic moment $\vec{\mu}$ (Carrington & McLachlan 1969). The relation between both quantities is given by the gyromagnetic ratio γ (Slichter 1963):

$$\vec{\mu} = \gamma \vec{I}. \tag{2.1}$$

The gyromagnetic ratio of hydrogen protons is 42.58 MHz/T.

In classical mechanics, particles with $\vec{I} = \frac{1}{2}$ can align themselves in parallel or antiparallel to an external homogeneous magnetic field $B_0 = \vec{B}\vec{e}_z$, resulting in two possible spin states. The difference in energy between both states is

$$\Delta E = \hbar \gamma B_0, \tag{2.2}$$

with the Planck constant $h = 2\pi\hbar$. Without an external magnetic field B_0, both spin states are of equal energy which is called degenerate. The separation induced by B_0 is known as the nuclear Zeeman effect.

The ratio between the quantity of nuclei located in the higher energy level ($N_\uparrow$) and those found in the lower energy level ($N_\downarrow$) is given by the Boltzmann distribution. It is approximated by (Hecht 1967; Slichter 1963)

$$\frac{N_\uparrow}{N_\downarrow} = \mathrm{e}^{-\frac{\hbar\gamma B_0}{k_\mathrm{B} T}}, \tag{2.3}$$

where k_B is the Boltzman constant and T the system temperature. There is a higher probability for spins to be in the lower energetic condition. Consequently, it is possible to flip spins, which is to bring nuclei from the lower to the higher energy level. This is accomplished by the application of radio frequency fields (radio frequency, RF) of an energy which equals the energy difference between both levels (Bushberg et al. 2001):

$$\hbar\omega_\mathrm{RF} = \Delta E = \hbar\gamma B_0 = \hbar\omega_0, \tag{2.4}$$

where ω_0 is called Larmor angular frequency with the resulting Larmor frequency $f_0 = \frac{\omega_0}{2\pi}$ (Farrar 1989).

The Larmor frequency depends on the magnetic field strength and is found via the gyromagnetic ratio. It amounts to 128 MHz for hydrogen protons in 3 T and 298 MHz in 7 T magnetic fields.

Summing up all magnetic moments $\vec{\mu}_n$ within a voxel gives the total macroscopic magnetization

$$\vec{M} = \begin{pmatrix} M_\mathrm{x} \\ M_\mathrm{y} \\ M_\mathrm{z} \end{pmatrix} = \sum_n \vec{\mu}_n. \tag{2.5}$$

If an external magnetic field is applied, magnetic moments align along this field in an Boltzmann distribution, which leads to a macroscopic magnetization M_0. To simplify, a B_0 field axis in z-direction is assumed subsequently. Accordingly, the z-component of the magnetization is named longitudinal magnetization M_z.

Quantum mechanics provide a complete theory of NMR, however its complexity would be beyond the scope of an introduction to the NMR principle. One crucial feature following from such comprehensive considerantions is the possibility to tip M_0 off its equilibrium by applying RF pulses (short: pulse) with a magnetic field B_1, which is oriented orthogonally to B_0. This produces a magnetization fraction perpendicular to B_0, denoted as the transverse magnetization M_xy. (Weishaupt et al. 2008)

If the magnetization is not aligned to the magnetic field B_0, a torque acts on the magnetization. It causes the transverse magnetization M_xy to precess around the B_0 field axis at Larmor angular frequency ω_0. The precessing transverse magnetization M_xy can be detected with receiver coils, as it induces an electric current. For comprehensibility, the perspective of a coordinate system rotating with ω_0 is considered (rotating frame of reference). Therein, it applies to the induced signal S (Bernstein et al. 2004):

$$S(t) \propto \int \mathrm{d}V \rho(\vec{r}) \mathrm{e}^{\mathrm{i}\omega_0 t}. \tag{2.6}$$

When deflecting the magnetization through RF pulses, the flip angle (FA) α is linearly dependent on the pulse

duration t and the magnetic field strength B_1 or the pulse frequency ω_1, respectively (Farrar 1989):

$$\alpha = \gamma B_1 t = \omega_1 t. \tag{2.7}$$

The signal obtained immediately after an excitation is called the free induction decay (FID).

Energy absorbed from excitation pulses is released back by the nuclei. This causes the preceding magnetization to relax, which restores the longitudinal and reduces the transverse magnetization. In the fully relaxed state, there is approximately only longitudinal magnetization present. The longitudinal relaxation is characterized by the T_1 relaxation time. The transverse relaxation is described by the T_2 relaxation time. These two relaxation processes are independent and their characterizing time constant depends not only on the nucleus but also on the belonging molecule and the surrounding matter.

The dynamics of magnetization $\vec{M}$ due to excitation, precession and relaxation processes in an external magnetic field $\vec{B}$ is described by the Bloch equations:

$$\frac{\mathrm{d}\vec{M}(t)}{\mathrm{d}t} = \gamma(\vec{M}(t) \times \vec{B}(t)) + \begin{pmatrix} -\frac{1}{T_2} & 0 & 0 \\ 0 & -\frac{1}{T_2} & 0 \\ 0 & 0 & -\frac{1}{T_1} \end{pmatrix} \vec{M}(t) + \begin{pmatrix} 0 \\ 0 \\ \frac{1}{T_1} \end{pmatrix} M_0. \tag{2.8}$$

Longitudinal relaxation is based on spin interaction with the homogeneous magnetic field and denoted as spin-lattice relaxation. Energy is released by entering the equilibrium state, which is absorbed by the environment considered as the lattice. Following a 90° pulse, longitudinal relaxation occurs according to (Bernstein et al. 2004; Suetens 2009):

$$M_\mathrm{z}(t) = M_0(1 - \mathrm{e}^{-\frac{t}{T_1}}). \tag{2.9}$$

Transverse relaxation results from interactions among the spins and is termed spin-spin relaxation. This causes a dephasing of the individual spins and the transverse magnetization decreases (Bernstein et al. 2004; Suetens 2009):

$$M_\mathrm{xy}(t) = M_\mathrm{xy}(0)\mathrm{e}^{-\frac{t}{T_2}}. \tag{2.10}$$

There are further effects, including magnetic field inhomogeneities, which contribute to a dephasing of the spin system and thus accelerate the relaxation. Accounting for these, an effective, shortened transverse relaxation time T_2^* can be defined (Farrar 1989; Hecht 1967):

$$\frac{1}{T_2^*} = \frac{1}{T_2} + \frac{1}{T_2^\mathrm{B}} \tag{2.11}$$

T_2 represents the dephasing time constant based on spin-spin interactions and T_2^B the one due to magnetic field inhomogeneities (Hecht 1967; Farrar 1989). In general, the relation $T_1 \geq T_2 \geq T_2^*$ is valid, because the transverse magnetization must decay before the equilibrium magnetization is restored and the consideration of additional dephasing effects causes a faster transverse magnetization decrease (Farrar 1989). Dephasing due to magnetic field inhomogeneities can be compensated via spin refocusing using 180° pulses and a subsequent rephasing. Contrary, the T_2-induced loss of coherence is irreversible (Bernstein et al. 2004; Suetens 2009).

2.2 Image formation (MRI)

NMR imaging or MRI is based on the visualization of spin densities, for which spatial encoding of the MR signal is required. By applying a linear magnetic field gradient $\vec{G} = (\frac{\partial B_z}{\partial x}, \frac{\partial B_z}{\partial y}, \frac{\partial B_z}{\partial z})$, the Larmor frequency becomes linearly dependent on the position within the gradient (Bernstein et al. 2004; Suetens 2009):

$$\omega(\vec{r}) = \gamma(B_0 + \vec{G}\vec{r}). \tag{2.12}$$

A constant gradient induces a specific phase of the spins dependent on time and position:

$$\phi(\vec{r}, t) = \int_0^t \gamma\vec{r}\vec{G}(t)\mathrm{d}t = \gamma\vec{r}\vec{G}t. \tag{2.13}$$

The introduction of the k-space (Bernstein et al. 2004; Bushberg et al. 2001), constructed by the vectors

$$\vec{k}_{\mathrm{x,y,z}} = \vec{k} = \gamma \int_0^t \vec{G}(t)\mathrm{d}t, \tag{2.14}$$

which represent spatial frequencies, simplifies the phase:

$$\vec{\phi}(\vec{k}, \vec{r}) = \vec{k}\vec{r}. \tag{2.15}$$

The signal (Bernstein et al. 2004) in the time domain

$$S(t) = \int \rho(\vec{r})\mathrm{e}^{\mathrm{i}\phi(\vec{r},t)}\mathrm{d}\vec{r} = \int \rho(\vec{r})\mathrm{e}^{\mathrm{i}\gamma\vec{G}\vec{r}t}\mathrm{d}\vec{r} \tag{2.16}$$

corresponds to

$$S(\vec{k}) = \int \rho(\vec{r})\mathrm{e}^{\mathrm{i}\vec{k}\vec{r}}\mathrm{d}\vec{r} \tag{2.17}$$

in frequency domain or k-space, ignoring relaxation effects.

Through systematic gradient switching, the k-space can be pointwise sampled on a Cartesian grid and the measured signal allocated to the respective location. The Fourier transform of the signals for each gradient direction gives a spectrum which corresponds to a projection of the spin density onto the respective gradient. The resultant spatial information of the spin density enables the generation of an image. Nonlinearities of the gradient system cause displacements on the spatial assignment and lead to artifacts, unless the mismatch is taken into account. (Bernstein et al. 2004; Bushberg et al. 2001)

Spatial encoding, or the sampling of the k-space (see e.g. Figure [2.4]B), is commonly achieved via frequency encoding, phase encoding and slice selection. For that purpose, three orthogonal gradients $G_{\mathrm{x,y,z}}$ are applied

in an appropriate sequence, with their directions being assigned to one of the encoding methods. (Bernstein et al. 2004; Worthoff et al. 2012)

The frequency encoding gradient G_x is applied during readout and therefore termed readout gradient. Thereby, the precession frequencies of the spins become dependent on the gradient strength and location in x-direction. A constant gradient G_x corresponds to a uniform traversal of the $\vec{k}_\mathrm{x}$ vector.

The phase encoding gradient G_y is applied temporarily between spin excitation and signal acquisition. In that way, the spins acquire an additional position-dependent phase $\phi(y,t)$. It persists after switching off the gradient and allows spatial allocation in this direction. G_y defines a specific $\vec{k}_\mathrm{y}$ value, so a stepwise variation of G_y must be performed in order to sample all $\vec{k}_\mathrm{y}$ components.

A surface is mapped by the vectors $\vec{k}_\mathrm{x}$ and $\vec{k}_\mathrm{y}$. For imaging, its thickness can be controlled via slice selection. Therefore, a slice selection gradient G_z is applied concurrently with RF pulses. The external magnetic field strength B_0 is maintained only at the location z_0 and the RF pulse only excites spins within the z_0-slice, as only these spins precess at a frequency within the bandwidth BW_RF of the pulse. The slice position z_0 depends on the RF pulse mean frequency ω_RF (Bernstein et al. 2004):

$$z_0 = \frac{\omega_\mathrm{RF} - \omega_0}{\gamma G_\mathrm{z}}. \tag{2.18}$$

The slice thickness is

$$\Delta z = \frac{BW_\mathrm{RF}}{\gamma G_\mathrm{z}}. \tag{2.19}$$

Broadband pulses excite thicker layers Δz. Correspondingly, a stronger gradient G_z leads to stronger shifts of the resonance frequency ω_0 and allows the selection of thinner layers.

A rectangular, slice-selective excitation is often realized using sinc-shaped pulses ($\mathrm{sinc}(x) = \frac{\sin(x)}{x}$), since their Fourier transform corresponds to rectangular-shaped functions (Bushberg et al. 2001). A 3D image can be obtained, by repeating the experiment with an appropriate variation of the RF pulse frequency offset and by merging the single 2D slice data or images subsequently.

Fourier transform of the k-space data from the plane defined by the vectors $\vec{k}_\mathrm{x}$- and $\vec{k}_\mathrm{y}$ creates a 2π-periodic image. The image area constrained to a single period is known as field of view (FOV) (Suetens 2009):

$$FOV_\mathrm{x,y} = \frac{2\pi}{\Delta k_\mathrm{x,y}} \quad \text{with} \quad \Delta k_\mathrm{x} = \gamma G_\mathrm{x} \Delta t_\mathrm{x} \quad \text{and} \quad \Delta k_\mathrm{y} = \gamma t_\mathrm{y} \Delta G_\mathrm{y}. \tag{2.20}$$

Here, Δk denotes the distance of adjacent points in k-space due to the discrete sampling. Δt_x represents the sampling rate of the frequency encoding, ΔG_y the increment of the phase encoding gradient strength and t_y the duration of the applied phase encoding gradient.

The spatial resolution of the image depends on the number of k-space points acquired within a FOV (Suetens 2009):

$$\Delta x = \frac{FOV_{\mathrm{x}}}{N_{\mathrm{x}}} = \frac{1}{2k_{\mathrm{x,max}}}, \Delta y = \frac{FOV_{\mathrm{y}}}{N_{\mathrm{y}}} = \frac{1}{2k_{\mathrm{y,max}}}. \tag{2.21}$$

N_{x} is the number of measured data points in frequency encoding direction and N_{y} is the number of phase encoding steps.

2.3 Imaging sequences

MR images can be derived from acquired k-space data via an inverse Fourier transform. So-called imaging (pulse) sequences are available for the purpose of measuring all or part of the needed k-space data. Thereby, two basic concepts for signal generation are distinguished: the gradient echo and the spin echo. Besides a separate application, it is also possible to combine both approaches within a single MRI sequence. (Bernstein et al. 2004)

2.3.1 Spin echo

A classical spin echo experiment, as for example the fast spin echo experiment (Figure [2.1]), starts with a (90°) excitation pulse, applied together with a slice selection gradient. This causes longitudinal magnetization of hydrogen protons, which are localized within the selected slice, to be (partially) transferred into transverse magnetization. The slice selection gradient G_{z} dephases the spins inside the slice. They are rephased with an inverted gradient $-G_{\mathrm{z}}$, which has half of the area of G_z and is applied subsequently. After excitation, spins in the transverse plane progressively dephase due to field inhomogeneities, leading to a T_2^*-weighted exponential signal decay, the FID. After the time $\frac{TE}{2}$ a refocusing pulse is applied, which leads to a refocusing of the magnetization within the selected slice. At TE, the phase coherence of the rephasing spins maximizes and so does the detectable signal.

Such a signal maximum succeeding a refocusing pulse is referred to as spin echo. It is the signal to be measured and may be 2D spatially encoded as shown in Figure [2.1]. A single k-space line is acquired by application of a phase encoding gradient and a subsequent frequency encoding during readout. The experiment is repeated, modifying the phase encoding gradient strength to measure another k-space line. For a faster sampling of the k-space, it is possible to refocus on half-integer echo times with an adjustment of the phase encoding gradient strength, instead of measuring a single k-space line after excitation. In this way, multiple k-space lines are acquired within the repetition time TR. This technique is used in so-called fast spin echo sequences.

Due to symmetry, the refocusing compensates T_2^*- but not T_2-relaxation processes, so that a repetitive refocusing results in a progressive T_2-weighted signal decay. (Bernstein et al. 2004; Jung & Weigel 2013; Mugler 2014)

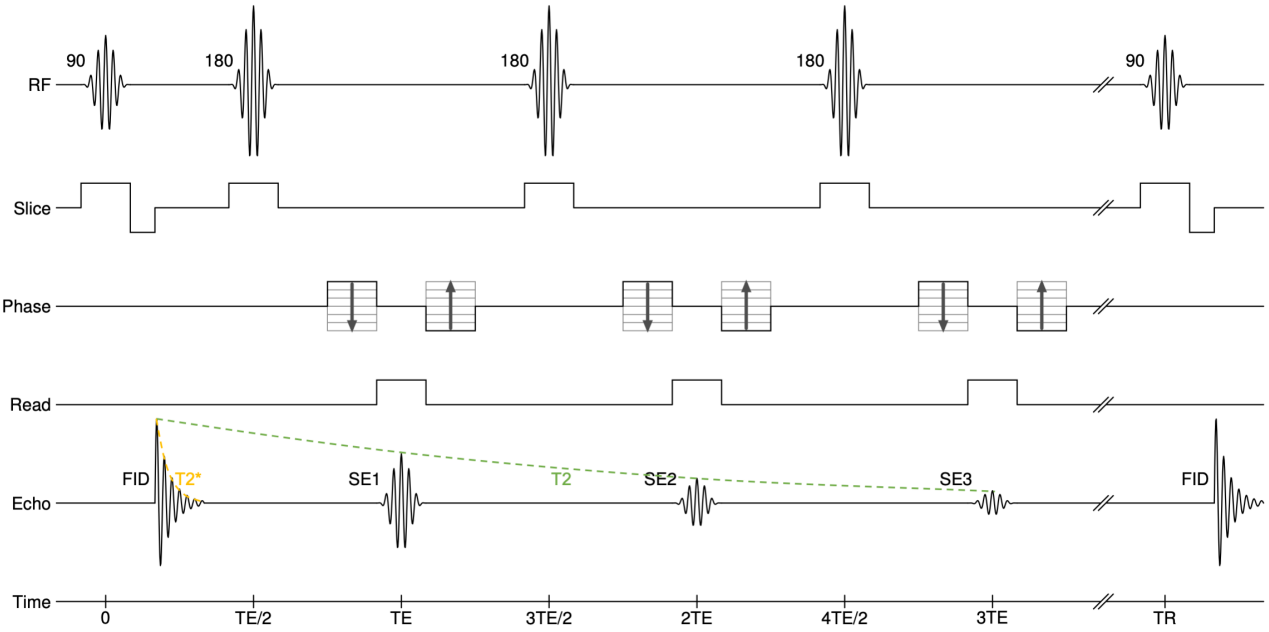

Figure 2.1: Sequence diagram of a fast spin echo experiment. Multiple spin echoes (SE) are generated through the application of refocusing pulses at the spacings $n \cdot TE$.

2.3.2 Gradient echo

A simple gradient echo (GRE) experiment (Figure [2.2]) is commonly started with a slice-selective excitation with the flip angle α. A compensation of the gradient-induced dephasing is achieved by a subsequent gradient inversion ($-G_z$). The FID signal is first dephased with a phase encoding gradient G_y and a prephaser $-G_x$. The readout gradient G_x rephases the signal in readout direction and generates a gradient echo at the time of maximal phase coherence TE. This gradient-induced peaking signal is termed a gradient echo.

For k-space sampling, a single k-space line is selected by a phase encoding gradient immediately after excitation and acquired with a frequency encoding gradient. The experiment is then repeated with adjusted phase encoding gradient areas to sample other k-space lines.

As the FID is acquired, shorter echo times are chosen by comparison to spin echo experiments. Often flip angles $\alpha < 90°$ are used, so that only a part of the magnetization is transferred to the transverse plane and the remaining longitudinal magnetization is available for the next repetition, which allows to realize short repetition times TR. In case of very short TR, the remaining transverse magnetization is dephased by so-called spoiler gradients at the end of each repetition, which causes an isotropic distribution of the spins' phases across the voxel. In this way, these do not contribute to the signal by a potential unintended refocusing in the subsequent repetitions.

As no 180° refocusing pulses are used, it is not required to wait for a refocused echo, so a gradient echo can be acquired within a shorter time compared to the spin echo. Therefore, the gradient echo experiment also does not compensate for the T_2^*-weighted dephasing. (Bernstein et al. 2004; Markl & Leupold 2012)

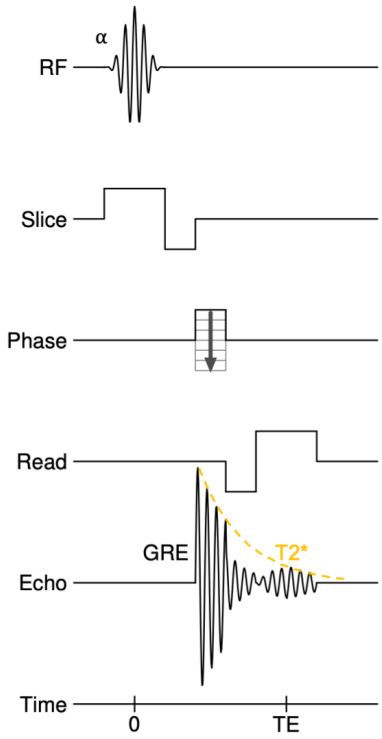

Figure 2.2: Sequence diagram of a simple gradient echo experiment. The gradient echo signal arising at TE is induced by a prior de- and rephasing gradient.

2.3.3 3D GRASE

The 3D gradient-and-spin-echo (GRASE) sequence is a hybrid imaging sequence involving both spin and gradient echoes (Figure [2.3]). It is introduced with a thick slice- or volume-selective excitation, which is followed by a series of non-selective refocusings at times corresponding to the half-integer echo times $\frac{n}{2} \cdot TE_{\mathrm{GRASE}}$. At full-integer echo times $n \cdot TE_{\mathrm{GRASE}}$ a spin echo is generated centrally between each successive pair of refocusing pulses. Spoiler gradients are applied before and after the refocusing pulses to dephase the FID signal.

For encoding of a k-space plane or partition, a second phase encoding gradient in slice direction is temporarily applied after the refocusing pulses. Correspondingly, the second phase encoding direction is termed partition encoding. Frequency encoding gradients are used to generate gradient echoes symmetrically surrounding the spin echo. The k-space of the current partition is sampled by incremental application of phase encoding gradients between two gradient echoes. A single gradient echo corresponds to one k-space line and the phase encoding steps to the k-space line distance. The serpentine-like sampling is shown in Figure [2.4]B. After the sampling of a partition, the partition encoding is reversed by the inverted gradient. Repeated refocusings along with modulated partition encoding gradient areas can be used to acquire further partitions, which can be merged to fill k-space.

A full k-space sampling after a single excitation is termed a single shot sequence. The number of succeeding refocusings or measured spin echoes is denotet as echo train length (ETL). The T_2-weighted spin echo signal

reduction increases with the echo train length and causes a so-called through-plane blurring in the reconstructed images (Zhao et al. 2018). This effect may be mitigated by dividing the volume into several sub-volumes and measuring each one separately with a shorter echo train length. Furthermore, both phase encoding directions can be accelerated in parallel imaging, which also leads to a reduction of the number of required spin echoes.

Gradient echo reference scans can be acquired immediately after the excitation and facilitate a phase correction (PC) of the spin echo data prior to the reconstruction. This may reduce artifacts arising from an erroneous phase relationship between adjacent k-space lines, which were aquired in opposite readout directions. (Feinberg & Oshio 1991; Grade et al. 2015)

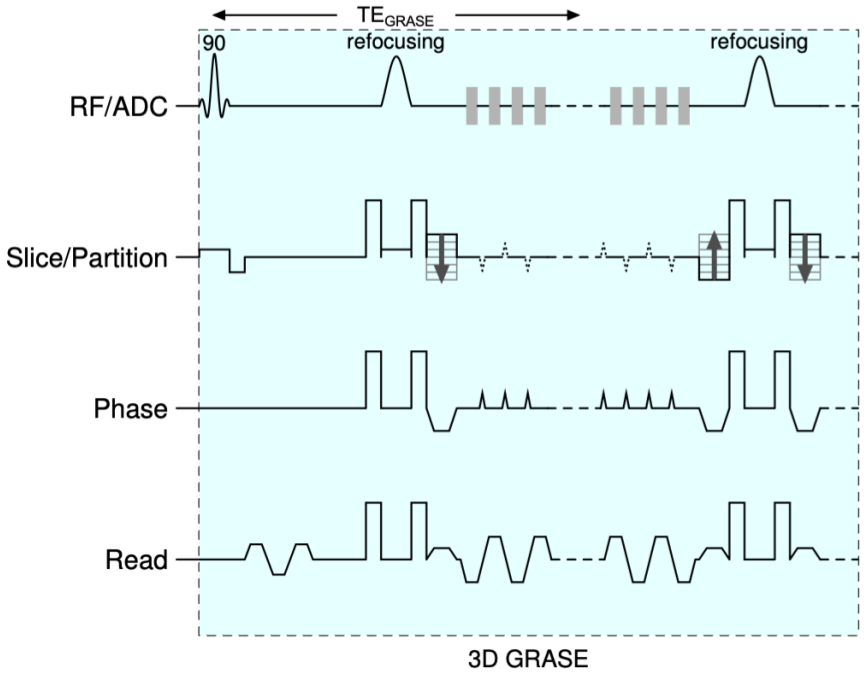

Figure 2.3: Sequence diagram of a 3D gradient-and-spin-echo (GRASE) sequence. Dotted gradient blips indicate optional CAIPIRINHA shifts in parallel imaging.

2.3.4 3D EPI

Echo-planar imaging (EPI) is a particularly fast readout technique with numerous variants existing. The presented EPI sequence in Figure [2.4]A is based on gradient echoes. It starts with a small flip angle ($\alpha < 90°$) slice-selective excitation pulse. Short frequency-encoded gradient echo reference scans are then acquired to allow a phase correction prior to reconstruction. For image data acquisition, or k-space sampling, a series of gradient echoes is generated. With frequency encoding during the readout and by using incremental phase encoding gradients, the k-space is acquired in a serpentine-like pattern according to Figure [2.4]B. Thereafter, spins are rephased and remaining transverse magnetization is dephased by a spoiler gradient. In 3D EPI, following an initial volume-selective excitation, the repetition of the experiment with an adjusted second phase encoding allows additional partitions to be acquired and combined to fill k-space. (Narsude et al. 2015; Stirnberg et al. 2017)

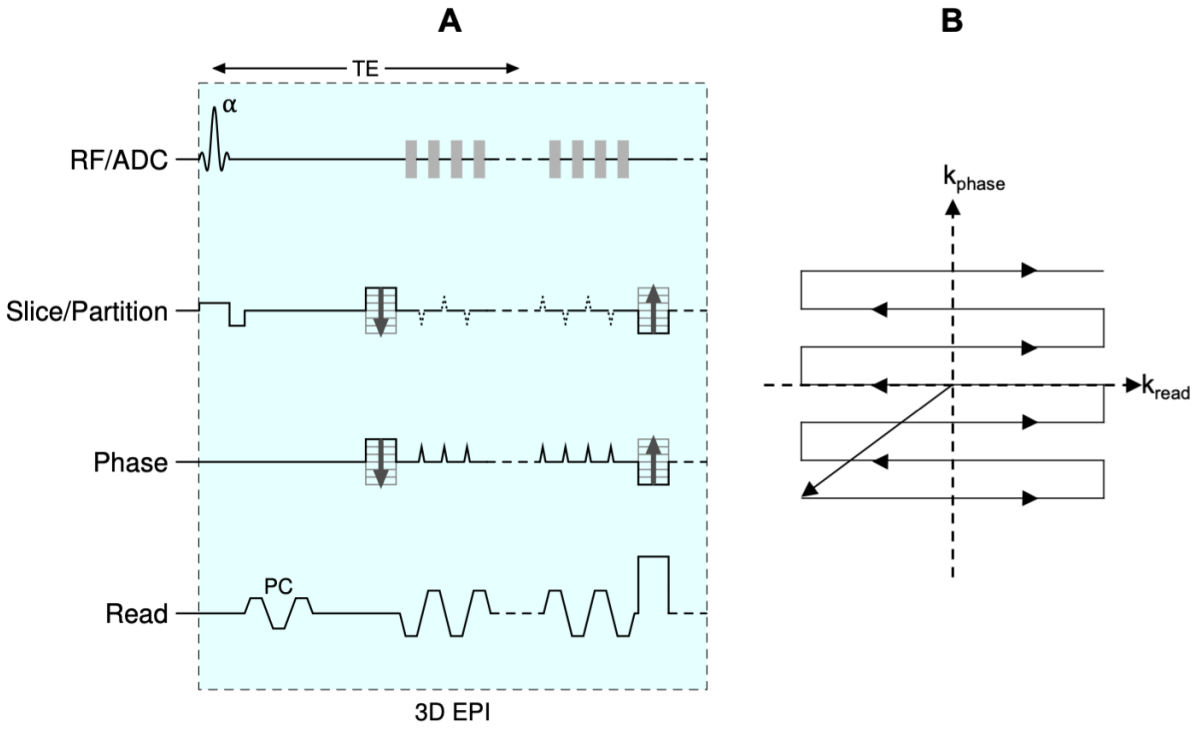

Figure 2.4: (A) Sequence diagram of an echo-planar imaging (EPI) sequence including phase correction reference scans and indicating possible CAIPIRINHA shifts in slice encoding direction. The acquisition of multiple partitions for 3D imaging is achieved by repetition of the presented experiment with a matched second phase encoding (partition encoding). (B) A schematic k-space trajectory of a single partition without CAIPIRINHA shifts.

2.4 Pulse transmission and signal reception

2.4.1 Hardware

The B_1 field, which is required for the spin excitation, is generated in transmit coils (Tx coils). Receive coils (Rx coils) measure the signal, which is then preamplified, discretized by an analog-to-digital converter, demodulated and stored as complex values allowing magnitude and phase information to be generated. (Gruber et al. 2018; Nitz 2012)

Different coil designs exist, which can be either pure receive or transmit coils or combine both. MRI scanners with a sub-7 T field strength usually contain an in-case coil which surrounds the entire bore. This coil is referred to as the body coil. Alternatively, surface coils can be used, which are matched to the shape of the measured body part. (Gruber et al. 2018)

Modern surface coils are composed of several smaller coils, so-called coil elements. These coil elements can, (partially) grouped or ungrouped, be equipped with dedicated receiving electronics. Such independent receiving elements are termed receive channels as they record the signal separately. The data of all channels can be combined into a single image afterwards. Therefore, this type of coil is referred to as multi-channel receive coil.

Similarly, the separate control of coil elements for pulse transmission is possible with special multi-channel transmit coils, known as parallel transmission (pTx). Exemplary data obtained with a multi-channel transmit and receive coil is given in Figure [2.9]. In contrast, the common control of the coil elements with a constant amplitude and phase relationship is termed single transmission (sTx). Conventionally, a circular polarized (CP) B_1 transmission is used, which specifies a phase increment of 45° between adjacent coil elements. The alternative elliptical polarized (CP2) transmission uses an phase increment of 90°. (Gruber et al. 2018; Rietsch et al. 2017)

Multi-channel transmit and multi-channel receive coils facilitate advanced techniques for pulse transmission and signal reception, respectively. In particular, parallel imaging is enabled by multi-channel receive coils. Furthermore, surface receive coils improve the SNR by reducing the distance to the sample. Surface transmit coils excite the imaging region locally, minimizing signals from other structures which may cause wrap-around artifacts. Thus, coils directly affect SNR, resolvability, sensitivity, and uniformity of data. (Gruber et al. 2018; Roemer et al. 1990)

For brain MR imaging, dedicated head coils are commonly used. At 3 T scanners, the transmission is usually performed in sTx mode through the body coil and multi-channel head receive coils are used for signal acquistion (Siemens Skyra 32Rx, Siemens Prisma 64Rx). On 7 T scanners (Siemens Magnetom 7 T), the transmission is also realized via a head transmit coil, either as a model with a single transmit channel for sTx (Nova Medical 1Tx/32Rx) or as a model with multiple transmit channels for pTx (Nova Medical 8Tx/32Rx).

Interference effects of transmitted pulses can lead to inhomogeneities in the field strength distribution and consequently to a non-uniform spin excitation. The electromagnetic wavelength decreases with an increasing field strength (26 cm at 3 T (Rajiah & Bolen 2014), 13 cm at 7 T (Collins & Wang 2011)). At 7 T, it is in the range of the size of the human head, so interference effects are more pronounced there. A compensatory approach is to use pTx transmission with adjusted channel weights or adapted pulse shapes of the individual channels so that the target B_1 field distribution is cumulatively achieved. An alternative strategy involves the placement of dielectric material with high relative permittivity on the target, so-called dielectric pads. These are fitted to the target structure and their property is to induce a secondary local electromagnetic field from the external excitation field. In this way, near-surface low B_1 field regions can be amplified. (Fagan et al. 2020; van Gemert et al. 2018; Padormo et al. 2015)

2.4.2 Imaging acceleration techniques

The total measurement time TA is a crucial parameter for the feasibility and in vivo practicability of a sequence protocol. Generally, it can be calculated using the relation

$$TA = REP \cdot N_{\mathrm{PE}} \cdot TR. \tag{2.22}$$

Given a fixed repetition number REP and a minimum repetition time TR, it predominantly can be reduced by decreasing the number of phase encoding steps N_{PE}. For 3D sequences the total number of phase encoding steps is $N_{\mathrm{PE}} = N_{\mathrm{PE1}} \cdot N_{\mathrm{PE2}}$.

Special acceleration techniques as partial Fourier imaging (PF) and parallel imaging (PI) allow image reconstruction from data of an incompletely measured k-space while maintaining the FOV and spatial resolution ($\Delta x, y$). In accordance with the Nyquist-Shannon sampling theorem, the k-space is considered complete if $\Delta k_{\mathrm{x,y}} \leq FOV_{\mathrm{x,y}}^{-1}$ holds for the minimal sampling rate. A lower rate causes ambiguities in the spatial frequency allocation and reduces the effective FOV, introducing wrapping artifacts known as aliasing. (Bernstein et al. 2004)

Partial Fourier imaging is based on the k-space property of a conjugate symmetry. Consequently, data points that are point reflected at the k-space origin provide redundant information, which gives the possibility to zero-fill a part or the entire half of the k-space and to generate the conjugated k-space data from the measured data (Farrar 1989). The fraction of measured k-space lines is given by the partial Fourier factor (PFF). Preferably, peripheral k-space lines are chosen for undersampling, since data points in the k-space center contain data of low spatial frequencies and therefore particularly affect the SNR, while outer data points cover higher spatial frequencies, thus encoding fine image structures. Acceleration is possible in both frequency and phase encoding directions, but for reduction of the acquisition time, acceleration in phase encoding direction is more effective. (Stenger et al. 1998)

Parallel imaging in k-space is based on information about the spatial sensitivity of the individual channels of multi-channel receive coils. Acceleration is achieved by an uniformly distributed undersampling of the k-space, usually performed in one or two phase encoding directions. The different patterns can be specified by the acceleration in each direction (R_{DIM}), with an acceleration of 1 corresponding to a full sampling. The total acceleration is given by the acceleration factor $R = R_{\mathrm{DIM1}} \times R_{\mathrm{DIM2}}$. By knowledge of the coil sensitivities, an unaliased image can be reconstructed with appropriate algorithms. Two main approaches for PI reconstruction are image-based techniques (SENSitivity Encoding, SENSE) and k-space-based methods. In the k-space-based approach, non-sampled points are synthesized with appropriate algorithms prior to image reconstruction. The one-dimensional acceleration is known as GRAPPA (GeneRalized Autocalibrating Partial Parallel Acquisition) and the undersampling in two directions as CAIPIRINHA (Controlled Aliasing in Parallel Imaging Results in Higher Acceleration). CAIPIRINHA provides the additional option to apply a shift of the size Δ in a zigzag-like pattern: $R = R_{\mathrm{DIM1}} \times R_{\mathrm{DIM2}}^{\Delta}$. The spatially dependent coil geometry or noise amplification factor $g \geq 1$ is a measure for the parallel imaging quality. Among other things, it depends on the receive coil design and the sampling pattern. (Breuer et al. 2005; Deshmane et al. 2012; Griswold et al. 2002)

2.4.3 Signal-to-noise ratio (SNR)

The signal-to-noise ratio is a measure for the achievable data and image quality, with a high SNR being favorable. It is given by the ratio of the mean image-related signal $\overline{S}$ and the mean background noise signal $\overline{N}$:

$$SNR = \frac{\overline{S}}{\overline{N}}. \tag{2.23}$$

The SNR is subject to numerous influencing factors. Factors determined by the hardware include the magnetic field strength ($\propto B_0$) and the coil design ($\propto$ measurement distance^{-1}; $\propto$ receive channel number$^{0.5}$).

Sequence- and protocol-determined factors comprise a relative signal gain with the voxel size ($\propto V_{\text{voxel}}$), increasing relaxation with the echo time ($\propto TE^{-1}$) and a potential echo train length ($\propto ETL^{-1}$). Also, the equilibrium magnetization recovery with a longer repetition time ($\propto TR$), the acceleration technique and strength ($\propto (PFF)^{0.5}$ and $\propto (g \cdot R^{0.5})^{-1}$, where $SNR/SNR_{\text{PI}} \geq 1$), and the acquisition bandwidth ($\propto BW^{0.5}$) or measurement time ($\propto TA^{-0.5}$) contribute to the SNR. (Bernstein et al. 2004; Breuer et al. 2005; Reeder et al. 2004)

In the case of repeated image acquisition, a temporal SNR (tSNR) can be defined for a single voxel within the time series. For this, the mean signal $\overline{S}$ of the voxel is set in relation to its standard deviation σ_{S} within the time series:

$$tSNR = \frac{\overline{S}}{\sigma_{\text{S}}}. \tag{2.24}$$

In order to compare the SNR for protocols of different lengths, the SNR and tSNR per unit time $TSNR$ and $tTSNR$ can be defined for the respective acquisition time TA:

$$TSNR = \frac{SNR}{\sqrt{TA}}, \tag{2.25}$$

$$tTSNR = \frac{tSNR}{\sqrt{TA}}. \tag{2.26}$$

2.4.4 Specific absorption rate (SAR)

Biological tissue absorbs the transmitted RF electromagnetic waves to some degree, resulting in tissue heating and the need for patient safety monitoring. The specific absorption rate (SAR) is a measure for the absorbed energy. SAR limits, which apply in the EU, are specified in the IEC standard (Table [2.1]). It covers two operating modes: the normal mode, which is used in routine operation, and the first level mode with higher limits, requiring particular supervision. Limits are defined for different target volumes and time intervals: whole body limits refer to the total body mass of the individual subject and additional local limits are defined for 10 g model mass of a particular body part. The $SAR_{6\text{min}}$ limits shown in Table [2.1] are specified as 6-minute moving average values. Based on these limits, the additional 10-second moving average condition $SAR_{10\text{s}} \leq 2 \cdot SAR_{6\text{min}}$ is specified. An exceedance of a single criterion requires the measurement to be stopped. (Cho & Yoo 2020; Fagan et al. 2020)

Table 2.1: $SAR_{6\text{min}}$ limits according to the IEC norm for transmit array coils. Whole body refers to the individual patient weight, head to a model head mass and local to 10 g model body mass. (Cho & Yoo 2020)

operating mode	whole body	head	local: head, trunk	local: extremities
normal	2 W/kg	3.2 W/kg	10 W/kg	20 W/kg
first level	4 W/kg	3.2 W/kg	20 W/kg	40 W/kg

Besides a subject dependence, the SAR is also dependent on the static magnetic field strength ($\propto B_0^2$), RF input power ($\propto P$), transmitted field strength ($\propto B_1$), flip angle ($\propto FA$), pulse duration ($\propto \mathrm{RF_{dur}}$), and repetition time ($\propto TR^{-1}$). (Weinberger et al. 2016)

It is not possible to directly measure the local SAR. Instead, it is estimated from models. Therefore, the electromagnetic field propagation is simulated for specific RF transmit coils and for several representative human body models. A worst-case conversion factor k [1/kg], which converts the power P [W] absorbed by the body into local SAR, is determined for the sTx mode: (Fagan et al. 2020)

$$SAR_{\mathrm{local}} = k \cdot P. \tag{2.27}$$

The absorbed power P can be derived from the known transmit power P_{in} and the measured reflected power P_{out}: $P = P_{\mathrm{in}} - P_{\mathrm{out}}$.

For a correct calculation of the SAR in pTx mode, it is required to take into account all possible phase relationships and associated interference effects for the individual coil elements. This is described by a conversion matrix $\underline{A}$ [S/kg] instead of a single conversion factor. This matrix can be used to convert the complex-valued RF voltage $\vec{U}$ [V] of each transmit channel into local SAR (Eichfelder & Gebhardt 2011; Weinberger et al. 2016):

$$SAR_{\mathrm{local}} = \vec{U}^H \underline{A} \vec{U}. \tag{2.28}$$

The multitude of phase-channel combinations with simultaneous consideration of each voxel within the body results in a high pTx SAR monitoring complexity. In order to make real-time monitoring feasible, $\underline{A}$ matrices, which yield the highest local SAR, are found in pTx simulations and compressed to so-called virtual observation point (VOP) matrices by clustering. Each VOP represents a sub-volume and allows for a controlled local SAR overestimation within it. During compression, it is ensured that SAR is not underestimated for any coil combination in any voxel. Potential SAR hotspots are considered, which may arise due to shorter wavelength related tissue interactions and B_1 non-uniformities especially at higher field strengths. (Eichfelder & Gebhardt 2011; Orzada et al. 2020)

2.5 RF pulses

The following sections on RF pulses, including a classification, characterizing properties, their calculation or modeling, and possible optimization techniques, are largely covered in (Bernstein et al. 2004; Brown et al. 2014). Where appropriate, additional reference is made to dedicated literature. For simplification and without loss of generality a coordinate system rotating around the main magnetic field B_0 at the Larmor frequency ω_0 is considered.

The magnetization $\vec{M}$, resulting from the spin alignment along B_0, is manipulated by the transmission of RF pulses. Suitable pulses or pulse sequences can be applied to generate detectable signals and achieve a specific

signal or image contrast. The extent of magnetization deflection is specified by the flip angle α [deg] relative to the initial direction of the magnetization vector before the pulse application. Starting from the fully relaxed magnetization along B_0, the deflection by an angle of 180° is called inversion and a general deflection by an arbitrary angle $\alpha < 180°$ is termed excitation. The 180° rotation of the magnetization within the transverse plane, aiming at spin re-phasing and magnetization recovery, is called refocusing. Pulse transmission for the purpose of suppressing signal or signal components is called saturation. Depending on their function, RF pulses can be classified into these four categories.

The RF pulse formation is based on a sinusoidal carrier wave, which is modulated by the envelope $B_1(t) = B_{1,\mathrm{x}}(t) + \mathrm{i}B_{1,\mathrm{y}}(t)$ [T]. This complex-valued description of the envelope allows to include phase modulations. According to the principle of slice selection, shifts of excitation can be achieved with a carrier wave frequency $\omega_0 = \omega_{\mathrm{Larmor}} \pm \omega_{\mathrm{off}}$ that deviates from the Larmor frequency ω_{Larmor}. Further pulse characterizing quantities are the pulse duration t_{pulse} [s] and the slice excitation profile, which can be specified by the RF excitation bandwidth (BW) [Hz] at FWHM. A transformation of RF pulses from the time domain to the frequency domain is possible with the fast Fourier transform (FFT) if the small-tip-angle approximation (STA, described in the subsequent section) is valid (Figure [2.5]). The STA also provides a slice profile approximation by the Fourier transform of $B_1(t)$. (Aibinu et al. 2008)

2.5.1 Pulse design

The magnetization dynamics inside magnetic fields can be described with the Bloch equations (Equation [2.8]). As the Bloch equations are non-linear if RF pulses are included, it is not trivial to model RF pulses for achieving a target excitation. Therefore, in order to solve the problem, simplifying approximations are commonly applied. The small-tip-angle approximation is a frequently used approach. It assumes small excitation angles $\alpha < 90°$ and infers an approximate preservation of the longitudinal magnetization component $M_{\mathrm{z}}(t) \approx M_0$ as well as the FA dependence of the transverse magnetization $M_{\mathrm{xy}} \propto \sin(\alpha) \approx \alpha$. The approximation of M_{xy} is not valid for α close to 90°, but still the STA provides good results. Including the STA assumptions in the Bloch equations, the simplified linear relationship

$$M_{\mathrm{xy}}(\vec{r}) = \mathrm{i}\gamma M_0 \int_0^{T_{\mathrm{pulse}}} B_1(t) \mathrm{e}^{\mathrm{i}\vec{r}\vec{k}(t)} \mathrm{d}t \tag{2.29}$$

with

$$\vec{k}(t) = -\gamma \int_t^{T_{\mathrm{pulse}}} \vec{G}(t') \mathrm{d}t' \tag{2.30}$$

is derived for the transverse magnetization M_{xy}. t_{pulse} is the duration of the RF pulse with the complex-valued magnitude $B_1(t)$. The STA divides the RF pulse into short sub-pulses, with each generating an independent transverse magnetization component, with each component being exposed to its respective remaining gradient $\vec{G}(t)$. This principle is resulting in an excitation k-space [2.30] with the k-space trajectory $\vec{k}(t)$. An excitation weighting in the course of the k-space trajectory is determined by the pulse shape and magnitude. When considering infinitesimal sub-pulse lengths, the integral of all generated magnetization components at the end

of the pulse - the achieved excitation profile - corresponds to the Fourier transform of the RF pulse. Using the linear Fourier relation [2.29] between RF pulse shape and transverse magnetization, it is possible to design RF pulses $B_1(t)$ via the inverse Fourier transform on the basis of a target excitation profile $M_{\mathrm{xy}}(\vec{r})$. This direct approach does not consider B_0 inhomogeneities leading to off-resonances, which can lead to a non-ideal actual excitation. Also, system and energy limitations are not taken into account. (Padormo et al. 2015; Pauly et al. 2011; Yip et al. 2005)

A more advanced, iterative approach for optimizing the target excitation extends the transverse magnetization profile $M_{\mathrm{xy}}(\vec{r})$ in [2.29] to include location-dependent resonance frequency offsets $\Delta\omega_0(\vec{r}) = \gamma\Delta B_0(\vec{r})$ in the pulse modeling:

$$M_{\mathrm{xy}}(\vec{r}) = \mathrm{i}\gamma M_0 \int_0^{t_{\mathrm{pulse}}} B_1(t)\mathrm{e}^{\mathrm{i}\left(\vec{r}\vec{k}(t)+\Delta\omega_0(\vec{r})(t-t_{\mathrm{pulse}})\right)}\mathrm{d}t. \tag{2.31}$$

This relation is discretized in place and time using N_{r} and N_{t} sampling points defined by

$$M_{\mathrm{xy}}(\vec{r}_{1\ldots N_{\mathrm{r}}}) = \underline{A}B_1(t_{1\ldots N_{\mathrm{t}}}) \tag{2.32}$$

and expressed in a simplified form as

$$\vec{m} = \underline{A}\vec{b}. \tag{2.33}$$

Corresponding to the applied discretization, $\vec{m}$ are the samples of the transverse magnetization and $\vec{b}$ the samples of the RF pulse shape. According to [2.31], the $N_{\mathrm{r}} \times N_{\mathrm{t}}$ system matrix $\underline{A}$ is composed of the elements $a_{ij} = \mathrm{i}\gamma M_0 \delta t \mathrm{e}^{\mathrm{i}\left(\vec{r}_i\vec{k}(t_j)+\Delta\omega_0(\vec{r}_i)(t_j-t_{\mathrm{pulse}})\right)}$ using the time discretization step size δt. It contains the k-space trajectory and the off-resonances during excitation. (Padormo et al. 2015; Yip et al. 2005)

This inverse problem of determining a targeted pulse shape $\vec{b}$ for a given target excitation $\vec{m}_{\mathrm{target}}$ is expressed as the minimization problem

$$\min_{\vec{b}} \left\{ \left\| \underline{A}\vec{b} - \vec{m}_{\mathrm{target}} \right\|_{\underline{W}}^2 + R(\vec{b}) \right\}. \tag{2.34}$$

Here, $\underline{W}$ is a weighting matrix used to define an optimization ROI, and $R(\vec{b})$ is a regularization term which may include system and energy limits. For constraining the applied energy, $R(\vec{b}) = \lambda\|\vec{b}\|_2^2$ can be used with the regularization parameter λ. Also, it is possible to replace the linear least squares based cost function by any different approach. (Padormo et al. 2015; Yip et al. 2005)

An alternative approach to this STA-based pulse modeling, which also holds for large FAs, is the Shinnar-Le Roux algorithm. Here, the inverse, non-linear problem is solved by suitable splitting and modeling. However, pulses generated by this method are only valid for the particular FA considered within the modeling. (Balchandani et al. 2010; Pauly et al. 1991)

Finally, Bloch equation based minimization problems can also be formulated and solved numerically in order to design pulses. (Hennel 2014)

2.5.2 Spatial non-selective RF pulses

Assuming a homogeneous main magnetic field, pulses will excite the magnetization in the entire covered volume if no additional gradients are applied simultaneously. According to the selected carrier frequency, spins are affected which have a frequency lying within the pulse-characteristic BW. The frequency distribution of the spins inside the volume can be modulated by applying gradients according to Equation [2.12]. Analogously, off-resonant spins are excited if the BW is high enough, resulting in a frequency selectivity which is dominated by the pulse length and shape. (Hennel 2014)

An example of this type of spatially non-selective RF pulses is a rectangular pulse, also known as a hard pulse (Figure [2.5]A). Its particular features are a low energy intensity, short realizable pulse durations, and a large BW ($FWHM \approx \frac{1.22}{t_{\text{pulse}}}$) of the SINC-shaped excitation profile. The frequency selectivity can be increased with alternative pulse shapes.

2.5.3 Composite pulses

In real experiments, B_0 and B_1 inhomogeneities lead to off-resonances and off-resonant excitations, respectively. One compensatory approach to achieve a target FA excitation is to apply a number of shorter sub-pulses in a short sequence instead of a single RF pulse. The time gap between the single pulses is small, so phase evolution and relaxation effects can be neglected and the overall response of a single RF pulse is assumed. In order to achieve the compensatory effects, sequences of single pulses are determined in (Bloch) simulations to induce a specific target excitation. Pulse parameters like shape, magnitude and phase are optimized and necessary interpulse gaps are determined. (Levitt 2007)

2.5.4 Spatial selective RF pulses

According to the Fourier transform, infinite SINC-shaped RF pulses are suitable to achieve rectangular-shaped excitation profiles (Figure [2.5]B). Contrary to the theory, pulses in real experiments have to be truncated to a finite length, which results in a non-ideal excitation profile with finite edge slopes and side ripples (Figure [2.5]C). Additionally, the excitation profile approximation applies to small FAs only. The excitation profile sharpness, or transition band, can be estimated by the so-called time-bandwidth product (TBW). A higher TBW yields a sharper profile, but necessitates a trade-off between pulse duration t_{pulse} and frequency selectivity Δf: $TBW = t_{\text{pulse}} \cdot \Delta f = N_{0,\text{left}} + N_{0,\text{right}}$. The numbers of the bilateral pulse zero-crossings $N_{0,\text{left}}$ and $N_{0,\text{right}}$ further characterize the excitation profile. For symmetric pulses it is $N_{0,\text{left}} = N_{0,\text{right}}$.

In order to improve the excitation profile, apodization functions, also called window functions, are applied to the SINC function instead of simply truncating it with a rectangular window. For this purpose often Hanning (Hann) and Hamming functions are used. In this way, side ripples are reduced or suppressed, but at the same time the sharpness of the excitation profile respectively the transition band is decreased (Figure [2.5]D).

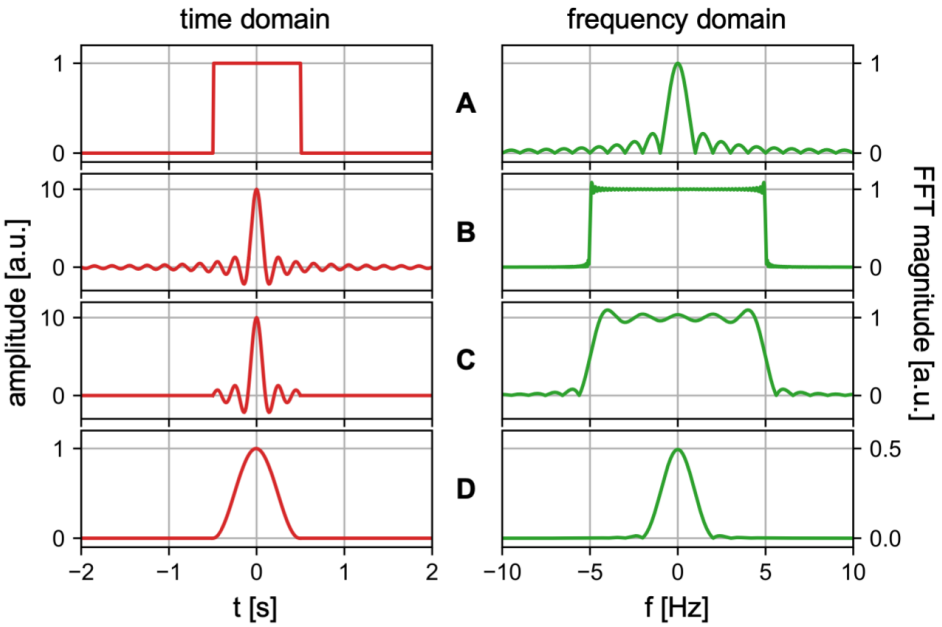

Figure 2.5: Different RF pulse shapes in the time domain and their representation in the frequency domain derived from a FFT for (A) a rectangular, (B) a SINC-shaped, (C) a strongly truncated SINC-shaped and (D) a Hanning-shaped pulse. The Fourier transform to the frequency domain allows to estimate the excitation profile of the RF pulse under the small-tip-angle approximation.

2.5.5 Adiabatic pulses and flow-induced inversion

So far, RF transmission at the Larmor frequency has been assumed. An off-resonant RF which is not transmitted at the Larmor frequency causes a precession of the magnetization around the resulting vector of the B_0 and B_1 field. The axis of this resultant or effective field $\vec{B}_{\text{eff}}$ can be modulated via the transmitted B_1. If the adiabatic condition

$$\left|\frac{\mathrm{d}\phi}{\mathrm{d}t}\right| \ll \gamma|\vec{B}_{\text{eff}}| \tag{2.35}$$

is met, that is a B_1 of a sufficient stregth and a sufficiently slow rotation $|\mathrm{d}\phi/\mathrm{d}t|$, then the magnetization can follow this field while preceding around it. This behavior is called the adiabatic principle and illustrated in Figure [2.6] (blue box). Here, the angle $\phi = \arctan(\vec{B}_{\text{eff}}(t)/B_{\text{z}}(t))$ is considered between the static B_0 and orthogonal B_1 field axes. Higher field strengths and slower field rotations provide a more reliable adiabatic following of the magnetization. Magnetization components initially oriented parallel or orthogonal to $\vec{B}_{\text{eff}}$ remain in their relative orientation to the re-oriented $\vec{B}_{\text{eff}}$.

The principle of an adiabatic following is realized by adiabatic pulses. Such pulses do not base on a simple amplitude modulation by means of a single envelope, but on an additional frequency modulation of the carrier wave. As off-resonant spins are also included in the rotation during the adiabatic following, those RF pulses provide increased robustness against B_0 and B_1 inhomogeneities and allow a more homogeneous excitation as long as the adiabatic condition is fulfilled. The pulse amplitude and frequency modulations are numerically

optimized as a function of the RF amplitude, the target flip angle and the bandwidth of off-resonances to be covered. Therefore, adiabatic pulses cannot be scaled by adjustment of the applied RF energy as it is possible for common amplitude-modulated pulses. Common designations are adiabatic half-passage (AHP) for a 90° excitation and adiabatic full-passage (AFP) for a 180° inversion.

A sub-class of adiabatic pulses are gradient-modulated offset-independent adiabaticity pulses (GOIA). Popular GOIA pulses are hyperbolic secant pulses of n-th order (HSn) and wideband, uniform rate, smooth truncation (WURST) pulses, with the latter featuring an improved slice excitation profile and a higher robustness to off-resonances. (Andronesi et al. 2010; Bernstein et al. 2004; Tannús & Garwood 1997)

2.5.5.1 Flow-induced continuous adiabatic inversion

Instead of a B_1 modulation, for moving protons the principle of adiabatic following can also be realized with a constant RF transmission (B_1) and a gradient $\vec{G}_\mathrm{r}$ applied in the flow direction $\vec{r}$. Spins moving at the velocity $\vec{v}_\mathrm{r}$ experience a frequency ω_r that is spatially dependent in the direction of the gradient. The position of the adiabatic following $\vec{r}_0$ is then determined through the constant B_1 frequency by satisfying the resonance condition $\omega(\vec{r}_0) = \omega(B_1)$. The frequency of the spins approaching $\vec{r}_0$ gradually becomes $\omega(B_1)$ and progressively diverges with distance afterwards (Figure [2.6], red box). Due to this flow-induced frequency modulation, a constant B_1 field becomes an effective rotating field $\vec{B}_\mathrm{eff}$ to the spins. For distant spins, $\vec{B}_\mathrm{eff}$ appears to be oriented in parallel to $\vec{r}$ and with increasing proximity to $\vec{r}_0$ it gradually aligns along B_1. According to the adiabatic principle, the spins follow $\vec{B}_\mathrm{eff}$.

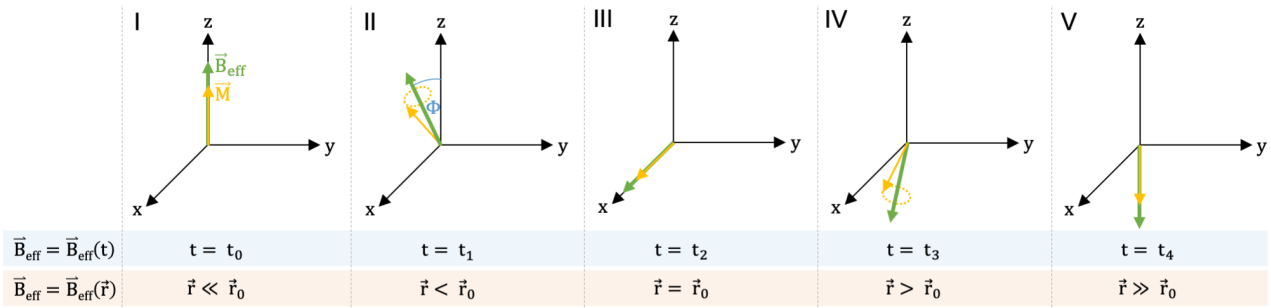

Figure 2.6: Schematic illustration of the adiabatic full-passage. The effective magnetic field $\vec{B}_\mathrm{eff}$ (green) at first is aligned along the z-axis (I) and gradually modulated (II-IV) until it is finally fully inverted (V). While satisfying the adiabatic condition, the spin magnetization (yellow) follows gradually and is also inverted. The modulation of $\vec{B}_\mathrm{eff}$ can be accomplished by special, so-called adiabatic RF pulses, resulting in a temporal modulation (blue). Alternatively, a spatially dependent modulation can be realized according to the principle of a flow-induced adiabatic following (red). Here, condition (III) equals an on-resonant excitation.

The flow-induced adiabatic condition is

$$\frac{1}{T_2} \ll \frac{\vec{G}_\mathrm{r}\vec{v}_\mathrm{r}}{|B_1|} \ll \gamma|B_1|. \tag{2.36}$$

A sufficient B_1 strength and a low flow velocity are required according to the $\vec{B}_\mathrm{eff}$ rotation speed. Additionally, T_2 relaxation effects are assumed to be negligible during the adiabatic following. (Dai et al. 2008; Detre & Alsop 1999)

2.5.5.2 Flow-induced pulsed adiabatic inversion

A constant RF transmission is not possible with conventional MRI hardware. In order to realize a flow-induced adiabatic inversion, the constant B_1 field can be approximated by applying successive B_1 pulses with an adjusted amplitude. According to the Fourier transform, the application of successive RECT pulses induces unwanted, periodically repeating secondary excitation planes in addition to the targeted one. This aliasing can be reduced by increasing the frequency selectivity via the RF pulse shape and by increasing the spatial selectivity with higher gradient strengths. Hanning-shaped pulses are frequently used for this purpose. In order to maintain the adiabatic condition, it is required that the mean gradient G_mean, the spins are exposed to on average, matches the constant gradient in the continuous approach. Therefore, the gradient is increased to G_max only while pulse application to enhance the selectivity. A compensatory gradient is applied in the inter-pulse gaps to preserve G_mean. Such exemplary RF- and gradient-patterns are shown in Figure [3.3]. For an effective suppression of additional excitation slices, the condition $\frac{G_\mathrm{max}}{G_\mathrm{mean}} \gg \frac{\Delta t}{t_\mathrm{pulse}}$ follows from the Fourier transform of the RF pulses. A high G_max and long (t_pulse), rapidly repeating (Δt) pulses are beneficial. Accordingly, for pulsed RF and gradients, the flow-induced adiabatic condition is

$$\frac{1}{T_2} \ll \frac{G_\mathrm{r,mean} \cdot v_\mathrm{r}}{|B_1|} \ll \gamma|B_1|. \tag{2.37}$$

From the alternative expression

$$\frac{|B_1|}{T_2 \cdot G_\mathrm{r,mean}} \ll v_\mathrm{r} \ll \frac{\gamma|B_1|^2}{G_\mathrm{r,mean}}, \tag{2.38}$$

it is immediately recognizable that a sufficiently high $|B_1|$ is required for fast moving spins, and that the transverse relaxation of too slowly moving spins hinders an adiabatic following. (Dai et al. 2008)

The excitation plane is defined by a frequency selection in the continuous method. In the pulsed approach, it can be controlled by an appropriate frequency offset $\Delta\omega = \gamma G_\mathrm{max}\Delta z$ and a phase offset $\Delta\phi = \gamma G_\mathrm{mean}\Delta z\Delta t$ of successive pulses, where Δz corresponds to the shift relative to the on-resonant plane. (Dai et al. 2008)

2.5.6 Variable-rate selective excitation (VERSE)

Amplitude-modulated, spatially selective RF pulses B_1, which are applied in the presence of a constant slice selection gradient G, can be stretched and compressed while maintaining the same excitation. This requires, the preservation of the cumulative RF energy and the simultaneous and proportional modification of the RF and gradient strengths, so that the relation between RF strength and k-space trajectory is maintained. The derived pulses are called variable-rate selective excitation (VERSE) pulses. The pulse modulation by compression and stretching corresponds to a negative and positive time dilation, respectively, and can be described by a transformation function $f_{\mathrm{VERSE}}(t)$. An input pulse-gradient combination (B_1, G) with the pulse length t_{pulse} and a constant gradient is transformed into the VERSE representation ($B_{1,\mathrm{VERSE}}$, G_{VERSE}) with the length $t_{\mathrm{pulse,VERSE}}$ as follows:

$$\begin{aligned} B_{1,\mathrm{VERSE}}(t) &= B_1(f_{\mathrm{VERSE}}(t)) \cdot \tfrac{\mathrm{d}}{\mathrm{d}t}\left\{f_{\mathrm{VERSE}}(t)\right\}, \\ G_{\mathrm{VERSE}}(t) &= G \cdot \tfrac{\mathrm{d}}{\mathrm{d}t}\left\{f_{\mathrm{VERSE}}(t)\right\}. \end{aligned} \tag{2.39}$$

The boundary conditions for the monotonically ascending transformation function are $f_{\mathrm{VERSE}}(0) = 0$ and $f_{\mathrm{VERSE}}(t_{\mathrm{pulse,VERSE}}) = t_{\mathrm{pulse}}$. VERSE modulations allow for a SAR reduction by decreasing the B_1 amplitude or for pulse duration shortening by increasing B_1. Limiting factors for VERSE transformations are the maximum permissible field strength, gradient strength and gradient slew rate, which must be satisfied for all pulse samples at all time points. (Hargreaves et al. 2004)

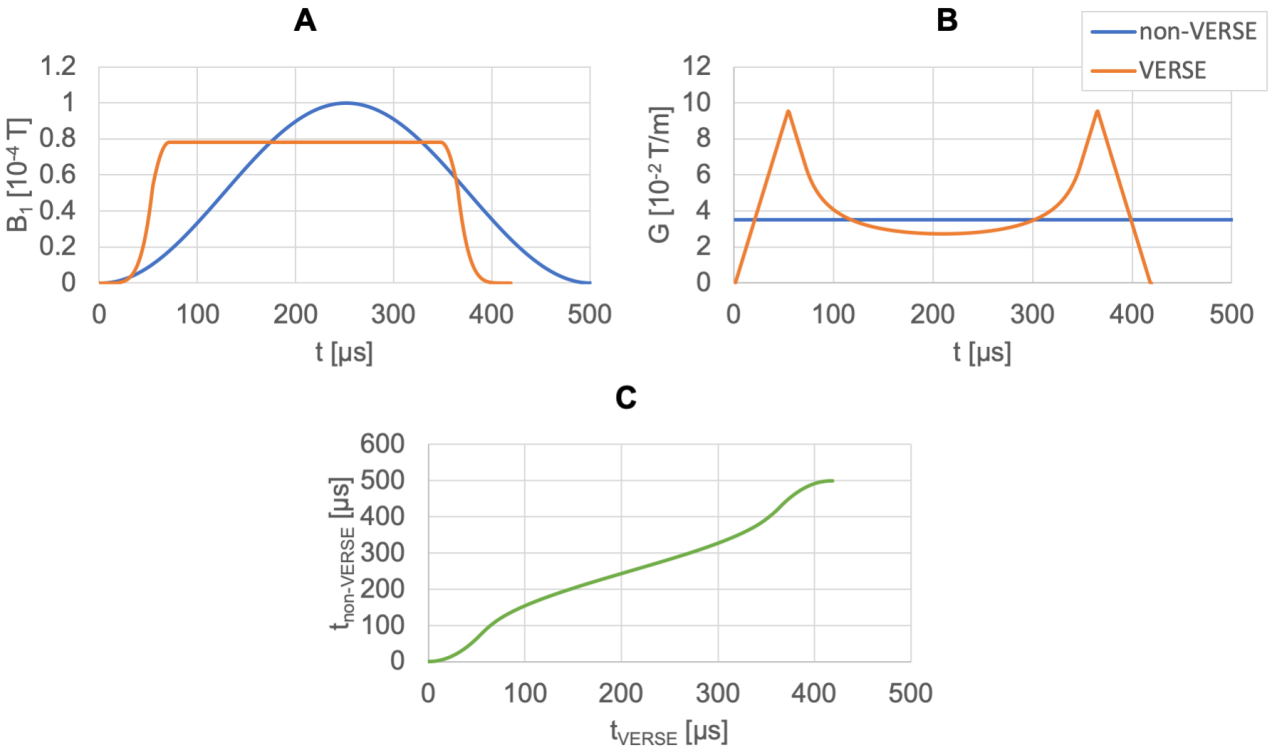

Figure 2.7: Exemplary VERSE modulation of a Hanning-shaped pulse with a constant gradient (blue) and the derived time-reduced, energy-constrained VERSE pulse (orange). The RF magnitude (A) and the gradient strength (B) can be transformed via the corresponding time dilation (C) according to Equation [2.39].

2.6 Parallel transmission (pTx)

In parallel transmission, the separate, independent control of the individual transmit coil channels provides additional degrees of freedom for achieving a target excitation. This may be used for an off-resonance compensation or a SAR distribution modulation. A possible STA-derived approach for pTx-based pulse design is the extension of Equation [2.31] with a weighting factor $S_c(\vec{r})$, which reflects the spatially dependent transmit sensitivity for C individual channels c, and the use of channel-specific pulse shapes $B_{1,c}(t)$:

$$M_{\mathrm{xy}}(\vec{r}) = \mathrm{i}\gamma M_0 \sum_{c=1}^{C} S_c(\vec{r}) \int_0^{t_{\mathrm{pulse}}} B_{1,c}(t) \mathrm{e}^{\mathrm{i}\left(\vec{r}\vec{k}(t)+\Delta\omega_0(\vec{r})(t-t_{\mathrm{pulse}})\right)} \mathrm{d}t. \tag{2.40}$$

The system matrix $\underline{A}$ (Equation [2.32]) can be expressed as an extended vectorial $N_{\mathrm{r}} \times CN_{\mathrm{t}}$ system matrix $\underline{A}_{\mathrm{pTx}}$. In order to differentiate the channels, the pulse shape may be formulated as a vector $\vec{b}_{\mathrm{pTx}}$. This leads to the expression

$$\vec{m} = [\mathrm{diag}\{S_1(\vec{r})\}\underline{A} \cdots \mathrm{diag}\{S_C(\vec{r})\}\underline{A}][\vec{b}_1 \cdots \vec{b}_C]^{\mathrm{T}} = \underline{A}_{\mathrm{pTx}}\vec{b}_{\mathrm{pTx}} \tag{2.41}$$

with the corresponding minimization problem

$$\min_{\vec{b}_{\mathrm{pTx}}} \left\{ \left\| \underline{A}_{\mathrm{pTx}}\vec{b}_{\mathrm{pTx}} - \vec{m}_{\mathrm{target}} \right\|_{\underline{W}}^2 + R\left(\vec{b}_{\mathrm{pTx}}\right) \right\}. \tag{2.42}$$

The increased degree of freedom due to variable pulse forms, including both the magnitudes and the phase relations between the channels, considerably enhances the problem and computational complexity, for which several solution approaches exist.

The resulting transmitted field is the superposition of all transmit fields from the individual transmit coil channels:

$$B_1(\vec{r}, t) = \sum_{c=1}^{C} B_{1,c}(\vec{r}, t). \tag{2.43}$$

From this equation, two fundamental pTx concepts can be derived. The use of a uniform pulse shape $p(t)$ for all channels while employing and optimizing individual complex-valued, channel-specific weights w_i to obtain a target B_1, gives the field

$$B_1(\vec{r}, t) = p(t) \sum_{c=1}^{C} w_c S_c(\vec{r}). \tag{2.44}$$

This is known as static pTx or B_1 shimming (Figure [2.8]B). It is often used to homogenize B_1 within a ROI. Especially when B_1 shimming cannot achieve sufficient B_1 field homogenization, the second concept, termed

dynamic pTx or full pTx, is employed (Figure [2.8]C). This concept targets at a FA homogenization and utilizes channel-specific pulse shapes $p_i(t)$ giving the resulting field

$$B_1(\vec{r},t) = \sum_{c=1}^{C} p_c(t) S_c(\vec{r}). \tag{2.45}$$

In full pTx, an optimization can be accomplished by applying several pulses with appropriate k-space trajectories, to successively modify the magnetization until the desired FA-distribution is reached.

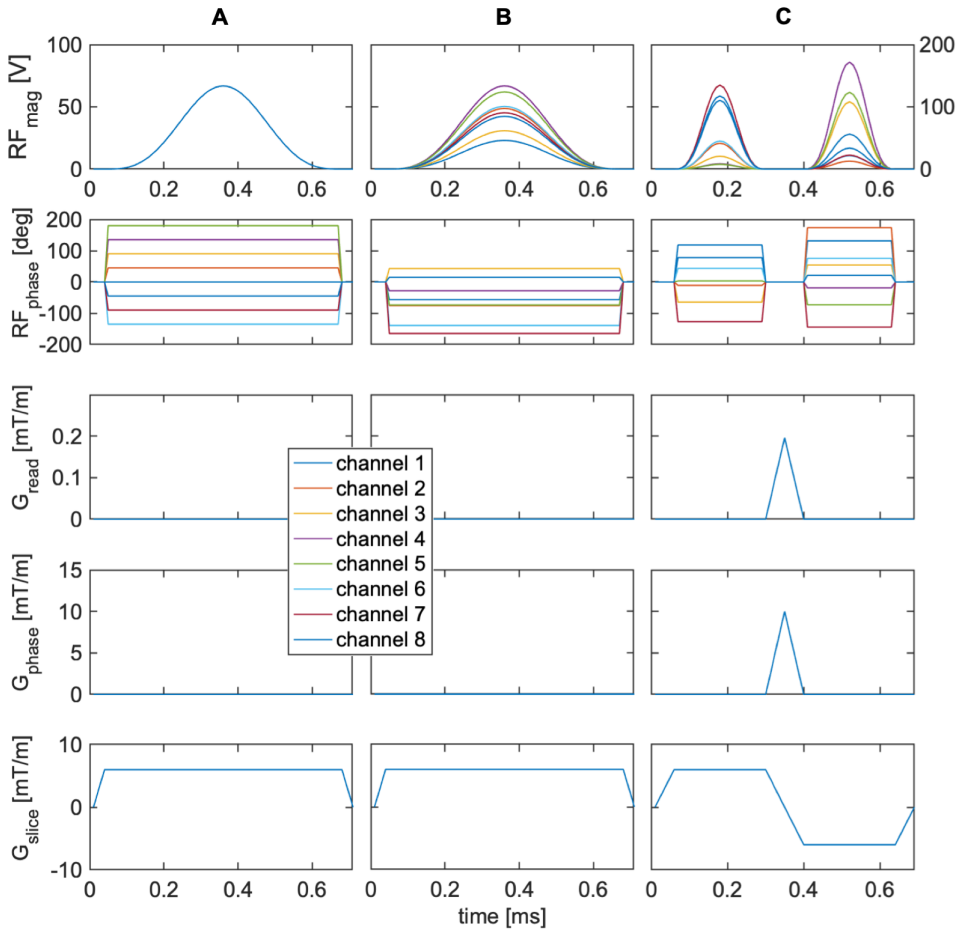

Figure 2.8: RF pulse transmission concepts: (A) non-shimmed, circular polarized transmission and shimmed mode using (B) the static pTx or (C) the dynamic pTx approach. Due to equal channel weighting and the resulting overlap, only a single channel is visible in the RF magnitude diagram in (A).

Regardless of the pTx concept, the required gradients of the optimized pulses result from the given k-space trajectory. A differentiation must be made between volume-selective and non-selective excitations. Two basic full pTx implementations are spokes for selective and kT-points for non-selective excitations. (Padormo et al. 2015; Saekho et al. 2006; Yip et al. 2005)

The pTx calculations base on the knowledge of channel-specific transmit sensitivities and have to also

incorporate the B_0 field distribution. Figure [2.9] shows an exemplary dataset taken as a basis for the pTx optimization with an 8-channel pTx system. It is acquired in CP mode prior to pTx calculation and comprises separate B_1 magnitude (Figure [2.9]A1-A8) and phase maps (Figure [2.9]B1-B8) for all individual channels and a B_0 map for the consideration of off-resonances (Figure [2.9]C). Additionally, a combined B_1 map is shown in Figure [2.9]D, which reveals the typical central signal maximum of the CP operating mode. Optimization is commonly performed within a defined ROI.

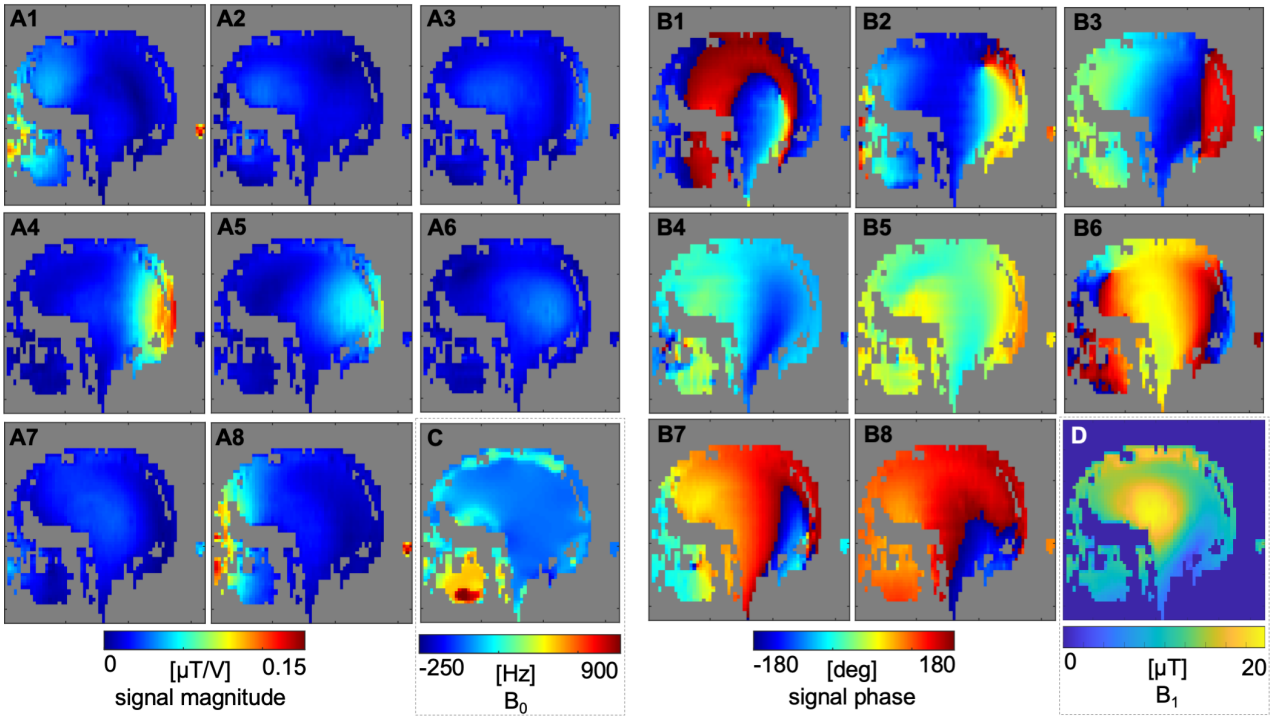

Figure 2.9: Adjustment data for the 8-channel pTx system: (A1-A8) B_1 magnitude map [µT/V], (B1-B8) B_1 phase map [deg] per channel, (C) B_0 map and (D) channel-combined B_1 base excitation map in µT with an excitation targeted at 20 µT.

The sTx mode can be emulated in pTx operation by adopting all of the sTx mode-defined phases and by weighting all coil elements equally as presented in Figure [2.8]A.

3

Fundamentals of brain perfusion MRI

3.1 Human brain anatomy and physiology

3.1.1 Tissue structure

The human brain is mainly composed of nerve tissue and surrounded by the cerebrospinal fluid (CSF). It is enclosed by the meninges. The brain has two symmetric halves, known as hemispheres, which are interconnected by nerve tracts. It can roughly be sub-divided into the cerebrum, diencephalon, cerebellum, and brainstem, whereby perfusion is of particular interest in the cerebrum. Further subdivisions into ROIs are based on function or anatomical location and often symmetrical between both hemispheres. ROI-based examples are shown in Figures [5.5]A, [5.16]D and [5.16]E. The surface layer is known as the (cerebral) cortex. It is strongly folded and characterized by a high nerve cell density, from which the histological designation of gray matter (GM) is derived (Figure [3.1]A-D). Beneath the cortex nerve fibers are located, which are covered by a myelin biomembrane to accelerate the transmission of signals or stimuli. As myelin has a high lipid content, this sub-cortical tissue is named white matter (WM) according to its appearance. (Mai et al. 2015; Schünke et al. 2006)

For the transport of oxygen and nutrients, a blood supply to the brain is required. Arterial blood delivery is mainly carried by two pairs of arteries: the internal carotid and vertebral arteries. These are presented in Figure [3.1]D and described in more detail in the associated caption. Metabolic products and carbon dioxide are cleared by the venous blood outflow. (Schünke et al. 2006; M. Zhao et al. 2007)

The blood vessels in the brain progressively become finer up to the smallest capillaries, which form a network and enable an exchange of substances through their thin vessel walls. Cerebral capillaries have the special property, that their endothelial cells, which form the outer layer, are tightly connected via so-called tight junctions. These constitute a diffusion barrier between the cerebral blood circulation and the central nervous

system. This physiological barrier is known as the blood-brain barrier (BBB) and enables a regulated transport of substances between the intravascular blood and the extravascular tissue system, providing a protective mechanism for the brain (Figure [3.1]E). (Paulson 2002; Schünke et al. 2006)

The cerebral blood flow (CBF) refers to the blood delivery to the capillaries, respectively the tissue perfusion. It has to be distinguished from the MR angiography which is used to image larger arteries. (Li et al. 2005)

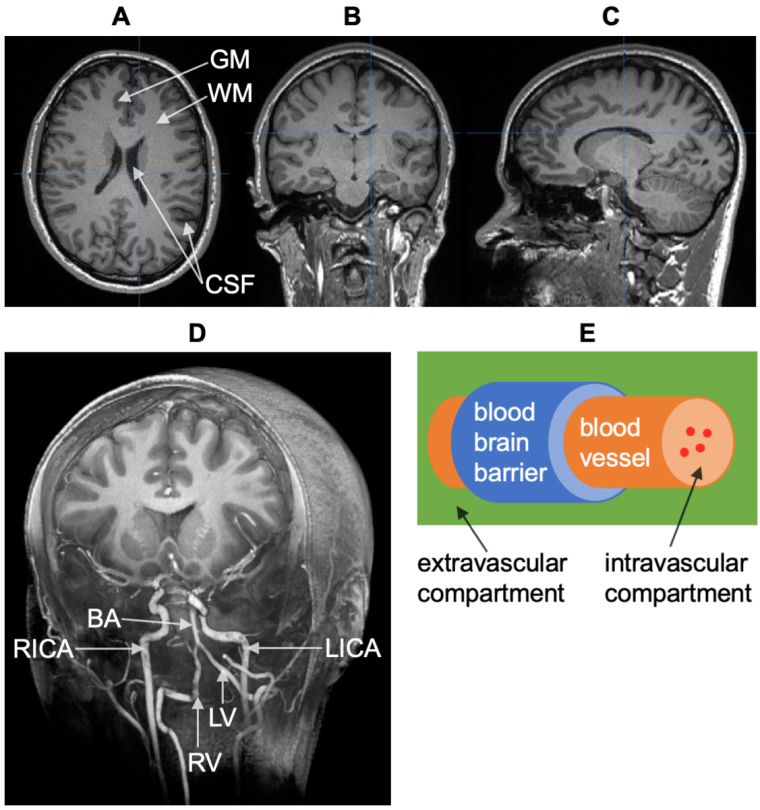

Figure 3.1: Overview of the human brain anatomy. (A-D) Structural T_1-weighted MP2RAGE 7 T MRI scan in (A) axial/transversal, (B) coronal/frontal and (C) sagittal/lateral 2D view as well as (D) a 3D rendering with annotated main blood supplying arteries: left/right internal carotid arteries (LICA/RICA), left/right vertebral arteries (LV/RV) and basilar artery (BA). In this image contrast white matter (WM) appears light, gray matter (GM) darker and cerebrospinal fluid (CSF) the darkest. The blue lines mark the slices of the 2D images. (E) A highly simplified representation of the blood-brain barrier, forming a boundary between the intravascular blood system and the surrounding extravascular tissue space.

3.1.2 Normal brain physiology

As a part of the cerebral vascular autoregulation, including vasodilatation and vasoconstriction, a sufficient blood supply to the brain is maintained ensuring sufficient oxygen and nutrient delivery (Paulson 2002). A regulatory response is induced dependent on blood pressure, the blood oxygenation level, the carbon dioxide concentration and certain metabolites (Smith & Ainslie 2017). In healthy adults, with a proper regulation, reported GM-CBF values are in the range of 40-100 ml/100g/min (Alsop et al. 2014). The CBF in WM is lower by a factor in the order of 1.6-3.2 (Álvarez et al. 2019). Moreover, there is a CBF decrease with age

(Leoni et al. 2017). No difference between genders has been reported (Leoni et al. 2017). Arterial transit times in GM are in the range of 600-1600 ms in a healthy adult (Chen et al. 2011) and prolonged in WM (Álvarez et al. 2019).

3.2 Perfusion MRI

3.2.1 Principles of (pC)ASL

Arterial spin labeling (ASL) is an MRI method suitable for the quantitative measurement of cerebral perfusion at the capillary level. The underlying concept is illustrated in Figure [3.2]. It uses arterial blood water protons as an endogenous tracer by a magnetic marking and is, in contrast to perfusion measurement with PET, SPECT and DSC-MRI, completely non-invasive.

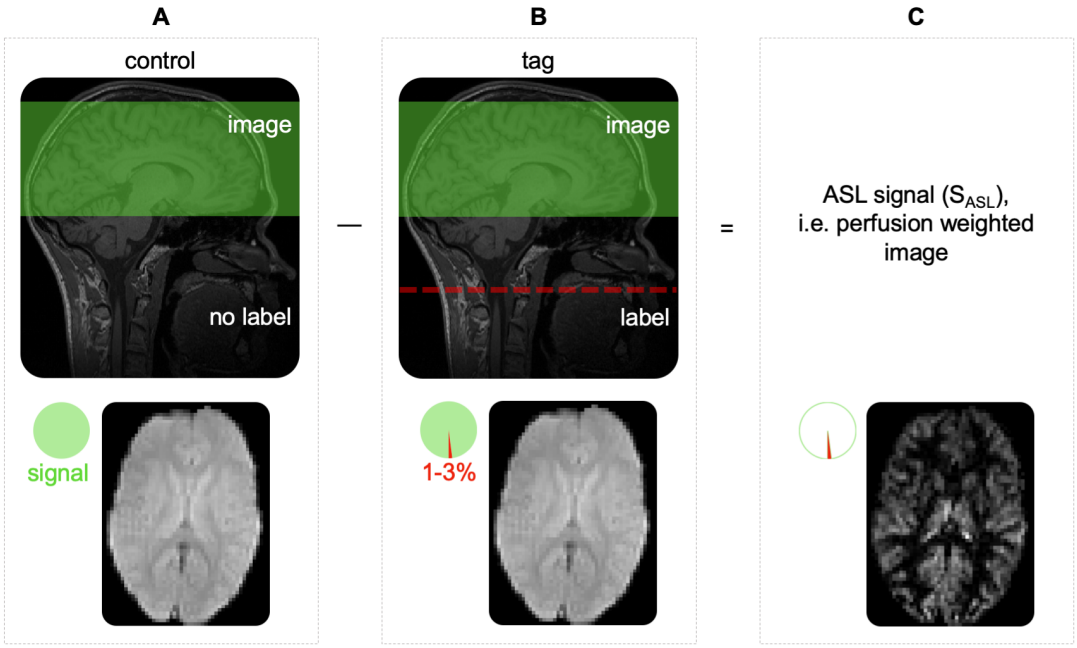

Figure 3.2: Basic principle of pseudo-continuous arterial spin labeling. The control image (A) without an effective labeling corresponds to the full signal in the imaging volume. Due to a previous arterial spin inversion within the labeling layer, the tag image shows a slightly reduced signal. A subtraction of these images isolates the ASL signal (C) respectively yields a perfusion-weighted image. Due to the low SNR of a single experiment, repetition and averaging is required, as done in the perfusion-weighted image shown.

Magnetic marking, or labeling, is performed via the application of RF pulses and corresponds to a (partial) spin inversion. The inverted, or labeled, arterial protons move with the blood flow into the cerebral structures while simultaneously relaxation processes occur. After a latency period, the so-called post-labeling delay (PLD), an image of the brain is acquired. At that time, the labeled blood water protons are not yet fully relaxed and the reduced longitudinal magnetization reduces the signal strength in the image.

With the sequence parameters unchanged, another non-labeled, so-called control image is acquired for each

labeled tag image, which corresponds to the fully relaxed magnetization. The static tissue signal can be eliminated by forming the difference of control and tag images since it is the same in both images. The remaining signal is the difference between labeled and unlabeled blood water protons, which corresponds to a perfusion-weighted signal. The labeling-induced signal reduction amounts about 1 % of the full signal, hence the SNR of a single difference image is low and an averaging of several repetitive measurements required (Alsaedi et al. 2018). Subsequently, the perfusion-weighted signal is also designated as the ASL signal (S_{ASL}), which relates to the averaged signal in the case of repeated experiments.

The local cerebral blood flow is the rate at which the tracer arrives at the capillary level within a voxel of interest (VOI). In order to quantify this flow rate, measurements are conducted, often with various PLDs, and the CBF is derived by a suitable modeling. Another quantity, which can be estimated from multi-PLD data is the arterial transit time (ATT). It quantifies the time between labeling and the arrival of labeled blood water molecules in the tissue compartment in the VOI. (Hernandez-Garcia et al. 2019)

Originally, the labeling, or magnetic inversion, was realized via a flow-driven adiabatic inversion of arterial protons by applying a constant RF pulse and gradient, which is termed continuous ASL (cASL) (Williams et al. 1992) (Section [2.5.5.1]). In this approach, a labeling layer is placed proximal to the imaging volume and creates a steady stream of endogenous tracer for a time known as labeling duration (LD).

However, applying constant RF power is not possible with conventional hardware, motivating the development of a modified cASL type approach called pseudo-cASL (pCASL) (Dai et al. 2008). As presented in Figure [3.3]A, in this approach the constant RF pulse and gradient are replaced or mimicked by a fast succession of short RF pulses and gradients resulting in a labeling which is realized according to the principle of the flow-induced pulsed adiabatic inversion (Section [2.5.5.2]). Typically, the pCASL labeling is applied distal to the cerebellum and aligned preferably orthogonal to the internal carotid and vertebral arteries (Figure [3.1]D). An exemplary placement of the labeling slab can be seen in Figure [5.3]. The labeling plane (Figure [3.2]B, red) matches the position r_0 in Figure [2.6] (red box) at which the resonance condition is satisfied. On-resonant static spins within the plane will be strongly stimulated, but in the case of ASL they do not contribute to the perfusion signal and can therefore be neglected.

The labeling pulses can also affect the adjacent imaging volume, known as magnetization transfer (MT) effects. These effects may have an impact on the perfusion signal. In order to compensate for it, the same pulse sequence is applied for the pCASL control condition with a 180° phase modulation between two consecutive pulses (Figure [3.3]B-C). In this way, the effect of each preceding pulse is compensated so that there is no effective excitation of arterial protons. The same MT effects are induced in the tag and the control condition and they cancel out in the difference image (Alsaedi et al. 2018).

Notwithstanding generality, there are different approaches for the measurement of the control signal. Two main approaches for the gradient design are presented in Figure [3.3]B-C. In the balanced control condition (Figure [3.3]B) the slice selection gradient matches the one of the tag condition ($G_{\mathrm{mean}} \neq 0$) (Wu, Fernández-Seara, et al. 2007; Zhao et al. 2016). The alternative unbalanced control condition (Figure [3.3]C) deviates from the tag condition by using a gradient in the gaps, which compensates the gradient applied during the pulses ($G_{\mathrm{mean}} = 0$). The latter approach has been shown to be less vulnerable to off-resonances and is therefore used in this work (Zhao et al. 2016).

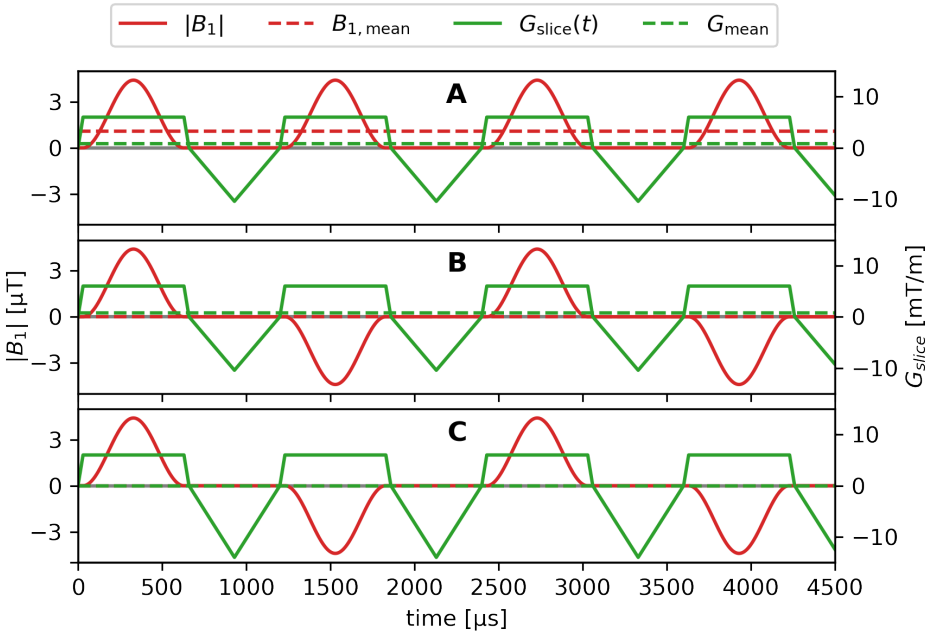

Figure 3.3: Exemplary pCASL pulse train with Hanning-shaped pulses of 600 µs pulse length and a spacing of 1200 µs respectively an inter-pulse gap of 600 µs. In the labeling condition (A), there is an average applied $B_{1,\mathrm{mean}} = 1.1$ µT, an average gradient $G_{\mathrm{mean}} = 0.8$ mT/m, and an on-pulse peak gradient $G_{\mathrm{max}} = 6$ mT/m. Negative pulses indicate a phase shift of 180°, so effectively no B_1 is applied in the control conditions (B) and (C) ($B_{1,\mathrm{mean}} = 0$ µT). Gradients used in the balanced control approach (B) are adopted from (A) ($G_{\mathrm{mean}} \neq 0$). On-pulse gradients are entirely compensated in the unbalanced control approach (C) ($G_{\mathrm{mean}} = 0$).

3.2.2 Magnetization relaxation

As the ASL signal generation bases on a reduction of the longitudiunal magnetization component, it is primarily subject to the longitudinal T_1 relaxation ($S_{\mathrm{ASL}} \propto T_1$) (Detre & Alsop 1999). With an increasing relaxation, the contrast between tag and control images diminishes, with the consequence that long T_1 times are advantageous and allow the measurement of longer PLDs with a sufficient SNR. Approximations of arterial blood T_1, frequently used for ASL analysis, are listed in Table [3.1]. It follows a PLD-dependent relative ASL signal gain at 7 T of approximately $e^{0.125 \cdot \mathrm{PLD}}$ (PLD [s]) compared to 3 T.

A shortening of the transverse T_2 relaxation time at a higher magnetic field strength is also evident. This parameter does not directly affect the ASL tracer lifetime. Due to its dependence on the surrounding, such as the local tissue type, it may be an interesting characterizing parameter in ASL investigations, as presented in Chapter [5].

Table 3.1: Approximate arterial blood proton relaxation times at 3 T and 7 T field strength used for ASL signal modeling and evaluation.

B_0 [T]	$T_{1,\text{blood}}$ [s]	$T_{2,\text{blood}}$ [s]
3	1.664 (Lu et al. 2004)	0.122 (J. M. Zhao et al. 2007)
7	2.1 (Zhang et al. 2012)	0.068 (Krishnamurthy et al. 2013)

3.2.3 SNR

The ASL signal is of low SNR, which may constitute a limiting factor in data evaluation and analysis. Therefore, several approaches exist to improve the SNR (Hernandez-Garcia et al. 2019). One example is the repetition of single ASL experiments and a subsequent averaging. Furthermore, additional, non-labeling RF pulses can be applied to selectively suppress background signal components. For enhancement of the labeling robustness, matched RF pulses and gradient schemes can be employed to reduce the off-resonance sensitivity and enhance the labeling efficiency. In particular, the ASL signal benefits from higher field strengths, as in addition to the inherently higher imaging SNR, longer T_1 relaxation times lead to a slower ASL signal decay. Finally, non-ASL-specific factors also affect the signal, including the influence of the imaging sequence type and acquisition parameters. (Alsaedi et al. 2018)

3.2.4 SAR

The large number of applied labeling pulses and energy-intense background suppression pulses lead to high SAR levels. Due to the field strength dependence of the Larmor frequency and consequently of the RF frequency, this becomes a limiting factor, especially in high field scanners. The SAR can be effectively reduced by shortening the labeling duration, by not using a background suppression or by lowering the RF transmit power. However, according to the adiabatic condition (Equation [2.37]), the latter reduces the labeling efficiency and all potentially degrade the SNR. One approach that reduces SAR by lowering the RF energy, but largely maintains the labeling efficiency, is the use of VERSE-type RF pulses (Section [2.5.6]) (Serrai et al. 2019).

3.2.5 Compartment model

The distribution or diffusion of imaged substances in the cerebral system, which in the case of ASL are blood water molecules, are described by mathematical models. Such models are the basis for the quantification of ASL data. The so-called compartment models subdivide the system into areas with uniform and homogeneous properties, which are the compartments.

The single compartment model is a highly simplified perfusion model and illustrated in Figure [3.4]A (Parkes 2005). It assumes that water molecules, after being transported through the vascular system, immediately and freely diffuse through the capillary walls into the cerebral tissue as they reach the considered voxel of interest. In this way, it models a single, homogeneous, well-mixed compartment. When quantifying ASL under the assumption of the single compartment model, commonly the T_1 relaxation time of brain tissue is assigned to

this compartment. In this model it is taken into account that the tissue water volume is lower than the blood water volume by use of a blood-tissue partition coefficient λ.

The two compartment model (Figure [3.4]B) is closer to the real situation and takes into account that the water molecules in a voxel initially remain intravascular and then pass through the capillary walls into the cerebral tissue at a finite exchange rate (Parkes 2005). Thus, two compartments are assumed, which are an intravascular blood compartment and an extravascular tissue compartment. Both compartments are characterized with specific relaxation times and water content densities. As the relation $T_{1,\text{blood}} > T_{1,\text{tissue}}$ applies, in the two compartment model the ASL signal is assumed to decay slower compared to the single compartment model.

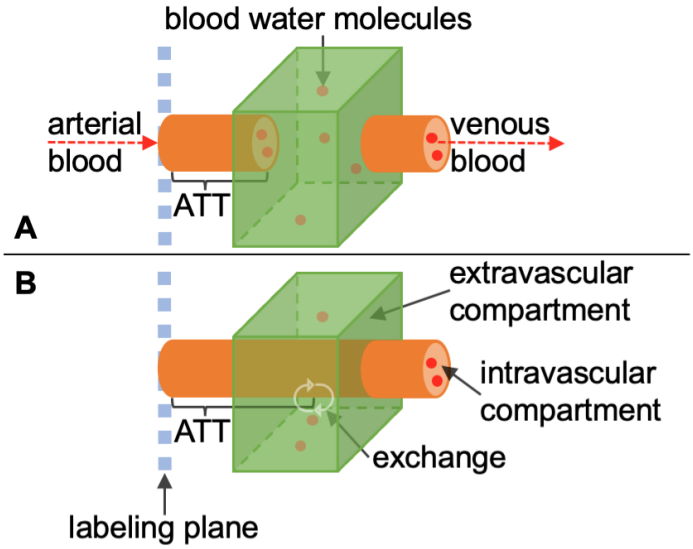

Figure 3.4: (A) Single and (B) two compartment ASL kinetic model schemes. In (A) inflowing labeled arterial blood instantaneously exchanges into the extravascular tissue compartment at a voxel of interest (VOI, green box). In (B) the labeled arterial blood first remains in the intravascular system before entering the extravascular system. The arterial transit time is the duration from labeling to transition into the extravascular tissue compartment at a VOI. Both compartments feature characteristic properties, including individual relaxation times.

A further extension of these models is possible (Sourbron & Buckley 2011). The more complex they become, the more additional, usually unknown parameters are being introduced, which may be difficult to derive from the SNR-limited ASL data.

3.2.6 Quantification

A model of the tracer signal strength and dynamics is required for the quantification of CBF and ATT, which commonly includes the arterial delivery, venous outflow and decay. For ASL, such a kinetic model can be derived based on a specific compartment model by using the Bloch equations, the General Kinetic Model (GKM) or other model-free approaches (Petersen et al. 2006). Subsequently, the GKM is considered and the ASL analyses of this work rely on it (Buxton et al. 1998).

In the GKM it is assumed that the difference signal $\Delta M(t) = M_{\text{control}}(t) - M_{\text{tag}}(t)$ arises purely from the altered longitudinal magnetization of labeled arterial protons and that it is proportional to the flow f. Furthermore, $\Delta M(t)$ is considered as a quantity being transported by the tracer, with a value depending on the arterial inflow, venous outflow, and the longitudinal relaxation. It can be described within a voxel at the time t as follows (Buxton et al. 1998):

$$\Delta M(t) = 2\alpha M_{0\text{a}} f \int_0^t c\,(t')\, r\,(t-t')\, m\,(t-t')\,\mathrm{d}t'. \tag{3.1}$$

The term $2\alpha M_{0\text{a}}$ specifies the difference of the longitudinal magnetization between the tag and the control condition, where the labeling efficiency $\alpha = 1$ corresponds to a perfect inversion in the tag condition. c characterizes the normalized tracer inflow, r its outflow and m the longitudinal relaxation of the tracer. In the convolution of inflow with outflow and longitudinal relaxation, the interval $t - t'$ selects only spins, which arrived in the VOI at the time point t' and are still located there at time point t.

A simplified standard GKM can be derived for (p)CASL by applying the following assumptions (Buxton et al. 1998): first, a uniform, plug-shaped blood flow, which corresponds to a rectangular-shaped arterial input function, and, second, the single compartment model with an instantaneous transition of the tracer into the tissue compartment after reaching the VOI and subsequently the immediate relaxation with the tissue relaxation time $T_{1\text{t}}$. The resulting model parameters are

$$\begin{aligned} c(t) &= \begin{cases} 0 & t < ATT \\ \mathrm{e}^{-\frac{ATT}{T_{1\text{a}}}} & ATT \leq \; t < ATT + LD \\ 0 & t \geq ATT + LD, \end{cases} \\ r(t) &= \mathrm{e}^{-\frac{ft}{\lambda}}, \\ m(t) &= \mathrm{e}^{-\frac{t}{T_{1\text{t}}}}, \end{aligned} \tag{3.2}$$

with the longitudinal relaxation time of arterial blood $T_{1\text{a}}$ and the coefficient $\lambda = \frac{M_{0\text{t}}}{M_{0\text{b}}}$ specifying the volume ratio of water in brain tissue and blood. From this model, the flow f and the ATT can be derived for ASL data. For modeling, the parameters $T_{1\text{a}}$, $T_{1\text{t}}$, $M_{0\text{a}}$, λ, and α are commonly approximated using literature values. The labeling duration is a user-defined parameter, set in the sequence protocol. The equilibrium magnetization of arterial blood $M_{0\text{a}}$ is often estimated by measuring the brain tissue equilibrium magnetization $M_{0\text{t}}$ and a subsequent transformation with λ. $M_{0\text{t}}$ is determined from the measurement of a proton density-weighted image, which is termed a calibration or M_0 reference scan.

The flow f in the physiological unit [ml/100g/min] is denoted as CBF. For single-PLD data using simplifying assumptions, the CBF can be determined as follows (Alsop et al. 2014; Buxton et al. 1998):

$$CBF = \frac{6000 \cdot \lambda \cdot \Delta M \cdot \mathrm{e}^{\frac{PLD}{T_{1\text{a}}}}}{2 \cdot \alpha \cdot T_{1\text{a}} \cdot M_{0\text{t}} \left(1 - \mathrm{e}^{\frac{-LD}{T_{1\text{a}}}}\right)}. \tag{3.3}$$

The underlying assumptions are a fully arrived tracer in the VOI (PLD > ATT), a fast exchange between

blood and tissue compartments and thus no outflow of the tracer, and a relaxation of labeled spins with T_{1a}. The factor 6000 converts the flow into the physiological unit [ml/100g/min].

In addition to the assumptions and approximations for a simplification of the GKM described above, further factors lead to inaccuracies in ASL quantification. For instance, variable and brain region dependent ATTs, which remain unknown, lead to errors in the quantification of single-PLD data (Qin et al. 2013). For multi-PLD measurements, it is possible to model such ATTs and to reduce the related quantification error. Furthermore, dispersion effects can cause tracer concentration changes and divergences between the labeling duration and the tracer bolus duration (Wu, Mazaheri, et al. 2007). Besides that, the inversion or labeling efficiency α depends on the flow velocity, resulting in non-uniform inversion efficiencies for real physiological blood flow profiles as they show a velocity distribution in the vessels (maximum velocities up to 60 cm/s) (Zhao et al. 2016). In anatomical conditions, it is not always possible to cover all arterial vessels orthogonally with the labeling slice, which may also lead to a spatially dependent reduction of α. Finally, MT effects can contribute spuriously to the perfusion signal, but may be compensated by appropriate labeling approaches (Section [3.2.1]).

3.2.7 pCASL sequence

A schematic view of the implemented pCASL sequence is shown in Figure [3.5]. As the brain tissue signal is considerably stronger than the signal generated by ASL, the latter can be enhanced by a suppression or saturation of the static tissue signal. Therefore, a presaturation of the water signal is applied on the imaging volume at the beginning of the ASL module by using water suppression enhanced through T_1 effects (WET) (Figure [3.5], purple) pulses (Ogg et al. 1994). The WET saturation technique employs several (in this case four) sequential, flip angle optimized pulses to transfer the magnetization of water-bound protons to the transverse plane via intermediate steps. In this way, the water suppression is more robust against B_1 imperfections and T_1 inhomogeneities.

After the presaturation, the pCASL labeling is executed for the labeling duration (Figure [3.5], red). It is composed of a series of labeling pulses, which are repeatedly applied in the presence of an optimized slice selection gradient to obtain a flow-induced pulsed adiabatic inversion at the labeling plane (Section [2.5.5.2]). The gradient required to fulfill the adiabatic condition is applied with inverted polarity in the gap between two pulses as presented in Figure [3.3]C.

The labeling is followed by a PLD, before the image volume is measured via the readout module (Figure [3.5], turquoise). A 3D GRASE readout module is implemented for experiments at 3 T and 3D EPI is used at 7 T.

In addition to the water signal presaturation, the static tissue is further suppressed with two or three adiabatic inversion pulses (Figure [3.5], green). The background suppression (BS) has been optimized to minimize CSF, GM, and WM signal contributions as a function of LD and PLD (Section [6.2.1.3]). If the calculated BS pulse coincides with the labeling train, the latter is temporarily interrupted. In order to not affect unlabeled protons in inferior slices, the BS pulse is applied slice-selectively on the imaging volume up to the boundary of the pCASL labeling layer. Resulting from the inversion of already labeled protons, it is required to invert the tag and control conditions in the subsequent labeling. BS pulses during the PLD are applied non-selectively. The background suppression is conducted with HSn pulses (n=14) at 3 T and GOIA-WURST-16-4 pulses are used at 7 T.

In ASL experiments, tag and control images are measured in alternation. The respective condition is generated by running the sequence with an adjusted labeling according to Section [3.2.1] and as demonstrated in Figure [3.3]. The unbalanced control condition is used.

For enabling a calibration of the perfusion-weighted signal within the quantitative modeling, a reference image of the equilibrium magnetization M_0 is acquired by running only the readout without executing the ASL module. In the case of EPI-based readouts, an additional image with an inverted polarity of the readout gradient may be acquired and used for a distortion correction in the postprocessing.

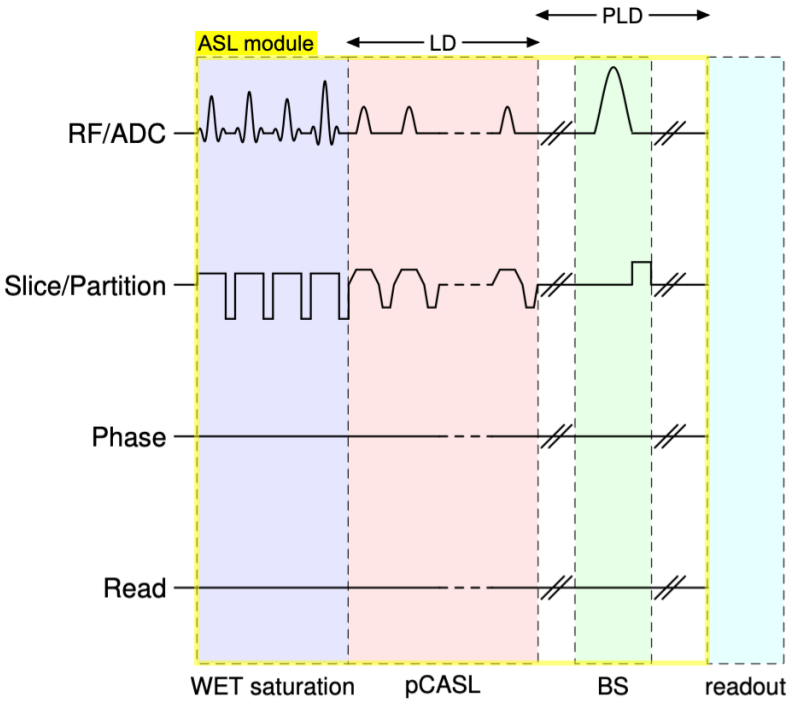

Figure 3.5: Diagram of the pCASL sequence. A WET presaturation of the imaging region is performed before pCASL labeling. Two or three background suppression pulses are timed to suppress static tissue signal. Only a single BS pulse is shown for clarity. The pulses may interrupt the labeling. In case of an interruption, tag and control conditions are switched in the subsequent labeling. Reference images of M_0 are obtained by a pure image readout without a preceding application of the ASL module.

4

Perfusion-weighted pCASL

This chapter is partly based on:

Schidlowski M, Bauer T, David B, Bitzer F, Ostermann L, Racz A, von Wrede R, Radbruch A, Stöcker T, Surges R and Rüber T (2021). Ictal hypoperfusion and iron deposition in symptomatogenic zone of epilepsia partialis continua - A case report. Seizure 89:56-58, doi:10.1016/j.seizure.2021.04.019.

Neumann K, **Schidlowski M**, Günther M, Stöcker T and Düzel E (2021). Reliability and reproducibility of Hadamard encoded pseudo-continuous arterial spin labeling in healthy elderly. Front Neurosci, doi:10.3389/fnins.2021.711898.

4.1 Introduction

The entirely non-invasiveness and good quantifiability of perfusion measurements using pCASL emphasize the great potential for an application in both clinical investigations and in scientific studies. The clinical breakthrough of this method is possibly hampered by the delayed availability of pCASL manufacturer product sequences but also by the multitude of different technical implementations and applied protocols. An attempt to homogenize sequences respectively protocols was made in 2014 by a consensus of the ISMRM perfusion study group and the European consortium for ASL in dementia. (Alsop et al. 2014)

In the following chapter, the practical application of pCASL is elaborated on the basis of these consensus recommendations. The objective is to develop an in vivo imaging framework for clinical and study purposes, which additionally is a prerequisite for the subsequent T_2-weighted ASL Chapter [5]. The sequence implementation is based on preliminary work of the MR physics group of Professor Tony Stöcker, which particularly has been developed by Markus Boland (Boland et al. 2018). An essential improvement of this work is the implementation of the advanced Hadamard encoding technique (Sections [4.2.1], [4.2.2] and [4.3.1]). Additionally, a suitable postprocessing is derived and scan protocols optimized for two application purposes: the first particular area of interest is the measurement in patients of the Clinic for Epileptology. Secondly, the German Center for Neurodegenerative Diseases (DZNE) motivates the use of pCASL in longitudinal studies to investigate processes of neurodegeneration or aging.

In collaboration with the DZNE Magdeburg, the final pCASL sequence and processing framework are investigated in a reproducibility study with elderly subjects for a suitability to be used in population-based studies (Section [4.3.3]). The clinical in vivo application is demonstrated in a patient with a special form of epilepsy (Section [4.3.4]).

4.2 Material and methods

4.2.1 Hadamard encoding

The low ASL signal obtained in a single experiment necessitates repetitions with a subsequent averaging to achieve a sufficient SNR. For a modeling of ATTs, data of more than a single time point or PLD is needed, whereby the modeling quality tends to increase with the number of available PLDs. Also, the quality of CBF quantification improves when multi-PLD data is included. Both, repetitions and the multiple PLDs, increase the acquisition time and thus inevitably lead to a trade-off between practical measurement duration and data quality. (Alsaedi et al. 2018; Hernandez-Garcia et al. 2019)

The conventional approach for the acquisition of multiple PLDs is the repeated measurement of control and tag experiments with adjusted PLDs and thus referred to as multi-PLD ASL. An alternative concept is the Hadamard encoding (Günther 2007). In this approach, tag and control conditions are changed several times during the labeling within a single experiment. The generated bolus is thus subdivided into multiple sub-boli. For a number of N_{bol} sub-boli with the respective sub-bolus labeling durations $LD_i \mid i \in [1, N_{\mathrm{bol}}]$, the total labeling duration of the single experiment is given by $LD_{\mathrm{tot}} = \sum_{i=1}^{N_{\mathrm{bol}}} LD_i$. When applying PLD_{const} subsequently

to the entire labeling, an isolated consideration of each sub-bolus yields the corresponding sub-bolus PLD $PLD_i = PLD_{\text{const}} - LD_i + \sum_{k=i}^{N_{\text{bol}}} LD_k$. From several experiments with equal LD_i and PLD_{const} but differing fitted tag-control sequences, it is possible to extract the signal of each sub-bolus. This is accomplished by appropriate addition and subtraction of the single experiments. These isolated sub-boli are equivalent to a pCASL experiment with the specific LD_i-PLD_i combination and thus correspond to multi-PLD data. One possibility of defining suitable tag-control sequences is the use of Hadamard matrices. Those quadratic $n \times n$ matrices $\underline{H}$ consist of the values ± 1 and have the property

$$\underline{H}\underline{H}^{\mathrm{T}} = n\mathbb{I}_n. \tag{4.1}$$

One possible definition of Hadamard matrices with the order 2^k is the Sylvester's construction (Mitrouli 2014):

$$\begin{aligned} \underline{H}_{2^k} &= \begin{bmatrix} +\underline{H}_{2^{k-1}} & +\underline{H}_{2^{k-1}} \\ +\underline{H}_{2^{k-1}} & -\underline{H}_{2^{k-1}} \end{bmatrix}, 2 \leq k \in \mathbb{N} \quad \text{with} \\ \underline{H}_1 &= \begin{bmatrix} +1 \end{bmatrix}, \\ \underline{H}_2 &= \begin{bmatrix} +1 & +1 \\ +1 & -1 \end{bmatrix}. \end{aligned} \tag{4.2}$$

An exemplary matrix derived this way is:

$$\underline{H}_8 = \begin{pmatrix} +1 & +1 & +1 & +1 & +1 & +1 & +1 & +1 \\ +1 & -1 & +1 & -1 & +1 & -1 & +1 & -1 \\ +1 & +1 & -1 & -1 & +1 & +1 & -1 & -1 \\ +1 & -1 & -1 & +1 & +1 & -1 & -1 & +1 \\ +1 & +1 & +1 & +1 & -1 & -1 & -1 & -1 \\ +1 & -1 & +1 & -1 & -1 & +1 & -1 & +1 \\ +1 & +1 & -1 & -1 & -1 & -1 & +1 & +1 \\ +1 & -1 & -1 & +1 & -1 & +1 & +1 & -1 \end{pmatrix}. \tag{4.3}$$

The matrix entries represent the single sub-boli and specify the labeling condition with the values $+1/-1$ denoting the tag/control condition. Each row i can be considered as a single experiment and the sum of all sub-boli generates a Hadamard-encoded image S_i^{had}. The inverse of H can be directly deduced from Equation [4.1]. By applying it to the encoded images $\vec{S}^{\text{had}} = [S_1^{\text{had}} \cdots S_n^{\text{had}}]^{\mathrm{T}}$, it is possible to decode the individual sub-bolus signals respectively sub-bolus images $\vec{S}^{\text{bol}} = [S_1^{\text{bol}} \cdots S_n^{\text{bol}}]^{\mathrm{T}}$:

$$\frac{1}{n}\underline{H}^{\mathrm{T}}\vec{S}^{\text{had}} = \vec{S}^{\text{bol}}. \tag{4.4}$$

Here it is $n = N_{\text{bol}}$. Since the first column of the Hadamard matrix does not encode a perfusion-weighted

signal, this column is omitted for the pCASL encoding. This way, the matrix is reduced to a size of $(n-1) \times n$ and the encoding of N_{bol} sub-boli requires the acquisition of $N_{\text{bol}} + 1$ single experiments.

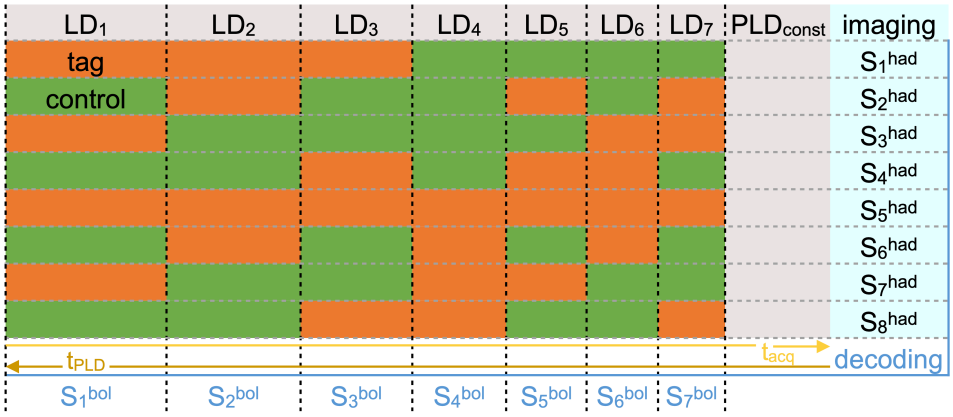

Figure 4.1: Exemplary illustration of the Hadamard encoded image aquisition and decoding using $N_{\text{bol}} = 7$ sub-boli. Note the inverse courses of the acquisition time t_{acq} and PLD time t_{PLD}.

Simultaneous measurement of multiple PLDs respectively sub-boli and a subsequent reconstruction provide two direct advantages in comparison to the conventional multi-PLD approach, which requires a separate control experiment for each tag acquisition and PLD. First, Hadamard encoding is more time-efficient as a number of PLDs equivalent to the multi-PLD approach can be generated with fewer single experiments N_{MEAS}:

$$\frac{t_{\text{had}}}{t_{\text{multi-PLD}}} = \frac{N_{\text{MEAS}}}{2(N_{\text{MEAS}} - 1)} \tag{4.5}$$

Second, the encoding of a *PLD* or sub-bolus involves all data in the Hadamard approach, whereas in the multi-PLD method only the relevant control tag pair data are included in the perfusion weighting. This leads to the SNR advantage

$$\frac{SNR_{\text{had}}}{SNR_{\text{multi-PLD}}} = \sqrt{\frac{N_{\text{MEAS}}}{2}}. \tag{4.6}$$

However, the Hadamard encoding also has potentially disadvantageous features. One of them is the not entirely arbitrarily selectable number of sub-boli $N_{\text{bol}} \in 2^k, k \in \mathbb{N}$. Also, the encoded LDs and PLDs are interdependent, not giving full flexibility in their choice. The increase of the matrix size and the simultaneous use of sub-bolus lengths that provide sufficient signal result in a LD_{tot} which may be SAR-critical, as the energy is dominantly depending on the number of applied labeling pulses. Additionally, a decoding is only possible for a completely acquired matrix, such that measurement interruptions make it impossible to reconstruct any sub-bolus from the current matrix. Finally, Hadamard encoding makes the postprocessing more complex, and by the longer data acquisition time, motion artifacts and short-term physiological effects may be more pronounced or poorer temporally resolved. (Bladt et al. 2020; van Osch et al. 2017)

Against this background, depending on the particular application, one of the two PLD-encoding approaches may be advantageous.

4.2.2 Optimization of Hadamard encoding

The Hadamard-based pCASL labeling can be specified by the Hadamard matrix size respectively the sub-bolus number N_{bol} with the corresponding durations LD_i. The resulting pattern is termed encoding scheme for which several variations exist (Teeuwisse et al. 2014). A trivial approach is the equal partitioning of the total labeling duration LD_{tot} among the sub-boli:

$$LD_i = \frac{LD_{\mathrm{tot}}}{N_{\mathrm{bol}}}. \tag{4.7}$$

Due to relaxation, there is a progressive weakening of the ASL signal with an increasing labeling duration. Considering PLD_{const} as a constant duration t_{const} in which relaxation occurs and starting from a full inversion, the time dependence of the longitudinal magnetization respectively the ASL signal strength can be described as:

$$M_{\mathrm{z}}(t, t_{\mathrm{const}}, T_1) = 1 - 2\mathrm{e}^{-\frac{t+t_{\mathrm{const}}}{T_1}}. \tag{4.8}$$

The general ASL signal decay through an increasing longitudinal relaxation according to Equation [4.8] is shown in Figure [4.2]. Accordingly, earlier generated sub-boli undergo a stronger signal decay due to a longer relaxation duration. This signal non-uniformity can be compensated for by using matched sub-bolus lengths, which, here, is referred to as the T_1 compensating approach. In this approach, the ASL signal decay is subdivided into a defined number of intervals with equivalent areas respectively with equivalent cumulative signals. The start and end times are specified by the total LD and the PLD. This approach can be expressed as a minimization problem by considering the zero crossing of M_{z}, as defined in Equation [4.8]:

$$\min_{LD_i | i \in \{[1, N_{\mathrm{bol}}] \cap \mathbb{N}\}} \sum_{j=1}^{N_{\mathrm{bol}}-1} \left| \int_{t=\sum_{k=0}^{j-1} LD_k}^{t=\sum_{k=0}^{j} LD_k} \{M_{\mathrm{z}}(t, PLD, T_{1\mathrm{blood}}) - 1\}\mathrm{d}t - \int_{t=\sum_{k=0}^{j} LD_k}^{t=\sum_{k=0}^{j+1} LD_k} \{M_{\mathrm{z}}(t, PLD, T_{1\mathrm{blood}}) - 1\}\mathrm{d}t \right| \tag{4.9}$$

with

$LD_0 = 0,$

$LD_{N_{\mathrm{bol}}} = LD_{\mathrm{tot}} - \sum_{l=0}^{N_{\mathrm{bol}}-1} LD_l.$

The optimization is based on the input parameters $N_{\mathrm{bol}}, LD_{\mathrm{tot}}, PLD_{\mathrm{const}}$ and $T_{1\mathrm{blood}}$. Due to the field strength dependence of the relaxation time, also the T_1 compensating encoding schemes are optimized for a specific field strength. The calculation is performed using the minimize function from the Scipy.Optimize library with the sequential least squares programming (SLSQP) optimizer.

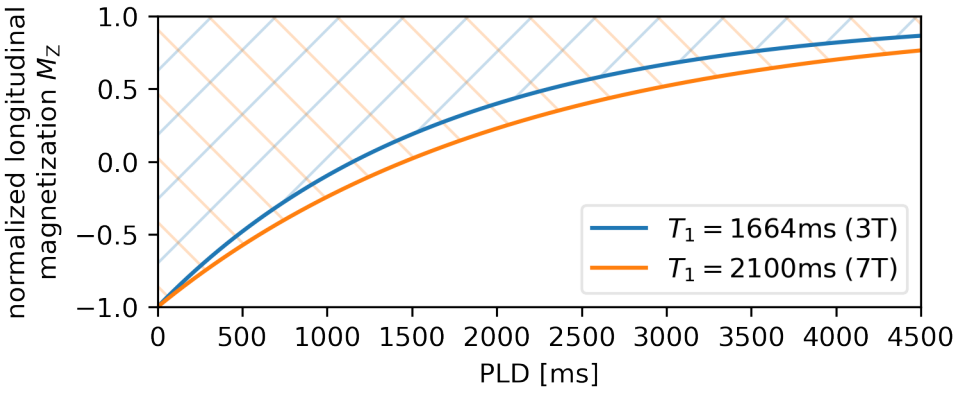

Figure 4.2: ASL tracer decay respectively longitudinal T_1 relaxation simulation for arterial blood water protons at 3 Tesla and 7 Tesla magnetic field strength.

4.2.3 Sequence implementation

The Hadamard encoding has been implemented in the sequence with the development software IDEA (integrated development environment for applications) for Siemens MRI scanners. Building on the existing pCASL sequence, it has been added as an alternative labeling module which creates tag-control conditions according to Section [4.2.1]. It involves the preparation of $N_{\text{bol}} + 1$ unique labeling trains. The sequence preparation is based on pre-defined Hadamard encoding schemes, which are specified by the sub-bolus number N_{bol}, the corresponding labeling durations LD_i and PLD_{const}, as well as the background suppression pulse times. The same LD_i are applied for all single Hadamard-encoded experiments and the tag-control conditions set accordingly. The background suppression pulses are calculated as a function of LD_{tot} and PLD_{const} and it is checked whether these coincide with the labeling train. In the case of an overlap, the labeling pulse train is interrupted for the duration of the background suppression pulse and the tag and control conditions are switched in the subsequent labeling. The labeling module ends with the delay PLD_{const}, during which BS pulses may be applied. The prepared pCASL labeling experiments are consecutively executed and repeated after a complete cycle.

4.2.4 Data processing and analysis

All measured data was reconstructed online on the MRI scanner via the integrated image reconstruction environment (ICE) and saved as a time series of 3D images. ASL-specific postprocessing, including the generation of perfusion-weighted images, was performed offline. For this, a suitable processing routine was implemented, as illustrated in Figure [4.3]. It involves the use of toolboxes from FMRIB's software library (FSL, v6.0.3) (Smith et al. 2004), which is a comprehensive library of analysis tools for brain imaging data.

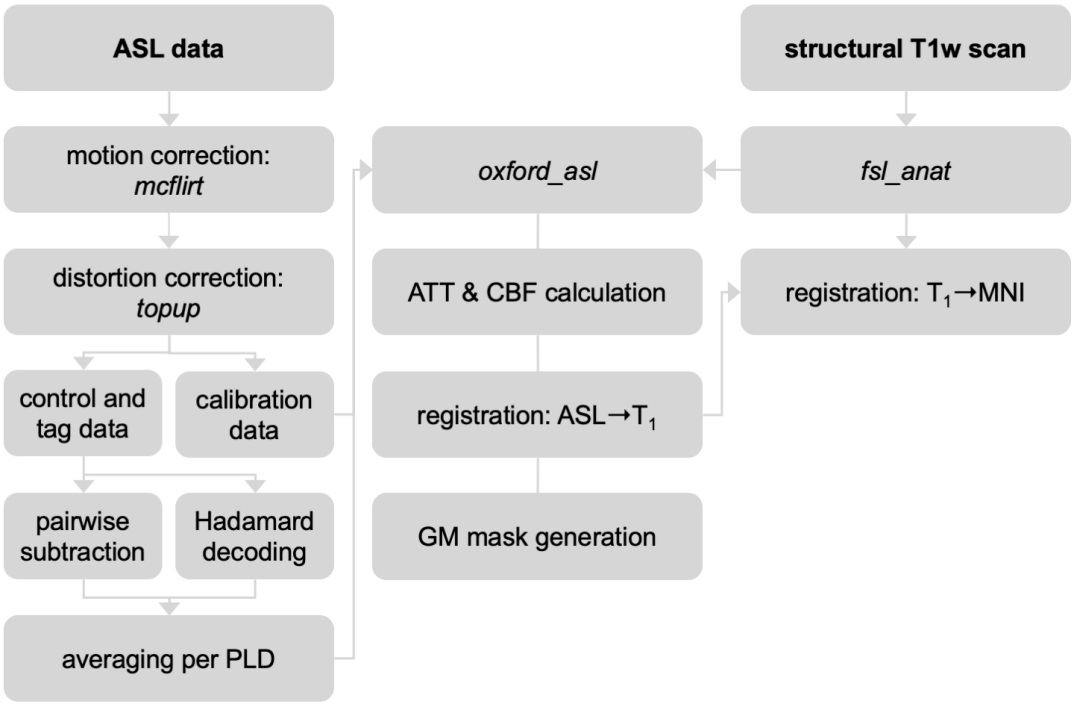

Figure 4.3: Schematic illustration of the ASL data postprocessing pipeline.

The postprocessing is based on the ASL data, made up of M_0 reference scans and a series of alternately acquired tag and control images, and a T_1-weighted structural image that has been included in the scan protocols. The ASL data are first corrected for motion using mcflirt (Jenkinson et al. 2002). Based on the calibration scans with alternating PE polarity, EPI-induced distortions (Figure [4.8], green arrows) are then corrected utilizing topup (Andersson et al. 2003). From these resulting data, mean perfusion-weighted images are then computed per PLD. In the single- and multi-PLD approach, it is achieved by a pairwise subtraction of the control-tag pairs and a subsequent averaging per PLD. In the case of Hadamard encoding, a decoding is performed for each repetition of the complete Hadamard matrix data set by an appropriate addition and subtraction of the images and a multiplication as specified by Equation [4.4]. The resulting multi-PLD images are then averaged for each PLD.

The structural scan is processed with fsl_anat (Smith et al. 2004), which is a general pipeline for processing anatomical images. It involves image correction and registration, brain extraction, and segmentations. In particular, the normalization warp field from structural to MNI space is computed.

The preprocessed data, comprising the calibration scan, PLD-averaged perfusion-weighted images, and fsl_anat output, are used as input for a subsequent modeling with oxford_asl (Chappell et al. 2009). From this data, the toolbox calculates quantitative, calibrated ATTs and CBFs, as well as transformations from native (ASL) space to structural space. Also, GM and WM masks are generated. The quantification builds on inverting the kinetic model of the ASL signal dynamics (Equation [3.2]) and takes advantage of the Bayesian inference theory (Chappell et al. 2009).

4.2.5 Data quality assessment

An assessment of the ASL data quality may be realized with different metrics, depending on the specific targeted information. Due to a data acquisition over a comparatively long time period and a subsequent averaging, it may be useful to assess the longitudinal signal stability. Such an ASL signal assessment can be accomplished by taking the non-averaged control-tag difference images and defining a time-weighted, longitudinal SNR:

$$tTSNR(\vec{r}_i, PLD) = \frac{\mu(\vec{r}_i, PLD)}{\sigma(\vec{r}_i, PLD)} \frac{1}{\sqrt{T_{\mathrm{acq}}(PLD)}}. \tag{4.10}$$

The calculation is performed per voxel $\vec{r}_i$ and separately for each PLD, using the mean value μ of the voxel within the non-averaged PLD time series, its associated standard deviation σ and the total acquisition time T_{acq}.

Alternatively, for a quality assessment, the quantity of the generated label may be considered. This can be realized, both, based on the relative ASL signal from the averaged difference images and also on the quantified CBF from the modeling. Since GM is perfused dominantly, it suggests to analyze perfusion within this ROI for a quality check. Also, a division into sub-ROIs is a common practice. A PLD-specific evaluation can be carried with the perfusion-weighted signal.

In addition to the ASL signal quality, model-derived ATT values and distributions, as well as ATT and CBF fit uncertainties provide an assessment criterion that may be used to evaluate the suitability of the applied protocol parameters and the derived data for the related modeling.

4.2.6 Protocol setup

The elaboration of a pCASL scan protocol can be informed by numerous requirements. Potentially relevant influencing factors are

- the hardware (MRI scanner model, software),
- targeted quantities (relative/absolute CBF, ATT),
- the labeling approach (single/multi-PLD, Hadamard encoding),
- ASL scan parameters (LD, PLD, BS),
- imaging parameters (FOV, PI, voxel size),
- the related number of required repetitions and
- the resulting, along with an optionally maximal, acquisition time T_{acq}.

These factors are partially interdependent and due to the intrinsically low SNR, a compromise between acquisition time and data quality must be found, especially for pCASL. Particularly for MR scanners of older generations, hardware and software limitations for the application of advanced MRI techniques may be

relevant. Against this background, an in vivo imaging framework will be derived which is suited for clinical and scientific or study applications.

A state-of-the-art protocol should make the advantages of perfusion imaging with ASL accessible and so the data should enable for a modeling of ATTs and absolute calibrated CBFs. This excludes the single-PLD approach. A target length of 7 minutes is specified for a possible inclusion in the free protocol of the Rhineland study. In addition to the application in this longitudinally oriented study, the protocol length also appears reasonable and feasible for single time point and/or clinical measurements, including examinations of diseased individuals. As no specific LD or PLD are requested and also no full flexibility in their choice is required, the Hadamard approach may be advantageous to be used in such an universal protocol. The prescribed time allows to use the 7 sub-bolus Hadamard encoding with a sufficient number of measurement repetitions. To facilitate advanced postprocessing techniques, reference scans shall be acquired with both phase encoding polarities. In order to ensure steady states, an additional reference and an additional labeling dummy scan can be acquired and the first measurement excluded from the analysis in each case. Imaging must include the entire cerebrum, whereby an isotropic voxel geometry is preferred. A use of PI techniques shortens the minimal TR and so the total scan time at the cost of a slight SNR-reduction, but increasing the number of realizable repetitions within the total scan time limit. The resulting protocol is specified in Table [4.1] and designated as $\mathrm{PROT}_{\mathrm{perfusion}}$. It meets all the abovementioned requirements.

In 3 T experiments, a 3D GRASE readout is used for data acquistion. Thereby a blurring may arise in the 3D phase encoding direction, which is substantially determined by the echo train length. For reducing the ETL respectively the blurring and thus achieving single-shot whole-brain images of an appropriate quality, a 2×2^1 CAIPIRINHA parallel imaging acceleration is preferred (Section [2.4.2]). However, this acceleration technique is not practicable on an older Siemens Trio 3 T scanner due to an earlier software version (VB17). The other available acceleration techniques are not capable to satisfactorily reduce the ETL with largely preserving the SNR and lead to an unsuitable blurring instead as illustrated in Figure [4.8] (blue arrows, top row).

To overcome these problems, an alternative readout is used at the Trio scanner. While preserving a whole-brain imaging and keeping all proposed ASL-specific parameters, first, a two-shot acquisition is introduced to reduce the ETL. Thereby, the FOV is split into two segments in 3D PE direction, which are measured in two separate ETL-reduced measurements and combined to a single whole-brain image afterwards. This results in a doubling of the acquistion time. Second, the number of 3D slices is reduced by adjusting the voxel geometry or size, which additionally shortens the ETL (Figure [4.8], blue arrows, bottom row). The resulting protocol proposal for the Trio scanner is shown in Table [4.1] and denoted as $\mathrm{PROT}^{\mathrm{Trio}}_{\mathrm{perfusion}}$.

Table 4.1: pCASL protocol $\mathrm{PROT}_{\mathrm{perfusion}}$ for Hadamard-encoded perfusion measurements and the adjusted protocol $\mathrm{PROT}^{\mathrm{Trio}}_{\mathrm{perfusion}}$ for an executability on the Trio scanner.

	perfusion protocol	
3D GRASE	$\mathrm{PROT}_{\mathrm{perfusion}}$	$\mathrm{PROT}^{\mathrm{Trio}}_{\mathrm{perfusion}}$
FOV	$211 \times 211 \times 119$ mm^3	$210 \times 210 \times 120$ mm^3
acquisition matrix	$64 \times 64 \times 36$	$70 \times 70 \times 30$
resolution	$3.3 \times 3.3 \times 3.3$ mm^3	$3 \times 3 \times 4$ mm^3
$\mathrm{TE}_{\mathrm{GRASE}}$	22.3 ms	22.9 ms
PAT (PE × 3D)	CAIPIRINHA 2×2^1	GRAPPA 2×1
3D segmentation	$1 \times$ SEG	$2 \times$ SEG
BW	2441 Hz/Px	2551 Hz/Px
ETL	413 ms	355 ms
ASL		
LD	3.5 s	3.5 s
PLD	0.5 s	0.5 s
labeling method	7HAD	7HAD
TR	7 s	7 s
BS	2 pulses	2 pulses
control method	unbalanced	unbalanced
pulse type	VERSE	VERSE
$\mathrm{G}_{\mathrm{mean}}$	0.5 mT/m	0.5 mT/m
$\mathrm{G}_{\mathrm{max}}$ (pre-VERSE)	3.5 mT/m	3.5 mT/m
RF duration	420 µs	500 µs
RF gap	180 µs	660 µs
MEAS	7 × 8 HAD + 1 dummy	(4 × 8 HAD + 1 dummy) × 2 SEG
M_0 calibration		
TR	6 s	6 s
MEAS	2 AP + 2 PA + 1 dummy	(2 AP + 2 PA + 1 dummy) × 2 SEG
TA	7 min 9 s	8 min 42 s

A rapid successive switching of gradients, as it is done particularly in the pCASL-labeling, can induce resonance effects in the powerful scanner gradient systems. Such effects must be avoided to ensure patient safety and to exclude damage of the system. The resonance frequencies are specific for each gradient system installed (Segbers et al. 2010; Tomasi & Ernst 2006). Thus, prior to the application of the pCASL sequence, its compatibility must be verified by checking the resonances for each individual pCASL labeling scheme. These frequencies are obtainable via the Fourier transform of the temporal gradient profile, whereby the labeling is realized with the z-gradient G_z. Figure [4.4] demonstrates an exemplary resonance check of two labeling schemes on the AS097 gradient system, which can be found in the Siemens Biograph-mMR. Due to occuring acoustic resonances the labeling must be adjusted for the execution on the Trio scanner. The modified timing is given in the protocol $\mathrm{PROT}^{\mathrm{Trio}}_{\mathrm{perfusion}}$ in Table [4.1]. In order to meet the adiabatic condition, the average B_1 is maintained by a proper RF pulse scaling.

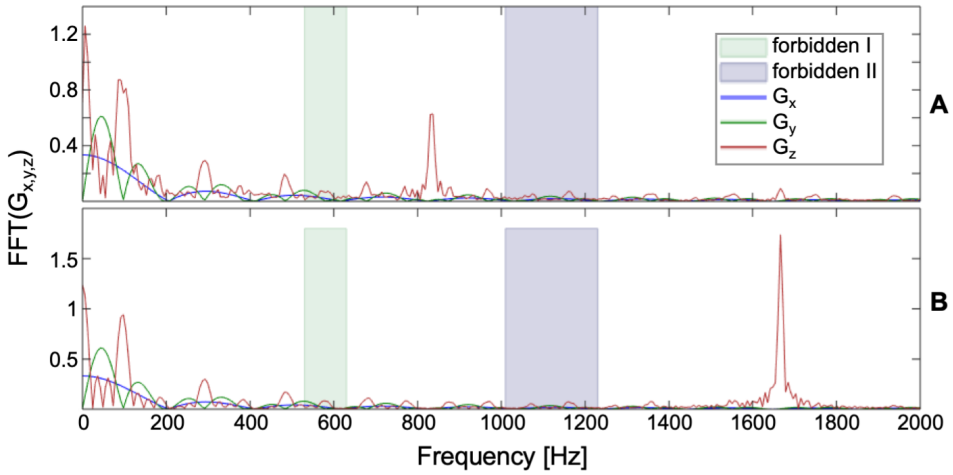

Figure 4.4: Resonance frequency check of two pCASL labeling gradient trains on the AS097 gradient system. Two forbidden frequency ranges [530,630] Hz and [1010,1230] Hz are specified in which the device main resonance frequencies lie. As required, the peaks of the G_z gradient frequency spectra (red) are outside these intervals for the labeling schemes with a pulse length/gap of 500 µs/700 µs (A) and 420 µs/180 µs (B) and hence allowed to be executed on this gradient system.

4.2.7 Reliability and reproducibility study design and experiments

The knowledge of a potential age dependence of perfusion is of clinical and scientific interest, especially for the investigation of neurodegeneration and dementia. Not exclusively, but in particular for the related comprehensive, longitudinal and often multicentric cohort studies, the information of the data reliability and reproducibility is of crucial importance. So, device independence would allow a pooling of measurement data and thus the generation of comprehensive data sets offering higher quality analyses and potentially new analytical features.

In this context, the suitability of the developed sequence and the protocol $\mathrm{PROT}_{\mathrm{perfusion}}$ (Table [4.1]) was investigated within a test-retest measurement series. It includes healthy elderly subjects, which were scanned on two MRI scanners of the DZNE Magdeburg at each, a test and a retest, session. One device is a 3 T Siemens Magnetom Skyra MRI scanner (Siemens, Erlangen, Germany) equipped with a 32-channel head coil (Nova Medical, Wilmington, Massachusetts, USA) and the other is a 3 T Siemens Biograph mMR (PET/MR) scanner also equipped with a 32-channel head coil. The parameters of interest are the CBF and the ATT. The ASL data analysis is based on the processing described in Section [4.2.4] and illustrated in Figure [4.3].

A total of 26 healthy elderly subjects underwent test-retest measurements (age range 56-84 years, mean age 68.3 ± 6.3 years, 15 female/11 male). The mean intersession interval is 78 ± 18 days. Complete and valid data are available for 18 subjects for both scanners, for 4 subjects only for the Skyra and for three subjects only for the mMR Biograph device. Data incompleteness is due to non-participation in single retest measurements and due to exclusion of non-physiological data in one experiment.

4.2.8 Statistical analysis

Multiple reproducibility metrics were inferred from the test-retest data set for the determined CBF and ATT values.

The longitudinal reliability was assessed by using the intraclass correlation coefficient (ICC) for one-way random-effects ANOVA model as proposed by Shrout and Fleiss (Bartlett & Frost 2008; Matheson 2019; Shoukri et al. 2008; Shrout & Fleiss 1979). It is calculated as follows

$$ICC = \frac{\sigma_{\text{bs}}^2}{\sigma_{\text{bs}}^2 + \sigma_{\text{ws}}^2}, \tag{4.11}$$

with σ_{ws} being the within-subject and σ_{bs} the between-subject standard deviation.

Qualitatively, a higher ICC, which can range from 0 to 1, indicates more reliable results. For quantitative assessments, the following value ranges were considered (Cicchetti 1994):

- poor: < 0.4,
- fair: $0.4 - 0.59$,
- good: $0.6 - 0.74$,
- excellent: > 0.75.

The measurement precision, which reflects the variability and the measurement error, was evaluated according to the within-subject coefficient of variation (WSCV) (Floyd et al. 2003; Lajoie et al. 2017; Matheson 2019). It quantifies the error relative to the size of the measurements and is calculated by a division of the within-subject standard deviation σ_{ws} by the global mean μ (Jiang et al. 2010):

$$WSCV = \frac{\sigma_{\text{ws}}}{\mu}. \tag{4.12}$$

Small values correspond to high precision.

4.2.9 Clinical case: epilepsia partialis continua

The protocol $\text{PROT}_{\text{perfusion}}^{\text{Trio}}$ has proven to be practical also for clinical study measurements involving diseased subjects. In addition to healthy subjects, the perfusion could be measured in stroke, brain tumor and epilepsy patients. The following focuses on the application for epilepsy imaging and includes an exemplary measurement.

A well-known phenomenon of epileptic seizures is the perfusion change in brain areas suspected to be the seizure origin (seizure onset zone). Mostly, an increased perfusion (hyperperfusion) compared to the normal level is observed during the seizure (ictal state) and a decreased perfusion (hypoperfusion) in the subsequent phase

after the seizure (post-ictal state) (Perera et al. 2020). Hence, it is possible to infer a potential seizure onset zone from contrasting the measurements of both conditions. Such a localization is essential for the treatment of epileptic disorders (Rosenow 2001). Since performing an MRI scan during an ongoing epileptic seizure, i.e. in the ictal state, is problematic due to patient safety reasons and seizure unpredictability, often the post-ictal state is contrasted with the patient's normal perfusion. Measurements for assessing this perfusion, which is not influenced by seizure, may be performed after a seizure-free period of more than 24 hours (Gaxiola-Valdez et al. 2017).

A particularly interesting case could be investigated in the Clinic for Epileptology of the University Hospital Bonn. In brief, the patient presented with a special form of epilepsy, which is known as epilepsia partialis continua (EPC). The special feature of this disease manifestation is a persistent seizure occurrence, which phenomenologically is not perceptible. The time of disease manifestation is referred to as the EPC onset. In this patient, a seizure interruption was present only during sleep. This gave rise to the justifiable possibility of measuring the ictal state while awake and the non-ictal state during drug-induced sleep.

The measurements were performed on a Magnetom Trio 3 T scanner (Siemens Healthineers, Erlangen, Germany) with a 32-channel head coil using the protocol $\mathrm{PROT}^{\mathrm{Trio}}_{\mathrm{perfusion}}$ (Table [4.1]). In addition to ASL measurements, the multimodal neuroimaging protocol included a conventional structural T_1-weighted scan (MPRAGE, TE=2.54 ms, TR=1660 ms, FOV=$166.4 \times 256 \times 256$ mm, voxel size=$0.8 \times 0.8 \times 0.8$ mm^3), a T_2-weighted fluid-attenuated inversion recovery scan (FLAIR, TE=388 ms, TR=5000 ms, FOV=$160 \times 256 \times 256$ mm, voxel size=$1 \times 1 \times 1$ mm^3) and a T_2^*-weighted multi-echo time gradient-recalled echo sequence suitable for QSM (Wang & Liu 2014) (3D FLASH, phase and magnitude image reconstruction, TE=3.98/9.8/18.27/26.74/35.21/43.68/52.15 ms, TR=59 ms, FOV=$172.5 \times 230 \times 144$ mm, voxel size=$0.898 \times 0.898 \times 1.5$ mm^3, flow compensation). Measurements were approved by the institutional review board of the medical faculty of the University of Bonn. All experiments were performed in accordance with the guidelines and regulations of this ethics board. Written informed consent was obtained from the patient.

These ictal and non-ictal measurements of the multimodal protocol were performed six months after the clinically proven disease manifestation, the EPC onset. Further FLAIR images are available for the EPC onset period.

The ASL data analysis was carried out with the developed processing pipeline (Section [4.2.4]). Here, instead of using absolute, quantified CBF values, perfusion images were per-scan-normalized by the mean gray matter perfusion to reduce a potential wake-sleep-bias. MNI space normalized perfusion maps were taken for a CBF comparison between both hemispheres.

4.3 Results

4.3.1 Optimization and comparison of Hadamard encoding

The determination of Hadamard encoding schemes is accomplished by using the T_1 compensating approach as described in Section [4.2.2]. On the basis of the minimization problem [4.9], a T_1 compensating Hadamard

encoding scheme with 3 sub-boli (3HAD) and one with 7 sub-boli (7HAD) is derived for 3 T and 7 T field strengths. In line with (van Osch et al. 2017) a PLD=500 ms and a LD=3500 ms is used for the 7HAD scheme calculation. For the 3HAD optimization, the PLD=500 ms is kept and in accordance with the consensus proposal (Alsop et al. 2014) the LD=1800 ms selected. The optimized parameters are summarized in Table [4.2].

Table 4.2: T_1 relaxation optimized 3 sub-bolus (3HAD) and 7 sub-bolus (7HAD) Hadamard-encoded labeling schemes for main magnetic field strengths of 3 Tesla and 7 Tesla.

B_0 [T]	LD [ms]							PLD [ms]	scheme
	VII	VI	V	IV	III	II	I		
3	1175	683	482	374	305	257	224	500	7HAD
3					833	553	414	500	3HAD
7	1005	677	511	411	343	295	258	500	7HAD
7					780	567	453	500	3HAD

Experimental in vivo results are shown in Figure [4.5] for the two 3 T schemes as decoded, perfusion-weighted images exemplarily for one subject. In both cases the labeling slab placement is identical. For the demonstration of a potential time reduction, a 4-fold repetition of the related full scheme has been performed, resulting in a total of 32/16 single experiments for the 7HAD/3HAD scheme and, using an identical TR, in a TA-ratio of 2 : 1.

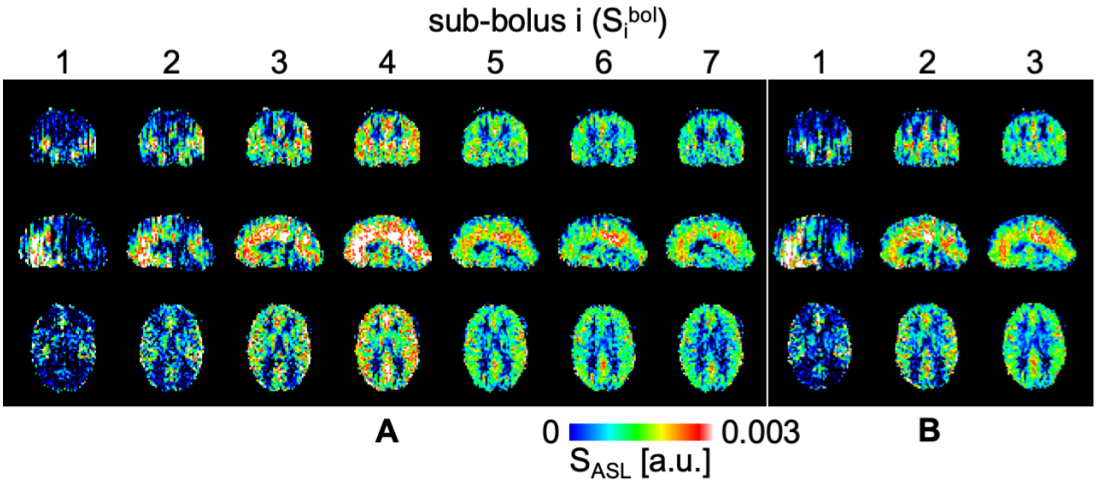

Figure 4.5: Hadamard-decoded perfusion-weighted images (S_{ASL}) of one subject using the T_1 relaxation optimized 7HAD (A) and 3HAD (B) protocols. Measurements with a 4-fold repetition of the full encoding scheme were performed in both conditions, resulting in 32 and 16 single experiments in scheme (A) and (B).

A comparison of the T_1 compensating with a non-compensating approach was performed in a further subject using the 7HAD encoding scheme and second Hadamard-based labeling with a uniform sub-bolus duration of 500 ms. All other parameters, including the PLD=500 ms, remained unchanged. Both protocols were acquired under identical experimental conditions and slice positionings. The decoded ASL signal per PLD is provided

in Figure [4.6]. In the optimized 7HAD scheme (Figure [4.6]A), after an initial inflow of the label at the early PLDs, the ASL signal remains on a balanced high level throughout the brain across the following PLDs. The early perfusing bolus is also visible in the uniform labeling (Figure [4.6]B). In the further course, the deviant pattern of a pronounced signal drop after reaching the whole-brain perfusion maximum in sub-bolus III is apparent, and so a reduced late signal.

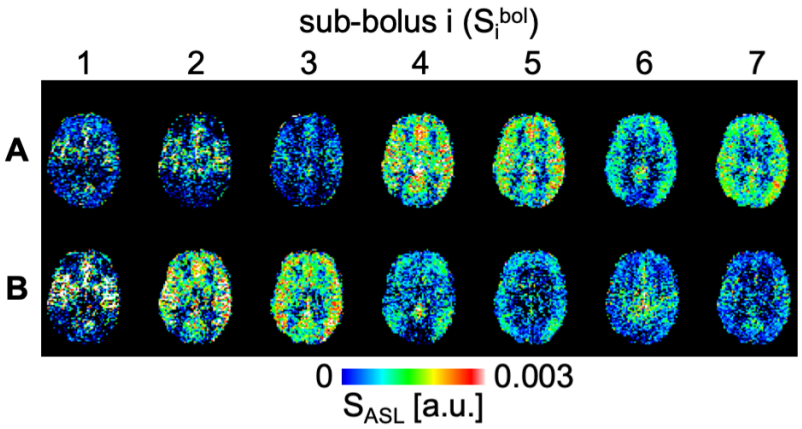

Figure 4.6: Hadamard-decoded perfusion-weighted images of one subject using (A) the T_1 relaxation optimized 7HAD labeling scheme and (B) a uniform 7 sub-bolus labeling scheme with an equal sub-bolus duration of 500 ms and a PLD of 500 ms. A lack of late signal is visible in the uniform approach.

For an assessment of the quantification or modeling quality, particularly of the ATT, $\text{PROT}^{\text{Trio}}_{\text{perfusion}}$ measurements and an additional multi-PLD-based comparative measurement $\text{PROT}^{\text{Trio}}_{\text{perfusion,multiPLD}}$ with LD=1800 ms and three PLDs=300/1050/1800 ms have been performed. Further $\text{PROT}^{\text{Trio}}_{\text{perfusion}}$/$\text{PROT}^{\text{Trio}}_{\text{perfusion,multiPLD}}$ differences are the background suppression pulse (2/3) and repetition (32/30) numbers, resulting in a measurement of 4 full encoding schemes respectively 6 CT pairs per PLD and the TAs of 448/420 s. It corresponds to a TA per PLD of 64/140 s. Results were obtained with the proposed standard processing pipeline. The postprocessing of the multi-PLD data differs in such, that, instead of a Hadamard decoding, the CT images are pairwise subtracted. Due to the well-matched TAs both approaches are directly compared. CBF, ATT and σ_{ATT} distributions of both protocols are presented in Figure [4.7] in an exemplary slice.

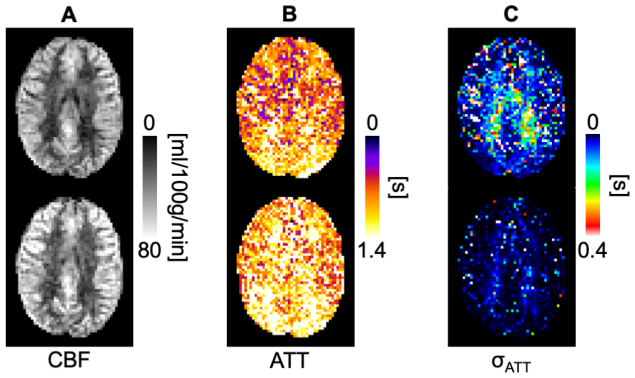

Figure 4.7: Comparison of (A) CBF and (B) ATT modeling resulting from multi-PLD (top row) and Hadamard-encoded (bottom row) data obtained with protocols of a comparable acquisition time. The (C) related standard error σ_{ATT} is calculated from the ATT fit parameter estimate.

Within a GM and a WM ROI for $\text{PROT}^{\text{Trio}}_{\text{perfusion}}$/$\text{PROT}^{\text{Trio}}_{\text{perfusion,multiPLD}}$ it is found: GM-CBF $56 \pm 18/51 \pm 13$ ml/100g/min, WM-CBF $32 \pm 12/29 \pm 10$ ml/100g/min, GM-ATT $1.06 \pm 0.35/0.92 \pm 0.32$ s and WM-ATT $1.15 \pm 0.34/1.00 \pm 0.42$ s. There is a median uncertainty in estimated ATT-values $\tilde{\sigma}_{\text{ATT}}$ of 0.006/0.040 s for GM and 0.017/0.088 s for WM.

4.3.2 Perfusion protocol application

The developed protocols are summarized in Table [4.1]. The illustrations and analytical results in Sections [4.3.3] and [4.3.4] are primarily built on them.

The effect of a segmented data acquisition for shortening the ETL respectively for reducing the blurring, as proposed for the Trio scanner ($\text{PROT}^{\text{Trio}}_{\text{perfusion}}$, Section [4.2.6]), is demonstrated in Figure [4.8].

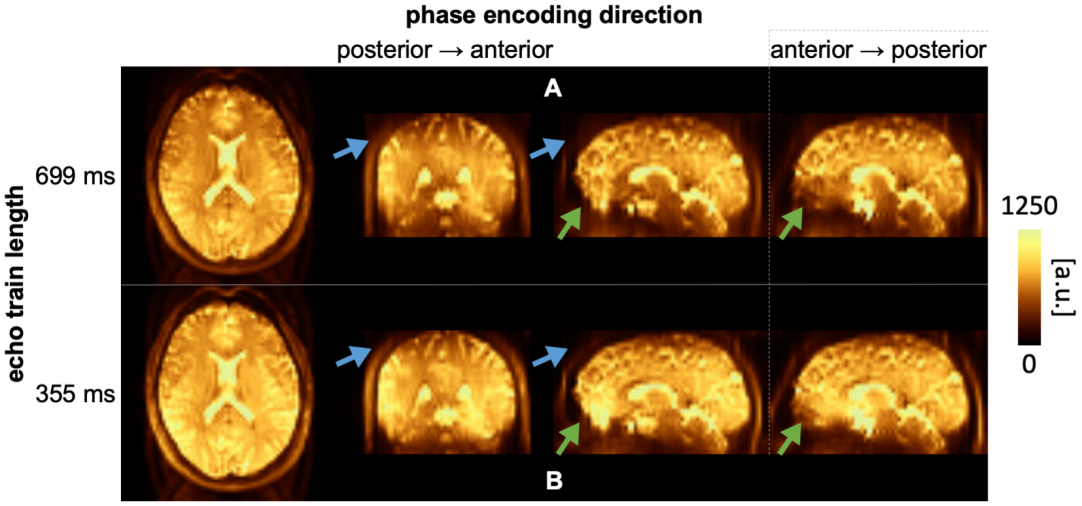

Figure 4.8: Effect of the ETL on blurring in 3D GRASE images. M_0 reference images are shown, obtained with the protocol $\text{PROT}^{\text{Trio}}_{\text{perfusion}}$ using (A) a single-shot acquisition and (B) the proposed twofold segmented (2× SEG) readout. The resulting ETLs are (A) 699 ms and (B) 355 ms. In the segmented image (A) a reduced blurring is noticeable in 3D PE direction (inferior-superior direction in the coronal and sagittal views) which is indicated with blue arrows. No blurring occurs in the frequency encoding direction (left-right direction in the axial view). A comparison with the additional measurement with an inverted phase encoding polarity demonstrates EPI distortion artifacts in the sagittal view, which are marked with green arrows.

4.3.3 Reliability and reproducibility in healthy elderly

Figure [4.9] shows the perfusion-weighted and per subject test-retest-averaged ASL signal for both scanners. The best-fit line represents the mean signal of all subjects at each PLD. It is complemented by the 95 % confidence interval. For both devices an initial signal increase can be observed, followed by a stabilization at later PLDs. This trend of a steadying signal level indicates a successful compensation of the T_1-induced signal loss with the applied Hadamard encoding.

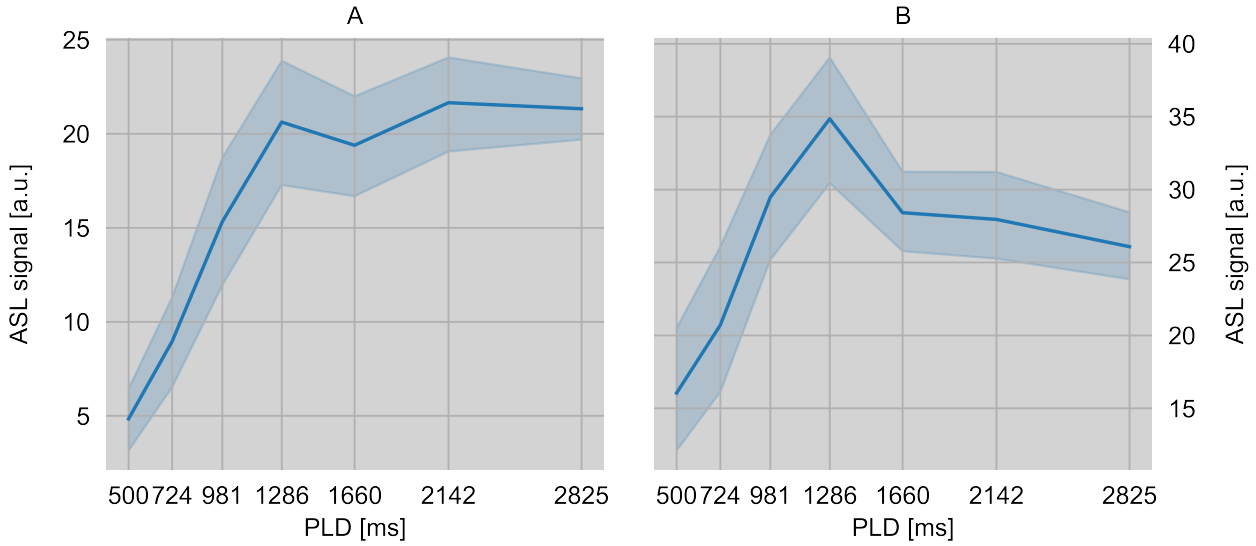

Figure 4.9: Mean ASL difference signal in GM ROI for all subjects at all decoded PLDs measured twice with the (A) Skyra (n=22) and (B) mMR Biograph scanner (n=21) using the protocol $\text{PROT}_{\text{perfusion}}$. The bold line represents all subjects' mean signal per PLD along with the 95 % confidence interval around the mean.

An excellent test-retest reliability of the cerebral perfusion is found for both MRI devices. The results in Table [4.3] suggest higher reliabilities of the CBF and ATT estimates for measurements at the Skyra scanner, indicated by smaller WSCVs. The perfect agreement of GM CBF results between both scans is demonstrated in Figure [4.10] for all subjects and measurements at the Skyra scanner. For both devices, a one-way ANOVA confirms that there are no significant intra-session CBF differences ($p > 0.05$).

Table 4.3: Test-retest reliabilities of mean CBF and ATT in GM and WM ROIs for measurements with the Skyra and the mMR Biograph scanner.

	WSCV [%]			
	CBF		ATT	
ROI	Skyra	mMR Biograph	Skyra	mMR Biograph
GM	2.9	5.6	2.3	2.9
WM	3.3	5.7	1.9	2.0

For the examination of a device independence respectively the reproducibility of perfusion measurements, the mean CBF and ATT were calculated per subject for both scans within a GM and a WM ROI. The subject-averaged GM CBF values are presented in Figure [4.11]. The resulting values were used for an intra-scanner comparison and the determined ICCs and WSCVs are provided in Table [4.4]. Overall, a good reproducibility of both quantities is evident. The related ICC analysis confirms a good up to an excellent agreement between both scans and devices. In this measurement series, the ATTs emerge as a more replicable quantity due to clearly lower WSCVs in all subjects as compared with the CBFs.

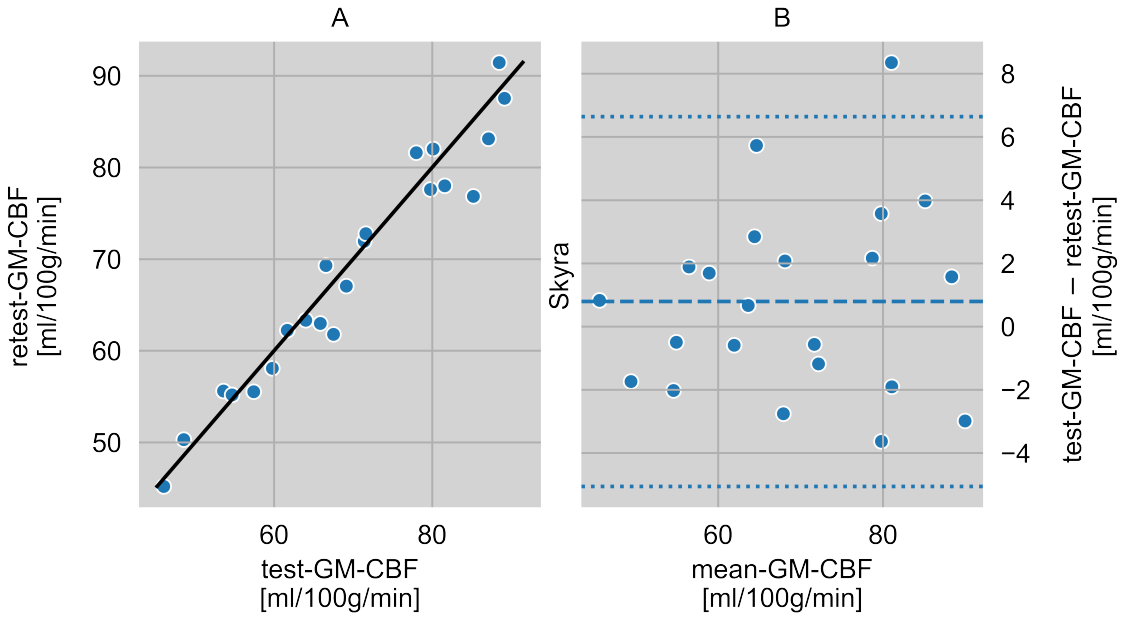

Figure 4.10: (A) Correlation of GM CBF values from repeated measurements of 22 subjects in GM ROI obtained with the Skyra scanner. The solid line is the identity function and represents an optimal correlation. (B) Agreement (Bland-Altman plot) between test and retest CBF values which are shown in (A). The mean differences between both scans are represented by the dashed lines and dotted lines display the corresponding limits of agreement (1.96× standard deviations of mean differences).

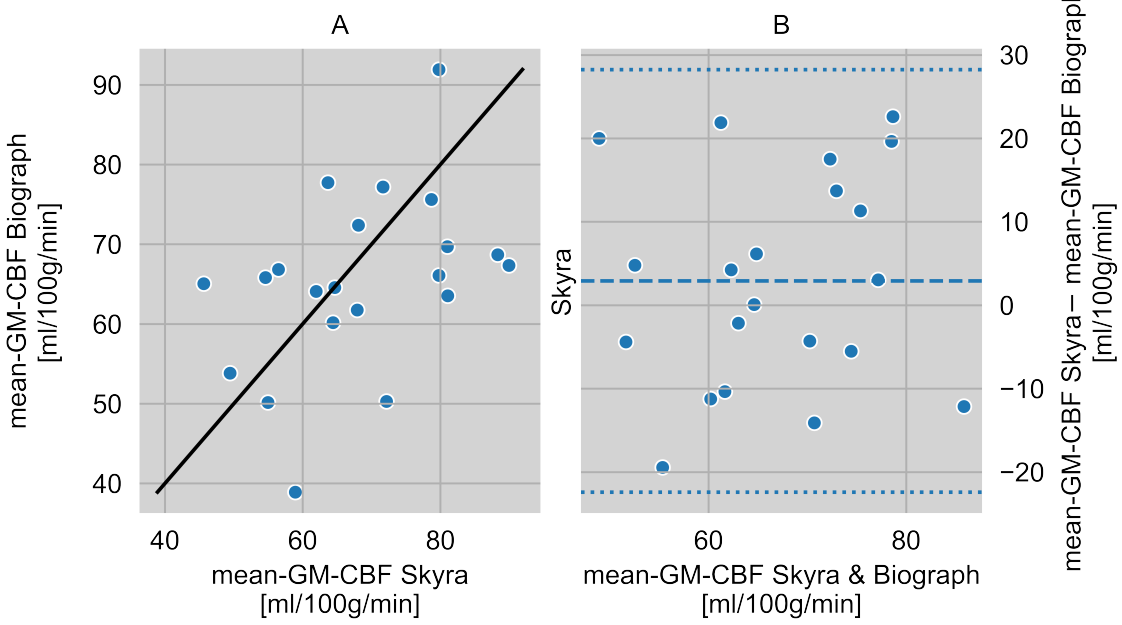

Figure 4.11: Correlation of scanner-averaged GM CBF values of 18 subjects from repeated measurements with the Skyra and the mMR Biograph scanner. The solid line is the identity function and represents optimal correlation.

Table 4.4: Intra-scanner reproducibility of mean CBF and ATT in GM and WM ROIs based on per scanner-averaged values from test and retest measurements.

	WSCV [%]		ICC	
ROI	CBF	ATT	CBF	ATT
GM	12.7	5.5	0.704	0.754
WM	13.2	3.6	0.758	0.713

4.3.4 Clinical case: epilepsia partialis continua

The clinical study measurement results of the patient with epilepsia partialis continua are shown in Figure [4.12]. Information on the MRI sequences and the underlying protocols are summarized in the related caption.

As outlined in Section [4.2.9], in this particular case the ASL analysis bases on mean-gray-matter-normalized values to control for the wake-sleep-influence. The resulting perfusion maps are shown in Figure [4.12]C. A hemispheric comparison between the ictal and the interictal scan reveals an unchanged perfusion (Δ0.5 %) in the non-lesional right hemisphere, whereas the lesional left hemisphere shows ictal hypoperfusion (Δ6.8 %) which is indicated by pink arrows in Figure [4.12]C. The within-scan comparison of both hemispheres suggests a higher gray matter asymmetry of perfusion in the ictal condition (+29 %, left < right).

For completeness, the FLAIR images and QSM results are provided below, however, an elaboration of the clinical context, MR physical details and the related methodology is beyond the scope of this work.

At the time of EPC onset, FLAIR images show a cortico-subcortical hyperintense lesion in the inferolateral postcentral gyrus lateral to the so-called hand-knob in the anatomical vicinity of somatotopic representation of the face as highlighted by green arrows in Figure [4.12]A. This lesion is no longer present in the scan six months later (Figure [4.12]B, green arrows).

QSM values were obtained by using the mean susceptibility of the whole brain as a reference. In relation to this reference, the ictal and the interictal scans show a consistently increased susceptibility (~0.08 ppm) in the inferolateral peri-central region close to the somatotopic representation of the face indicated by blue arrows in Figure [4.12]D. The mean increase within this region is equally high in both states ($< \Delta 3$ %). The contra-hemispheric region does not show remarkably increased susceptibilities.

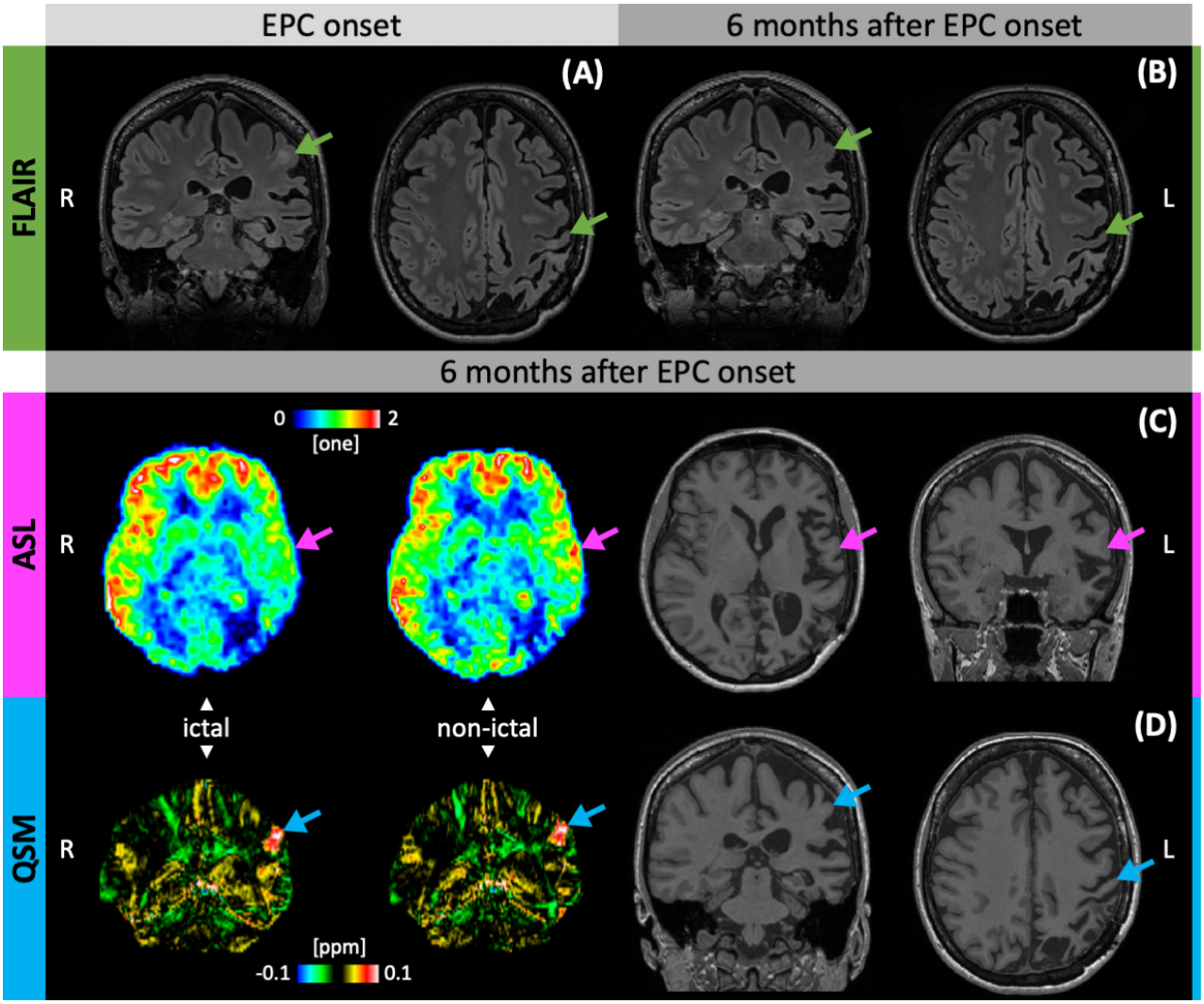

Figure 4.12: FLAIR images show (A) a hyperintense lesion in the inferolateral postcentral gyrus at the time of epilepsia partialis continua onset, which (B) is no longer visible six months later (green arrow). (C) Mean-gray-matter-normalized arterial spin labeling perfusion values show an ictal hypoperfusion of the lesional and a consistent perfusion of the non-lesional hemisphere between the ictal and non-ictal scan six months after EPC onset. An inferolateral pericentral ictal hypoperfusion is also notable (pink arrow). (D) Quantitative susceptibility mapping (QSM) shows an area of increased susceptibility in the same region in both the ictal and in the non-ictal condition six months after EPC onset (blue arrow).

4.4 Discussion

Chapter [4] presents an application-oriented perfusion imaging framework composed of a pCASL sequence for Siemens scanners, measurement protocols, and a postprocessing pipeline. It is inspired by the consensus proposal (Alsop et al. 2014) and the known Hadamard method (Günther 2007; van Osch et al. 2017) and designed for whole-brain measurements.

Two T_1 compensating Hadamard encoding schemes (3HAD and 7HAD) were optimized for 3 and 7 decoded

PLDs. In vivo results present the ASL signal dynamics in the course of the PLDs. From these it is clearly recognizable, that both schemes include a snapshot of the early perfusion up to a progressive label distribution throughout the brain tissue at different temporal resolutions (Figure [4.5]). The application of the 3HAD scheme may be motivated by a smaller labeling encoding matrix size and thus shorter feasible measurement times. Also, a shorter total LD may be chosen in the 3HAD scheme in order to reduce SAR, while preserving a sufficient sub-bolus length and signal strength.

Measurements with the T_1 compensating Hadamard encoding and a second, non-compensating uniform scheme demonstrate a different ASL signal evolution after the initial arrival of the label: in the compensating scheme, the ASL signal remains on a balanced high level throughout the brain across later PLDs (Figure [4.6]A). In contrast, the initial label inflow is resolved more coarsely in the uniform scheme and a pronounced signal drop occurs after reaching a whole-brain perfusion maximum providing a reduced late signal (Figure [4.6]B). Both, the finer temporal resolution of the label arrival and the stable signal level qualify the optimized scheme as a preferable modeling data basis.

A comparison of the CBF and ATT modeling with Hadamard-derived data (7HAD) and *TA*-matched multi-PLD data (3 PLDs), shows slightly higher Hadamard-based CBF values ($\Delta_{\text{relative}} = 10$ % in GM and in WM), but overall comparable CBF distributions (Figure [4.7]A). Especially at this low level of deviation and as physiology-related there is no homogeneous CBF to be expected, the distributions do not permit a conclusion on the CBF quality in favor of a particular labeling approach (Clement et al. 2017). In contrast, there is a more pronounced deviation of the mean ATTs ($\Delta_{\text{relative}} = 14$ % in GM and in WM), with Hadamard encoded data leading to longer modeled times (Figure [4.7]B). A considerably lower uncertainty of the ATT fit parameter estimates ($\Delta_{\text{relative}} = 148/135$ % in GM/WM) can be observed in the error maps (Figure [4.7]C) revealing a better ATT modelability for Hadamard data. It supports the superior quality of ATTs derived from a higher number of PLDs, as provided with the Hadamard encoding within an equal scan time.

The clinical applicability of the 8:42 min long protocol $\text{PROT}^{\text{Trio}}_{\text{perfusion}}$ was demonstrated in an epilepsy patient with epilepsia partialis continua. Perfusion changes were found in an anatomical location which functionally matched the patient's clinical seizure presentation. Interestingly, the validity of the ASL-based findings could be strengthened with structural FLAIR images and QSM results, which also revealed conspicuities in functionally associated brain regions.

The practical feasibility and suitability of the framework for longitudinal, multicenter studies was analyzed in a test-retest measurement series with healthy elderly on two different 3 T Siemens MRI systems (Skyra and mMR Biograph) using the 7:09 min long protocol $\text{PROT}_{\text{perfusion}}$. There resulted excellent intra-session reliabilities and good device independences. In these measurements, ATTs were found as the more reliable perfusion parameter compared to CBF and estimations of both parameters were even more reliable if acquired at the Skyra scanner. Longer mean ATTs were obtained from Skyra scans, whereas the CBF values showed only minor differences. A possible reason for the ATT differences may be a more inferior placement of the labeling plane in Skyra scans and the longer distance the tracer had to pass. The observation, that longer ATTs did not show strong effects on the CBF quantification is particularly important and enhancing the suitability for an application in multicenter studies involving different operators.

Beyond the impact on ATT estimates, the labeling plane placement also immediately affects the labeling efficiency and, in the case of an unsuitable positioning, (partial) signal dropouts may occur (Grade et al. 2015;

Sokolska et al. 2019). In this work, a manual placement adjusted to the subject-specific vascular anatomy was performed. However, in large cohort studies involving many different sequences and operators, such as the Rhineland study, an automated positioning may be required. This can be accomplished by the use of an anatomical localizer scout with a predefined gap between the image volume and the labeling plane. The applicability of this generic approach has to be tested within pilot measurements.

4.5 Conclusion

The presented chapter focuses on the practical application of pCASL for perfusion measurements. The advanced Hadamard encoding was implemented and related labeling schemes were optimized. Based on this, a pCASL protocol was implemented which facilitates whole-brain perfusion measurements within ~7 minutes. It is targeted to the needs of the Rhineland study and optimized for the application on modern Siemens scanners. A second protocol (~9 minutes) enables an executability on earlier scanner systems. A suitable processing pipeline has been implemented which generates quantitative perfusion data, in particular the CBF and the ATT.

This perfusion imaging framework was proven within a test-retest study, validating its suitability for the use in multicenter, long-term studies, also including different MRI scanner models. The clinical feasibility was exemplarily demonstrated in an epilepsy patient, further motivating a clinical applicaton for brain perfusion imaging.

5

T_2-weighted pCASL

This chapter is partly based on:

Schidlowski M, Boland M, Rüber T and Stöcker T (2020). Blood-brain barrier permeability measurement by biexponentially modeling whole-brain arterial spin labeling data with multiple T2-weightings. NMR Biomed 33:e4374, doi:10.1002/nbm.4374.

Schidlowski M, Stirnberg R, Stöcker T and Rüber T (2020). Reliability of quantitative transverse relaxation time mapping with T2-prepared whole brain pCASL. SciRep 10:18299, doi: 10.1038/s41598-020-74680-y.

5.1 Introduction

The previous Chapter [4] focused on perfusion imaging with pCASL. In particular, the measures CBF and ATT were considered. These quantities are frequently used in scientific and clinical practice. Those perfusion experiments base on the creation and subtraction of the ASL label, which is primarily determined by the longitudinal T_1 decay. However, the transverse relaxation time (T_2) of the ASL signal magnetization has yet received little attention.

The determination of blood-brain barrier permeability is the subject of current research and for instance examined using dynamic contrast enhanced (DCE) MRI. In this technique, an exogenous, often gadolinium-(Gd-)based, contrast agent is applied (Cuenod & Balvay 2013; Galbraith et al. 2002) and pathological passages of the injected molecules detected (Heye et al. 2014). Such a contrast agent-based approach not only tends to be invasive, but also methodological disadvantages can result from the properties of the injected molecules, including size, charge and hydrophilicity, which may influence and hinder a BBB passage (Veiseh et al. 2009). Contrarily, ASL is a contrast agent-free perfusion technique suitable for the daily scanning routine due to its non-invasiveness and a fairly simple processing for quantification (Borogovac & Asllani 2012; Grade et al. 2015).

Previous studies have shown that labeled arterial protons flow into cerebral structures, where an exchange of water molecules takes place between intravascular (IV) and extravascular (EV) space. When the labeled protons cross the semipermeable blood-brain barrier, the observed T_2 values change (Gregori et al. 2012; Liu et al. 2010; Schmid et al. 2015). Water molecules freely diffuse across this membrane and are also transported through aquaporin channels, with latter being the faster mechanism. The water transport rate, which also is referred to as permeability, represents an approach to infer the functionality of the BBB (Dickie et al. 2020; Ohene et al. 2019).

Those earlier studies have tried to exploit this benefit of ASL. Some approaches estimated the extravascular signal fraction or the water exchange rate based on the suppression of intravascular signal and a following comparison with unsuppressed reference measurements (Lawrence et al. 2011; Wells et al. 2009). The suppression of intravascular signal was in this case achieved via diffusion-weighting or vascular crushing gradients. Another method modeled global tissue extraction rate and BBB transitions by quantifying the venous ASL signal in the sagittal sinus, i.e. outflowing arterially labeled spins (Lin et al. 2018). Further studies have investigated a signal allocation by applying T_2-weighted ASL data to a two-compartment model with numerous input and fit parameters (Gregori et al. 2012; Liu et al. 2010). However, those approaches have predominantly been able to make global statements within a region of interest (ROI) or lead to a poorly conditioned complex model inversion resulting in large error bounds.

Therefore, T_2 of the ASL signal might be a parameter of interest, but the potential and suitability is little known. In the following Chapter [5], the reliability and precision of current state-of-the-art ASL-T_2 measurements are investigated within test-restest experiments. Then, a simplified T_2-based permeability modeling approach is derived from previous attempts (Ohene et al. 2019; Wells et al. 2012) to overcome the abovementioned limitations (Dickie et al. 2020; Lin et al. 2018).

5.2 Material and methods

5.2.1 T_2 mapping using T_2 preparation

The most basic approach of determining the transverse relaxation time T_2 is to perform multiple-echo time experiments, which is to conduct repeated measurements with a variation of TE. The resulting TE-dependent and T_2-weighted signal magnitudes can be voxel-wise fitted to the monoexponential T_2 decay function (Bernstein et al. 2004; Milford et al. 2015)

$$M_{\mathrm{xy}}(TE) = M_0 \cdot \mathrm{e}^{-TE/T_2}, \tag{5.1}$$

determining a T_2 value per voxel and therefore termed T_2 mapping.

An alternative method is the multi-echo experiment. It utilizes a repeated refocusing of the transverse magnetization after initial excitation, featuring the advantage of measuring multiple TEs within a single experiment. At the same, a disadvantage arises in the case of an imperfect refocusing: it induces additional longitudinal components and causes an incomplete rephasing of the transverse magnetization, leading to a degraded signal. Such additional longitudinal magnetization components may affect the signal in the subsequent refocusings by providing extra transverse contributions. (Bernstein et al. 2004; Majumdar et al. 1986)

Another, different concept does not introduce a T_2 weighting by varying the echo time of the readout, but uses a so-called T_2 preparation (T2Prep) instead (Figure [5.1], yellow shaded). In the preparation, the magnetization is transferred to the transverse plane and kept in this plane by repeated refocusings for a specified time, in which the magnetization is subjected to transverse relaxation processes. Accordingly, this duration is denoted as the effective echo time TE_{eff} or the T_2 preparation length TE_{T2Prep} (Figure [5.1]A). At the end of the preparation and prior to the signal readout, the magnetization is re-aligned longitudinally. Due to T_2 relaxation, the resulting magnetization is reduced as compared to the initial magnetization. For T_2 mapping, repeated experiments are performed with a varying TE_{T2Prep} and a constant TE of the readout module. The data is then fitted again as an exponential decay (Equation [5.1] with $TE = TE_{\mathrm{T2Prep}}$). (Bernstein et al. 2004)

In all reported T_2 weighting approaches, B_0 and B_1 inhomogeneities may affect the magnetization excitation and thus the signal weighting used to quantify T_2 relaxation times. This effect increases with the precession time respectively with TE and, where applicable, with the number of refocusings. In in vivo measurements, it may also be amplified by physiological effects. (Bernstein et al. 2004; Majumdar et al. 1986)

One compensating approach to this is the use of composite pulses for a T_2 preparation. A prominent pulse pattern is the so-called Malcom Levitt (MLEV) phase cycling scheme, which is specified in Figures [5.1]B-C. Here, after an initial 90° excitation, a series of composite 180° refocusing pulses are executed and, after a time TE_{T2Prep} during which transverse relaxation occurs, a final -90° composite pulse is executed to re-align the magnetization longitudinally. Thereby, a refocusing pulse is composed of three closely succeeding pulses (90°-180°-90°). The -90°-tip-up pulse is composed of a pair of pulses (270°-360°). According to Figures [5.1]B-C,

the phase of the individual pulse elements is chosen and changed in the course of the module, such that after a complete iteration of the T_2 preparation, B_0 and B_1 imperfection effects are compensated. (Nezafat et al. 2006)

5.2.2 Sequence implementation

The T_2 preparation approach with composite pulses arranged in MLEV schemes (Section [5.2.1]) is chosen for the generation of a T_2-weighted ASL signal. In the realized implementation, non-selective 90°/180°/270°/360° RECT pulses with lengths of 0.8/1.6/2.4/3.2 ms are used. The time gap t_{gap} between the composite pulse elements is 0.15 ms. Depending on the desired T_2 preparation duration, there are 4, 8 or 16 refocusings evenly distributed between the 90° and the -90° excitation. The echo spacing results from this positioning. A final spoiler gradient destroys any residual transverse magnetization. The implemented parameters are summarized in Table [5.1].

Table 5.1: Specification of the T_2 preparation module implementation.

TE_{T2Prep} [ms]	refocusing pulse number	echo spacing [ms]
30	4	7.5
40	4	10
60	8	7.5
80	8	10
120	16	7.5
160	16	10

The T_2 preparation module was implemented after the ASL module and prior to the GRASE readout module in the pCASL sequence (Figure [3.5], (Boland et al. 2018)) as shown in Figure [5.1]A. It enables the acquisition of various T_2 weightings, respecively TE_{T2Prep} with variable lengths, and the acquisition of multiple PLDs. The background suppression pulse timing was optimized for the T_2-weighted pCASL sequence under the constraint to have finished before the start of the T_2 preparation module.

A comprehensive diagram with a detailed presentation of all sequence elements is provided in the supplementing Figure [5.14].

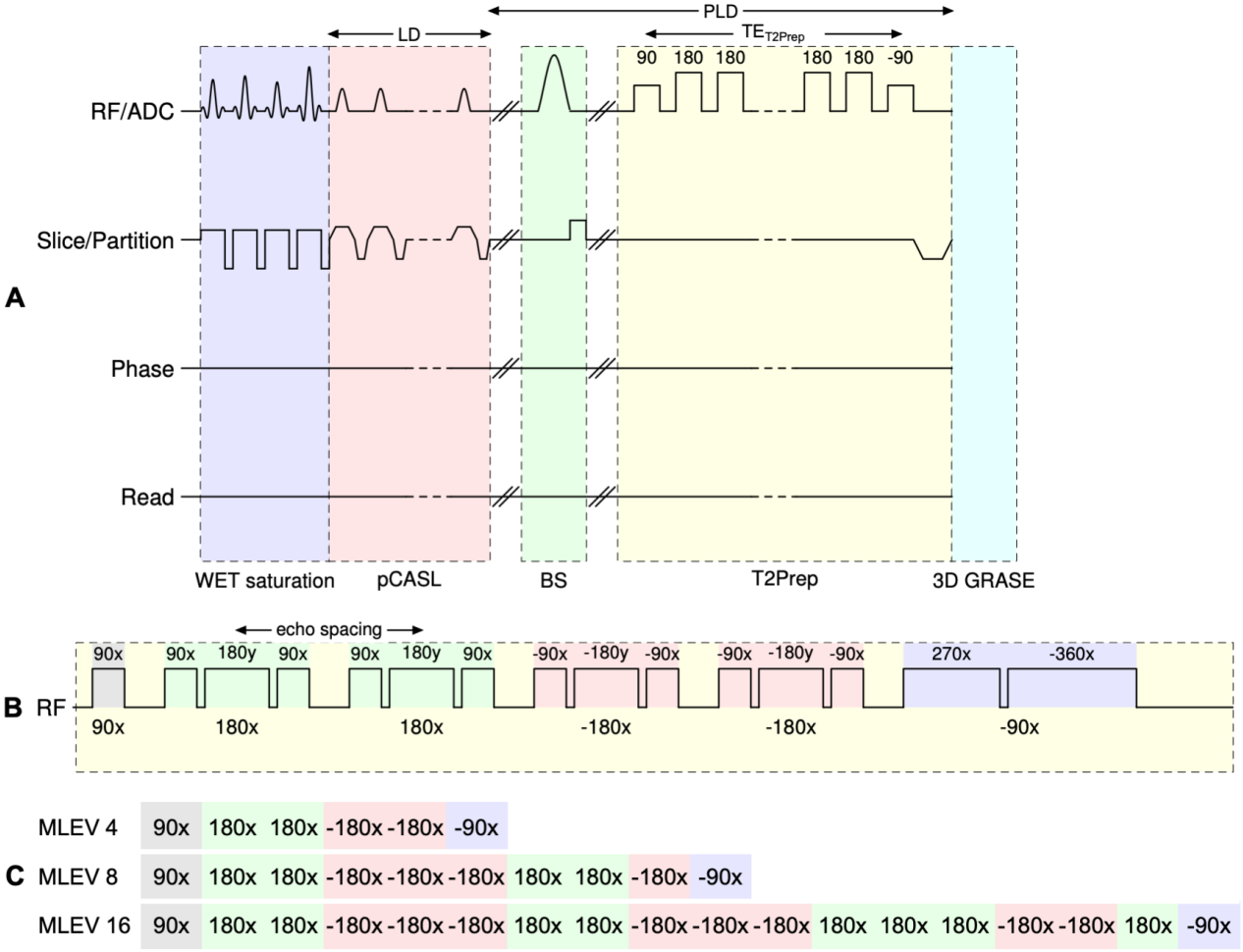

Figure 5.1: (A) Diagram of the T_2-prepared pCASL sequence. A WET presaturation (purple) of the imaging region is performed before pCASL labeling (red). Two or three background suppression pulses (green) are timed to suppress static tissue signal. Only a single BS pulse is shown for clarity. The pulses may interrupt the labeling but not the T_2 preparation (yellow) which is played out immediately before the 3D GRASE readout (blue). In the case of an interruption, the following tag and control conditions are switched. M_0 reference images are obtained by a pure image readout without the ASL and the T_2 preparation modules. For a simpler representation, only the shortest T_2 preparation is shown and dashed lines indicate further repetitions. (B) Exemplary (MLEV 4) composite pulse illustration of the T_2 preparation with 4 (180°) refocusing pulses. Flip angles and rotation axes are specified above each single pulse element and the effective composite pulse values are provided below. Single pulses and grouped composite pulse elements are differentiated by colors. (C) MLEV phase cycling schemes for all used T_2 preparations with 4, 8 and 16 refocusing pulses. Each color-encoded (composite) pulse matches the full representation in (B).

5.2.3 Compartment model simplification

The biexponential compartment modeling of ASL data is based on studies, showing that intra- and extravascular T_2 differ and T_2-weighted ASL signal proportions of both spaces can be separated (Gregori et al. 2012; Liu et al. 2010). Previously presented approaches were adopted, modified and extended (Ohene et al. 2019; Wells et al. 2012) and processing steps and model assumptions newly introduced.

The effective transverse relaxation time T_2 depends on numerous factors. Particularly for blood water protons it depends on the properties of the surrounding tissue including the blood oxygenation level and hematocrit. Accordingly, the T_2 of water protons located in the arteries, veins, gray and white matter is different. An even more detailed segmentation into further compartments with characteristic T_2 times can be made (Chen & Pike 2009; Li & Zijl 2020). The two-compartment model simplifies the complex structure (Figure [3.4]B). It builds on the assumption that the labeled water protons are located in the arterial compartment initially and directly pass into the cerebral tissue compartment. Consequently, only the transverse relaxation times of arterial blood and tissue water protons are considered (Hales & Clark 2012; Liu et al. 2010).

Furthermore, in the modeling equal water densities within both compartments were assumed and partial volume effects with white matter and CSF to be negligible. Additional model simplifications are the disregard of the blood oxygenation level, the hematocrit and a possible signal contribution of venous blood flow. These possibly affect the T_2 determination and biexponential compartmentalization. (Dickie et al. 2020; Krishnamurthy et al. 2013; J. M. Zhao et al. 2007)

These assumptions were integrated into a strongly simplified model for the localization of arterially labeled water protons, considering two compartments with two distinct transverse relaxation times, referred to as $T_{2,\mathrm{IV}}$ for arterial water protons located inside the first, intravascular compartment, and $T_{2,\mathrm{EV}}$ for those inside the second, extravascular cerebral gray matter tissue compartment.

The simplifications allowed to design two dedicated measurements for a ROI-based monoexponential modeling of $T_{2,\mathrm{IV}}$ and $T_{2,\mathrm{EV}}$. The resulting model times were then taken as input parameters for the biexponential compartmentalization of the SNR-limited T_2-weighted ASL data from a third, extensive measurement protocol and stabilized the fit. An overview of the measurements is given in Figure [5.2] and the processing is illustrated in Figure [5.4].

5.2.4 In vivo experiments

5.2.4.1 pCASL protocol overview

The in vivo experiments consisted of three separate scanning protocols:

1. For compartmentalization
   (a) the *monoexponential T_2 estimation protocols* $\mathrm{PROT_{IV}}$ and $\mathrm{PROT_{EV}}$ were used to analyze the intravascular ($\mathrm{PROT_{IV}}$) and the extravascular ($\mathrm{PROT_{EV}}$) water proton T_2 values, and
   (b) the *biexponential compartmentalization protocol* $\mathrm{PROT_{IV+EV}}$ provided the input data for the modeling of the ASL signal compartment fractions.
2. For T_2 reliability analysis of the ASL signal, test-retest measurements were performed using the same protocol $\mathrm{PROT_{IV+EV}}$. In this context it is referred to as *T_2 reliability analysis protocol*.

Figure [5.2] provides an overview of the application and the purpose of each protocol.

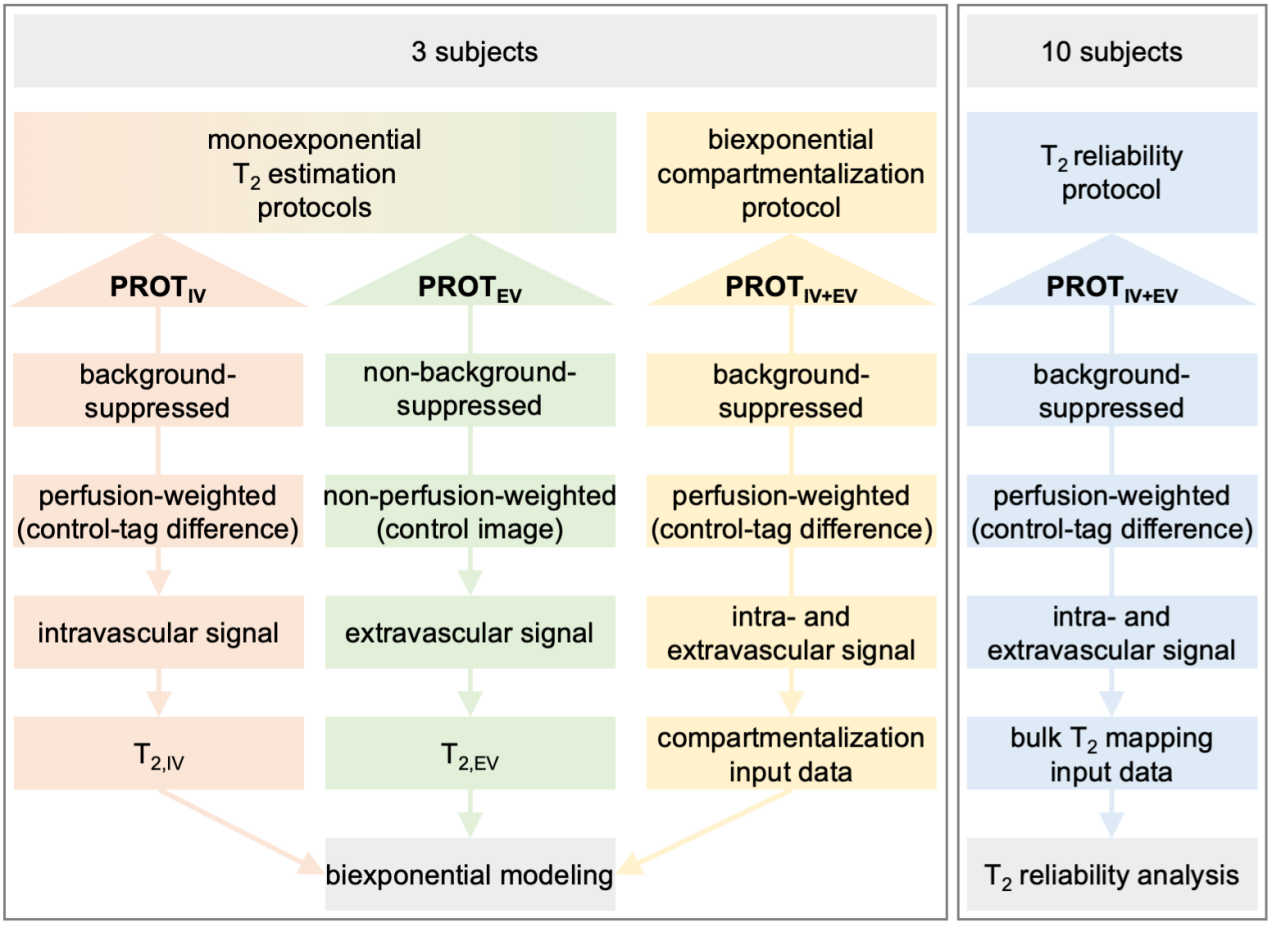

Figure 5.2: Overview of ASL data and in vivo experiments. The T_2 estimation protocols comprise two series: background-suppressed and perfusion-weighted images (red) from series PROT_{IV} were used for an analysis of intravascular $T_{2,\text{IV}}$ and non-background-suppressed control images (green) from series PROT_{EV} provided an approximation basis for extravascular $T_{2,\text{EV}}$. The compartmentalization protocol $\text{PROT}_{\text{IV+EV}}$ (yellow) provided the data for compartmentalization, which together with both T_2 estimates, were input for the biexponential modeling. Test-retest investigations for T_2 reliability analysis also based on protocol $\text{PROT}_{\text{IV+EV}}$, but here data of ten subjects was included instead of three. The protocols are specified in Table [5.2].

The protocols and ASL parameters are summarized in Table [5.2] and base on the results of Chapter [4], including recommendations of the ISMRM consensus paper on ASL imaging (Alsop et al. 2014) and a previous study (Boland et al. 2018). In brief, the voxel size of the twofold segmented 3D GRASE readout (Boland et al. 2018) was $3 \times 3 \times 4$ mm^3 and an unbalanced pCASL labeling with a labeling duration of 1.8 s (as a compromise between signal strength for T_2-weighting, acquisition time and SAR) and seven T_2 preparation lengths TE_{T2Prep}=0/30/40/60/80/120/160 ms was applied.

Table 5.2: Acquisition protocol $\text{PROT}_{\text{IV+EV}}$ for the T_2 reliability analysis and the biexponential compartmentalization and protocols PROT_{IV}/PROT_{EV} for the monoexponential T_2 estimation.

	protocols	
	monoexponential T_2 estimation	biexponential compartmentalization & T_2 reliability analysis
3D GRASE	PROT_{IV}/PROT_{EV}	$\text{PROT}_{\text{IV+EV}}$
FOV	$210 \times 210 \times 120$ mm^3	$210 \times 210 \times 120$ mm^3
acquisition matrix	$42 \times 42 \times 24$	$70 \times 70 \times 30$
resolution	$5 \times 5 \times 5$ mm^3	$3 \times 3 \times 4$ mm^3
TE_{GRASE}	16 ms	22.9 ms
PE	GRAPPA 2×	GRAPPA 2×
3D	1× SEG	2× SEG
BW	2588 Hz/Px	2551 Hz/Px
ETL	392 ms	355 ms
ASL		
LD	1.8 s	1.8 s
PLD	0.25 s	0.9/1.2/1.5/1.8 s
$\text{TE}_{\text{T2Prep}}$	0/30/40/60/80/120/160 ms	0/30/40/60/80/120/160 ms
TR	4.02 s	4.02 s
BS	on (PROT_{IV}) / off (PROT_{EV})	on
ASL labeling		
control method		unbalanced
G_{mean}		0.5 mT/m
G_{max}		3.5 mT/m
pulse type		Hann
FA		34°
RF duration		500 µs
RF gap		660 µs
M_0 calibration		
TR		6 s

Test-retest and compartmentalization experiments ($\text{PROT}_{\text{IV+EV}}$) were performed with four post labeling delays PLD=0.9/1.2/1.5/1.8 s to ensure sufficient time for compartment transitions of labeled spins. Each control-tag (CT) pair and segment (SEG) was measured six times for each PLD and each TE_{T2Prep}, resulting in a scan time of 45:20 min. For quantification, proton density-weighted M_0 reference scans were acquired without background suppression and a longer TR of 6 s. The otherwise same readout, differed in an alternating orientation of the phase encoding (PE) polarity between each of four measurements (1:15 min in total). This allowed for geometric distortion estimation and correction in the post processing. In order to achieve a steady state, two preparation scans were acquired and removed before data analysis.

For the analysis of intravascular and extravascular T_2 under simplified model assumptions, two separate measurement series were included with background suppression enabled (PROT_{IV}) and disabled (PROT_{EV}). These T_2 estimation scans were acquired with a larger voxel size of (5 mm)^3 as a tradeoff between acquisition

time (1× SEG) and signal-to-noise ratio. A reduced PLD of 0.25 s in these scans lead to a measurement of the label shortly after arrival in cerebral structures. Each perfusion-weighted volume (CT pair) acquisition was measured six times for each TE_{T2Prep}. The corresponding M_0 reference images were measured twice per PE polarity resulting in a total scan time of 6:04 min for the T_2 estimation protocols.

5.2.4.2 In vivo measurements

Experiments were performed on a Magnetom Trio 3 T scanner (Siemens Healthineers, Erlangen, Germany) using a 32-channel head coil. All protocols and measurements were approved in accordance with the institutional review board of the medical faculty of the University of Bonn. Written informed consent was obtained from all subjects.

Test-retest measurements included ten young healthy volunteers of a balanced gender distribution with an average age of 28±3 years. All three compartmentalization modeling protocols were measured in three healthy volunteers for proof-of-concept (2 female, 1 male, 25±2 years).

For registration purposes, an additional structural T_1-weighted image with an isotropic resolution of 0.8 mm was acquired (6:32 min) once per subject.

The total acquisition time, including the calibration images and the structural scan, was 53:07 min for a single test-retest measurement and 59:11 min for compartmentalization measurements, respectively.

In order not to affect the CBF, the participants were asked to abstain from nicotine one hour before measurements and caffeine three hours before measurements (Dager & Friedman 2000; Laurienti et al. 2003). Following the auto-align anatomical localizer scout, a time of flight vascular scout was acquired. The latter was used to position the ASL labeling plane slightly inferior to the lower end of the cerebellum by adjusting the gap between the lower edge of the ASL imaging volume and the parallel labeling plane. This ensured an inversion of blood water magnetization in the basilar and the right and left internal carotid arteries (Zhao et al. 2016).

Test-retest scans were conducted at about the same time of day to reduce the impact of circadian rhythms. The interscan latency between test and retest measurements was 24±15 days. A screenshot of the ASL planning has been taken during the first scan. The labeling slab was positioned individually and adjusted via the distance to the lower edge of the imaging volume with an average of 31±8 mm. The same gap has been applied in the second scan as to minimize label placement influences and to correct for changes in head position between both sessions (Figure [5.3]). Adjustments of the automatic MRI planning, and in particular the alignment of the ASL plane, was carried out by a single operator in all measurements to minimize variance of the operator bias. Subject specific scanner SAR rates for the pCASL sequence were 72±17 %.

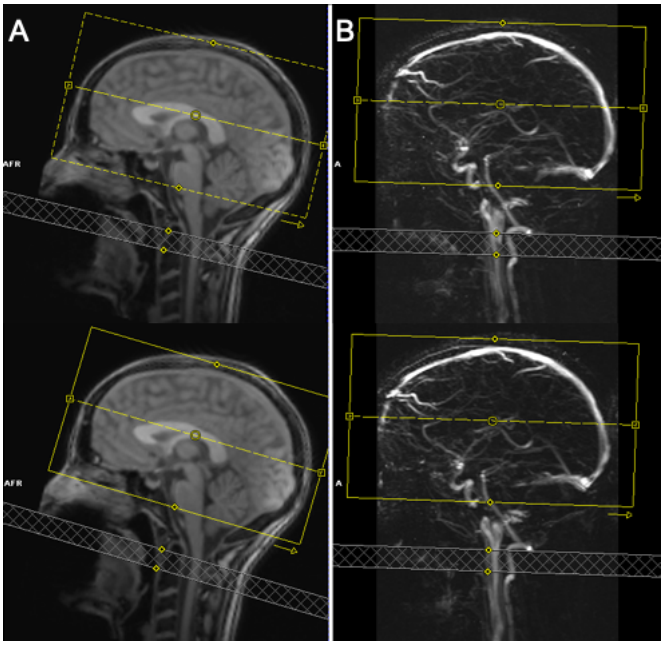

Figure 5.3: (A) Structural localizer and (B) time of flight (TOF) vascular scout for the placement and alignment of the labeling volume (gray hatched) in the test (top) and the retest (bottom) scan to invert blood in basilar, right and left internal carotid arteries. The same gap to the imaging volume (yellow) was used in both measurements performed by the same operator.

5.2.5 Signal modeling overview

Figure [5.4] provides an overview of the data processing for the T_2 reliability analysis and the biexponential modeling.

In a first step, the data of all protocols was preprocessed as described in the subsequent Section [5.2.6]. Next, bulk ASL signal T_2 values were obtained from a monoexponential fit of the test-retest series data ($\text{PROT}_{\text{IV+EV}}$). A monoexponential fit of the T_2 estimation protocols data was conducted to determine the T_2 for intravascular (PROT_{IV}) and extravascular (PROT_{EV}) water protons within gray matter. The latter results were then used as subject-specific input parameters for a biexponential fit of the more comprehensive biexponential compartmentalization protocol data ($\text{PROT}_{\text{IV+EV}}$) to localize labeled spins.

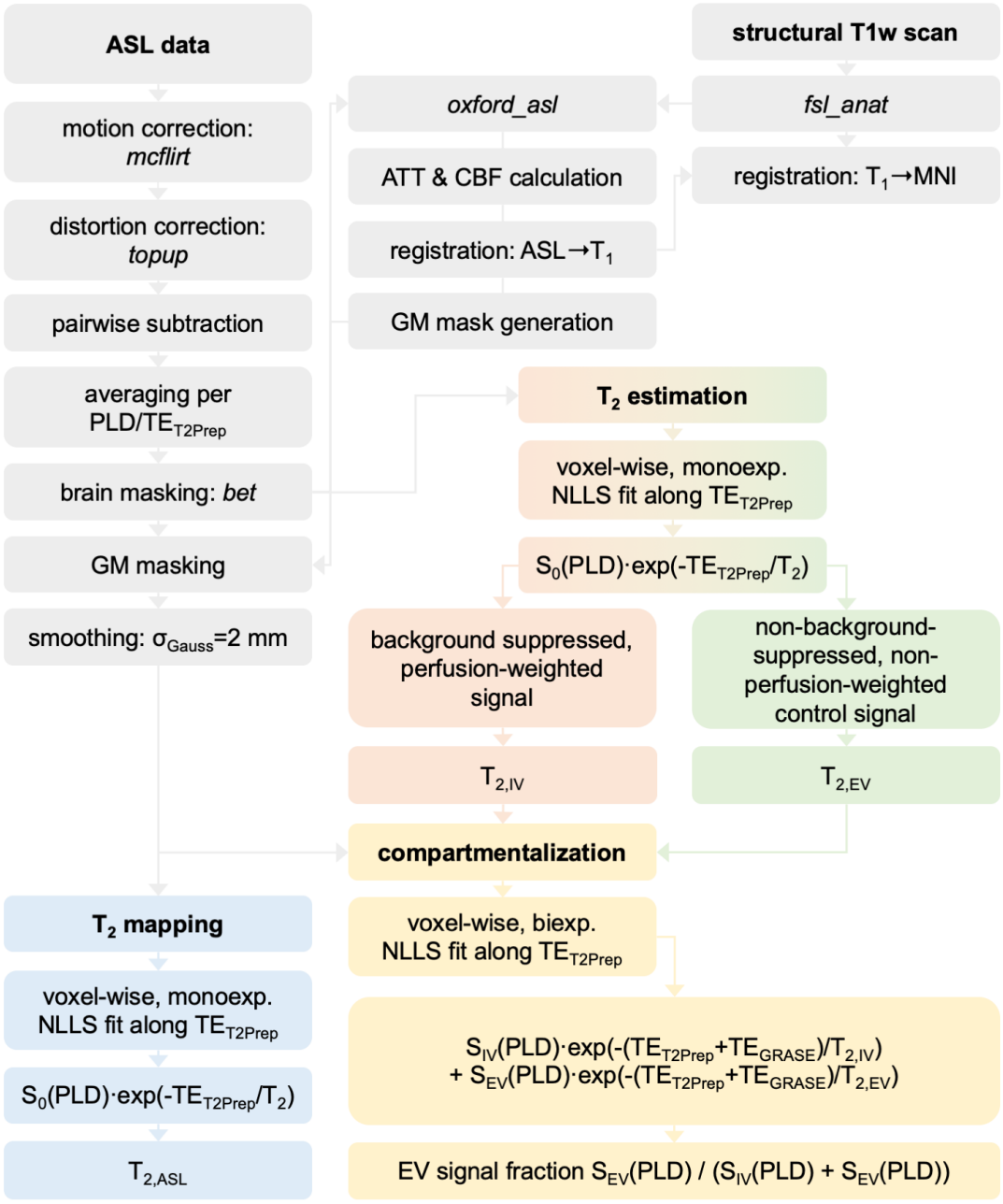

Figure 5.4: Schematic illustration of the T_2-weighted ASL data processing. The data preprocessing is shown in gray. Test-retest measurement processing for T_2 reliability analysis is colored in blue. Biexponential modeling processing is composed of T_2 estimations (red and green) and the biexponential compartmentalization (yellow). The input data and protocols are color-matched shown in Figure [5.2].

5.2.6 Data preprocessing

Preprocessing of online reconstructed data included the application of toolboxes from FMRIB's software library (FSL, v6.0.3) (Smith et al. 2004). The ASL data was first corrected for motion using mcflirt (Jenkinson et al. 2002) followed by distortion correction utilizing topup (Andersson et al. 2003) on the basis of the calibration

scans with alternating PE polarity. Then, mean perfusion images were computed for every PLD and TE_{T2Prep} by a pairwise subtraction of CT pairs:

$$S_{\mathrm{ASL}}(PLD, TE_{\mathrm{T2Prep}}) = \frac{M_{\mathrm{control}}(PLD, TE_{\mathrm{T2Prep}}) - M_{\mathrm{tag}}(PLD, TE_{\mathrm{T2Prep}})}{M_0}. \tag{5.2}$$

A brain mask was generated based on the corrected calibration scans using FSL's brain extraction tool bet (Smith 2002). In order to obtain the normalization warp field from structural to MNI space, the T_1-weighted structural scan was processed with fsl_anat (Smith et al. 2004).

The preprocessed ASL data and fsl_anat results were taken as input for oxford_asl (Chappell et al. 2009) to calculate arterial transit times, cerebral blood flow, transformations from native to structural space and a GM mask. The latter was then applied to the preprocessed ASL data. Finally, the $\mathrm{PROT}_{\mathrm{IV+EV}}$ data was smoothed with a three-dimensional 4.7 mm full width at half maximum isotropic Gaussian kernel to reduce the random noise and increase the SNR for the subsequent modeling (Tabelow et al. 2009; Triantafyllou et al. 2006).

5.2.7 Bulk ASL signal T_2 mapping

For reliability analysis, T_2 mapping was performed with the preprocessed, i.e. GM-masked and smoothed, perfusion-weighted mean difference images from the test-retest measurements. T_2 values and the extrapolated baseline signal at $TE = 0$ ms ($S_0(PLD)$) were calculated for each post labeling delay and for each voxel by applying a monoexponential non-linear least squares (NLLS) fit along TE_{T2Prep} using the python function curve_fit from the Scipy.Optimize library (v1.4.1):

$$S_{\mathrm{ASL}}(PLD, TE_{\mathrm{T2Prep}}) = S_0(PLD) \cdot \mathrm{e}^{-TE_{\mathrm{T2Prep}}/T_2}. \tag{5.3}$$

The derived T_2 values correspond to the bulk T_2 of the ASL signal magnetization within a voxel at a particular post labeling delay. Finally, the T_2 maps were spatially normalized using the previously calculated transformations.

The monoexponential model was also applied to the preprocessed perfusion-weighted $\mathrm{PROT}_{\mathrm{IV+EV}}$ data from the biexponential modeling measurements to allow for a comparison of bulk T_2 times and compartmentalization results.

5.2.8 IV and EV monoexponential T_2 estimation

For the approximation of intravascular arterial water proton $T_{2,\mathrm{IV}}$ and extravascular tissue water proton $T_{2,\mathrm{EV}}$, data obtained from both T_2 estimation protocols $\mathrm{PROT}_{\mathrm{IV}}$ and $\mathrm{PROT}_{\mathrm{EV}}$ were analyzed separately for each subject as illustrated in Figure [5.2]. Since it is challenging to quantify T_2 values on low SNR perfusion-weighted images (Istratov & Vyvenko 1999), the following assumptions were made:

1. Perfusion-weighted images were created from the background-suppressed series $\mathrm{PROT_{IV}}$. Subsequently, a GM masking was performed and T_2 maps were generated. Due to background suppression and subtraction, the signal was largely free of static tissue, so that blood was dominant. Because of the short PLD, it was furthermore reasonable to assume that the spins were still predominantly located in the IV compartment. Therefore, the median T_2 of the obtained maps in this series approximately represented the intravascular $T_{2,\mathrm{IV}}$.

2. In contrast to this, a GM masking was also performed in the unsuppressed series $\mathrm{PROT_{EV}}$, but T_2 maps were fitted from control images, which means that no differences were formed. The signal was almost PLD independent and predominantly corresponded to the static GM, since neither background suppression nor difference formation were present. So, from the series $\mathrm{PROT_{EV}}$ resulting median T_2 could be assigned to the extravascular GM compartment and might be referred to as extravascular $T_{2,\mathrm{EV}}$.

In both approximations, T_2 maps were generated by applying the monoexponential Equation [5.3] along TE_{T2Prep}.

5.2.9 Biexponential compartmentalization

The biexponential two-parameter model requires knowledge of T_2 of intravascular and extravascular GM compartment. Both values were obtained for each subject within the previously described monoexponential T_2 estimations (Section [5.2.8]) and taken as input parameters.

In order to separate the signal source into IV and EV compartments, and given the aforementioned assumptions, a simplified biexponential model

$$\begin{aligned} S_{\mathrm{ASL}}(PLD, TE_{\mathrm{T2Prep}}, TE_{\mathrm{GRASE}}) &= S_{\mathrm{IV}}(PLD) \cdot \mathrm{e}^{-(TE_{\mathrm{T2Prep}}+TE_{\mathrm{GRASE}})/T_{2,\mathrm{IV}}} \\ &+ S_{\mathrm{EV}}(PLD) \cdot \mathrm{e}^{-(TE_{\mathrm{T2Prep}}+TE_{\mathrm{GRASE}})/T_{2,\mathrm{EV}}} \end{aligned} \tag{5.4}$$

along $TE_{\mathrm{T2Prep}} + TE_{\mathrm{GRASE}}$ was applied to the preprocessed perfusion-weighted data of the compartmentalization protocol ($\mathrm{PROT_{IV+EV}}$) scans. S_{IV} and S_{EV} represent the signal magnitudes from IV and EV compartment, respectively. The fit was performed in a voxel-wise manner, using a NLLS approach (curve_fit) for optimization. No additional bounds or constraints for S_{IV} and S_{EV} were used. Accordingly, the extravascular PLD-dependent S_{ASL} fraction f_{EV} is given by

$$f_{\mathrm{EV}}(PLD) = \frac{S_{\mathrm{EV}}(PLD)}{S_{\mathrm{IV}}(PLD) + S_{\mathrm{EV}}(PLD)}. \tag{5.5}$$

5.2.10 Compartment transition rate modeling

Water proton quantities separated into IV and EV compartments at different post labeling delays were used to model transition rates between both compartments. First, frequency histograms of the extravascular PLD-dependent S_{ASL} fraction f_{EV} were smoothed by applying a five bin wide moving average filter for each PLD

and subject. Subsequently, peak fractions $f_{\mathrm{EV,peak}}$ were detected. Along with the corresponding post labeling delays, these were applied to a linear model

$$f_{\mathrm{EV}}(PLD) = k_{\mathrm{lin}} \cdot PLD + b \tag{5.6}$$

and an exponential model

$$f_{\mathrm{EV}}(PLD) = a \cdot (1 - \mathrm{e}^{-k_{\mathrm{exp}} \cdot PLD}) + b. \tag{5.7}$$

The slope parameter k_{lin} in the linear model and the parameter k_{exp} in the exponential model were considered as measures reflecting water proton transition rates between both compartments.

5.2.11 Statistical analysis

For test-retest measurements, the determined T_2 values were statistically analyzed by performing computations with the package agRee (v0.5-2 (Feng 2018)) from the R project (v3.6.2 (R Core Team 2017)).

For this, the intraclass correlation coefficient was determined according to Equation [4.11] and the within-subject coefficient of variation according to Equation [4.12]. A detailed description of these statistical quantities is given in Section [4.2.8]. Furthermore, a Bland-Altman plot was created, which can be taken for visual review of the reliabilities (Sabour et al. 2017).

A third parameter utilized for statistical evaluation of the experiments is the smallest detectable difference (SDD). Here, it is defined as the minimum critical value of change which is above the statistical uncertainty or measurement error at 95 % confidence level ($\alpha = 0.05$, $z_{0.975} = 1.96$):

$$SDD = \sqrt{2} \cdot z_{1-\alpha/2} \cdot \sigma_{\mathrm{ws}}. \tag{5.8}$$

The SDDs are shown as limits of agreement in the Bland-Altman plots. Small SDDs are preferable.

For a ROI-based statistical analysis of test-retest T_2 quantifications, previously normalized T_2 maps in the MNI space were taken and evaluated in four GM ROIs obtained from the MNI structural atlas (2 mm, zero thresholded) (Lancaster et al. 2000; Mazziotta et al. 2001) provided with FSL, namely frontal, occipital, parietal and temporal ROI (Figure [5.5]A). For this purpose, the median T_2 values within the individual ROIs were determined and assigned to test and retest groups for ten subjects with each of four PLDs. Based on these median scan and rescan T_2 values, statistical parameters were calculated in two different ways: (a) across subjects at every PLD and (b) across PLDs for every single subject. According to method (a) parameters ICC_{PLD}, $WSCV_{\mathrm{PLD}}$ and SDD_{PLD} were derived and according to method (b) the parameters ICC_{subj}, $WSCV_{\mathrm{subj}}$ and SDD_{subj} were obtained analogously.

5.3 Results

5.3.1 Bulk ASL signal T_2 reliability

For the T_2 reliability measurements based on protocol $\text{PROT}_{\text{IV+EV}}$ (Figure [5.2], blue), mean perfusion-weighted, non-smoothed, brain-extracted images are shown in Figure [5.5]D for one subject comprising all post labeling delays and T_2 weightings. For the same subject, representative T_2 maps, which have been obtained with Equation [5.3], are presented in Figure [5.5]B for test measurements, and in Figure [5.5]C for retest measurements. Median T_2 values in four GM regions of interest, according to Figure [5.5]A, are shown in Figure [5.6]A for all ten participants and all PLDs of both measurements separately. Figure [5.6]B provides the corresponding Bland-Altman plots. Additionally, averaged median T_2 values for perfusion-weighted ASL signal and ASL control signal are shown in supplementing Figure [5.15].

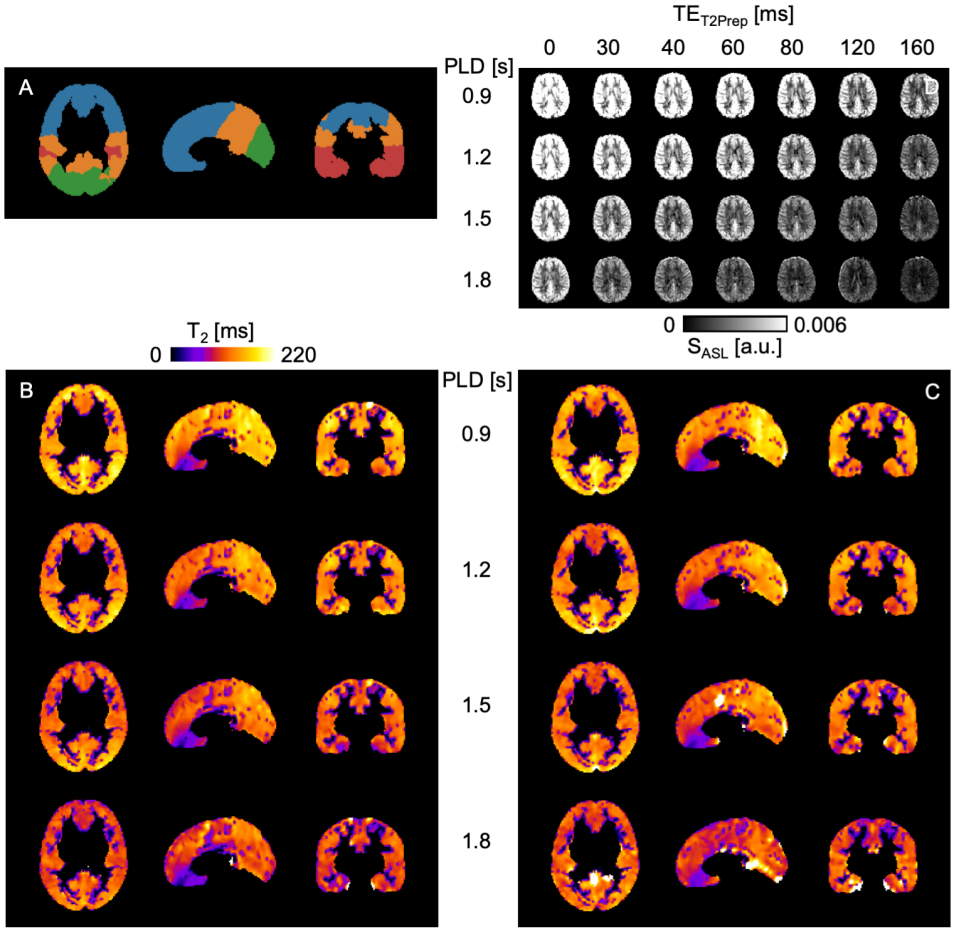

Figure 5.5: (A) Regions of interest of the MNI reference map: frontal (blue), occipital (green), parietal (orange), temporal (red) and corresponding masked gray matter T_2 maps in MNI space for all post labeling delays PLD=0.9/1.2/1.5/1.8 s for (B) test and (C) retest scans of one subject. (D) Mean perfusion-weighted, non-smoothed whole-brain ASL signal maps in native space for all PLDs and T_2 preparation times TE_{T2Prep}=0/30/40/60/80/120/160 ms.

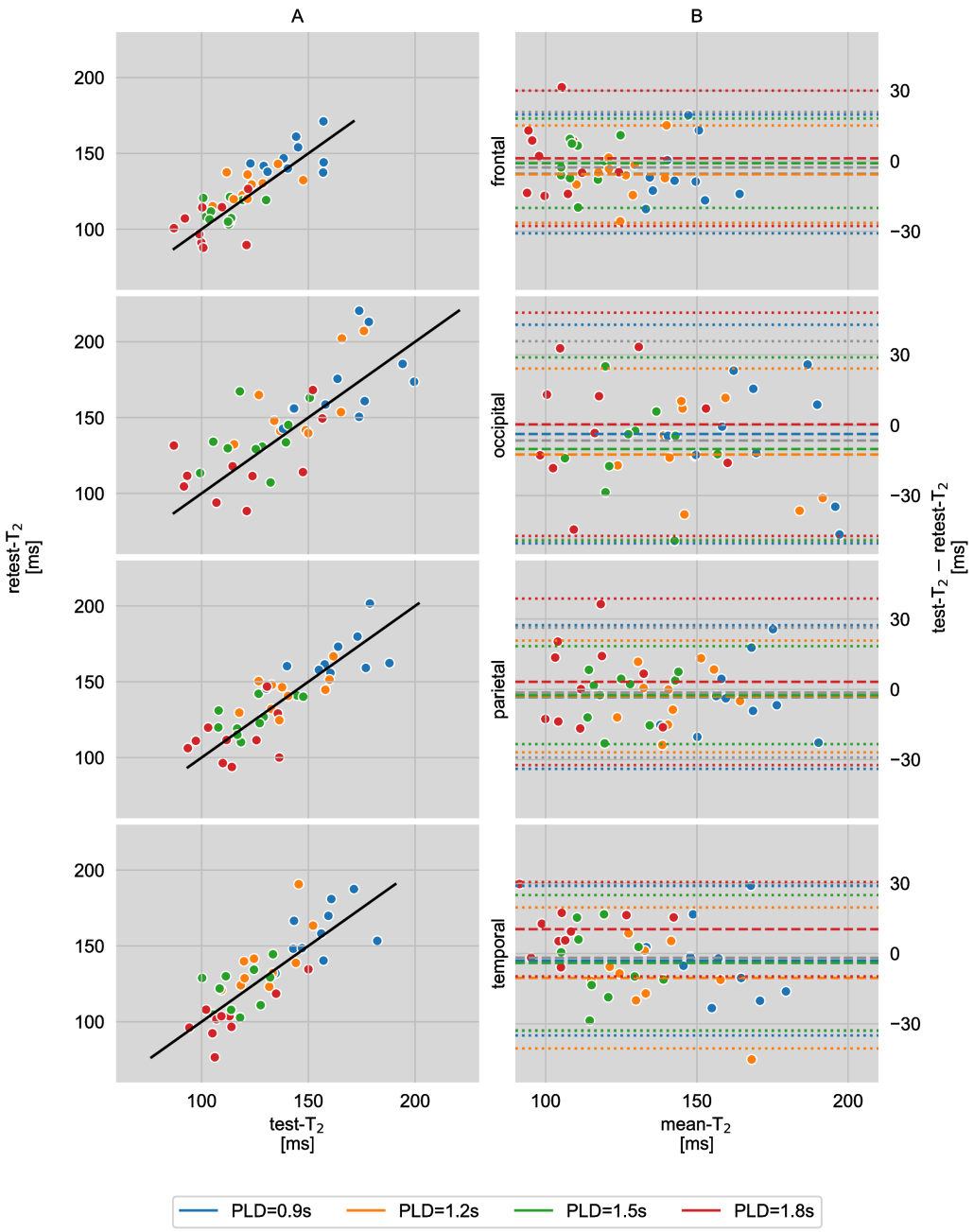

Figure 5.6: (A) Correlation of median T_2 values from repeated measurements of ten subjects in four gray matter regions of interest at four post labeling delays PLD=0.9/1.2/1.5/1.8 s. The solid line is the identity function and represents optimal correlation. (B) Agreement (Bland-Altman plot) between test and retest T_2 values which are shown in (A). The mean differences between both scans at each PLD are represented by the dashed lines and dotted lines display the corresponding limits of agreement (1.96× standard deviations of mean differences).

Subject-averaged ICC_{PLD} values are displayed in Figure [5.7]A. Averaging over all PLDs yields the following mean ICCs per ROI: frontal $\overline{ICC}_{\mathrm{PLD}}$=0.36, occipital $\overline{ICC}_{\mathrm{PLD}}$=0.49, parietal $\overline{ICC}_{\mathrm{PLD}}$=0.56 and temporal $\overline{ICC}_{\mathrm{PLD}}$=0.52. The corresponding PLD-averaged ICC_{subj} results are presented in Figure [5.8]A.

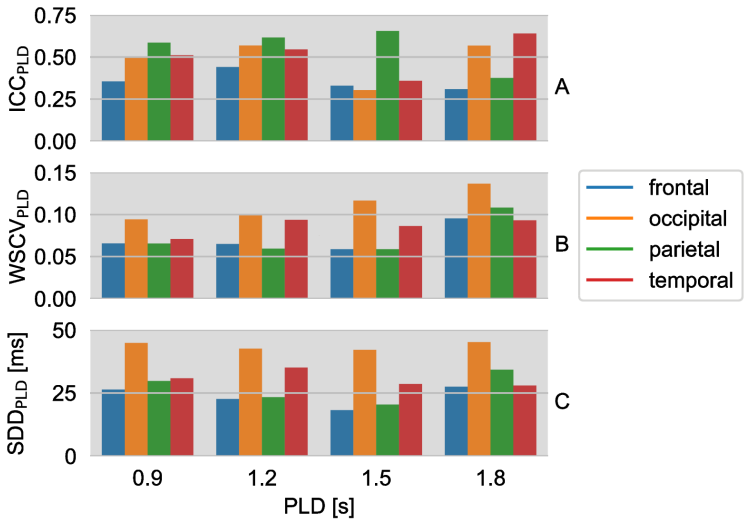

Figure 5.7: Subject-averaged (A) intraclass correlation coefficient ICC_{PLD}, (B) within-subject coefficient of variation $WSCV_{\mathrm{PLD}}$ and (C) smallest detectable difference SDD_{PLD} of median T_2 values from repeated measurements of ten subjects in four gray matter regions of interest.

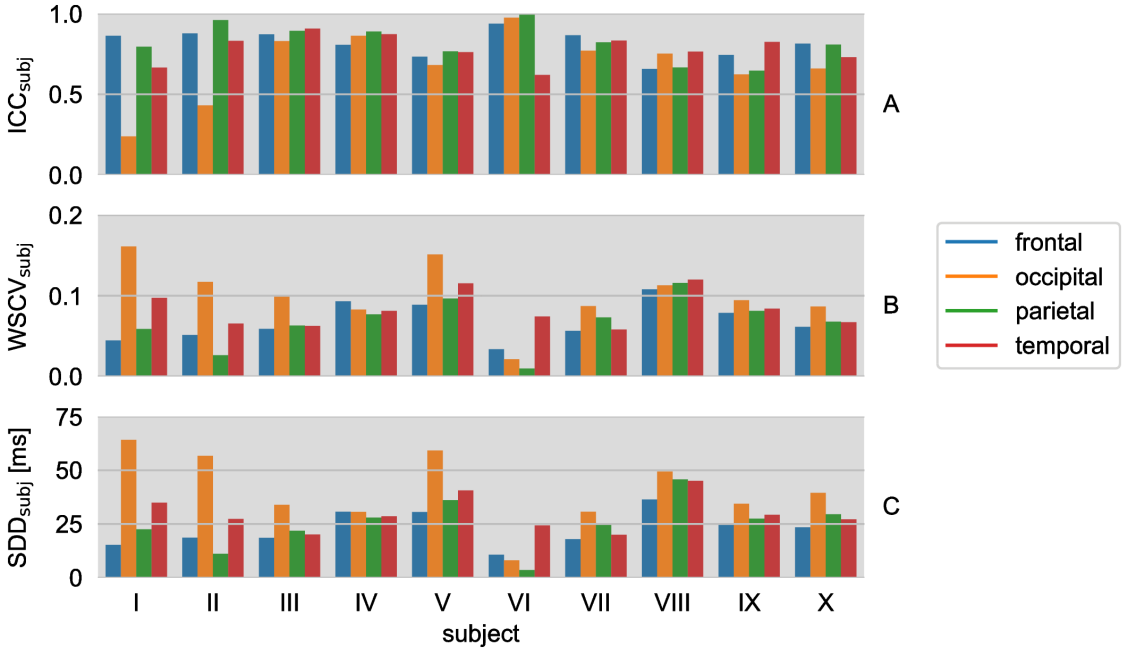

Figure 5.8: PLD-averaged (A) intraclass correlation coefficient ICC_{subj}, (B) within-subject coefficient of variation $WSCV_{\mathrm{subj}}$ and (C) smallest detectable difference SDD_{subj} of median T_2 values from repeated measurements at four post labeling delays in four gray matter regions of interest.

According to Figure [5.7]B, subject-averaged $WSCV_{\mathrm{PLD}} \leq 0.14$ for all PLDs and ROIs. Corresponding PLD-averaged $WSCV_{\mathrm{subj}} \leq 0.16$ are shown in Figure [5.8]B for all subjects.

The smallest detectable differences averaged across all subjects SDD_{PLD} are presented in Figure [5.7]C. PLD-averaged these are 24 ms in the frontal, 44 ms in the occipital, 27 ms in the parietal, and 31 ms in the temporal ROI. The SDDs are also shown as the limits of agreement in the Bland-Altman plots (Figure [5.6]B). Corresponding PLD-averaged SDD_{subj} are shown in Figure [5.8]C.

5.3.2 IV and EV monoexponential T_2 estimation

For the monoexponential T_2 estimation measurements (Figure [5.2], red and green), the following results were obtained: the background-suppressed and perfusion-weighted series based on protocol $\mathrm{PROT_{IV}}$ yielded a subject-averaged $\widetilde{T}_{2,\mathrm{IV}} = 200 \pm 18$ ms within GM-ROI, which is slightly higher than reported literature blood water proton T_2 values of 175-186 ms (Chen & Pike 2009; Li & Zijl 2020). The T_2 estimation based on non-background suppressed control images of protocol $\mathrm{PROT_{EV}}$ provides a subject-averaged $\widetilde{T}_{2,\mathrm{EV}} = 91 \pm 2$ ms, which is in good agreement with literature reference T_2 of 71-110 ms (Lu et al. 2005).

5.3.3 Biexponential compartmentalization

For the biexponential compartmentalization measurements utilizing protocol $\mathrm{PROT_{IV+EV}}$ (Figure [5.2], yellow), perfusion-weighted gray matter-masked images of one subject are shown in Figure [5.9] for all post labeling delays and T_2 weightings.

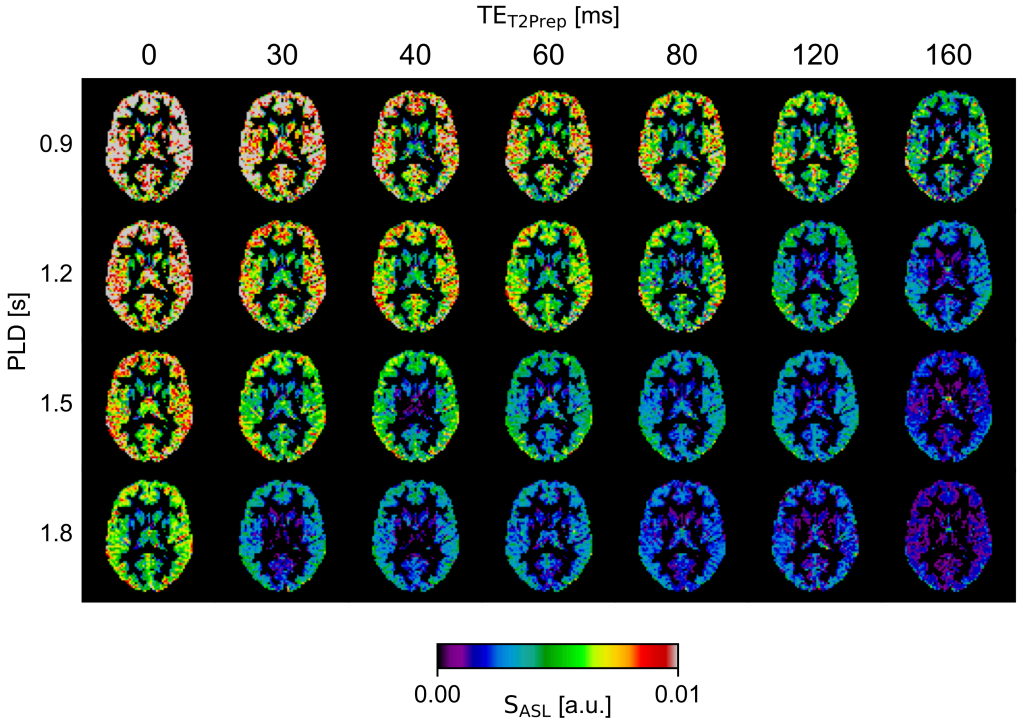

Figure 5.9: Mean perfusion-weighted ASL signal maps (S_{ASL}=($M_{\mathrm{control}} - M_{\mathrm{tag}}$)/$M_0$) in GM-ROI for all post labeling delays PLD=0.9/1.2/1.5/1.8 s and T_2 preparation times TE_{T2Prep}=0/30/40/60/80/120/160 ms of one subject. The data is displayed in native space without smoothing.

For the other two participants these are provided as supplementing Figure [5.19]. The GM-SNR of the non-smoothed data SNR_{GM} is summarized in supplementing Figure [5.20] for all three subjects. It is considered to be sufficient for a biexponential modeling even for the low SNR images with the longest PLD and the most pronounced T_2 weighting.

Compartmentalization maps of exemplary slices are presented in Figure [5.10]A for all subjects and PLDs. At short PLDs, the extravascular ASL signal fraction in the occipital lobe is small. An increase of f_{EV} can be appreciated with longer PLD. The frequency distributions of f_{EV} within the gray matter mask in Figure [5.11]B support this trend. Quantified f_{EV} in GM-ROI as mean values for all subjects are 0.31±0.11 at PLD=0.9 s, increase to 0.52±0.01 at PLD=1.2 s, 0.66±0.03 at PLD=1.5 s until they reach 0.73±0.02 at PLD=1.8 s. The standard error of f_{EV} determination $\sigma_{f_{\mathrm{EV}}}$ is shown in the corresponding error maps (Figure [5.12]A).

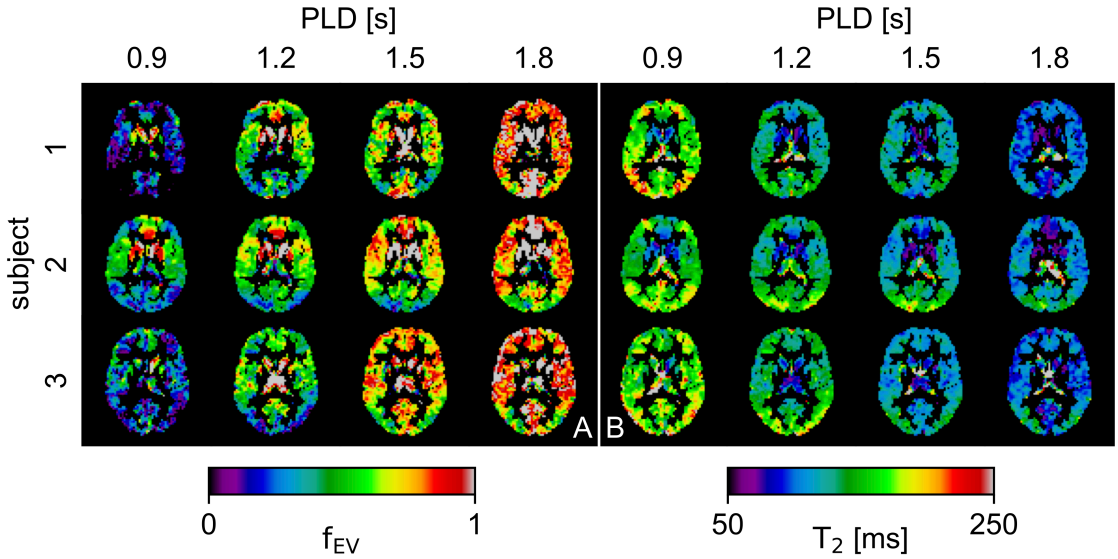

Figure 5.10: Extravascular ASL signal fraction f_{EV} (A) and T_2 maps (B) in GM-ROI. Analysis results of all subjects are shown in native space for all post labeling delays PLD=0.9/1.2/1.5/1.8 s. Small f_{EV} at the shortest PLD lead to signal drops in the displayed maps.

Instead of using subject-specific estimates as model input parameters, two additional compartmentalizations with fixed values $T_{2,\mathrm{IV},181} = 181$ ms for the intravascular and $T_{2,\mathrm{EV},91} = 91$ ms respectively $T_{2,\mathrm{EV},68} = 68$ ms for the extravascular compartment for all subjects provide frequency distributions of $f_{\mathrm{EV},181/91}$ and $f_{\mathrm{EV},181/68}$, which are shown in Figure [5.11]C-D.

Additionally to the compartmentalization maps, corresponding bulk ASL-T_2 maps of the perfusion-weighted signal are shown in Figure [5.10]B. T_2 is prolonged in the occipital lobe, which is especially dominant at shorter PLDs. The region of prolonged T_2 values matches an area of longer ATTs in Figure [5.12]B. There is a variance in T_2 between cerebral structures at different PLDs. An obvious trend of an overall decreasing T_2 with increasing post labeling delay can be clearly observed in the frequency distributions in Figure [5.11]A.

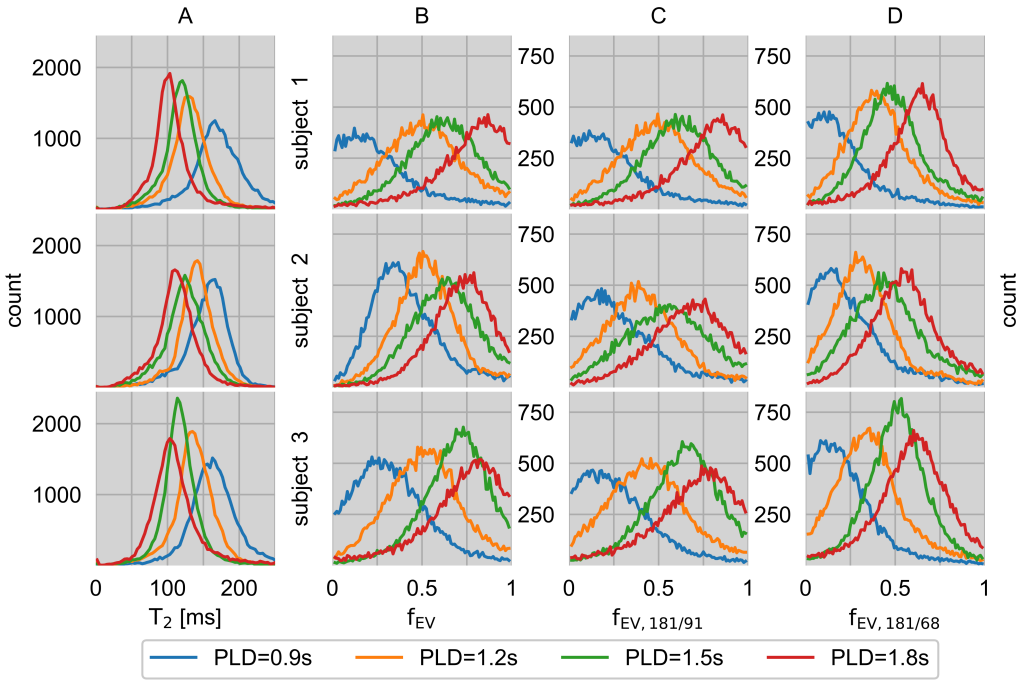

Figure 5.11: Frequency distributions of T_2 relaxation times of the ASL signal (A) and estimated extravascular ASL signal fractions in GM-ROI for all post labeling delays PLD=0.9/1.2/1.5/1.8 s: f_{EV} by using subject-specific $T_{2,\mathrm{IV}}$ and $T_{2,\mathrm{EV}}$ (B), $f_{\mathrm{EV},181/91}$ by applying fixed literature values $T_{2,\mathrm{IV},181}$=181 ms and $T_{2,\mathrm{EV},91}$=91 ms (C) and $f_{\mathrm{EV},181/68}$ based on fixed literature values $T_{2,\mathrm{IV},181}$=181 ms and a shorter $T_{2,\mathrm{EV},68}$=68 ms (D). The decrease of T_2 relaxation time with rising PLD indicates that the labeled water protons adopted EV T_2 and were increasingly located in the extravascular compartment.

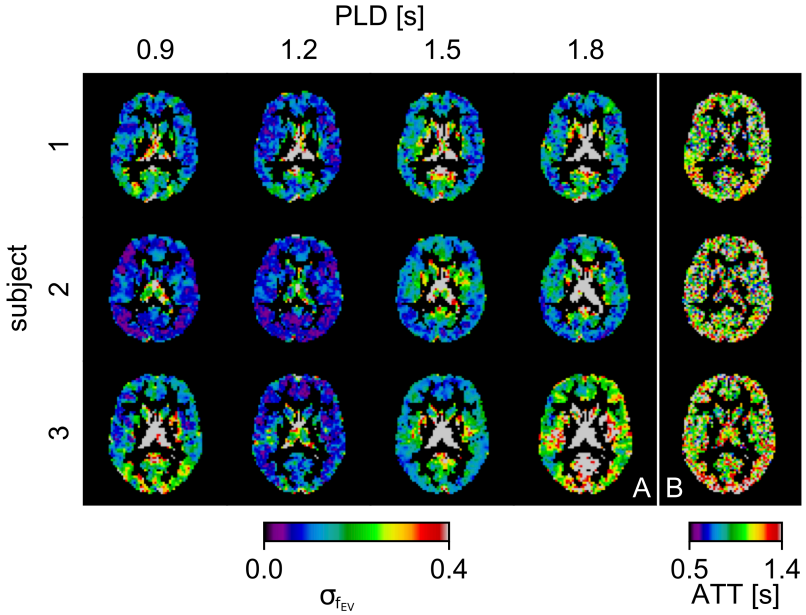

Figure 5.12: Extravascular ASL signal fraction standard error maps $\sigma_{f_{\mathrm{EV}}}$ calculated from the fit parameter estimate variances (A) and arterial transit times ATT (B) in GM-ROI. Analysis results of all subjects are shown in native space for all post labeling delays PLD=0.9/1.2/1.5/1.8 s.

5.3.4 Compartment transition rate modeling

The temporal dynamics of the extravascular fraction estimation from the previous Section [5.3.3] are visible in the PLD-course of the f_{EV} histograms and also in the detected peak fractions $f_{\mathrm{EV,peak}}$ in Figure [5.13]A. Linear and biexponential modeling results are presented in Figure [5.13]B for all subjects. The subject-averaged parameters of interest are $k_{\mathrm{lin}} = 0.62 \pm 0.15$ s^{-1} for the linear (Equation [5.6]) and $k_{\mathrm{exp}} = 0.88 \pm 0.56$ s^{-1} for the exponential (Equation [5.7]) model.

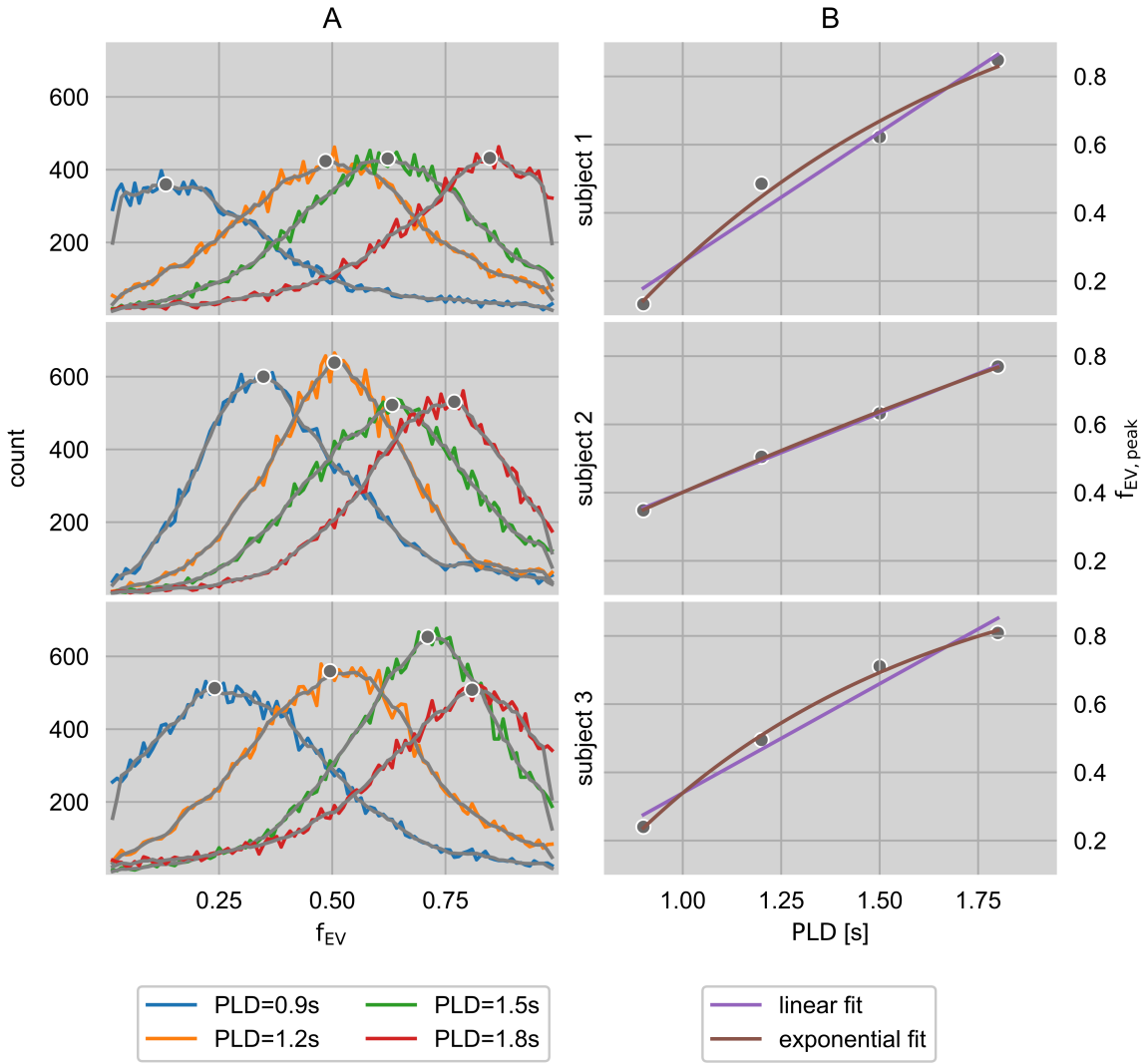

Figure 5.13: (A) Frequency distributions of estimated extravascular ASL signal fractions f_{EV} in GM-ROI for all post labeling delays PLD=0.9/1.2/1.5/1.8 s by using subject-specific $T_{2,\mathrm{IV}}$ and $T_{2,\mathrm{EV}}$, moving average filter smoothed data (gray) and detected peaks $f_{\mathrm{EV,peak}}$ (gray dot marker). (B) Transition dynamic modeling based on the detected peaks $f_{\mathrm{EV,peak}}$ from (A) by considering a linear (purple, see Equation [5.6]) and an exponential (brown, see Equation [5.7]) approach.

5.4 Discussion

Chapter [5] presents the implementation, the processing and the potential use for a compartment modeling of T_2-weighted ASL signal. First, the reliability and precision of current state-of-the-art ASL-T_2 measurements were investigated within test-restest experiments. Then, a simplified T_2-based permeability biexponential modeling approach was derived and tested for proof in vivo.

5.4.1 Bulk ASL signal T_2 reliability

In the test-retest investigations, medium reliabilities of the quantified ASL-T_2 data were found in healthy young adults. ICC_{PLD} show the highest (fair) test-retest reliability in the parietal ROI followed by the temporal and the occipital ROI. The frontal ROI is to be considered as least reliable ROI (poor). A differentiation between the four PLDs leads to a good reliability of the parietal ROI at the shorter PLDs, whereas the ICC_{PLD} of the temporal ROI tends to increase with PLD, apart from PLD=1.5 s. In this context, the occipital and frontal ROIs indicate no distinct PLD dependence. One possible explanation for the low frontal reliability may be that this largest ROI includes areas directly above the nasal cavities. Strong B_0 inhomogeneities in that area, which is notoriously difficult to shim with conventional shim coils, causes inter-voxel dephasing and poor signal-to-noise ratio. According to the example data shown in Figure [5.5], this can locally result in reduced measured T_2 across all PLDs. An additional analysis of the frontal ROI with a caudal-cranial subdivision, however, does not confirm that the caudal segment yields particularly poor PLD-specific reliability metrics across subjects (supplementing Figures [5.16] and [5.17]). On the contrary, the cranial segment seems to drive the poor overall frontal reliability, in particular at long PLDs. An analysis of the single subject parameters reveals a homogeneous distribution of ICC_{subj} within the individual ROIs, except for the occipital ROI in two participants.

Generally, there is a moderate precision, $WSCV_{\mathrm{PLD}} \leq 0.14$, for all PLDs and ROIs with the highest precision in the frontal and parietal ROIs and the lowest precision in the occipital ROI. A loss of precision in T_2 measurement seems to occur at the longest PLD. $WSCV_{\mathrm{subj}}$ analysis reveals strong differences between subjects and frequently elevated values in the occipital ROI.

With regard to PLD-dependence, the smallest detectable differences SDD_{PLD} share the same characteristics as the WSCVs. Importantly, the bulk T_2 estimates decrease with increasing PLD in all ROIs. One-way analysis of variance (ANOVA) with repeated measures indicates significant differences in T_2 of the PLDs among each other ($p < 0.001$) except for measurements at PLD=1.5 s compared to those at PLD=1.8 s ($p = 0.183$). This strongly supports that measuring T_2-prepared pCASL at different labeling and post labeling delays may be a useful strategy, and that the corresponding bulk T_2 may be a useful biomarker. For instance, there is already evidence for brain tumor classification utilizing conventional T_2 relaxometrie (Hattingen et al. 2013; Radbruch et al. 2011). In tumors, the tissue characteristics and vascularization change, impacting the blood oxygenation status and tissue perfusion (Ahir et al. 2020; Johnson et al. 2017). As the transverse relaxation time of blood water protons depends to some extent on the surrounding tissue properties and also on the blood oxygenation level, it may be presumed that the T_2-weighted ASL signal will be also altered. Therefore T_2, combined with the perfusion parameters CBF and ATT, might provide a non-invasive basis for a comprehensive model for disease characterization.

5.4.2 Limitations of ASL signal T_2 determination

Physiological fluctuations can be minimized but not completely suppressed by background saturation and may disturb the ASL data (Alsop et al. 2014; Boland et al. 2018). In addition, the patient positioning and labeling alignment may affect the measurements twofold (Zhao et al. 2016): first, an unfavorable placement of the frequency-sensitive and vessel-flow-dependent labeling slab leads to a lower ASL signal and thus to potential CBF underestimations. Second, different labeling alignments between scans lead to a decrease in test-retest reproducibility and precision. Minimizing the latter error source was attempted by using screenshots to recall labeling positions by a single operator. An advanced automatic positioning method would be highly desirable. However, current automatic positioning methods are often not suited for optimal labeling alignment in ASL. Nevertheless, assuming common arterial blood flow velocities (~20 cm/s (Alsop et al. 2014)), the wide variance in applied imaging-labeling gaps and the related time it takes the labeled blood to arrive in brain areas, should not have any measurable impact on T_2. Generally, a low SNR can lead to inaccuracies and reduced precision at the parameter fitting stage, but also during preprocessing, in particular motion correction and normalization. One option to achieve better SNR per image or more SNR-equivalent images in the same scan time in parallel imaging, is to employ CAIPIRINHA instead of conventional GRAPPA sampling (Boland et al. 2018; Breuer et al. 2005). Unfortunately, the scanner software used did not allow for online reconstruction of CAIPIRINHA data. However, given that only a parallel imaging acceleration factor of two was used, the expected gain in SNR (reduced geometry factor (Pruessmann et al. 1999)) when compared to GRAPPA would have been small. The use of parallel imaging and a twofold segmented readout reduced the echo train length. Still remaining blurring can be considered to be of equal extent throughout the T_2 weightings as the preparation does not affect the 3D GRASE readout.

5.4.3 Compartmentalization model stabilization

The SNR of T_2- and perfusion-weighted signal and the limited number of T_2 weightings make it unfeasible to accurately estimate compartment fractions and relaxation times from a biexponential four-parameter fit. Application of this full model failed entirely with the acquired data (supplementing Figure [5.21]). A better fit would require more repetitions as well as an increase and extended coverage of T_2 weightings, which results in unfeasible long scan protocols (Haller et al. 2016). Even then accurate estimates are difficult to achieve, since multiexponential fitting is in general an ill-posed inverse problem (Istratov & Vyvenko 1999). However, the problem is no longer ill-posed, if the exponential time constants are known in beforehand. Therefore, in order to perform a stable fit and obtain a method that is applicable in vivo, mono- and biexponential two-parameter fitting techniques with approaches of ASL signal source allocation have been applied. Assuming monoexponential IV and EV signal decays in two appropriately designed measurements, which take only 10 % of the total acquisition time and provide subject-specific $T_{2,\mathrm{IV}}$ and $T_{2,\mathrm{EV}}$ estimates, the feasibility of a compartmentalization was demonstrated in three subjects using seven different T_2 weightings within a total acquisition time of less than one hour. The derived simplified monoexponential model stabilized the two-compartment modeling of the SNR-limited T_2-weighted ASL human data.

5.4.4 T_2 dynamics and transition modeling

Results show a distinct dynamic in the transverse relaxation times: labeled water protons inherit $T_{2,\mathrm{IV}}$ initially and adapt shorter $T_{2,\mathrm{EV}}$ over time (Liu et al. 2010). This progress indicates the transition of these protons from intravascular into the extravascular compartment (Wells et al. 2009). Thereby, these pass the BBB, which is a central assumption in the presented compartmentalization concept (Li et al. 2005). Consistently, the obtained mean extravascular compartmentalization fraction f_{EV} in GM-ROI averaged over all subjects is 0.31±0.11 at the shortest post labeling delay PLD=0.9 s. It increases to 0.52±0.01 at a longer PLD=1.2 s and 0.66±0.03 at PLD=1.5 s until a fraction of 0.73±0.02 is reached at the longest PLD=1.8 s. This ascending course with post labeling delay supports the hypothesis of a BBB transition of labeled spins. However, an increasing contribution of non-exchanged, backflowing labeled venous spins with a shorter T_2 also cannot be excluded. With respect to differences in brain regions, bulk T_2 mapping shows higher values in the occipital lobe at shorter PLDs. This is presumably caused by CSF signal contributions, along with prolonged arterial transit times in this area (MacIntosh et al. 2010; MacIntosh et al. 2014). Consistent with characteristic regional ATTs, f_{EV} results are remarkably lower in the occipital lobe. Therefore, these could as well be linked to later arriving label, causing a possible underestimation of the extravascular signal component due to reduced ASL signal at short PLD (Hernandez-Garcia et al. 2019; MacIntosh et al. 2014). This is reflected by enlarged occipital compartmentalization uncertainties relative to other regions in two subjects, which is especially dominant at PLD=0.9 s. A possibility to consider this influence consists of a PLD- and ATT-dependent masking to ensure that the compartmentalization is only performed for sufficiently large signal. Comparatively rapid transitions into EV compartment tend to occur in the temporal lobes. Relative to this, labeled spins in the frontal lobe leave the IV compartment delayed. A largely balanced f_{EV} distribution in the GM structures is present at the longest PLD=1.8 s. Likewise, these transition patterns correspond with known ATT dynamics (MacIntosh et al. 2010).

Several observations can be made: compartmentalization results show the increase of f_{EV} with retention time of labeled water protons in cerebral structures (He et al. 2011). Also, the left-right symmetry in both hemispheres suggests balanced blood-brain barrier transitions in all three subjects. Except for the shortest PLD, there even is a good quantitative inter-subject agreement in the temporal course of f_{EV} as it can be seen in the progression of the related frequency distributions (Figure [5.11]B-D).

The transitions of water molecules between both compartments reflect the regular transport via aquaporin channels or by diffusion. The underlying hypothesis is that, depending on the BBB breakdown extent, this water permeability may be also sensitive to reflect the permeability of larger molecules. A related assessment is conceivable by comparing the f_{EV} maps (e.g. between healthy and diseased tissue, hemispheres, or different PLDs). Another approach is the modeling of exchange times. Therefore, a three-compartment model including the capillary level and related capillary transit times would lead to more sophisticated approximations (Li et al. 2005), but it might be limited by SNR and the PLD sampling range. To still obtain an estimate, the global trend of the transition dynamics was modeled in two ways (Figure [5.13]). A suspected saturation effect of the labeled water proton exchange could not be demonstrated within the biexponential model. This could be caused by the narrow range of time points that characterize a linear regime. Transition dynamics derived from the linear model show comparable values in all three subjects and imply a relatively slower exchange in subject 2.

5.4.5 Limitations of biexponential compartmentalization

In order to achieve a stable fit, both the determination of the model input T_2 values and the biexponential compartmentalization approach include strong simplifications and assumptions which are limiting factors: the presence of two compartments of equal water densities is assumed. Partial volume effects with white matter and CSF as well as an impact of venous blood are regarded as negligible. Furthermore, the blood oxygenation level and hematocrit are not considered, whereby the latter could even lead to a gender dependence in the arterial blood water proton T_2 values (Murphy 2014).

The main assumption in the presented approach, which also has to be considered as a limiting factor, is the knowledge of T_2 values for IV and EV water protons in GM. They are obtained from monoexponential T_2 fitting of short-PLD labeled and unlabeled acquisitions, respectively. These values are essential for compartmentalization and specify the quality, contrast and ultimately the differentiability between both compartments.

Inevitably, the aforementioned assumptions and simplifications lead to inaccuracies in the determination of the T_2 values and also in the biexponential modeling. In the simplified approximation $T_{2,\mathrm{EV}}$ fits literature estimates better while $T_{2,\mathrm{IV}}$ shows deviations (Chen & Pike 2009; Li & Zijl 2020; Lu et al. 2005). The latter might be caused by physiological and subject-specific factors as well as different blood extravasation levels, which are particularly dominant at short PLDs and do not affect data for $T_{2,\mathrm{EV}}$ estimation (Alsop et al. 2014). The increased uncertainty of obtained $T_{2,\mathrm{IV}}$ might be also attributed to the lower SNR of IV signal compared to total gray matter. This reduction is also caused by non-suppressed static tissue signal remaining in these data. Furthermore, individual vessels are not distinguished, in which the degree of blood oxygenation has a particularly strong effect on T_2. Altogehter, approximation results can be considered to be in good agreement with literature values resulting from dedicated studies particularly designed for T_2 determination (Chen & Pike 2009; Li & Zijl 2020; Lu et al. 2005).

Even though $T_{2,\mathrm{EV}}$ is in accordance with the literature, a lengthening of the cortical $T_{2,\mathrm{EV}}$ due to partial volume effects with CSF cannot be excluded. Especially at longer TE_{T2Prep} the fraction of CSF would become more prominent. Along with known increased iron depositions in deep gray matter structures, this encourages a compartmentalization with a shorter time $T_{2,\mathrm{EV},68}$ (Figure [5.11]D) (Lu et al. 2005). Therefore, two additional compartmentalizations were performed for all subjects using fixed literature values instead of subject-specific values. The corresponding frequency distributions are shown in Figure [5.11]C-D. The results are largely comparable with slight shifts and width variations of the distribution peaks, which suggests the use of universal fit input parameters to be a practicable option. However, the results also show a dependence on the selected transverse relaxation times. Moreover, a modeling based on fixed input parameters may not fit well in subjects who deviate from the assumed norm. Particularly in those cases and as the approach increases the measurement time only slightly, the application of subject-specific values may be advantageous.

The in vivo applicable scan time limits the parameters, which can be acquired within a single session. In particular a greater coverage of TEs would allow for a more accurate fitting and probably further improve the compartmentalization quality (Istratov & Vyvenko 1999; Wells et al. 2012). The standard error of f_{EV} determination based on the measurement protocol TEs is shown in Figure [5.12]A.

The simplifications stated above lead to further limitations, as for instance the approach does not account for

the fact that blood oxygen level directly impacts water proton T_2 relaxation time (Chen & Pike 2009; Li & Zijl 2020). This results in biased fraction estimates. However, the bias can be assumed to be constant throughout the measurements, so that it is reasonable to compare f_{EV} within the proposed method.

5.4.6 Future directions

For future research, it is important to consider that SNR-limited ASL data require repeated measurements to boost statistical power for CBF and ATT quantification, and also a reasonable number of T_2 weightings to fit the data to the T_2 relaxation model (Equation [5.3]) and the biexponential compartmentalization model (Equation [5.4]), respectively. Longer scan times would improve T_2 fit and compartmentalization modeling quality. However, for clinical applications a shorter scan protocol would be required. For that purpose, the number of post labeling delays could be reduced: the BBB transition dynamics may already be studied by contrasting f_{EV} at only two PLDs instead of four. This corresponds to the measurement of only two f_{EV} data series in Figure [5.11]B. Depending on the selected PLDs, it would halve the measurement time of the extensive $\mathrm{PROT}_{\mathrm{IV+EV}}$ compartmentalization data. Even a single PLD could be adequate for intra-subject comparisons (e.g. pre- and posttreatment).

A further possibility to shorten the acquisition is to reduce the number of measurement repetitions used for data averaging. For this purpose, a subsampling of the data was performed. The biexponential modeling included all T_2 weightings and was based on a single measurement per PLD up to the mean data of the complete data set (supplementing Figure [5.22]A). The associated standard errors seem to stabilize at an average of four individual measurements for all PLDs (supplementing Figure [5.22]B). This corresponds to a reduction of the compartmentalization data acquisition length by one third.

Also, a shortening can be achieved by reducing the number of T_2 weightings. A choice of four, for example, would save about 43 % of time. However, this would also degrade T_2 fit quality as it is reflected by poorer ICC_{PLD}, $WSCV_{\mathrm{PLD}}$ and SDD_{PLD} especially at longer PLDs (supplementing Figure [5.18]).

Presently, no specific protocols can be recommended. Optimal values may vary with the measurement objective and likely are related to the subject group, what remains to be explored (Alsop et al. 2014; Kilroy et al. 2014; Wang et al. 2013). The combined reduction of acquired PLDs, T_2 weightings and averages would substantially reduce the measurement time and thereby clearly increase the clinical relevance of the proposed method.

Based on the results of the proof-of-concept compartmentalization measurements, further investigations are needed. In particular animal studies would allow more complex protocols which could be applied to investigate animal models of blood-brain barrier disorders (Zhao et al. 2017). Another promising approach would be to apply the method in patients with known BBB dysfunction as in brain tumors (Arvanitis et al. 2019) or induce a temporary BBB permeability change in healthy subjects with transcranial magnetic stimulation (TMS) (Vazana et al. 2016).

5.5 Conclusion

The presented chapter is focused on T_2- and perfusion-weighted ASL measurements including a related BBB permeability modeling.

The implemented T_2-prepared pCASL sequence enables the measurement of T_2- and perfusion-weighted data of high quality. Assessed precision and reproducibilities of the ASL signal T_2 times allow to conclude, that ASL-T_2 is an interesting and promising metric to investigate cerebral abnormalities and a potential marker for disease-related T_2 changes (Gregori et al. 2012; Ohene et al. 2019). For instance, the T_2-prepared pCASL method may prove useful to classify brain tumors, where altered perfusion or T_2 times can be expected as previously shown in conventional T_2-weighted images (Hattingen et al. 2013; Razek et al. 2019).

The results also justify the developed compartmentalization approach based on T_2-weighted ASL data. Although the presented approach does not obtain exact permeabilities of the BBB, it provides an opportunity to estimate intra- and extravascular water pool fractions. This might be of interest in the research of numerous pathologies like Alzheimer disease, multiple sclerosis and brain tumors (Arvanitis et al. 2019; Shimizu et al. 2018; Sweeney et al. 2018), in particular due to missing alternative non-invasive BBB assessment techniques (He et al. 2011; Lin et al. 2018; Wells et al. 2009). At present, it may be especially suitable for studying whole-brain or at least large-scaled BBB disorders. The plausible results obtained suggest that this method has the potential to be used in future applications.

5.6 Supplementary material

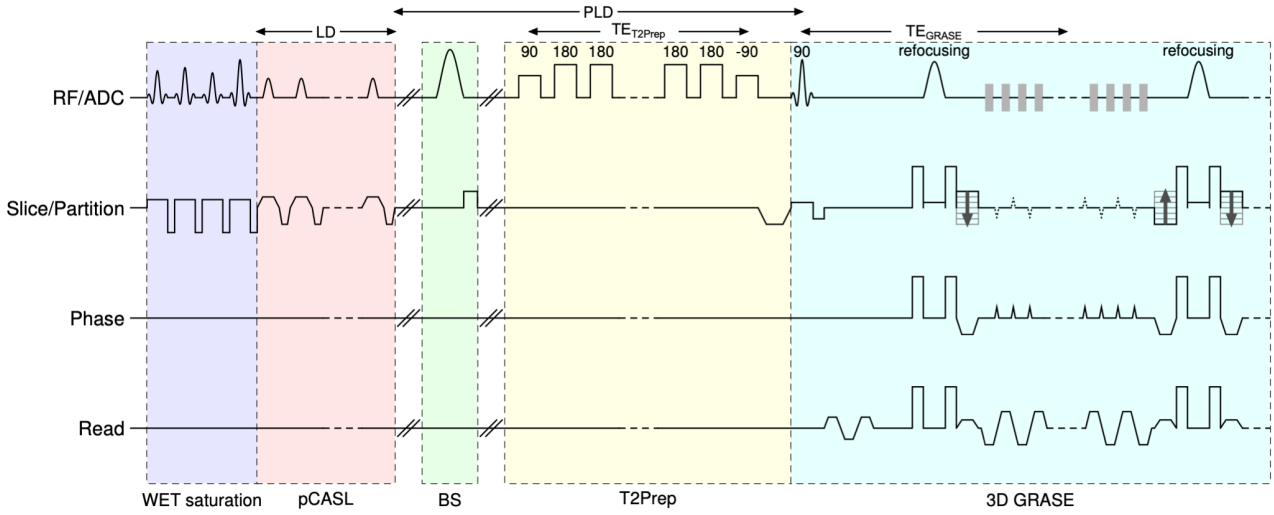

Figure 5.14: Full sequence diagram of the T_2-prepared pCASL sequence. For a simpler representation, only the shortest T_2 preparation is shown and dashed lines indicate further repetitions.

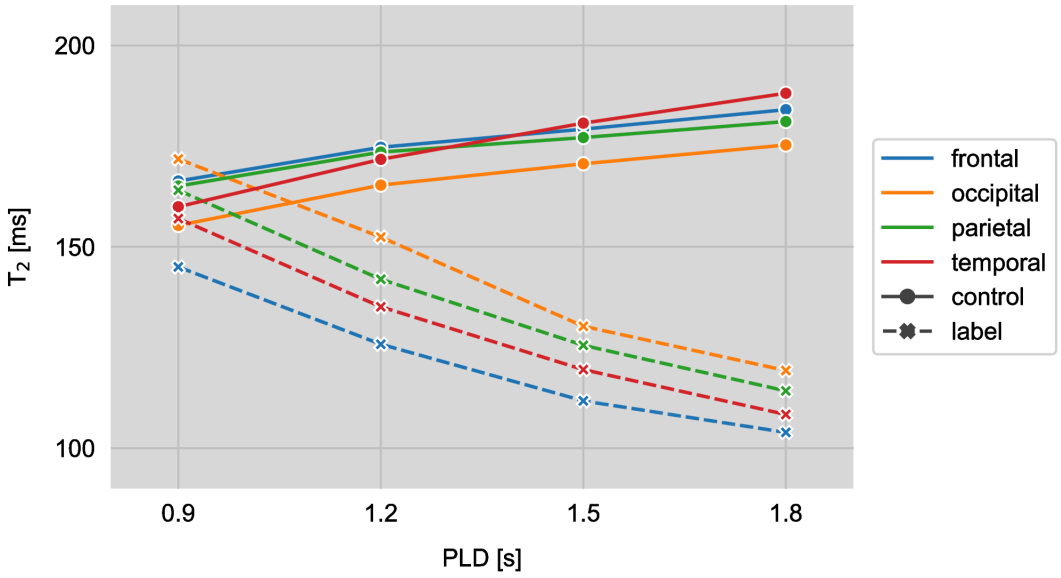

Figure 5.15: Averaged median T_2 values of perfusion-weighted ASL signal (solid) and ASL control signal (dashed) from repeated measurements of ten subjects at four post labeling delays PLD=0.9/1.2/1.5/1.8 s in four gray matter regions of interest.

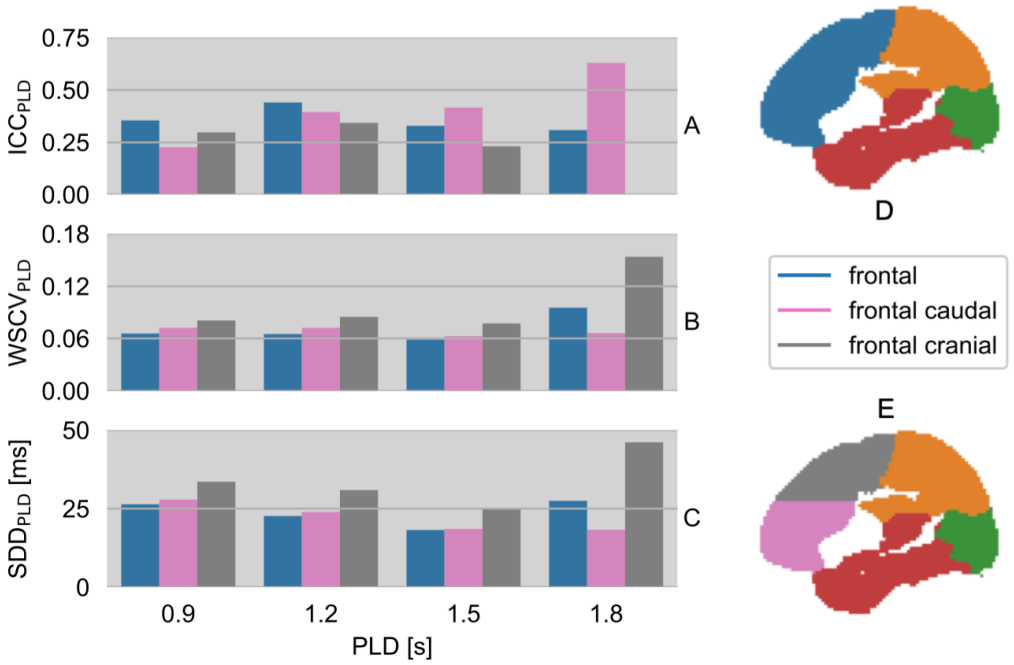

Figure 5.16: (A) Intraclass correlation coefficient ICC_{PLD}, (B) within-subject coefficient of variation $WSCV_{\mathrm{PLD}}$ and (C) smallest detectable difference SDD_{PLD} of median T_2 values from repeated measurements of ten subjects. Results are shown for four post labeling delays PLD=0.9/1.2/1.5/1.8 s in frontal gray matter regions of interest. The frontal ROI (blue in D) corresponds to the region used for the previous statistical analysis. This region was subdivided into a caudal (pink) and a cranial (gray) segment according to (E). The frontal caudal segment, which suffers from susceptibility-induced T_2 reduction, does not yield poorer measurement reliability than the large frontal ROI. Interestingly, however, the frontal cranial segment yields a considerably poorer measurement reliability, in particular at longer PLDs. For comparison, the same analysis without the two most unreliable subjects (V, VIII) provides a frontal-cranial ICC_{PLD} of 0.37 at PLD=1.8 s.

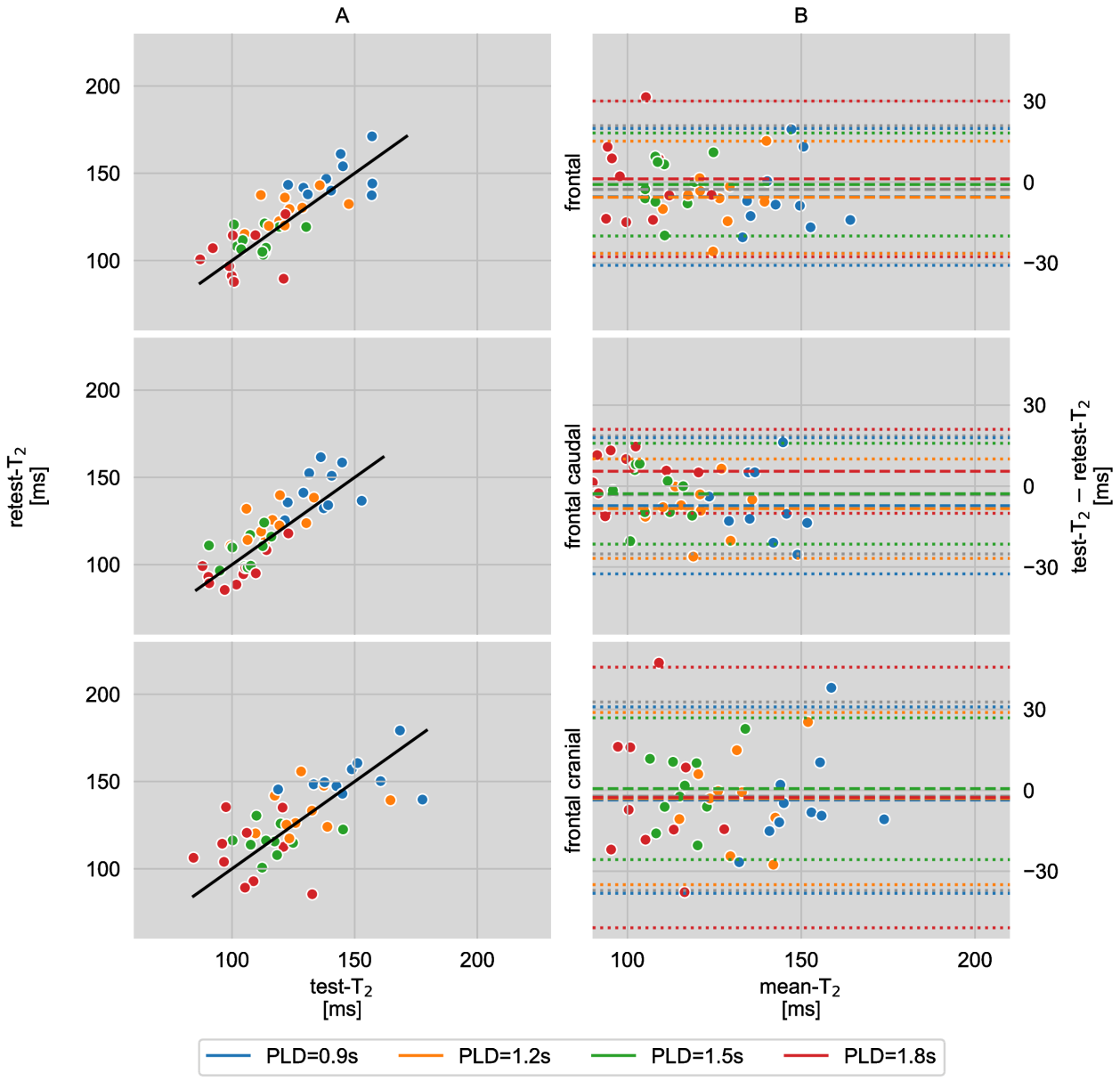

Figure 5.17: (A) Correlation of median T_2 values from repeated measurements of ten subjects in frontal gray matter regions of interest at four post labeling delays PLD=0.9/1.2/1.5/1.8 s. The subdivision of the frontal ROI into a cranial and a caudal segment is shown in Figure [5.16]E. The solid line is the identity function and represents optimal correlation. (B) Agreement (Bland-Altman plot) between test and retest T_2 values which are shown in (A). The mean differences between both scans at each PLD are represented by the dashed lines and dotted lines display the corresponding limits of agreement (1.96× standard deviations of mean differences).

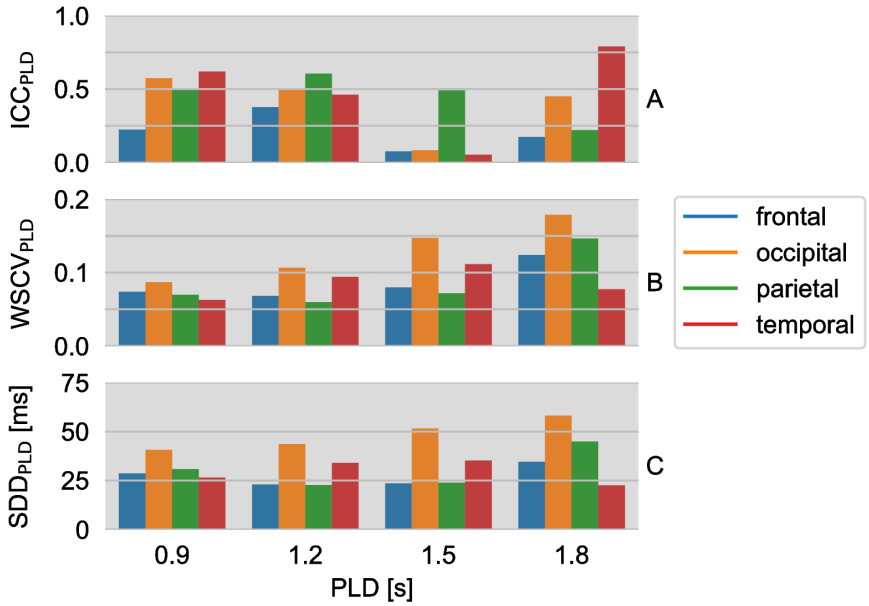

Figure 5.18: (A) Intraclass correlation coefficient ICC_{PLD}, (B) within-subject coefficient of variation $WSCV_{\mathrm{PLD}}$ and (C) smallest detectable difference SDD_{PLD} of median T_2 values from repeated measurements of ten subjects based on a reduced T_2 preparation time subset TE_{T2Prep}=0/40/80/160 ms in four gray matter regions of interest.

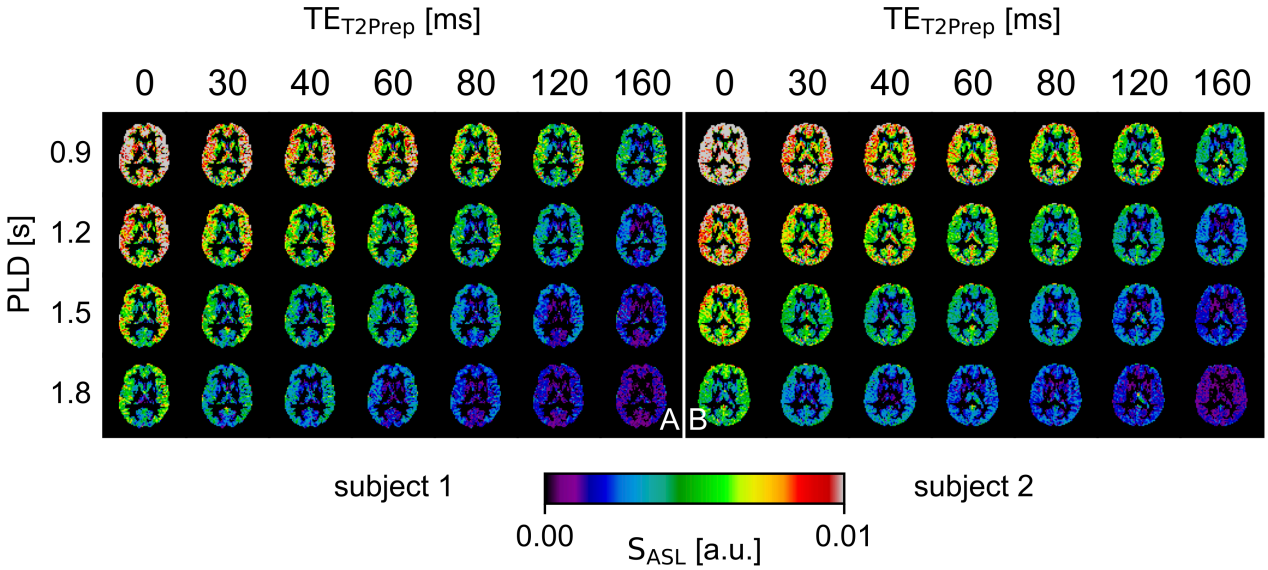

Figure 5.19: Mean perfusion-weighted ASL signal maps ($S_{\mathrm{ASL}} = (M_{\mathrm{control}} - M_{\mathrm{tag}})/M_0$) in GM-ROI for all post labeling delays PLD=0.9/1.2/1.5/1.8 s and T_2 preparation times TE_{T2Prep}=0/30/40/60/80/120/160 ms for the remaining two subjects from the biexponential compartmentalization measurements. The data is displayed in native space without smoothing.

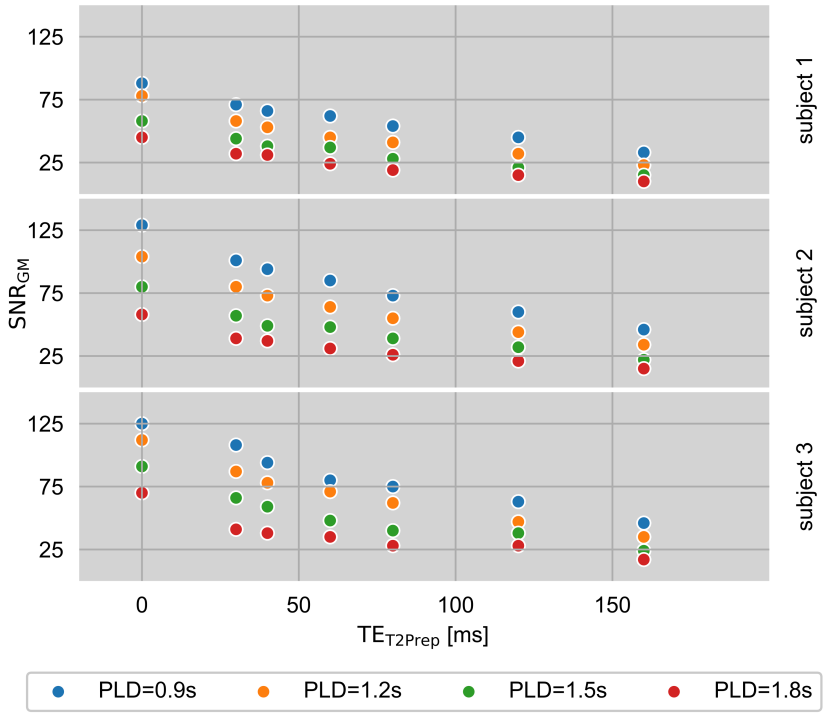

Figure 5.20: Signal-to-noise ratios in GM ($SNR_{\mathrm{GM}} = \overline{SNR}_{\mathrm{ASL,GM}}/\overline{S}_{\mathrm{noise}}$) for the three subjects from the biexponential compartmentalization for all post labeling delays and T_2 weightings.

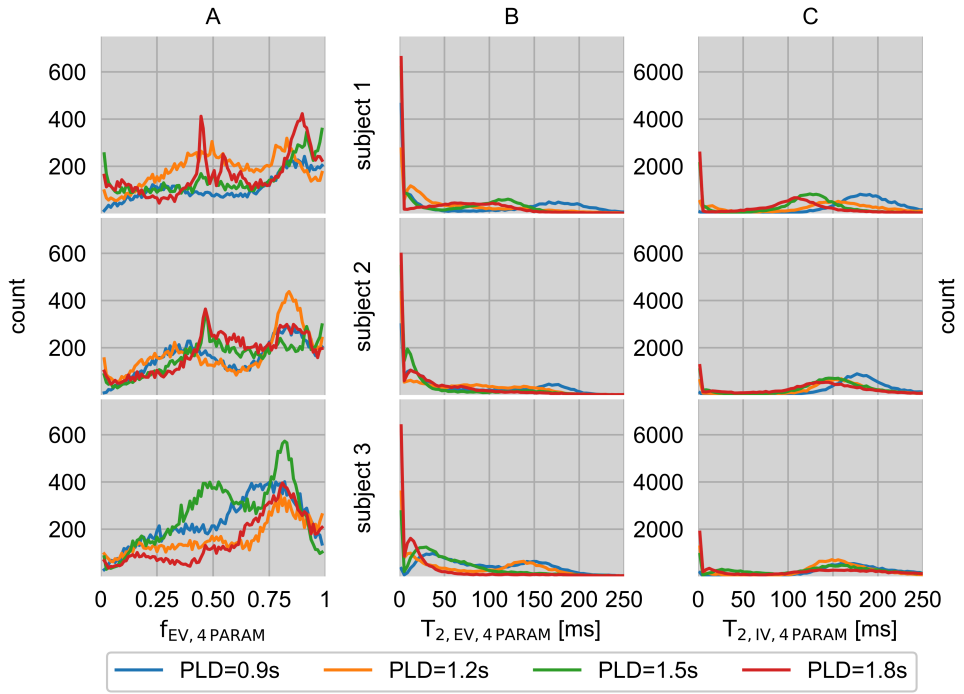

Figure 5.21: Frequency distributions of estimated extravascular ASL signal fractions $f_{\mathrm{EV,4PARAM}}$ in GM-ROI for all post labeling delays by applying a biexponential four-parameter fit (A) with the corresponding transverse relaxation time estimates of the ASL signal for the extravascular compartment $T_{2,\mathrm{EV,4PARAM}}$ (B) and the intravascular compartment $T_{2,\mathrm{IV,4PARAM}}$ (C).

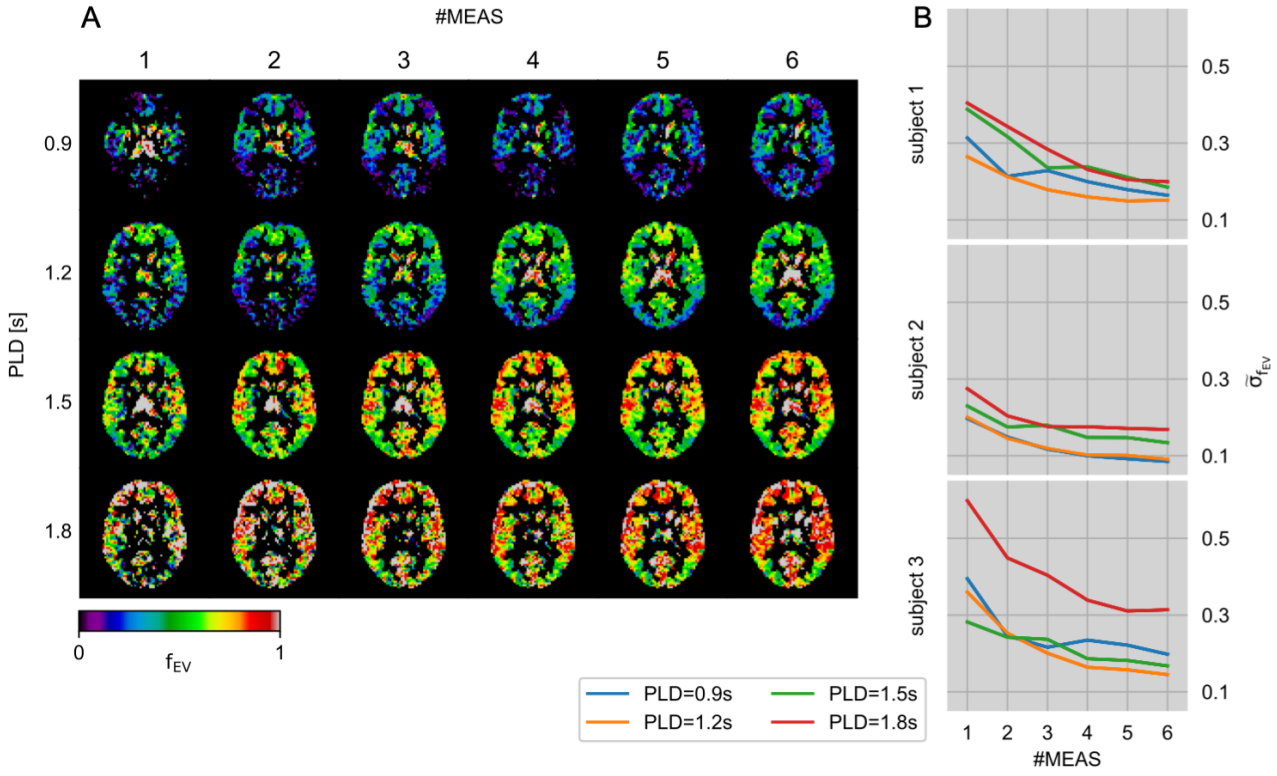

Figure 5.22: (A) Extravascular ASL signal fraction f_{EV} maps for subject 3 and (B) corresponding median standard errors $\widetilde{\sigma}_{f_{\mathrm{EV}}}$ of fraction estimation for all subjects and post labeling delays. Results base on subsampled mean perfusion-weighted data composed of a stepwise increasing number of measurements #MEAS per PLD, starting at a single #MEAS=1 until the full dataset #MEAS=6 is used. Each measurement includes all T_2 weightings.

6

pCASL at 7 T

6.1 Introduction

An intrinsically low SNR of pCASL constrains the image resolution which can be achieved within in vivo feasible scan times. Relative to experiments at 3 T, higher field strengths provide an inherently higher SNR due to the stronger spin polarization and the higher Larmor frequency. In particular for pCASL, high field strengths further enhance the SNR by a prolonged T_1 relaxation time and a correspondingly slower decay of the ASL signal. (Balchandani & Naidich 2014; Ghariq et al. 2011)

Conversely, shortened T_2 relaxation times can be detrimental for a potential T_2 weighting. Another disadvantage of higher fields is an increased SAR, which makes the legal local SAR limits a substantial limiting factor for pCASL. Also, the homogeneity of the static magnetic field B_0 deteriorates. The electromagnetic wavelength decreases with higher field. At 7 T it is about 13 cm in brain tissue (Collins & Wang 2011), which is in the range of the human head size (Yang et al. 2002). This leads to increased wave interference effects and attenuation, resulting in a more inhomogeneous transmit RF field B_1. As a result, the contrast is reduced and, due to the coil design, especially the coverage of caudally located head regions is worse. (Balchandani & Naidich 2014; Ghariq et al. 2011)

For the pCASL labeling, a sufficiently high B_1 is required within the arteries to meet the adiabatic condition. A homogeneous excitation is only a minor objective. One approach to enhance the B_1 field, meaning the selective field amplification and/or homogenization, is to use parallel RF transmission. (Katscher et al. 2002; Zhu 2004)

The current progress for in vivo pCASL imaging at ultra-high field is demonstrated by a recent study (Tong et al. 2020). These state of the art measurements were performed on the Magnetom 7 T Terra scanner (Siemens Healthineers, Erlangen) employing Gaussian-shaped labeling pulses in CP mode and also applying a static B_1 shim. The latter approach was additionally executed with VERSE labeling pulses. A presaturation was

used, but due to SAR restrictions no further BS pulses were applied. In this study, results from matched 3 T experiments outperformed 7 T results.

Given these constraints and limitations, in the following chapter the pCASL sequence is further developed on a Magnetom 7 T Plus scanner (Siemens Healthineers, Erlangen). It comprises the first time in vivo application in CP mode, the advanced development and in vivo application using static pTx and the initial implementation of a framework for applying full pTx in the pCASL sequence. An overview of the development stage reached is given in Figure [6.1].

6.2 Material and methods

6.2.1 pCASL sequence

6.2.1.1 Sequence development

Aforementioned limitations, in particular the increased SAR and pronounced B_1 inhomogeneities, lead to improved technical requirements and a more restrictive in vivo applicability. Thus, compared to the 3 T application, modular sequence changes and protocol adjustments are needed. It includes the use of a 3D EPI readout (Stirnberg & Stöcker 2020), which is presented in Section [2.3.4] and offers a more advantageous SAR management, compared to the 3D GRASE imaging (Barth & Poser 2011; Beckett et al. 2020).

Static and dynamic pTx was implemented for an application in the pCASL labeling. The calculation can be performed online on the scanner or offline. Additionally, for static pTx, a dedicated sequence was implemented for exclusively calculating the B_1 shim within a ROI online and to save it in a file. The pCASL sequence was extended to read this static B_1 shim and prepare the pCASL labeling pulses accordingly. The application of static pTx was also extended to non-labeling, but imaging-relevant pulses.

6.2.1.2 Labeling efficiency simulation

The application of VERSE labeling pulses was continued to reduce the SAR burden. Using these pulses, in vivo measurements could already generate a perfusion-weighted pCASL signal (Boland et al. 2019). To further verify the suitability of the VERSE labeling pulses for 7 T, the labeling efficiency was calculated for moving spins, also considering off-resonance effects. The simulation was performed similar to (Maccotta et al. 1997). In short, simulation intervals for off-resonances and flow velocities were defined as well as a simulation respective labeling duration. At each off-resonance Δf, the phase shift $\Delta\phi = 2\pi\Delta f(t_{\mathrm{pulse}}+t_{\mathrm{gap}})$ between two consecutive pulses of the labeling pulse train was determined. The n-th pulse of the pulse train was then extended by the related additional phase $n \cdot \Delta\phi$. By assuming flow along the pCASL gradient direction $\vec{G}_{\mathrm{z}}$, a spatial distribution of the spins along the flow direction was determined for each off-resonance and flow velocity v emerging within the labeling duration. This spatial distribution was then used to determine the position-dependent off-resonances $\Delta\omega(z) = 2\pi z G_z \gamma$ which were induced by the labeling gradients. Subsequently, Bloch simulations were performed. For one thing, these were based on finite rotations about the axis of the effective

field, which is composed of the labeling pulses and spatially dependent resonance frequencies. For the other, relaxations of arterial blood protons at 7 T were considered in terms of relaxation times T_1 and T_2 (Table [3.1]). Simulations were performed for tag and control labeling trains and the residual longitudinal magnetization $M_{\mathrm{res,z,tag}}$ and $M_{\mathrm{res,z,control}}$, which is present at the end of each labeling train, was used to calculate the respective inversion efficiency ϵ:

$$M_{\mathrm{res,z,tag/control}} = M_{0,\mathrm{z}} \cdot (1 - 2\epsilon_{\mathrm{tag/control}}) \cdot \mathrm{e}^{-\frac{t}{T_1}}. \tag{6.1}$$

Given the simulated initial magnetization $\vec{M} = (0, 0, 1)$, it is $M_{0,\mathrm{z}} = 1$. An inversion efficiency of $\epsilon = 1$ corresponds to perfect inversion, $\epsilon = \frac{1}{2}$ to complete saturation, and $\epsilon = 0$ to unchanged magnetization, such as desired in the ASL control image. Finally, the difference in inversion efficiencies between tag and control experiments was defined as the labeling efficiency: $\alpha = \epsilon_{\mathrm{tag}} - \epsilon_{\mathrm{control}}$. From the arterial blood flow velocity distribution (Zhao et al. 2016) it is possible to consider individual velocity contributions and to calculate a velocity-weighted inversion efficiency α_v per off-resonance.

6.2.1.3 Background suppression optimization

In addition to a presaturation and to further enhance the ASL signal, also at 7 T the application of a background suppression is aimed to suppress static tissue signals, which are primarily contributions by CSF, GM, and WM. Table [6.1] provides approximations of the relevant longitudinal relaxation times at 3 T and 7 T. In particular for GM and WM these are markedly prolonged at higher field strength, necessitating an adjusted optimization for a successful background suppression.

Table 6.1: Approximate longitudinal relaxation times for background suppression relevant tissues at 3 Tesla and 7 Tesla magnetic field strength. (Rooney et al. 2007)

T_1 [ms]	3 T	7 T
CSF	4300	4425
GM	1283	2132
WM	838	1220

The elaboration of the background suppression was carried in analogy to the existing implementation (Boland et al. 2018), which is mainly based on the approach of (Maleki et al. 2011) and subsequently summarized. The inversion time $TI = LD + PLD$ is the time between the presaturation and the data acquisition. Within this period TI, a number n of inversion pulses is applied at times τ_i which are defined relatively to the presaturation. Thereby, it is assumed that each applied BS pulse achieves a perfect inversion. From this, it is possible to describe the longitudinal magnetization M_z or the remaining signal at the end of TI for a certain relaxation time $T_{1,i}$ as follows:

$$M_\mathrm{z} = 1 + (-1)^{n+1}\mathrm{e}^{-TI/T_{1,i}} + \sum_{m=1}^{n} \left((-1)^m - (-1)^{m-1}\right) \mathrm{e}^{-\tau_i/T_{1,i}}. \tag{6.2}$$

Aiming at a residual magnetization of 10 %, a minimization problem

$$\min_{\tau_i} \left\{ \sqrt{\sum_{T_{1,i}} (M_z(\tau_i) + 0.1)^2} \right\}. \tag{6.3}$$

can be defined, which considers individual relaxation times $T_{1,i}$ for a tissue i and a fixed TI. Optimized τ_i were determined for $n = 2$ and $n = 3$ BS pulses using the CSF, GM, and WM relaxation times at 7 T from Table [6.1].

Separate optimized τ_i were determined for several TI in the interval [100, 6000] ms, thereby covering the entire range of common LD-PLD combinations used in pCASL experiments (Figure [6.5]). These TI-specific BS times were then fitted as a sixth-order polynomial function to analytically determine optimized times as a function of LD and PLD.

6.2.2 pTx labeling pulses

The underlying basic B_1 transmission concepts are described in Chapter [2.6] in detail. From them, there result three fundamental pulse or B_1 transmission types: CP mode, static pTx, and full pTx.

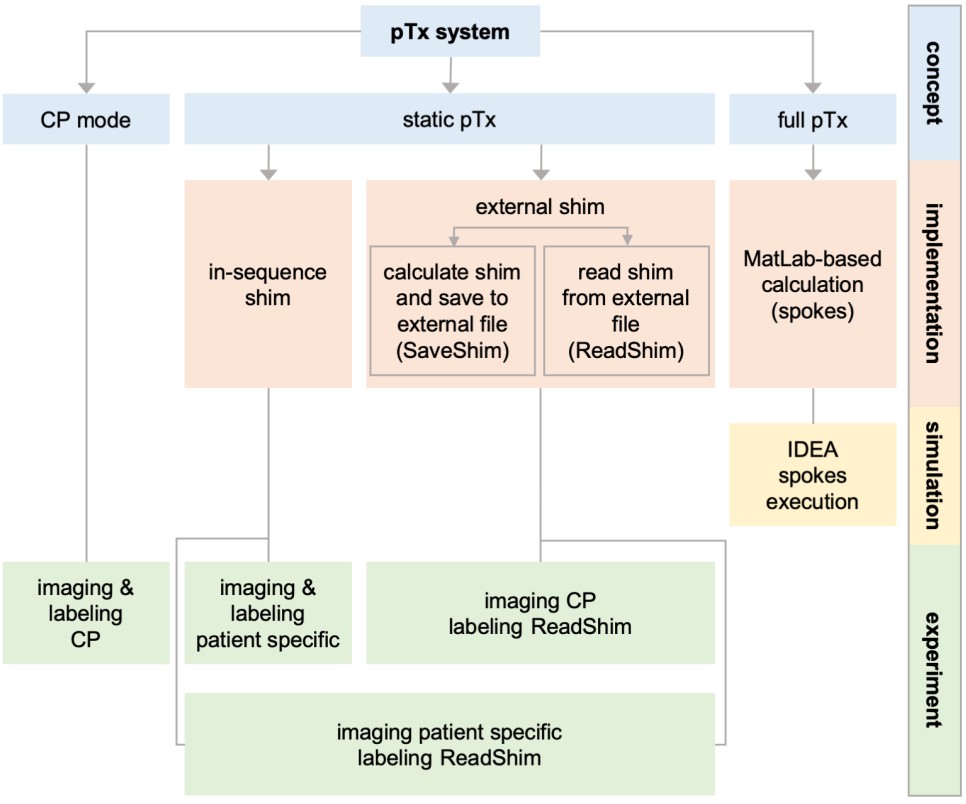

Figure 6.1: Status overview of the state of development and the performed in vivo experiments for the different pTx concepts. Labeling refers to the B_1 adjustment of the pCASL labeling pulses and imaging to the B_1 adjustment of all remaining pulses, including 3D EPI imaging pulses.

An application of these concepts to the pCASL labeling pulses is aimed in order to improve the labeling efficiency and consequently the ASL signal. VERSE pulses were used in CP and static pTx mode. Full pTx considerations build on Hann-shaped spokes pulses. Figure [6.1] provides an overview of these concepts (blue). It also shows the state of development, starting from sequence implementation (red), over full pTx simulations (yellow) up to experimental in vivo application using CP and static pTx mode (green).

6.2.2.1 CP transmission

In CP mode, no adjustment of the labeling pulses to a target volume is performed to improve the effectively applied B_1 field, but instead predefined coil phases and magnitudes are employed. This transmission type can be realized either in sTx mode with the 1Tx/32Rx head coil or in pTx mode with the 8Tx/32Rx head coil using the matching channel phases and magnitudes. Less restrictive SAR estimation models and limits apply in the CP mode (Section [2.4.4]). CP mode experiments performed in this work, refer to the emulation in pTx operational mode. Such measurements differ at 7 T, such that instead of a vendor-supplied vascular scout as provided at 3 T, an additional preparatory T_1-weighted GRE imaging sequence was used to generate planning images for the visualization of the relevant arterial blood vessels (Section [6.2.4]). For CP mode experiments it follows the procedure:

1) generation of a suitable vascular planning image (Section [6.2.4])

2) adjustment of the pCASL sequence

- placement of the imaging volume and the labeling slab (Figures [6.3]A-B)

3) running of the pCASL sequence

- the sequence prepares and executes all pulses in CP mode

6.2.2.2 static pTx

In static pTx mode, individual phases and amplitude weightings are applied to each channel for optimizing the B_1 field in a target volume (Section [2.6]). Several vendor-provided options exist for defining a target and presumably also different optimization algorithms are available for determining the B_1 shim parameters. One or two volumes can be defined in the volume-selective mode in which the optimization is performed. The patient-specific mode corresponds to a volume-selective shim with a single volume congruent to the FOV. Both options are also provided in a potentially SAR-optimized low SAR version. A further optimum peak B1 option is unkown. For characterization and to investigate a possible SAR reduction, all methods were compared within a FA mapping series (Section [6.2.3]). In this way, the potential suitability for improving B_1 in labeling regions was assessed.

Within pCASL test series, it has been found that the definition of a B_1 shim volume with the scanner UI leads to an optimization within the intersection with the pCASL imaging volume. Since labeling is applied outside

the imaging volume (Figure [6.3]A-B, gray hatched), it is necessary to also define optimization ROIs outside the imaging volume to obtain an adequate shim set (Figure [6.3]C, yellow). In this setting, there is no common intersection between the imaging and the shim volumes, hence a volume-selective shim would not be feasible. A possible workaround is the implementation of a sequence which saves the optimized shim parameters to a file on the scanner. Thereby, a sufficiently large imaging volume or FOV can be chosen in the protocol to cover the entire labeling shim volume. Since only the B_1 shim is of interest, no imaging is performed, and thus no pulses are played out or data is acquired to save time. According to its function, this sequence respectively approach is referred to as SaveShim. The import of the saved shim in the pCASL sequence and a thereon based RF pulse preparation (ReadShim) effectively leads to a volume-selective shim outside the pCASL imaging volume using but still using an UI-selected region. This capability was implemented in the pCASL sequence. The SaveShim-ReadShim-based scanning procedure is summarized below:

1) generation of a suitable vascular planning image (Section [6.2.4])

2) preparation of the pCASL sequence: determination of the labeling pulse static B_1 shim

- loading the SaveShim sequence
- volume placement in the labeling region for a volume-selective B_1 shim (Figure [6.3]C, orange)
- running of the SaveShim sequence
- the sequence determines and saves the B_1 shim parameters to a file on the scanner

3) adjustment of the pCASL sequence

- placement of the imaging volume and the labeling slab (Figures [6.3]A-B)
- free choice of a provided imaging B_1 adjustment method (e.g. patient-specific)
- optional activation of the option to save the pCASL imaging B_1 shim to a file
- activation of the option ReadShim to use an external shim set for labeling pulses

4) running of the pCASL sequence

- the sequence reads the saved shim from (2) and prepares the pCASL labeling pulse with it
- the sequence performs the selected B_1 adjustment from (3) and applies this shim to all other pulses
- if selected, the sequence saves the imaging shim set to a file

6.2.2.3 full pTx

For the calculation of pTx pulses in pTx operating mode, the Siemens Magnetom 7 T Plus scanner software provides an embedded MatLab-based MR pTx pulse design (PPD) suite. With the objective to potentially derive a full pTx based pCASL labeling, this complex framework is subsequently introduced and the implemented modifications and extensions are demonstrated.

The calculation bases on preacquired adjustment data containing B_0 and B_1 information and optional target ROI(s), as well as scanner specific system data (e.g. $G_{\max}$, $S_{\max}$) and SAR data (e.g. VOP matrix information). In the following, the STA-based calculation of 3D-selective spoke pTx pulses is considered.

The first spoke is placed in the k-space center. Then the pulse form and k-space trajectory with matching gradients are calculated. On-pulse gradients allow a slice selection and inter-pulse gradients the spoke positioning in k-space. For a potential pCASL labeling, the PPD suite has been extended by a Hann spoke pulse shape. The resulting spoke pulse is then used to calculate the system matrix $\underline{A}$ (Section [2.6]) and solve the minimization problem [2.42] to optimize the transmit channel-specific magnitudes and phases for a target magentization within the ROI. In the optimization, inherent system limits are taken into account, such as gradients, slew rate and RF amplitudes.

Depending on the total spoke pulse number, further spoke positions and pulses are determined and $\underline{A}$ respectively the target magnetization is sequentially optimized by considering all available pulses. For determining additional spoke positions, the excitation difference between the currently reached magnetization and the target magnetization is determined and the spectrum of deviation calculated by means of an FFT. The highest value in this spectrum is used as the new spoke position in k-space, as it contributes the most to an excitation.

For a flow-induced pulsed adiabatic inversion it is necessary to specify the on-pulse z-gradient according to Section [2.5.5.2], instead of calculating it as a function of the slice thickness. The capability to apply a fix on-pulse z-gradient magnitude ([mT/m]) has been implemented, which also includes a negative gradient of the same magnitude for bipolar spokes. By default, rewinder gradients are applied after the spokes. To match the adiabatic condition, a predefined average z-gradient G_{mean} must be generated by using suitable inter-pulse gradients, taking into account the pulse durations and the spoke polarities (Figure [3.3]). Therefore, the possibility to disable rewinder gradients has been added. This allows the required inter-pulse gradient to be determined and executed in the pCASL sequence depending on the labeling pulse and gradient scheme specification.

The STA-derived pulses can optionally be adapted by a VERSE transformation (Section [2.5.6]). The PPD suite only provides the possibility of a minimum time VERSE transformation, which in the case of pCASL yields a favorable pulse shortening but also amplifies the SAR problem. Therefore, two possibilities to indirectly control for the SAR in the VERSE transformation have been introduced. First, the VERSE target pulse duration [s] can be specified. Longer pulses lead to a lower SAR burden. Second, the pulse energy can be specified relative to the minimum time VERSE pulse, with smaller target fractions resulting in longer pulse durations.

In ROI-constrained calculations with very small ROIs, as in the case of limiting the optimization to single arteries, there may not be enough voxels available within the adjustment data to serve as calculation basis. To still conduct this, a higher number of voxels is required and, as B_1 changes slowly, not necessarily a higher resolution of the B_1 maps. Therefore the option was implemented to perform a relative scaling $\xi^{-1} \mid \xi \in 2^{\mathbf{N}_0}$ of the adjustment data, where the scaling value $\xi = 1$ corresponds to native resolution, $\xi > 1$ to downscaling, and $\xi < 1$ to upscaling. Figure [6.2] demonstrates exemplary scalings in the sagittal view.

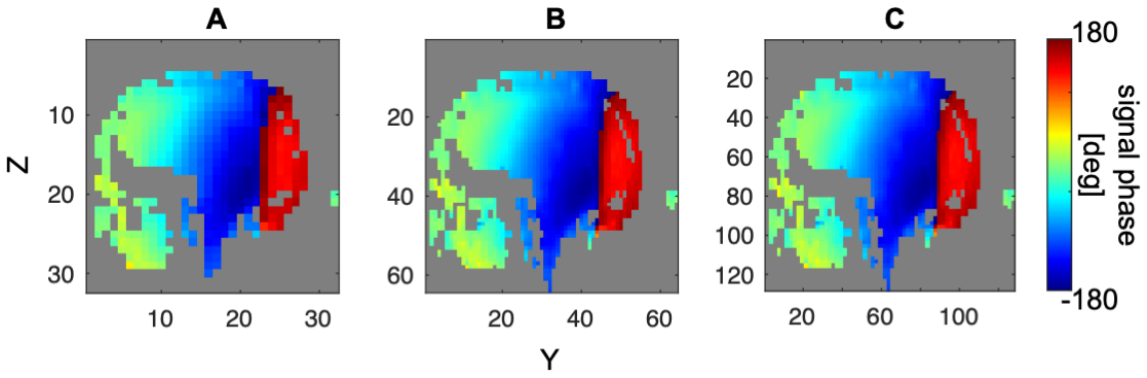

Figure 6.2: Adjustment data rescaling demonstrated for an exemplary single channel B_1 phase adjustment data slice with a relative resolution of (A) 50 % ($\xi = 2$), (B) 100 % ($\xi = 1$), (C) 200 % ($\xi = 0.5$).

6.2.3 B_1 mapping

FA maps were obtained in a subject using an in-house developed actual flip angle imaging (AFI) sequence (Yarnykh 2007) to characterize the available static shim methods. Two different configurations were included in the volume-selective methods: the first is a single caudally located volume in a potential labeling location and in the second it is extended by an additional, larger, cerebrum-enclosing volume that encompasses the potential imaging area in the pCASL sequence. This yields the following shim settings:

- CP,
- CP2,
- patient-specific,
- 1-volume-selective,
- 2-volume-selective,
- low SAR patient-specific,
- low SAR 1-volume-selective,
- low SAR 2-volume-selective,
- optimum peak B1.

In vivo FA maps were obtained within a single session and, to conclude a potentially advantageous suitability for labeling or imaging, compared in a ROI-based analysis within two ROIs afterwards. Additionally, the SAR impact and the shim (homogeneity) deviation were clarified for the low SAR modes and the optimum peak B1 option by comparison. This was accomplished based on the single transmit channel phases and magnitudes as well as the transmit energies, which resulted from the application of the B_1 shim sets for the otherwise identical AFI experiments.

6.2.4 In vivo experiments

The single-PLD protocol $PROT_{7T}$ from Table [6.2] was applied in a single subject with the imaging and labeling shim settings provided in Table [6.3] to investigate the in vivo shim respectively pTx labeling pulse impact on the ASL signal. At this, Figure [6.12]A provides the adjustment of the pCASL sequence, which was identical for all measurements: the imaging volume (yellow) largely covered the cerebrum, the B_0 adjustment volume (green) was congruent, and the labeling layer (gray hatched) was placed at the superior position according to Figure [6.3]B. The gap between labeling and imaging was 20 mm. Figure [6.12]B shows the shim volume for the SaveShim-ReadShim approach (AP $\times$ RL $\times$ FH = $150 \times 100 \times 50$ mm^3).

Table 6.2: Single-PLD protocol $PROT_{7T}$ for experimental perfusion measurements at 7 T. Dependent on the SAR- and Tx-mode used, the *TR* is adjusted to stay within the applicable SAR limits, resulting in a varying *TA*.

7 T protocol ($PROT_{7T}$)			
ASL		3D EPI	
LD	1.5 s	FOV	$200 \times 200 \times 80$ mm^3
PLD	1.5 s	acquisition matrix	$80 \times 80 \times 32$
labeling method	single-PLD	resolution	$2.5 \times 2.5 \times 2.5$ mm^3
TR	8 s	TE_{EPI}	6.6 ms
BS	2 pulse (7 T)	PAT (PE $\times$ 3D)	CAIPIRINHA 2×1^0
method	unbalanced	Partial Fourier	6/8
pulse type	VERSE	3D segmentation	1$\times$ SEG
G_{mean}	0.5 mT/m	BW	2232 Hz/Px
G_{max} (pre-VERSE)	3.5 mT/m	ETL	218 ms
RF duration	420 µs	B_0 shim	brain
RF gap	180 µs		
MEAS	22 CT pairs		
M_0 calibration			
TR	6 s		
MEAS	2		
TA	3 min 11 s		

Table 6.3: B_1 shim methods used for pCASL labeling pulses (labeling) and all remaining pulses (imaging) within an in vivo investigation using the protocol $PROT_{7T}$ from Table [6.2]. An overview of the applied methods is given in Figure [6.1] (green).

imaging	labeling
CP	CP
patient-specific	patient-specific
patient-specific	ReadShim
CP	ReadShim

For data analysis, the mean perfusion-weighted signal of the 22 control-tag pairs was formed for each shim setting. A qualitative rating was made by visual assessment. A semi-quantitative evaluation was realized by a GM-ROI-based analysis. Therefore, 95 % percentiles of the mean perfusion-weighted signal ($P_{95\%}^{\text{GM - S}_{\text{ASL}}}$) were calculated within a GM-ROI, with higher values indicating a stronger signal. To account for the different TAs, an additional time weighting $P_{95\%}^{\text{GM - S}_{\text{ASL}}}/\sqrt{TR}$ was introduced.

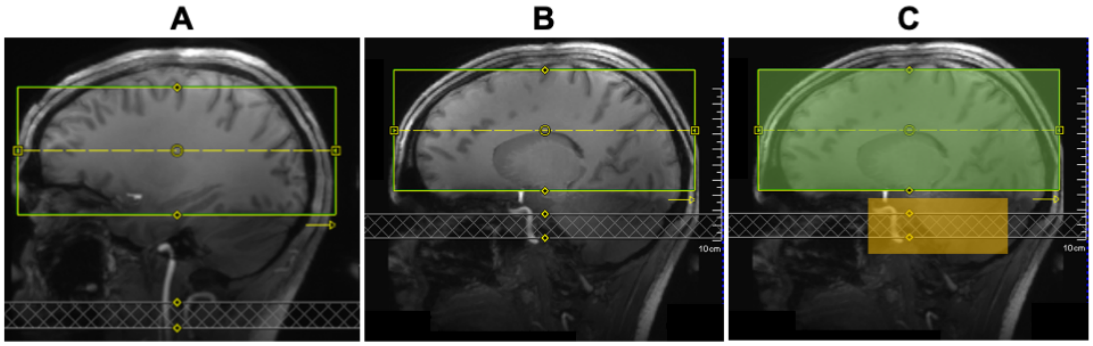

Figure 6.3: Sagittal maximum intensity projections using adjacent slices of a T_1-weighted GRE sequence acquired at 7 T for a placement of the imaging volume (yellow) and the labeling plane (gray hatched). The B_0 adjustment volume (green) matches the imaging volume. The inferior labeling plane positioning in (A) corresponds to the placement used in 3 T measurements (Figures [3.1] and [5.3]). The superior positioning in (B) yields a higher B_1 quality at the labeling plane level. The configured protocol obtains 1.3 mm isotropic images within 55 seconds, thus being suitable for the use as a localizer. (C) presents B_1 adjustment of the respective volume which was used in vivo for the labeling pulse (orange, labeling B_1 adjustment volume) and all remaining pulses (green). The latter includes 3D EPI imaging pulses and therefore is denoted as imaging B_1 adjustment volume. For static pTx, it equals a patient-specific shim by congruency with the imaging volume.

The vascular scout provided on 3 T devices is not available on the 7 T scanner. Therefore, a T_1-weighted GRE imaging sequence was applied and the signal in large arterial vessels, which presents high at 7 T, exploited. From this, maximum intensity projections (MIP) were created using adjacent slices within the region relevant for the labeling. Two different MIPs are shown in Figure [6.3]A and B. The configured protocol obtains 1.3 mm isotropic images within 55 seconds, thus being suitable for use as a localizer. The following procedure results for creating a vascular scout to adjust the pCASL sequence:

1) generation of a suitable vascular planning image

- running of the default localizer
- running of the GRE sequence
- generation of a suitable MIP from the GRE image, for visualization of the arteries in the labeling area
- loading of the generated MIP into the planning interface

2) preparation, adjustment, and running of the pCASL sequence with one of the pTx approach specific procedures previously described

6.3 Results

6.3.1 pCASL sequence

6.3.1.1 Labeling efficiency simulation

Figure [6.4]A shows Bloch simulation derived labeling efficiencies α_v at 7 T for the VERSE pulse labeling scheme specified in Table [6.2] and $B_{1,\text{mean}} = 1.5$ µT for a range of physiological flow velocities (Section [6.2.1.2]). The efficiency for a flow velocity of $v = 30$ cm/s, which tends to have the largest arterial blood flow contribution (Zhao et al. 2016), is additionally presented in Figure [6.4]B. The simulation results suggest an efficiency $\alpha_v > 0.8$ for a wide velocity and off-resonance range, whereby the off-resonance susceptibility increases with higher flow velocity. Also, very slowly flowing blood is labeled inefficiently, however, this is an inherent property of the flow-induced adiabatic inversion (Sections [2.5.5.1] and [2.5.5.2]).

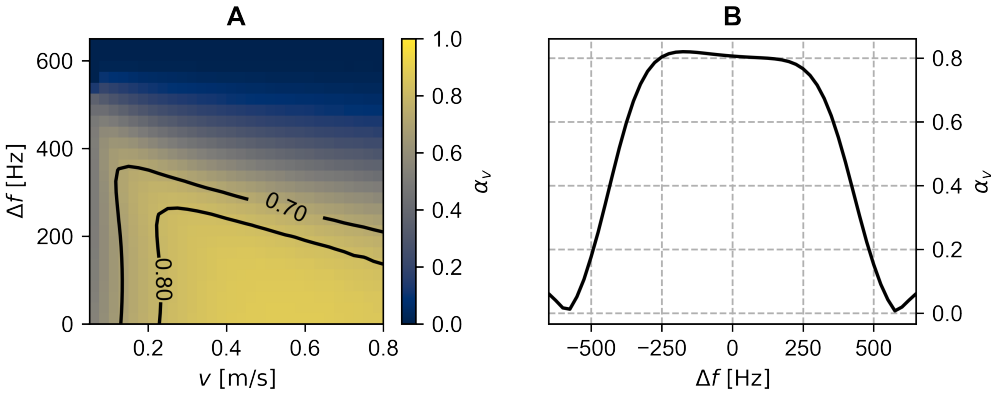

Figure 6.4: Simulated flow-weighted labeling efficiency α_v using 7 T relaxation times for arterial blood for a range of off-resonances Δf and flow velocities v (A). Additionally, α_v is shown for $v = 30$ cm/s (B).

6.3.1.2 Background suppression optimization

Based on the field strength-specific T_1 times listed in Table [6.1] for 3 T and 7 T and by considering 2 and 3 background suppression pulses, BS times were optimized as a function of the inversion time ($TI = LD + PLD$). The magnetization fraction relative to the initial longitudinal magnetization, which is present at TI, is simulated according to Equation [6.2] for a wide T_1 range. Results are presented for 3 T and 2/3 pulses in Figure [6.5]A/B as well as for 7 T and 2/3 pulses in Figure [6.5]C/D. The upper and lower bounds of the value range encompassing the T_1 times of GM, WM, and CSF, for which the optimization was performed, are marked in green/red for 3 T/7 T.

Consistent with the longer T_1, at 7 T the intended suppression is achieved in a closer interval including longer T_1 times. A shift of the lower optimization limit is evident, in particular, when two pulses are applied (Figures [6.5]A/C). Also, an improved BS is seen for high T_1 values. Furthermore, a better suppression is achieved for long TI in the 7 T optimization using two pulses, which is advantageous since longer TIs may

be potentially of interest at high field due to the slower ASL signal decay. In the field strength-internal comparison, theoretically, the three-pulse-based BS is superior to the two-pulse-based BS. However, due to the SAR limitation at 7 T, the use of two pulses may be advantageous in terms of energy.

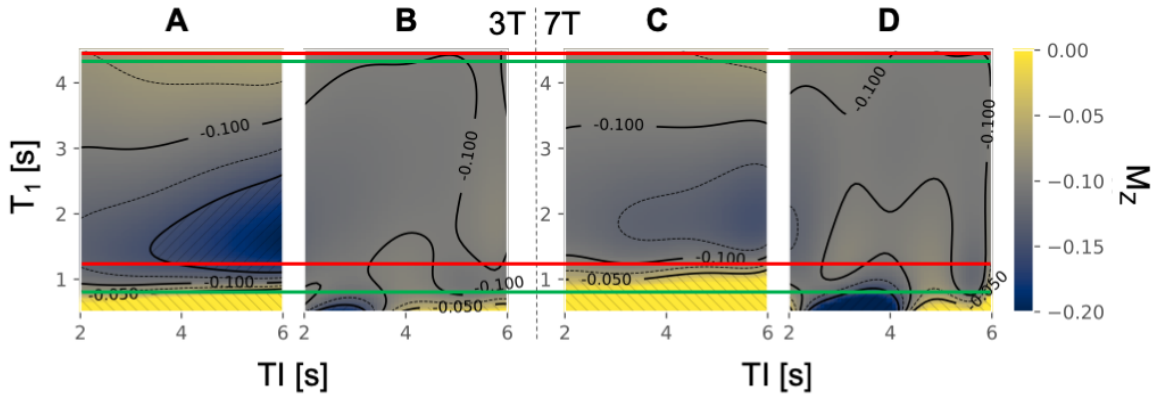

Figure 6.5: Simulated residual relative magnetization M_z as a function of the inversion time TI and the T_1 relaxation time using the optimized BS pulses for 3 T with (A/B) 2/3 pulses and the matched 7 T BS timings with (C/D) 2/3 pulses. The upper and lower bound of the T_1 range at which the optimization was performed, covering the tissues to be suppressed, are marked in green/red for 3 T/7 T.

Non-perfusion-weighted 7 T scans in Figure [6.6] demonstrate the two-pulse BS application. Figure [6.6]A/B builds on 3 T/7 T BS times and a TI=3 s following the in vivo protocol from Table [6.2]. For comparison, both scans were acquired within a single session and same slices are shown. In agreement with the simulations, the 7 T optimized BS times achieve an adequate background suppression at 7 T, which is particularly evident from the marked regions (yellow arrows) including high CSF signal contributions.

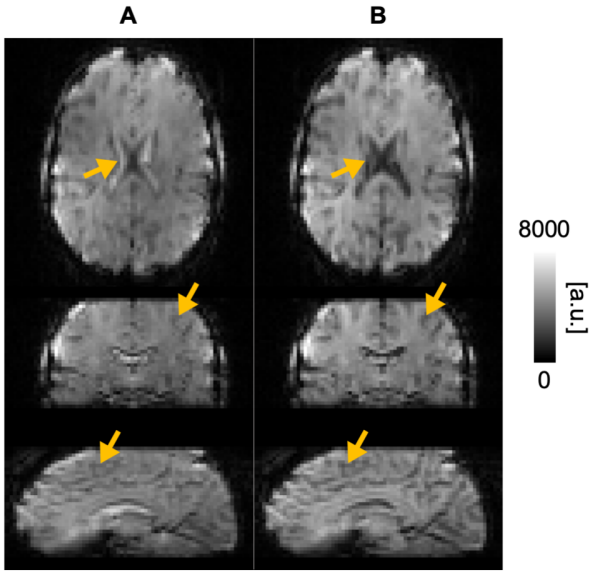

Figure 6.6: Background-suppressed non-perfusion-weighted ASL raw images of one subject acquired at 7 T using two BS pulses. An application of the 3 T optimized BS timing (Boland et al. 2018) in (A) results in an insufficient suppression, particularly visible from the CSF signal. The 7 T optimized timing in (B) yields an adequate signal suppression, also of CSF signal.

6.3.2 B_1 mapping

The respective AFI sequence energies, which resulted from the application of all available shim methods, are summarized in Figure [6.7]A. As the experiments were acquired within a single scan session and only differ in their B_1 shim setup, a comparison is applicable. The MRI image in Figure [6.8] shows the applied volume-selective shim ROIs: the smaller volume ($100 \times 100 \times 75$ mm, light blue) was used for the 1-volume-selective shim and for the 2-volume-selective shim the larger volume ($200 \times 200 \times 100$ mm, dark blue) was added. Each shim set is specified in Figures [6.7]B-C by channel specific phases and the associated scalings, respectively. The phases are given relative to the first channel (0°).

In CP and CP2 mode, predefined phases and equal scalings were applied. For both volume-selective and the patient-specific mode, equal shim parameters result for the conventional and the low SAR setting. Likewise, there follows an equality between the patient-specific and the optimum peak B1 shim. Apart from the CP and CP2 mode, there seem to effectively exist only three different optimization methods: volume-selective with one or two volumes and patient-specific.

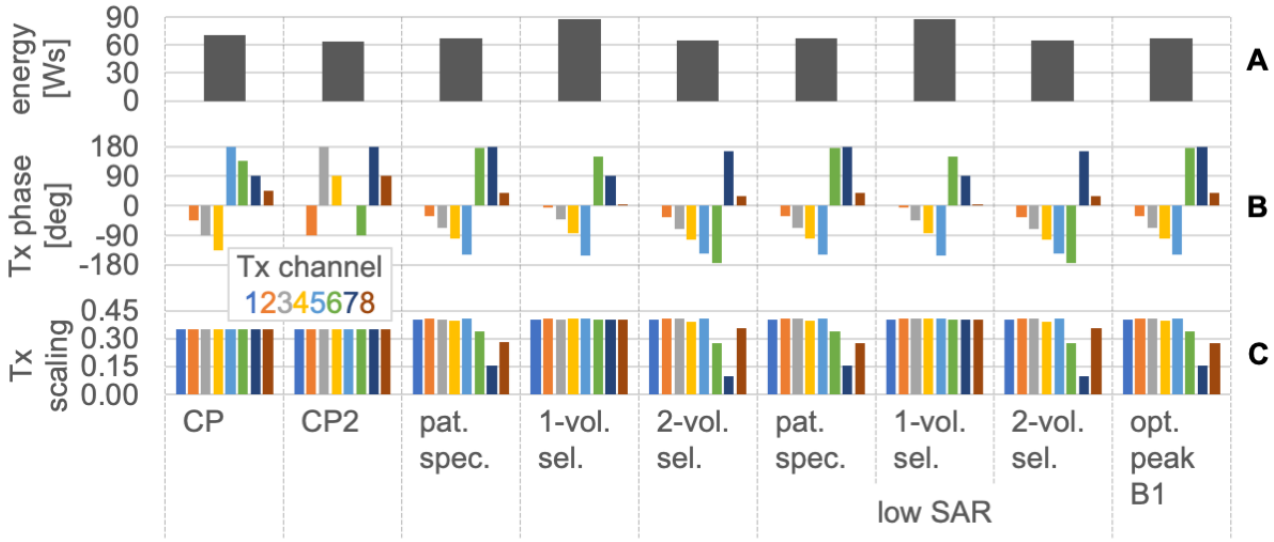

Figure 6.7: (A) Energy of measurement and (B,C) parameters for all static B_1 shim methods obtained in the experiments presented in Figure [6.8]. The individual channel phases in (B) are specified relative to the phase of channel 1 (0°). The scaling in (C) gives the individual channel weighting with respect to the reference voltage. The latter is equal in all measurements shown.

Figure [6.8] provides an overview of the obtained FA maps. The FAs were normalized to the nominal FA=50°. In line with the shim and energy comparison results, FA maps of the conventional and low SAR settings as well as maps of the patient-specific and the optimum peak B1 approach match.

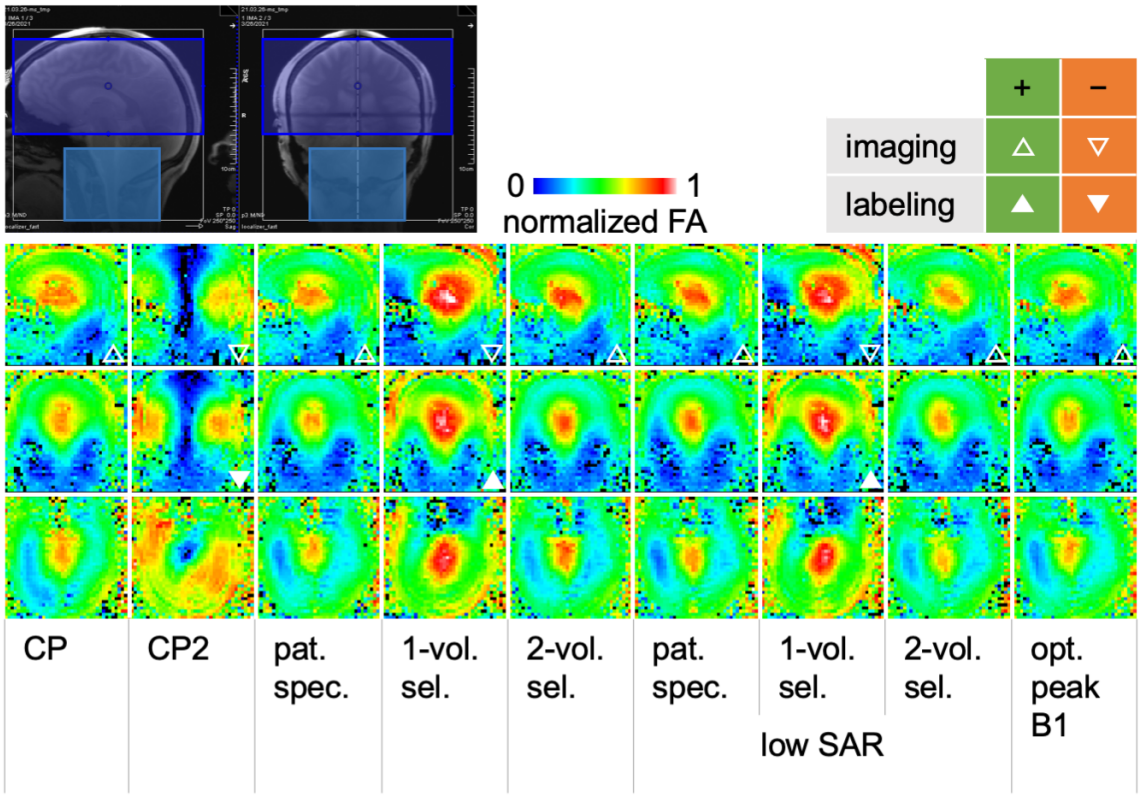

Figure 6.8: Application of all static B_1 shim modes available on the 7 T scanner (Section 6.2.2.2) within an AFI sequence in one subject. The flip angle maps shown are normalized to the nominal FA=50°. The planning images illustrate the adjustment volumes used: the patient-specific mode optimizes within the entire FOV, the 1-volume-selective mode considers the lower, light blue adjustment volume ($100 \times 100 \times 75$ mm), and the 2-volume-selective mode extends 1-volume-selective mode to also include the upper, dark blue adjustment volume ($200 \times 200 \times 100$ mm). Triangle symbols mark potentially beneficial (upward) or unfavorable (downward) FA distributions for imaging (non-filled) and labeling (filled).

For pCASL imaging a complete coverage of the cerebrum with a high FA level is advantageous. FA distributions meeting these requirements are outlined with a non-filled upward triangle symbol and those less suitable with a downward pointing marker. The latter include the CP2 mode, which shows a FA underrepresentation in the center, and, as expected, the 1-volume-selective measurement using a shim volume that is outside the imaging region, introducing low FAs in the frontal area.

For pCASL labeling high FAs in inferior areas where the labeling may be performed are considered as potentially favorable. Adverse and beneficial distributions are outlined with filled triangle symbols following the previous pointing scheme. As expected, an improved field results in the 1-volume-selective case, which is a shim optimization targeted in the inferior region.

Additionally to a qualitative view of potentially advantageous shim settings for a labeling, the FA maps are quantified in two isovolumetric ROIs given in Figure [6.9]B. The lower ROI (orange) represents an inferior labeling according to Figure [6.3]A and the upper ROI (blue) represents a superior labeling as shown in Figure [6.3]B. The mean normalized FAs in both ROIs are shown in Figure [6.9]A with the related standard deviations. Of course, duplicate shim sets present equal FAs. There result two conspicuities: first, the mean

FAs in the upper ROI always present noticeably higher than those in the lower ROI and, second, the shim method has a greater impact in the upper ROI than in the lower ROI. Actually, the latter appears to be mainly unaffected.

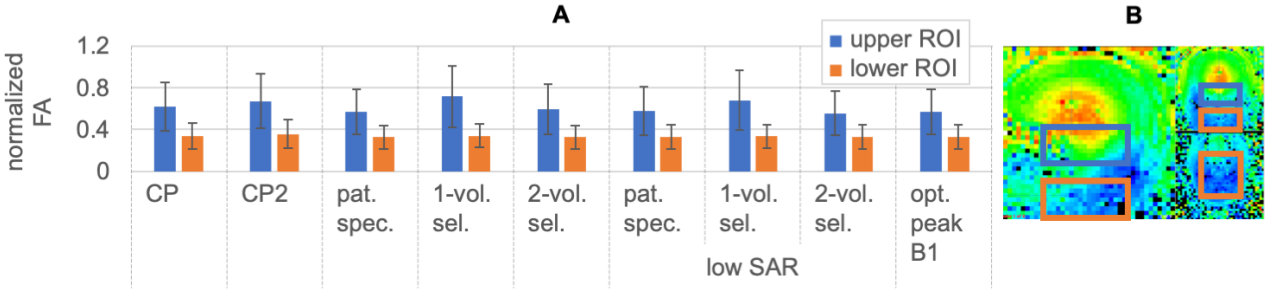

Figure 6.9: ROI-based comparison of mean FA-normalized values (A) for all static B_1 shim modes obtained in the experiments presented in Figure [6.8] using the two isovolumetric ROIs from (B).

6.3.3 Full pTx simulations

Figure [6.10] presents the main features and resultant pulses calculated respectively designed with the pTx pulse design suite using previously acquired in vivo adjustment data. Here, two spokes with a length of 350 µs were chosen as an example for a possible pCASL labeling, as well as a non-ROI-constrained target FA of 20° and a fixed z-gradient (G_{slice}) strength of 6 mT/m.

Figures [6.10]A-C show Hann-shaped spokes. In the monopolar design in [6.10]A, the spokes are applied only during a positive gradient G_{slice} with a rephasing gradient in between the two spokes. In the bipolar design shown in [6.10]B, spokes are applied at both polarities and a rephasing gradient is not needed. At unchanged RF energy, here, the bipolar design with a length of 830 µs leads to a significant pulse shortening compared to the monopolar design with a length of 1110 µs.

Figure [6.10]C corresponds to the bipolar design from [6.10]B except that no rewinder gradient is used. Thus, in a pCASL labeling, a negative gradient may be immediately applied to obtain the required mean labeling gradient with a time saving achieved by omitting a prior rewinder. The RF design shown in Figure [6.10]C has a length of 690 µs.

Figure [6.10]D corresponds to the design from [6.10]C after a minimum time VERSE transformation. There result compressed spokes with an accordingly modified gradient G_{slice}. The VERSE pulse has a shortened total length of 520 µs and a higher energy due to the increased spoke amplitude. The VERSE RF energy may be reduced in the reverse approach of stretching (Section [6.2.2.3]).

The gradients G_{read} and G_{phase} are applied in between the spokes and provide a navigation in k-space, so these do not change in the modifications in [6.10]C and [6.10]D with respect to [6.10]B.

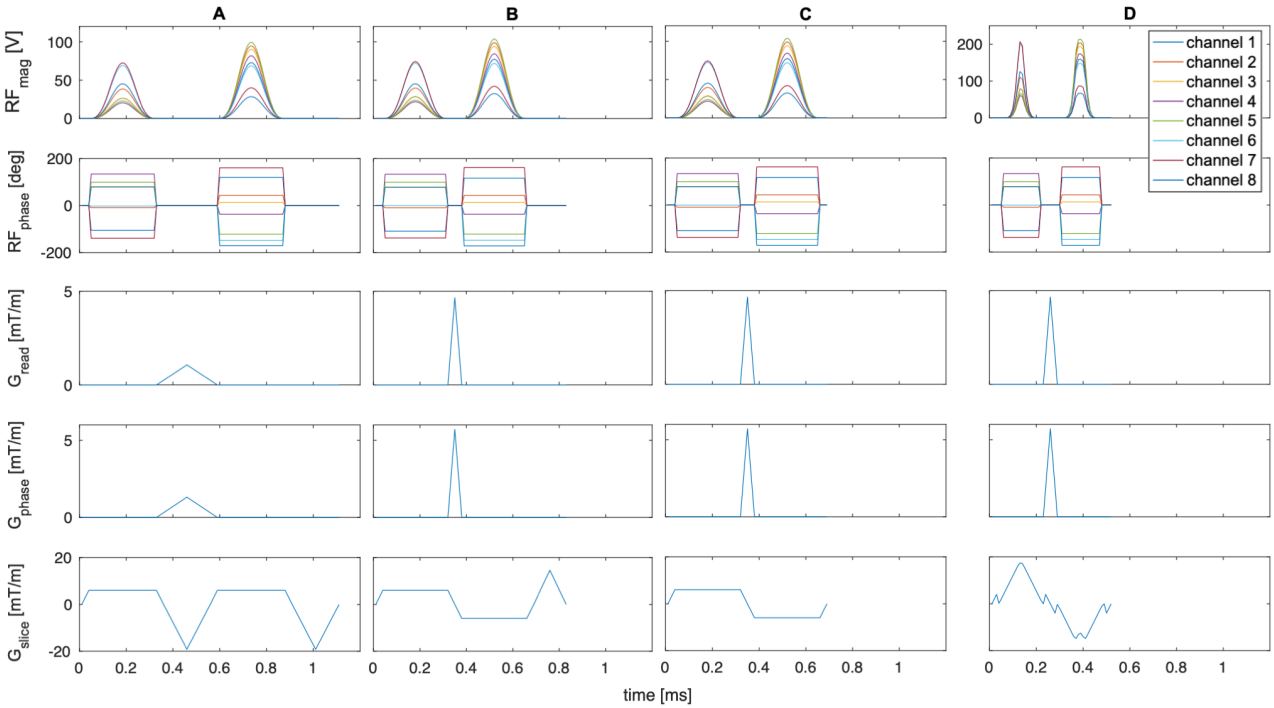

Figure 6.10: Two-spoke full pTx pulses with a target Hann-shaped spoke duration of 350 µs, a target flip angle of 20° and a fixed z-gradient (G_{slice}) strength of 6 mT/m. The monopolar approach (A) takes more time relative to the bipolar design (B), both finishing with a rewinder gradient. This gradient is suppressed in (C) for the bipolar design. The pulse from (C) is shown in (D) after minimum time VERSE transformation using the scanner system component protection limits as constraints.

Figure [6.11] is a simulation of an exemplary full pTx pulse for pCASL labeling as it has been implemented in the sequence. Here, the applied pulses are composed of two spokes without a rewinder corresponding to Figure [6.10]C. Two pulses of a single transmit channel for the control/tag condition are representatively shown in Figure [6.11]A/C, as well as the corresponding labeling gradients G_{slice} in Figure [6.11]B/D. Between both conditions, there is only a difference in the gradient. The application of the bipolar design, spokes with identical lengths and equal gradient amplitudes leads to a compensation of the two pulse gradient lobes and a mean gradient $G_{\text{mean}} = 0$. This already meets the pCASL control condition and so no further inter-pulse gradient is required (Figure [6.11]B). For achieving a $G_{\text{mean}} \neq 0$, in order to satisfy the tag condition, a matching inter-pulse gradient is applied. In this example it is $G_{\text{mean}} = 3.5$ mT/m, whereby the simulation exhibits an inverted sign convention.

Currently, the full pTx pulses shown cannot be run on the scanner due to energy constraints, especially SAR limitations.

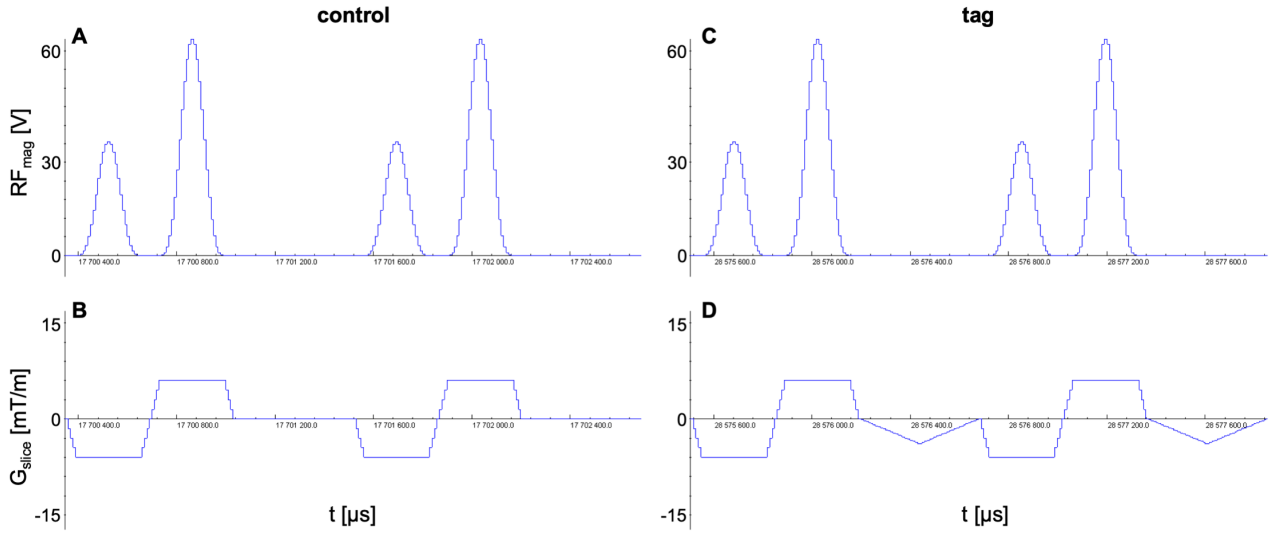

Figure 6.11: Sequence simulation of a two-spoke pCASL labeling pulse calculated with the MatLab-based MR pTx pulse design suite showing the control (A,B) and the tag (C,D) condition. Two RF pulses from the labeling train, each composed of two spokes, are shown in (A) and in (C). These are identical for both conditions. The related z-gradients (G_{slice}) differ for the control (B) and the tag (D) condition.

6.3.4 In vivo experiments

Figure [6.12] presents an overview of all in vivo 7 T results of one subject using protocol $\text{PROT}_{7\text{T}}$ (Table [6.2]) and applying the B_1 adjustment configurations from Table [6.3]. Measurements were performed in the first level SAR supervision mode and deviating from the protocol value, an increase of TR was required to stay within the SAR limits for the scans in which not exclusively the CP mode was used. Table [6.4] lists the applied TRs, which in the experiments lead to the maximal permissible SAR.

Table 6.4: In vivo measurement repetition times TR resulting from SAR constraints for experimental B_1 shim settings shown in Figure [6.1] (green) using the protocol $\text{PROT}_{7\text{T}}$ (Table [6.2]) in a single subject. 95 % percentiles of the mean GM ASL signal $P_{95\%}^{\text{GM-S}_{\text{ASL}}}$ reflect the perfusion signal strength. The TR-weighted values $P_{95\%}^{\text{GM-S}_{\text{ASL}}}/\sqrt{TR}$ additionally account for the time efficiency.

imaging	labeling	TR [s]	$P_{95\%}(\text{GM-S}_{\text{ASL}})$ [a.u.]	$P_{95\%}(\text{GM-S}_{\text{ASL}})/\sqrt{\text{TR}}$ [a.u.]
CP	CP	8	128	45
patient-specific	patient-specific	12.35	134	38
patient-specific	ReadShim	12.35	156	44
CP	ReadShim	10.92	130	39

In Figures [6.12]C-E, each column corresponds to a combination of imaging and labeling B_1 adjustment methods from Table [6.4] as annotated below. The transverse views present the same slice. The M_0 reference scans in Figure [6.12]C and the non-perfusion-weighted ASL control scans in Figure [6.12]D reveal no visually detectable differences between the individual B_1 adjustments.

The mean perfusion-weighted signal of 22 CT pairs is shown in Figure [6.12]E in the three main anatomical views. In all images, a perfusion signal is evident. As expected, it presents dominantly in GM areas. By comparison, the perfusion-weighted image using the patient-specific B_1 shim for imaging and the ReadShim approach for labeling qualitatively stands out. In this image, a consistently higher perfusion signal level is apparent in the axial view. Also, the temporally located areas present a comparatively improved perfusion signal.

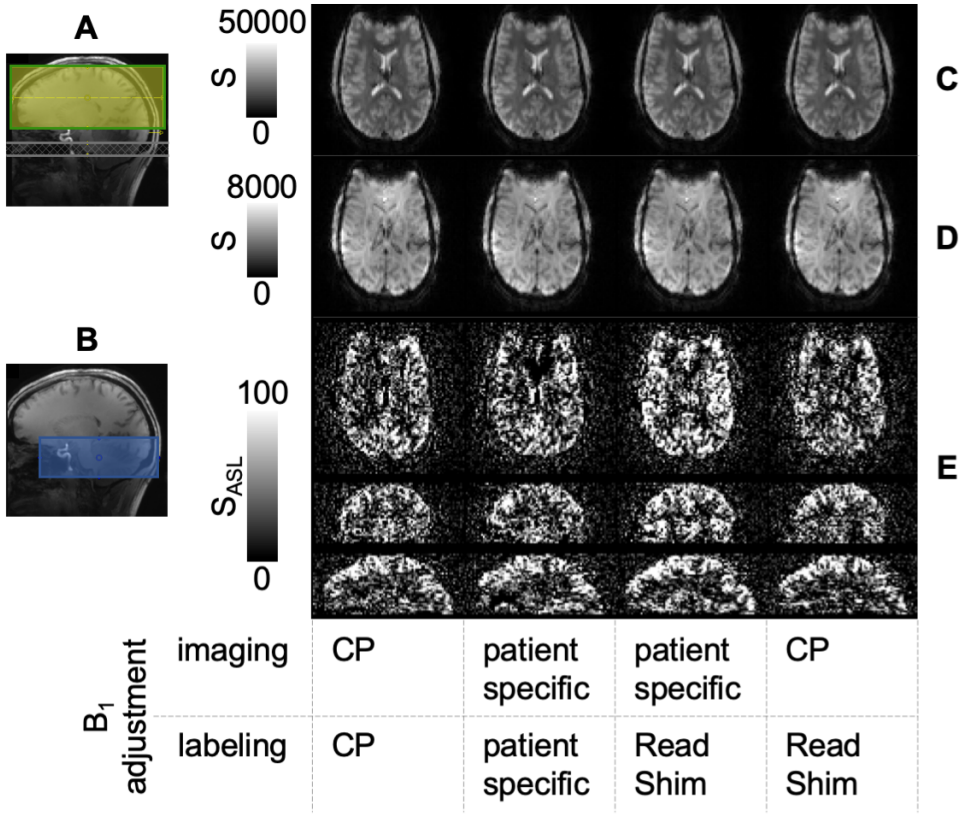

Figure 6.12: 7 T in vivo results for experimental shim settings shown in Figure [6.1] (green) using the protocol $\text{PROT}_{7\text{T}}$ (Table [6.2]) in a single subject. (A) pCASL imaging volume (yellow), congruent B_0 adjustment volume (green) and labeling plane (gray hatched, gap=20 mm). (B) Labeling B_1 adjustment volume (blue, AP $\times$ RL $\times$ FH $=$ 50 $\times$ 100 $\times$ 50 mm^3) applied in the SaveShim sequence. (C) M_0 reference scans and (D) non-perfusion-weighted control images of a representative slice. (E) Mean perfusion-weighted images of the same slice, extended by the remaining main anatomical views.

Figure [6.13]B shows the perfusion-weighted images after applying a common GM mask, with the transverse view of a more superior slice. The upper diagram [6.13]A illustrates the respective 95 % percentiles of the mean GM signal $P_{95\%}^{\text{GM-S}_{\text{ASL}}}$. These are additionally summarized in Table [6.4]. $P_{95\%}^{\text{GM-S}_{\text{ASL}}}$ is highest for the data using the patient-specific B_1 shim for imaging and the ReadShim approach for labeling. It is consistent with the previous qualitative assessment showing this approach to generate improved pCASL data. This is followed by the data using the patient-specific shim for all pulses with a clearly lower $P_{95\%}^{\text{GM-S}_{\text{ASL}}}$. The two remaining experiments exhibit comparable values, whereby in absolute terms the exclusive CP mode use yields the smallest value.

The time-weighted $P_{95\%}^{\text{GM-S}_{\text{ASL}}}/\sqrt{TR}$ values are also given in Table [6.4]. For the imaging/labeling shim combinations it results the descending ranking: CP/CP, patient-specific/ReadShim, CP/ReadShim and, as the last, patient-specific/patient-specific.

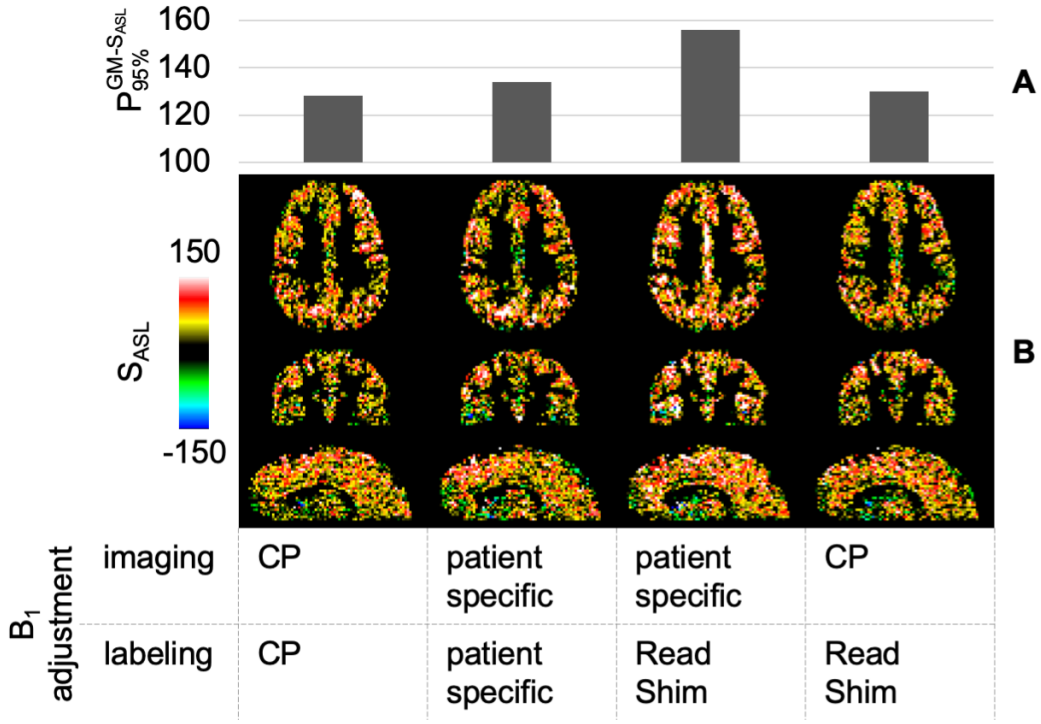

Figure 6.13: (A) 95 % percentile of mean GM in vivo ASL signal $P_{95\%}^{\text{GM-S}_{\text{ASL}}}$ and (B) GM-masked mean perfusion-weighted images obtained with an experimental setup according to Figure [6.12].

6.4 Discussion

Chapter [6] presents the development of the pCASL sequence on the Siemens 7 T Plus scanner platform, focusing on the implementation of pTx-based labeling pulses.

The VERSE simulation results suggest a suitability of the implemented VERSE labeling pulses also at 7 T (Figure [6.4]) for a range of blood flow velocities and off-resonances. A theoretical labeling efficiency of 80 % is achieved for the representative flow velocity of $v = 30$ cm/s and comparable flows. However, in the in vivo experiment a lower efficiency must be assumed, for instance due to anatomically not best suited arteries, B_0 and/or B_1 inhomogeneities. Against this background, a further development of the VERSE labeling would be useful to improve the efficiency and the achievable maximum signal. Also, the simulations performed assume a mean labeling $B_{1,\text{mean}} = 1.5$ µT. Depending on the LD, the SAR limit and the maximum TA, it may be necessary to lower energy for in vivo application, possibly by downscaling the pulse amplitude. This way, a shorter TR may be realized, but it inevitably would lead to a further reduction of the labeling efficiency. For the so-called saturation labeling, this strategy is used to specifically induce a saturation instead of an inversion (Taso & Alsop 2020).

The background suppression was adapted for 7 T. Especially when using two pulses, simulations (Figure [6.5]) demonstrate an improved suppression of signals particularly originating from longer T_1, as visible in the adequate suppression of CSF signal contributions (Figure [6.6]). Due to the narrower T_1 range at 7 T, simulations also indicate a superior suppression of WM and GM signal components.

The FA map analysis demonstrates a volume-selective shim within the labeling region as most suitable for labeling pulses. For imaging pulses a second volume-selective shim with a single volume on the imaging volume may be advantageous. These two conditions exclude an overall head/neck shim setup and correspond to a patient-specific shim for imaging and a dedicated shim for labeling. In addition to intrinsically higher B_1 values in superior areas, the ROI-based FA map analysis demonstrates also a better shim control in these ROIs, suggesting a labeling at such a location as potentially beneficial. However, it must be noted that the ROI-based consideration largely represents homogeneity and the B_1 in the arteries is crucial for the labeling.

In vivo measurements demonstrate a promising perfusion-weighted signal using both the CP mode and static B_1 shim methods. The results strengthen the FA map-derived suggestion that it is favorable to apply a patient-specific shim to the imaging pulses and to use a volume-selective shim of the labeling region for pCASL labeling pulses. Such data provided the strongest perfusion-weighted signal with an improved whole-brain coverage. Due to a more restrictive SAR supervision, B_1 shimmed experiments required a longer TR compared to CP mode, which presents disadvantageous in a signal-per-time comparison.

Full pTx labeling pulses have been implemented, but SAR restrictions prevented an application on the scanner. To date, no pCASL studies are known using full pTx for labeling, but merely a B_1 shimming (Meixner et al. 2021; Tong et al. 2020; Wang et al. 2021). A further development should focus on a FA optimization within arterial ROIs. The implemented possibility of an adjustment data upscaling should help to achieve such a small-volume optimization.

Also B_0 magnetic field inhomogeneities can influence the labeling efficiency. These effects have not been considered. In future developments it may be of interest to account for them. As demonstrated in earlier studies, this may be accomplished by a dedicated B_0 mapping of the labeling plane and the application of phase-offset and/or correction terms to compensate for off-resonances and imperfect phase accruals (Berry et al. 2019).

The in vivo experiments indicate that an optimized B_1 in the imaging volume may also improve the perfusion-weighted data. The ASL signal quality thus depends on both, the labeling performance and the data acquisition respectively the imaging quality. Therefore, it may be worth to also consider an application of full pTx pulses within the 3D EPI framework.

6.5 Conclusion

The presented chapter is focused on pCASL perfusion MRI at 7 T. In theory, ASL imaging strongly benefits from high main magnetic field strength. However, there are many technical challenges at 7 T which require substantial modifications of the ASL sequence. High energy deposition within human tissue as well as large inhomogeneities of the B_1 transmit field hinder efficient spin labeling. The implemented specialized labeling pulses account for these challenges and already achieved promising preliminary in vivo results. Advanced B_1

adjustment techniques using parallel transmission improved the ASL perfusion signal quality, thus serving as an advanced interstage justifying a further pTx-based sequence development.

7

Conclusion and outlook

Pseudo-continuous arterial spin labeling is a magnetic resonance perfusion imaging technique. It magentically labels inflowing arterial blood to serve as an endogeneous tracer, resulting in complete non-invasiveness and study applicability (Grade et al. 2015). In this work, cerebral blood flow was imaged at 3 Tesla and at 7 Tesla, and an approach was developed to study blood-brain barrier integrity.

The measurement of cerebral blood flow is of interest for clinical investigations, neuroscientific research and population studies. The low signal-to-noise ratio of pCASL data necessitates a trade-off between measurement time and data quality (Grade et al. 2015). Therefore, in this work, first the SNR efficiency enhancing Hadamard encoding was implemented and encoding schemes optimized for 3 Tesla and 7 Tesla field strengths including 3 and 7 PLDs. Then, two dedicated protocols were implemented, one of which enables an executability on earlier scanner systems. Additionally, a pipeline was developed for data postprocessing and perfusion quantification. In vivo measurements using the two 7:09 min and 8:42 min long protocols obtained data and quantified perfusions of high quality. A comparison of Hadamard-derived data and multi-PLD data with matched measurement duration, demonstrated the efficiency and a markedly improved modelability of arterial transit times for Hadamard-encoded data. For a potential application in longitudinal, multicenter studies, such as the Rhineland study, a test-retest measurement series was performed on two MRI scanners with elderly subjects. The resulting excellent test-retest reliabilities and good device independences suggest a suitability of the sequence, the implemented protocols and the processing routine for such study purposes. The clinical applicability of the protocol was also demonstrated in an epilepsy patient. In this case, the anatomical location of observed perfusion changes was functionally consistent with the clinical seizure presentation.

In addition to cerebral perfusion, also the T_2 relaxation time of the ASL signal may be a parameter of interest. However, it is rarely considered in the current application of ASL. This quantity offers an modeling approach to spatially assign the magnetically labeled blood-water protons to the intravascular or extravascular compartment based on their characteristic T_2 times (Ohene et al. 2019; Wells et al. 2012). This localization approach may also allow the analysis of transitions between cerebral compartments and thus conclusions

about the permeability of the blood-brain barrier. Therefore, in this work, a preparation module for inducing a T_2 weighting was implemented and the reliability and reproducibility of this little studied quantity practically proven within a test-retest study including 10 young subjects. A regional variance of the reliabilities was found as well as a dependence on the PLDs at which the T_2 weighting was performed. Further, an approach for the compartmentalization of T_2-weighted ASL data was developed. The result were simplified model assumptions and additional supporting measurements for the approximation of input model parameters, which stabilized the biexponential compartmentalization of the SNR-limited ASL data. Including the supporting measurements, the total measurement time of the protocol with 7 T_2 weighting times and 4 PLDs was below one hour. A compartmentalization was successfully demonstrated in three subjects for proof-of-concept. The modeled extravascular fractions of labeled blood water protons in GM increased for longer PLDs in qualitative agreement with the expected blood-brain barrier transition dynamics.

At ultra-high field, pCASL perfusion imaging benefits not only from the inherently higher SNR, but also from longer T_1 relaxation times and a slower decay of the ASL signal. However, there is a rise in the specific absorption rate with increasing magnetic field strength, which is a limiting factor for the spin labeling (Teeuwisse et al. 2010). In this work, the sequence was ported to the latest Siemens Magnetom 7 T scanner system. The energy applied through RF pulses was reduced by the application of a 3D EPI sequence, parallel imaging, and SAR-matched VERSE labeling pulses. An optimization of the background suppression for 7 T relaxation times of CSF, GM and WM demonstrated an adequate signal suppression in simulations and also for in vivo measurement data. At the first time, VERSE pulse-based pCASL imaging was performed with the current scanner system in CP mode using the in-house developed pCASL sequence. A perfusion-weighted signal was obtained throughout the cerebrum. This signal is deteriorated by magnetic field inhomogeneities, which are more pronounced at higher field strengths and reduce the labeling efficiency. One compensation approach is the adjustment of the labeling pulses in parallel pulse transmission, which was addressed by implementing two pTx concepts: static pTx (or B_1 shimming) and full pTx. Sequence simulations show the capability to calculate full pTx pulses using the implemented software and sequence framework, which are Hann-shaped spokes with matched pCASL labeling gradients. For static pTx, B_1 mappig results reveal a volume-selective B_1 shim of the labeling region as beneficial for the labeling pulses. Results also indicate a patient-specific shim to be advantageous for the imaging pulses. In vivo measurements support these findings and demonstrated an improvement of absolute perfusion-weighted data when applying a static shimming compared to measurements with a pulse transmission in CP mode.

To summarize, protocols and a postprocessing routine for clinical and research ASL perfusion measurements emerge from this work, a suitable modeling approach for compartmentalizing T_2-weighted ASL data is presented, and a contribution to the improvement of ASL perfusion imaging at 7 Tesla is made.

It remains to be clarified if reliable perfusion data can also be obtained in large-scale cohort studies. These studies may need to use a predefined, fixed gap instead of aligning the labeling slab to the individual vessel anatomy. Its impact and the rate of study participants with an inadequate labeling must be determined in order to assess the trade-off to a manual adjustment. This in turn would be subjected to a multiple operator variability.

The compartmentalization approach and the inference of blood-brain barrier permeabilities remains to be validated. This could be accomplished by an application in patients with know blood-brain barrier dysfunction, as glioblastoma brain tumors (Karmur et al. 2020).

A major, not yet established approach to improve perfusion measurements at 7 Tesla is the use of full pTx pulses. In this work, SAR limitations prevent their executability on the scanner. In the future, this limitation could be mitigated by adjusted SAR models (Eichfelder & Gebhardt 2011). In this case, a ROI-based pulse optimization within the arterial blood-supplying vessels would be of interest, as well as a comparison with static pTx results.

References

Abragam, A., 1961. *The principles of nuclear magnetism*, Clarendon Press.

Ahir, B.K., Engelhard, H.H. & Lakka, S.S., 2020. Tumor development and angiogenesis in adult brain tumor: glioblastoma. *Molecular Neurobiology*, 57(5), pp.2461–2478. Available at: https://doi.org/10.1007/s12035-020-01892-8.

Aibinu, A. et al., 2008. MRI reconstruction using discrete fourier transform: A tutorial. *World Academy of Science Engineering and Technology*, 42, p.

Alsaedi, A. et al., 2018. Overview and critical appraisal of arterial spin labelling technique in brain perfusion imaging. *Contrast Media & Molecular Imaging*, 2018, pp.1–15. Available at: https://doi.org/10.1155/2018/5360375.

Alsop, D.C. et al., 2014. Recommended implementation of arterial spin-labeled perfusion MRI for clinical applications: A consensus of the ISMRM perfusion study group and the european consortium for ASL in dementia. *Magnetic Resonance in Medicine*, 73(1), pp.102–116. Available at: https://doi.org/10.1002/mrm.25197.

Andersson, J.L.R., Skare, S. & Ashburner, J., 2003. How to correct susceptibility distortions in spin-echo echo-planar images: Application to diffusion tensor imaging. *NeuroImage*, 20(2), pp.870–888. Available at: https://doi.org/10.1016/s1053-8119(03)00336-7.

Andronesi, O.C. et al., 2010. Spectroscopic imaging with improved gradient modulated constant adiabaticity pulses on high-field clinical scanners. *Journal of Magnetic Resonance*, 203(2), pp.283–293. Available at: https://doi.org/10.1016/j.jmr.2010.01.010.

Arvanitis, C.D., Ferraro, G.B. & Jain, R.K., 2019. The blood-brain barrier and blood-tumour barrier

in brain tumours and metastases. *Nature Reviews Cancer*. Available at: https://doi.org/10.1038/s41568-019-0205-x.

Álvarez, M.G.M., Stobbe, R.W. & Beaulieu, C., 2019. High resolution continuous arterial spin labeling of human cerebral perfusion using a separate neck tagging RF coil Q. Jiang, ed. *PLOS ONE*, 14(4), p.e0215998. Available at: https://doi.org/10.1371/journal.pone.0215998.

Balchandani, P. & Naidich, T.P., 2014. Ultra-high-field MR neuroimaging. *American Journal of Neuroradiology*, 36(7), pp.1204–1215. Available at: https://doi.org/10.3174/ajnr.a4180.

Balchandani, P., Pauly, J. & Spielman, D., 2010. Designing adiabatic radio frequency pulses using the Shinnar-Le Roux algorithm. *Magnetic Resonance in Medicine*, 64(3), pp.843–851. Available at: https://doi.org/10.1002/mrm.22473.

Barth, M. & Poser, B.A., 2011. Advances in high-field BOLD fMRI. *Materials*, 4(11), pp.1941–1955. Available at: https://doi.org/10.3390/ma4111941.

Bartlett, J.W. & Frost, C., 2008. Reliability, repeatability and reproducibility: Analysis of measurement errors in continuous variables. *Ultrasound in Obstetrics and Gynecology*, 31(4), pp.466–475. Available at: https://doi.org/10.1002/uog.5256.

Beckett, A.J.S. et al., 2020. Comparison of BOLD and CBV using 3D EPI and 3D GRASE for cortical layer functional MRI at 7 T. *Magnetic Resonance in Medicine*, 84(6), pp.3128–3145. Available at: https://doi.org/10.1002/mrm.28347.

Bernstein, M.A., King, K.F. & Zhou, X.J., 2004. *Handbook of MRI pulse sequences*, Elsevier. Available at: https://doi.org/10.1016/b978-0-12-092861-3.x5000-6.

Berry, E.S.K., Jezzard, P. & Okell, T.W., 2019. Off-resonance correction for pseudo-continuous arterial spin labeling using the optimized encoding scheme. *NeuroImage*, 199, pp.304–312. Available at: https://doi.org/10.1016/j.neuroimage.2019.05.083.

Bladt, P. et al., 2020. Supporting measurements or more averages? How to quantify cerebral blood flow most reliably in 5 minutes by arterial spin labeling. *Magnetic Resonance in Medicine*, 84(5), pp.2523–2536. Available at: https://doi.org/10.1002/mrm.28314.

Boland, M. et al., 2018. Accelerated 3D-GRASE imaging improves quantitative multiple post labeling delay arterial spin labeling. *Magnetic Resonance in Medicine*, 80(6), pp.2475–2484. Available at: https://doi.org/10.1002/mrm.27226.

Boland, M. et al., 2019. Robust and SAR-efficient whole-brain pseudo-continuous ASL at 7T. *In: Proc. Intl. Soc. Mag. Reson. Med. 27, 2019. Abstract 4963.*

Borogovac, A. & Asllani, I., 2012. Arterial spin labeling (ASL) fMRI: Advantages, theoretical constrains and experimental challenges in neurosciences. *International Journal of Biomedical Imaging*, 2012, pp.1–13. Available at: https://doi.org/10.1155/2012/818456.

Breuer, F.A. et al., 2005. Controlled aliasing in parallel imaging results in higher acceleration (CAIPIRINHA)

for multi-slice imaging. *Magnetic Resonance in Medicine*, 53(3), pp.684–691. Available at: https://doi.org/10.1002/mrm.20401.

Brown, R.W. et al. eds., 2014. *Magnetic resonance imaging*, John Wiley & Sons Ltd. Available at: https://doi.org/10.1002/9781118633953.

Bushberg, J.T. et al., 2001. *The essential physics of medical imaging* 2. ed., Lippincott Williams & Wilkins.

Buxton, R.B. et al., 1998. A general kinetic model for quantitative perfusion imaging with arterial spin labeling. *Magnetic Resonance in Medicine*, 40(3), pp.383–396. Available at: https://doi.org/10.1002/mrm.1910400308.

Callaghan, P.T., 1993. *Principles of nuclear magnetic resonance microscopy*, Oxford: Clarendon Press.

Carrington, A. & McLachlan, A.D., 1969. *Introduction to magnetic resonance*, Harper & Row.

Chappell, M.A. et al., 2009. Variational bayesian inference for a nonlinear forward model. *IEEE Transactions on Signal Processing*, 57(1), pp.223–236. Available at: https://doi.org/10.1109/tsp.2008.2005752.

Chen, J.J. & Pike, G.B., 2009. Human whole blood T2 relaxometry at 3 Tesla. *Magnetic Resonance in Medicine*, 61(2), pp.249–254. Available at: https://doi.org/10.1002/mrm.21858.

Chen, Y., Wang, D.J.J. & Detre, J.A., 2011. Comparison of arterial transit times estimated using arterial spin labeling. *Magnetic Resonance Materials in Physics, Biology and Medicine*, 25(2), pp.135–144. Available at: https://doi.org/10.1007/s10334-011-0276-5.

Cho, Y. & Yoo, H., 2020. RF heating of implants in MRI: Electromagnetic analysis and solutions. *Investigative Magnetic Resonance Imaging*, 24(2), p.67. Available at: https://doi.org/10.13104/imri.2020.24.2.67.

Cicchetti, D.V., 1994. Guidelines, criteria, and rules of thumb for evaluating normed and standardized assessment instruments in psychology. *Psychological Assessment*, 6(4), pp.284–290. Available at: https://doi.org/10.1037/1040-3590.6.4.284.

Clement, P. et al., 2017. Variability of physiological brain perfusion in healthy subjects - a systematic review of modifiers. Considerations for multi-center ASL studies. *Journal of Cerebral Blood Flow & Metabolism*, 38(9), pp.1418–1437. Available at: https://doi.org/10.1177/0271678x17702156.

Collins, C.M. & Wang, Z., 2011. Calculation of radiofrequency electromagnetic fields and their effects in MRI of human subjects. *Magnetic Resonance in Medicine*, 65(5), pp.1470–1482. Available at: https://doi.org/10.1002/mrm.22845.

Cuenod, C.A. & Balvay, D., 2013. Perfusion and vascular permeability: Basic concepts and measurement in DCE-CT and DCE-MRI. *Diagnostic and Interventional Imaging*, 94(12), pp.1187–1204. Available at: https://doi.org/10.1016/j.diii.2013.10.010.

Dager, S.R. & Friedman, S.D., 2000. Brain imaging and the effects of caffeine and nicotine. *Annals of Medicine*, 32(9), pp.592–599. Available at: https://doi.org/10.3109/07853890009002029.

Dai, W. et al., 2008. Continuous flow-driven inversion for arterial spin labeling using pulsed radio

frequency and gradient fields. *Magnetic Resonance in Medicine*, 60(6), pp.1488–1497. Available at: https://doi.org/10.1002/mrm.21790.

Davidovits, P., 2008. *Physics in biology and medicine* 3rd ed., Academic Press.

Deshmane, A. et al., 2012. Parallel MR imaging. *Journal of Magnetic Resonance Imaging*, 36(1), pp.55–72. Available at: https://doi.org/10.1002/jmri.23639.

Detre, J.A., 2006. Clinical applicability of functional MRI. *Journal of Magnetic Resonance Imaging*, 23(6), pp.808–815. Available at: https://doi.org/10.1002/jmri.20585.

Detre, J.A. & Alsop, D.C., 1999. Perfusion magnetic resonance imaging with continuous arterial spin labeling: Methods and clinical applications in the central nervous system. *European Journal of Radiology*, 30(2), pp.115–124. Available at: https://doi.org/10.1016/s0720-048x(99)00050-9.

Dickie, B.R., Parker, G.J.M. & Parkes, L.M., 2020. Measuring water exchange across the blood-brain barrier using MRI. *Progress in Nuclear Magnetic Resonance Spectroscopy*, 116, pp.19–39. Available at: https://doi.org/10.1016/j.pnmrs.2019.09.002.

Eichfelder, G. & Gebhardt, M., 2011. Local specific absorption rate control for parallel transmission by virtual observation points. *Magnetic Resonance in Medicine*, 66(5), pp.1468–1476. Available at: https://doi.org/10.1002/mrm.22927.

Fagan, A.J. et al., 2020. 7T MR safety. *Journal of Magnetic Resonance Imaging*, 53(2), pp.333–346. Available at: https://doi.org/10.1002/jmri.27319.

Farrar, T.C., 1989. *Introduction to pulse NMR spectroscopy*, Farragut Press.

Feinberg, D.A. & Oshio, K., 1991. GRASE (gradient- and spin-echo) MR imaging: A new fast clinical imaging technique. *Radiology*, 181(2), pp.597–602. Available at: https://doi.org/10.1148/radiology.181.2.1924811.

Feng, D., 2018. *agRee: Various methods for measuring agreement*, Available at: https://CRAN.R-project.org/package=agRee.

Floyd, T.F. et al., 2003. Precision of the CASL-perfusion MRI technique for the measurement of cerebral blood flow in whole brain and vascular territories. *Journal of Magnetic Resonance Imaging*, 18(6), pp.649–655. Available at: https://doi.org/10.1002/jmri.10416.

Galbraith, S.M. et al., 2002. Reproducibility of dynamic contrast-enhanced MRI in human muscle and tumours: Comparison of quantitative and semi-quantitative analysis. *NMR in Biomedicine*, 15(2), pp.132–142. Available at: https://doi.org/10.1002/nbm.731.

Gaxiola-Valdez, I. et al., 2017. Seizure onset zone localization using postictal hypoperfusion detected by arterial spin labelling MRI. *Brain*, 140(11), pp.2895–2911. Available at: https://doi.org/10.1093/brain/awx241.

Ghariq, E. et al., 2011. Feasibility of pseudocontinuous arterial spin labeling at 7 T with whole-brain coverage. *Magnetic Resonance Materials in Physics, Biology and Medicine*, 25(2), pp.83–93. Available at: https://doi.org/10.1007/s10334-011-0297-0.

Grade, M. et al., 2015. A neuroradiologist's guide to arterial spin labeling MRI in clinical practice. *Neuroradiology*, 57(12), pp.1181–1202. Available at: https://doi.org/10.1007/s00234-015-1571-z.

Gregori, J. et al., 2012. T2-based arterial spin labeling measurements of blood to tissue water transfer in human brain. *Journal of Magnetic Resonance Imaging*, 37(2), pp.332–342. Available at: https://doi.org/10.1002/jmri.23822.

Griswold, M.A. et al., 2002. Generalized autocalibrating partially parallel acquisitions (GRAPPA). *Magnetic Resonance in Medicine*, 47(6), pp.1202–1210. Available at: https://doi.org/10.1002/mrm.10171.

Gruber, B. et al., 2018. RF coils: A practical guide for nonphysicists. *Journal of Magnetic Resonance Imaging*, 48(3), pp.590–604. Available at: https://doi.org/10.1002/jmri.26187.

Günther, M., 2007. Highly efficient accelerated acquisition of perfusion inflow series by cycled arterial spin labeling. *Proc. Intl. Soc. Mag. Reson. Med.*, 15, p.380.

Hales, P.W. & Clark, C.A., 2012. Combined arterial spin labeling and diffusion-weighted imaging for noninvasive estimation of capillary volume fraction and permeability-surface product in the human brain. *Journal of Cerebral Blood Flow & Metabolism*, 33(1), pp.67–75. Available at: https://doi.org/10.1038/jcbfm.2012.125.

Haller, S. et al., 2016. Arterial spin labeling perfusion of the brain: Emerging clinical applications. *Radiology*, 281(2), pp.337–356. Available at: https://doi.org/10.1148/radiol.2016150789.

Hargreaves, B.A. et al., 2004. Variable-rate selective excitation for rapid MRI sequences. *Magnetic Resonance in Medicine*, 52(3), pp.590–597. Available at: https://doi.org/10.1002/mrm.20168.

Hattingen, E. et al., 2013. Quantitative T2 mapping of recurrent glioblastoma under bevacizumab improves monitoring for non-enhancing tumor progression and predicts overall survival. *Neuro-Oncology*, 15(10), pp.1395–1404. Available at: https://doi.org/10.1093/neuonc/not105.

He, X., Raichle, M.E. & Yablonskiy, D.A., 2011. Transmembrane dynamics of water exchange in human brain. *Magnetic Resonance in Medicine*, 67(2), pp.562–571. Available at: https://doi.org/10.1002/mrm.23019.

Hecht, H.G., 1967. *Magnetic resonance spectroscopy*, John Wiley & Sons.

Hennel, F., 2014. The effective phase of soft RF pulses. *Concepts in Magnetic Resonance Part A*, 43(4), pp.127–137. Available at: https://doi.org/10.1002/cmr.a.21312.

Hernandez-Garcia, L., Lahiri, A. & Schollenberger, J., 2019. Recent progress in ASL. *NeuroImage*, 187, pp.3–16. Available at: https://doi.org/10.1016/j.neuroimage.2017.12.095.

Heye, A.K. et al., 2014. Assessment of blood-brain barrier disruption using dynamic contrast-enhanced MRI. A systematic review. *NeuroImage: Clinical*, 6, pp.262–274. Available at: https://doi.org/10.1016/j.nicl.2014.09.002.

Istratov, A.A. & Vyvenko, O.F., 1999. Exponential analysis in physical phenomena. *Review of Scientific Instruments*, 70(2), pp.1233–1257. Available at: https://doi.org/10.1063/1.1149581.

Jancke, H., 1998. NMR als primäre analytische Meßmethode. *Nachrichten aus Chemie, Technik und Laboratorium*, 46(7-8), pp.720–722. Available at: http://dx.doi.org/10.1002/nadc.19980460711.

Jenkinson, M. et al., 2002. Improved optimization for the robust and accurate linear registration and motion correction of brain images. *NeuroImage*, 17(2), pp.825–841. Available at: https://doi.org/10.1006/nimg.2002.1132.

Jiang, L. et al., 2010. Reliability and reproducibility of perfusion MRI in cognitively normal subjects. *Magnetic Resonance Imaging*, 28(9), pp.1283–1289. Available at: https://doi.org/10.1016/j.mri.2010.05.002.

Johnson, D.R. et al., 2017. 2016 updates to the WHO brain tumor classification system: What the radiologist needs to know. *RadioGraphics*, 37(7), pp.2164–2180. Available at: https://doi.org/10.1148/rg.2017170037.

Jung, B.A. & Weigel, M., 2013. Spin echo magnetic resonance imaging. *Journal of Magnetic Resonance Imaging*, 37(4), pp.805–817. Available at: https://doi.org/10.1002/jmri.24068.

Karmur, B.S. et al., 2020. Blood-brain barrier disruption in neuro-oncology: Strategies, failures, and challenges to overcome. *Frontiers in Oncology*, 10. Available at: https://doi.org/10.3389/fonc.2020.563840.

Katscher, U. et al., 2002. Transmit SENSE. *Magnetic Resonance in Medicine*, 49(1), pp.144–150. Available at: https://doi.org/10.1002/mrm.10353.

Kilroy, E. et al., 2014. Reliability of two-dimensional and three-dimensional pseudo-continuous arterial spin labeling perfusion MRI in elderly populations: Comparison with 15o-water positron emission tomography. *Journal of Magnetic Resonance Imaging*, 39(4), pp.931–939. Available at: https://doi.org/10.1002/jmri.24246.

Krishnamurthy, L.C. et al., 2013. Dependence of blood T2 on oxygenation at 7 t: In vitro calibration and in vivo application. *Magnetic Resonance in Medicine*, 71(6), pp.2035–2042. Available at: https://doi.org/10.1002/mrm.24868.

Lajoie, I., Tancredi, F.B. & Hoge, R.D., 2017. The impact of inspired oxygen levels on calibrated fMRI measurements of M, OEF and resting CMRO2 using combined hypercapnia and hyperoxia N. Zhang, ed. *PLOS ONE*, 12(3), p.e0174932. Available at: https://doi.org/10.1371/journal.pone.0174932.

Lancaster, J.L. et al., 2000. Automated talairach atlas labels for functional brain mapping. *Human Brain Mapping*, 10(3), pp.120–131. Available at: https://doi.org/10.1002/1097-0193(200007)10:3%3C120::aid-hbm30%3E3.0.co;2-8.

Laurienti, P.J. et al., 2003. Relationship between caffeine-induced changes in resting cerebral perfusion and blood oxygenation level-dependent signal. *American Journal of Neuroradiology*, 24(8), pp.1607–1611. Available at: http://www.ajnr.org/content/24/8/1607.

Lawrence, K.S.St., Owen, D. & Wang, D.J.J., 2011. A two-stage approach for measuring vascular water exchange and arterial transit time by diffusion-weighted perfusion MRI. *Magnetic Resonance in Medicine*, 67(5), pp.1275–1284. Available at: https://doi.org/10.1002/mrm.23104.

Leoni, R.F. et al., 2017. Cerebral blood flow and vasoreactivity in aging: An arterial spin labeling study.

Brazilian Journal of Medical and Biological Research, 50(4). Available at: https://doi.org/10.1590/1414-431x20175670.

Levitt, M.H., 2007. Composite pulses. In *eMagRes*. American Cancer Society.

Li, K. et al., 2005. Four-phase single-capillary stepwise model for kinetics in arterial spin labeling MRI. *Magnetic Resonance in Medicine*, 53(3), pp.511–518. Available at: https://doi.org/10.1002/mrm.20390.

Li, W. & Zijl, P.C.M., 2020. Quantitative theory for the transverse relaxation time of blood water. *NMR in Biomedicine*. Available at: https://doi.org/10.1002/nbm.4207.

Lin, Z. et al., 2018. Non-contrast MR imaging of blood-brain barrier permeability to water. *Magnetic Resonance in Medicine*, 80(4), pp.1507–1520. Available at: https://doi.org/10.1002/mrm.27141.

Liu, P., Uh, J. & Lu, H., 2010. Determination of spin compartment in arterial spin labeling MRI. *Magnetic Resonance in Medicine*, 65(1), pp.120–127. Available at: https://doi.org/10.1002/mrm.22601.

Lu, H. et al., 2004. Determining the longitudinal relaxation time (T1) of blood at 3.0 Tesla. *Magnetic Resonance in Medicine*, 52(3), pp.679–682. Available at: https://doi.org/10.1002/mrm.20178.

Lu, H. et al., 2005. Routine clinical brain MRI sequences for use at 3.0 Tesla. *Journal of Magnetic Resonance Imaging*, 22(1), pp.13–22. Available at: https://doi.org/10.1002/jmri.20356.

Maccotta, L., Detre, J.A. & Alsop, D.C., 1997. The efficiency of adiabatic inversion for perfusion imaging by arterial spin labeling. *NMR in Biomedicine*, 10(4-5), pp.216–221. Available at: https://doi.org/10.1002/(sici)1099-1492(199706/08)10:4/5%3C216::aid-nbm468%3E3.0.co;2-u.

MacIntosh, B.J. et al., 2010. Assessment of arterial arrival times derived from multiple inversion time pulsed arterial spin labeling MRI. *Magnetic Resonance in Medicine*, 63(3), pp.641–647. Available at: https://doi.org/10.1002/mrm.22256.

MacIntosh, B.J. et al., 2014. Regional cerebral arterial transit time hemodynamics correlate with vascular risk factors and cognitive function in men with coronary artery disease. *American Journal of Neuroradiology*, 36(2), pp.295–301. Available at: https://doi.org/10.3174/ajnr.a4094.

Mai, J.K., Majtanik, M. & Paxinos, G., 2015. *Atlas of the human brain*, Amsterdam Boston: Academic Press.

Majumdar, S. et al., 1986. Errors in the measurements ofT2 using multiple-echo MRI techniques. I. Effects of radiofrequency pulse imperfections. *Magnetic Resonance in Medicine*, 3(3), pp.397–417. Available at: https://doi.org/10.1002/mrm.1910030305.

Maleki, N., Dai, W. & Alsop, D.C., 2011. Optimization of background suppression for arterial spin labeling perfusion imaging. *Magnetic Resonance Materials in Physics, Biology and Medicine*, 25(2), pp.127–133. Available at: https://doi.org/10.1007/s10334-011-0286-3.

Markl, M. & Leupold, J., 2012. Gradient echo imaging. *Journal of Magnetic Resonance Imaging*, 35(6), pp.1274–1289. Available at: https://doi.org/10.1002/jmri.23638.

Matheson, G.J., 2019. We need to talk about reliability: Making better use of test-retest studies for study

design and interpretation. *PeerJ*, 7, p.e6918. Available at: https://doi.org/10.7717/peerj.6918.

Mazziotta, J. et al., 2001. A probabilistic atlas and reference system for the human brain: International consortium for brain mapping (ICBM) R. Kötter, ed. *Philosophical Transactions of the Royal Society of London. Series B: Biological Sciences*, 356(1412), pp.1293–1322. Available at: https://doi.org/10.1098/rstb.2001.0915.

Meixner, C.R. et al., 2021. Hybrid B1+-shimming and gradient adaptions for improved pseudo-continuous arterial spin labeling at 7 Tesla. *Magnetic Resonance in Medicine*. Available at: https://doi.org/10.1002/mrm.28982.

Meyerand, M.E. et al., 1999. Classification of biopsy-confirmed brain tumors using single-voxel MR spectroscopy. *American Journal of Neuroradiology*, 20(1), pp.117–123. Available at: http://www.ajnr.org/content/20/1/117.abstract.

Milford, D. et al., 2015. Mono-exponential fitting in T2-relaxometry: Relevance of offset and first echo X. Fan, ed. *PLOS ONE*, 10(12), p.e0145255. Available at: https://doi.org/10.1371/journal.pone.0145255.

Mitrouli, M., 2014. Sylvester hadamard matrices revisited. *Special Matrices*, 2(1). Available at: https://doi.org/10.2478/spma-2014-0013.

Mugler, J.P., 2014. Optimized three-dimensional fast-spin-echo MRI. *Journal of Magnetic Resonance Imaging*, 39(4), pp.745–767. Available at: https://doi.org/10.1002/jmri.24542.

Murphy, W.G., 2014. The sex difference in haemoglobin levels in adults - mechanisms, causes, and consequences. *Blood Reviews*, 28(2), pp.41–47. Available at: https://doi.org/10.1016/j.blre.2013.12.003.

Narsude, M. et al., 2015. Three-dimensional echo planar imaging with controlled aliasing: A sequence for high temporal resolution functional MRI. *Magnetic Resonance in Medicine*, 75(6), pp.2350–2361. Available at: https://doi.org/10.1002/mrm.25835.

Nezafat, R. et al., 2006. B1-insensitive T2 preparation for improved coronary magnetic resonance angiography at 3 T. *Magnetic Resonance in Medicine*, 55(4), pp.858–864. Available at: https://doi.org/10.1002/mrm.20835.

Nitz, W.R. ed., 2012. Systemkomponenten eines MRT. In *MRT-Guide für MTRA/RT*. Georg Thieme Verlag. Available at: https://doi.org/10.1055/b-0036-136486.

Ogg, R.J., Kingsley, R.B. & Taylor, J.S., 1994. WET, a T1- and B1-insensitive water-suppression method for in vivo localized 1H NMR spectroscopy. *Journal of Magnetic Resonance, Series B*, 104(1), pp.1–10. Available at: https://doi.org/10.1006/jmrb.1994.1048.

Ohene, Y. et al., 2019. Non-invasive MRI of brain clearance pathways using multiple echo time arterial spin labelling: An aquaporin-4 study. *NeuroImage*, 188, pp.515–523. Available at: https://doi.org/10.1016/j.neuroimage.2018.12.026.

Orzada, S. et al., 2020. Local SAR compression with overestimation control to reduce maximum relative SAR overestimation and improve multi-channel RF array performance. *Magnetic Resonance*

Materials in Physics, Biology and Medicine, 34(1), pp.153–163. Available at: https://doi.org/10.1007/s10334-020-00890-0.

Padormo, F. et al., 2015. Parallel transmission for ultrahigh-field imaging. *NMR in Biomedicine*, 29(9), pp.1145–1161. Available at: https://doi.org/10.1002/nbm.3313.

Parkes, L.M., 2005. Quantification of cerebral perfusion using arterial spin labeling: Two-compartment models. *Journal of Magnetic Resonance Imaging*, 22(6), pp.732–736. Available at: https://doi.org/10.1002/jmri.20456.

Paulson, O., 2002. Blood-brain barrier, brain metabolism and cerebral blood flow. *European Neuropsychopharmacology*, 12(6), pp.495–501. Available at: https://doi.org/10.1016/s0924-977x(02)00098-6.

Pauly, J. et al., 1991. Parameter relations for the Shinnar-Le Roux selective excitation pulse design algorithm (NMR imaging). *IEEE Transactions on Medical Imaging*, 10(1), pp.53–65. Available at: https://doi.org/10.1109/42.75611.

Pauly, J., Nishimura, D. & Macovski, A., 2011. A *k*-space analysis of small-tip-angle excitation. *Journal of Magnetic Resonance*, 213(2), pp.544–557. Available at: https://doi.org/10.1016/j.jmr.2011.09.023.

Perera, T. et al., 2020. Localizing the seizure onset zone by comparing patient postictal hypoperfusion to healthy controls. *Journal of Neuroscience Research*, 98(8), pp.1517–1531. Available at: https://doi.org/10.1002/jnr.24646.

Petersen, E.T., Lim, T. & Golay, X., 2006. Model-free arterial spin labeling quantification approach for perfusion MRI. *Magnetic Resonance in Medicine*, 55(2), pp.219–232. Available at: https://doi.org/10.1002/mrm.20784.

Pruessmann, K.P. et al., 1999. SENSE: Sensitivity encoding for fast MRI. *Magnetic Resonance in Medicine*, 42(5), pp.952–962. Available at: https://doi.org/10.1002/(sici)1522-2594(199911)42:5%3C952::aid-mrm16%3E3.0.co;2-s.

Qin, Q. et al., 2013. Three-dimensional whole-brain perfusion quantification using pseudo-continuous arterial spin labeling MRI at multiple post-labeling delays: Accounting for both arterial transit time and impulse response function. *NMR in Biomedicine*, 27(2), pp.116–128. Available at: https://doi.org/10.1002/nbm.3040.

R Core Team, 2017. *R: A language and environment for statistical computing*, Vienna: R Foundation for Statistical Computing. Available at: https://www.R-project.org/.

Radbruch, A. et al., 2011. Relevance of T2 signal changes in the assessment of progression of glioblastoma according to the response assessment in neurooncology criteria. *Neuro-Oncology*, 14(2), pp.222–229. Available at: https://doi.org/10.1093/neuonc/nor200.

Rajiah, P. & Bolen, M.A., 2014. Cardiovascular MR imaging at 3 T: Opportunities, challenges, and solutions. *RadioGraphics*, 34(6), pp.1612–1635. Available at: https://doi.org/10.1148/rg.346140048.

Razek, A.A.K.A. et al., 2019. Clinical applications of arterial spin labeling in brain tumors. *Journal of Computer Assisted Tomography*, 43(4), pp.525–532. Available at: https://doi.org/10.1097/rct.0000000000000873.

Reeder, S.B., Herzka, D.A. & McVeigh, E.R., 2004. Signal-to-noise ratio behavior of steady-state free precession. *Magnetic Resonance in Medicine*, 52(1), pp.123–130. Available at: https://doi.org/10.1002/mrm.20126.

Rietsch, S.H.G. et al., 2017. An 8-channel transceiver 7-channel receive RF coil setup for high SNR ultrahigh-field MRI of the shoulder at 7T. *Medical Physics*, 44(12), pp.6195–6208. Available at: https://doi.org/10.1002/mp.12612.

Roemer, P.B. et al., 1990. The NMR phased array. *Magnetic Resonance in Medicine*, 16(2), pp.192–225. Available at: https://doi.org/10.1002/mrm.1910160203.

Rooney, W.D. et al., 2007. Magnetic field and tissue dependencies of human brain longitudinal 1H2O relaxation in vivo. *Magnetic Resonance in Medicine*, 57(2), pp.308–318. Available at: https://doi.org/10.1002/mrm.21122.

Rosenow, F., 2001. Presurgical evaluation of epilepsy. *Brain*, 124(9), pp.1683–1700. Available at: https://doi.org/10.1093/brain/124.9.1683.

Sabour, S. et al., 2017. Accuracy and precision in medical researches; common mistakes and misinterpretations. *World Journal of Research and Review (WJRR)*, 4, pp.058–060.

Saekho, S. et al., 2006. Fast-kz three-dimensional tailored radiofrequency pulse for reduced B1 inhomogeneity. *Magnetic Resonance in Medicine*, 55(4), pp.719–724. Available at: https://doi.org/10.1002/mrm.20840.

Schmid, S. et al., 2015. Time-efficient determination of spin compartments by time-encoded pCASL T2-relaxation-under-spin-tagging and its application in hemodynamic characterization of the cerebral border zones. *NeuroImage*, 123, pp.72–79. Available at: https://doi.org/10.1016/j.neuroimage.2015.08.025.

Schünke, M. et al., 2006. *Prometheus: LernAtlas der Anatomie*, Stuttgart New York: Georg Thieme Verlag.

Segbers, M. et al., 2010. Shaping and timing gradient pulses to reduce MRI acoustic noise. *Magnetic Resonance in Medicine*, 64(2), pp.546–553. Available at: https://doi.org/10.1002/mrm.22366.

Serrai, H. et al., 2019. Using variable-rate selective excitation (VERSE) radiofrequency pulses to reduce power deposition in pulsed arterial spin labeling sequence at 7 Tesla. *Magnetic Resonance in Medicine*, 83(2), pp.645–652. Available at: https://doi.org/10.1002/mrm.27944.

Shimizu, F., Nishihara, H. & Kanda, T., 2018. Blood-brain barrier dysfunction in immuno-mediated neurological diseases. *Immunological Medicine*, 41(3), pp.120–128. Available at: https://doi.org/10.1080/25785826.2018.1531190.

Shoukri, M.M. et al., 2008. Comparison of two dependent within subject coefficients of variation to evaluate the reproducibility of measurement devices. *BMC Medical Research Methodology*, 8(1). Available at: https://doi.org/10.1186/1471-2288-8-24.

Shrout, P.E. & Fleiss, J.L., 1979. Intraclass correlations: Uses in assessing rater reliability. *Psychological Bulletin*, 86(2), pp.420–428. Available at: https://doi.org/10.1037/0033-2909.86.2.420.

Slichter, C.P., 1963. *Principles of magnetic resonance*, Harper & Row.

Smith, K.J. & Ainslie, P.N., 2017. Regulation of cerebral blood flow and metabolism during exercise. *Experimental Physiology*, 102(11), pp.1356–1371. Available at: https://doi.org/10.1113/ep086249.

Smith, S.M. et al., 2004. Advances in functional and structural MR image analysis and implementation as FSL. *NeuroImage*, 23, pp.S208–S219. Available at: https://doi.org/10.1016/j.neuroimage.2004.07.051.

Smith, S.M., 2002. Fast robust automated brain extraction. *Human Brain Mapping*, 17(3), pp.143–155. Available at: https://doi.org/10.1002/hbm.10062.

Sokolska, M. et al., 2019. Effect of labelling plane angulation and position on labelling efficiency and cerebral blood flow quantification in pseudo-continuous arterial spin labelling. *Magnetic Resonance Imaging*, 59, pp.61–67. Available at: https://doi.org/10.1016/j.mri.2019.02.007.

Sourbron, S.P. & Buckley, D.L., 2011. Tracer kinetic modelling in MRI: Estimating perfusion and capillary permeability. *Physics in Medicine and Biology*, 57(2), pp.R1–R33. Available at: https://doi.org/10.1088/0031-9155/57/2/r1.

Stenger, V.A., Noll, D.C. & Boada, F.E., 1998. Partial fourier reconstruction for three-dimensional gradient echo functional MRI: Comparison of phase correction methods. *Magnetic Resonance in Medicine*, 40(3), pp.481–490. Available at: https://doi.org/10.1002/mrm.1910400320.

Stirnberg, R. et al., 2017. Rapid whole-brain resting-state fMRI at 3 T: Efficiency-optimized three-dimensional EPI versus repetition time-matched simultaneous-multi-slice EPI. *NeuroImage*, 163, pp.81–92. Available at: https://doi.org/10.1016/j.neuroimage.2017.08.031.

Stirnberg, R. & Stöcker, T., 2020. Segmented k-space blipped-controlled aliasing in parallel imaging for high spatiotemporal resolution EPI. *Magnetic Resonance in Medicine*, 85(3), pp.1540–1551. Available at: https://doi.org/10.1002/mrm.28486.

Suetens, P., 2009. *Fundamentals of medical imaging*, Cambridge University Press. Available at: https://doi.org/10.1017/cbo9780511596803.

Sweeney, M.D., Sagare, A.P. & Zlokovic, B.V., 2018. Blood-brain barrier breakdown in alzheimer disease and other neurodegenerative disorders. *Nature Reviews Neurology*, 14(3), pp.133–150. Available at: https://doi.org/10.1038/nrneurol.2017.188.

Symms, M. et al., 2004. A review of structural magnetic resonance neuroimaging. *Journal of Neurology, Neurosurgery & Psychiatry*, 75(9), pp.1235–1244. Available at: https://jnnp.bmj.com/content/75/9/1235.

Tabelow, K. et al., 2009. High-resolution fMRI: Overcoming the signal-to-noise problem. *Journal of Neuroscience Methods*, 178(2), pp.357–365. Available at: https://doi.org/10.1016/j.jneumeth.2008.12.011.

Tannús, A. & Garwood, M., 1997. Adiabatic pulses. *NMR in Biomedicine*, 10(8), pp.423–434. Available at: https://doi.org/10.1002/(sici)1099-1492(199712)10:8%3C423::aid-nbm488%3E3.0.co;2-x.

Taso, M. & Alsop, D.C., 2020. Off-resonance and flow-velocity immune ASL at low-power using pseudo-continuous saturation labeling. *In: Proc. Intl. Soc. Mag. Reson. Med. 28, 2020. Abstract 3276.*

Teeuwisse, W.M. et al., 2014. Time-encoded pseudocontinuous arterial spin labeling: Basic properties and timing strategies for human applications. *Magnetic Resonance in Medicine*, 72(6), pp.1712–1722. Available at: https://doi.org/10.1002/mrm.25083.

Teeuwisse, W.M., Webb, A.G. & van Osch, M.J.P., 2010. Arterial spin labeling at ultra-high field: All that glitters is not gold. *International Journal of Imaging Systems and Technology*, 20(1), pp.62–70. Available at: https://doi.org/10.1002/ima.20218.

Tomasi, D. & Ernst, T., 2006. A simple theory for vibration of MRI gradient coils. *Brazilian Journal of Physics*, 36(1a). Available at: https://doi.org/10.1590/s0103-97332006000100009.

Tong, Y. et al., 2020. Improving PCASL at ultra-high field using a VERSE-guided parallel transmission strategy. *Magnetic Resonance in Medicine*, 84(2), pp.777–786. Available at: https://doi.org/10.1002/mrm.28173.

Triantafyllou, C., Hoge, R.D. & Wald, L.L., 2006. Effect of spatial smoothing on physiological noise in high-resolution fMRI. *NeuroImage*, 32(2), pp.551–557. Available at: https://doi.org/10.1016/j.neuroimage.2006.04.182.

van Gemert, J. et al., 2018. High-permittivity pad design tool for 7T neuroimaging and 3T body imaging. *Magnetic Resonance in Medicine*, 81(5), pp.3370–3378. Available at: https://doi.org/10.1002/mrm.27629.

van Osch, M.J. et al., 2017. Advances in arterial spin labelling MRI methods for measuring perfusion and collateral flow. *Journal of Cerebral Blood Flow & Metabolism*, 38(9), pp.1461–1480. Available at: https://doi.org/10.1177/0271678x17713434.

Vazana, U. et al., 2016. Glutamate-mediated blood-brain barrier opening: Implications for neuroprotection and drug delivery. *Journal of Neuroscience*, 36(29), pp.7727–7739. Available at: https://doi.org/10.1523/jneurosci.0587-16.2016.

Veiseh, O. et al., 2009. Specific targeting of brain tumors with an optical/magnetic resonance imaging nanoprobe across the blood-brain barrier. *Cancer Research*, 69(15), pp.6200–6207. Available at: https://doi.org/10.1158/0008-5472.can-09-1157.

Wang, D.J.J. et al., 2013. Multi-delay multi-parametric arterial spin-labeled perfusion MRI in acute ischemic stroke - comparison with dynamic susceptibility contrast enhanced perfusion imaging. *NeuroImage: Clinical*, 3, pp.1–7. Available at: https://doi.org/10.1016/j.nicl.2013.06.017.

Wang, K. et al., 2021. Optimization of pseudo-continuous arterial spin labeling at 7T with parallel transmission B1 shimming. *Magnetic Resonance in Medicine*. Available at: https://doi.org/10.1002/mrm.28988.

Wang, Y. & Liu, T., 2014. Quantitative susceptibility mapping (QSM): Decoding MRI data for a tissue magnetic biomarker. *Magnetic Resonance in Medicine*, 73(1), pp.82–101. Available at: https://doi.org/10.1002/mrm.25358.

Weinberger, O. et al., 2016. Local multi-channel RF surface coil versus body RF coil transmission for cardiac magnetic resonance at 3 Tesla: Which configuration is winning the game? H. Zhang, ed. *PLOS ONE*, 11(9), p.e0161863. Available at: https://doi.org/10.1371/journal.pone.0161863.

Weishaupt, D., Koechli, V.D. & Marincek, B., 2008. *How does MRI work? - an introduction to the physics and function of magnetic resonance imaging*, Berlin Heidelberg: Springer.

Wells, J.A. et al., 2009. Characterizing the origin of the arterial spin labelling signal in MRI using a multiecho acquisition approach. *Journal of Cerebral Blood Flow & Metabolism*, 29(11), pp.1836–1845. Available at: https://doi.org/10.1038/jcbfm.2009.99.

Wells, J.A. et al., 2012. Measuring biexponential transverse relaxation of the ASL signal at 9.4 T to estimate arterial oxygen saturation and the time of exchange of labeled blood water into cortical brain tissue. *Journal of Cerebral Blood Flow & Metabolism*, 33(2), pp.215–224. Available at: https://doi.org/10.1038/jcbfm.2012.156.

Williams, D.S. et al., 1992. Magnetic resonance imaging of perfusion using spin inversion of arterial water. *Proceedings of the National Academy of Sciences*, 89(1), pp.212–216. Available at: https://doi.org/10.1073/pnas.89.1.212.

Worthoff, W.A., Krojanski, H.G. & Suter, D., 2012. *Medizinphysik in Übungen und Beispielen*, Berlin: De Gruyter.

Wu, W.-C., Fernández-Seara, M., et al., 2007. A theoretical and experimental investigation of the tagging efficiency of pseudocontinuous arterial spin labeling. *Magnetic Resonance in Medicine*, 58(5), pp.1020–1027. Available at: https://doi.org/10.1002/mrm.21403.

Wu, W.-C., Mazaheri, Y. & Wong, E.C., 2007. The effects of flow dispersion and cardiac pulsation in arterial spin labeling. *IEEE Transactions on Medical Imaging*, 26(1), pp.84–92. Available at: https://doi.org/10.1109/tmi.2006.886807.

Yang, Q.X. et al., 2002. Analysis of wave behavior in lossy dielectric samples at high field. *Magnetic Resonance in Medicine*, 47(5), pp.982–989. Available at: https://doi.org/10.1002/mrm.10137.

Yarnykh, V.L., 2007. Actual flip-angle imaging in the pulsed steady state: A method for rapid three-dimensional mapping of the transmitted radiofrequency field. *Magnetic Resonance in Medicine*, 57(1), pp.192–200. Available at: https://doi.org/10.1002/mrm.21120.

Yip, C., Fessler, J.A. & Noll, D.C., 2005. Iterative RF pulse design for multidimensional, small-tip-angle selective excitation. *Magnetic Resonance in Medicine*, 54(4), pp.908–917. Available at: https://doi.org/10.1002/mrm.20631.

Zhang, X. et al., 2012. In vivo blood T1 measurements at 1.5 T, 3 T, and 7 T. *Magnetic Resonance in Medicine*, 70(4), pp.1082–1086. Available at: https://doi.org/10.1002/mrm.24550.

Zhao, B. et al., 2017. Blood-brain barrier disruption induced by diagnostic ultrasound combined with microbubbles in mice. *Oncotarget*, 9(4). Available at: https://doi.org/10.18632/oncotarget.23527.

Zhao, J.M. et al., 2007. Oxygenation and hematocrit dependence of transverse relaxation rates of blood at 3T. *Magnetic Resonance in Medicine*, 58(3), pp.592–597. Available at: https://doi.org/10.1002/mrm.21342.

Zhao, L. et al., 2016. Improving the robustness of pseudo-continuous arterial spin labeling to off-resonance and pulsatile flow velocity. *Magnetic Resonance in Medicine*, 78(4), pp.1342–1351. Available at: https://doi.org/10.1002/mrm.26513.

Zhao, L., Chang, C.-D. & Alsop, D.C., 2018. Controlling T2 blurring in 3D RARE arterial spin labeling acquisition through optimal combination of variable flip angles and k-space filtering. *Magnetic Resonance in Medicine*, 80(4), pp.1391–1401. Available at: https://doi.org/10.1002/mrm.27118.

Zhao, M. et al., 2007. Regional cerebral blood flow using quantitative MR angiography. *American Journal of Neuroradiology*, 28(8), pp.1470–1473. Available at: https://doi.org/10.3174/ajnr.a0582.

Zhu, Y., 2004. Parallel excitation with an array of transmit coils. *Magnetic Resonance in Medicine*, 51(4), pp.775–784. Available at: https://doi.org/10.1002/mrm.20011.

Acknowledgements

Hiermit bedanke ich mich bei allen Menschen, die mir durch ihre Unterstützung und Begleitung das Erstellen dieser Arbeit ermöglicht und die Zeit in Bonn schön gemacht haben. Hierzu zählen gemeinsame Projekte, fachlicher Rat, (freiwillige) Teilnahmen an MRT-Messungen, gemeinsame Kaffepausen, viele offene Ohren und aufbauende Worte. Ich möchte mich bei meinen Betreuern, Kollegen und Freunden bedanken. Ganz besonders freue ich mich, dass die Grenzen zwischen diesen Kategorien schwach geworden sind.

Bei einigen Menschen bedanke ich mich ganz besonders, allen vorangestellt meinen Eltern: Barbara und Siegmund Schidlowski, Anke Rühling, Annika Herbort-Willms, Bastian David, Bettina Mahlow, Christian Erich Elger, Conrad Prillwitz, Cora Berger, Difei Wang, Eberhard Pracht, Elisabeth Neuhaus, Elisabeth Soergel, Elke Hattigen, Fabian Buslaff, Florian Heesen, Frank Bertoldi, Ida Sdahl, Irene Domínguez Narciso, Jasminda Eberle, Jennifer Schlee, Jolanda Schwarz, Kai Kindsgrab, Kathrin Drossart, Lisa Gumz, Lisa Heck, Lukas vom Kolke, Maria Carolina Vargas Rivero, Mark Sdahl, Markus Boland, Marten Veldmann, Matthias Müller, Miriam Haller, Moritz Gumz, Nanette Range, Nurida Boddenberg, Peter Trautner, Philipp Ehses, Rainer Surges, Rüdiger Stirnberg, Sascha Brunheim, Stefan Arndt, Suzan Akbey, Theodor Rüber, Thomas Schultz, Tobias Bauer, Tony Stöcker, Yannik Völzke et al.